

Electrochemical Behaviour of Nanomaterials

Xiaosheng Cai

St Edmund Hall, University of Oxford

A thesis submitted for the degree of Doctor of Philosophy in

Physical and Theoretical Chemistry

Trinity Term 2019

Abstract

This thesis reports the electrochemical modification of boron doped diamond with metal nanoparticles and investigates the resulting electrochemical behaviour for common analytes in the food industry, especially in terms of fundamental mechanistic analysis. The first chapter gives a brief introduction to boron doped diamond including its synthesis, properties, and electrochemical applications. The second chapter introduces the experimental techniques used in this thesis and the theory behind them, particularly the basic principles of electrochemistry.

Chapter 3 investigates the electro-oxidation reaction mechanism of sulphite on gold macroelectrodes and on gold nanoparticle array modified boron doped diamond electrodes. A facile procedure which controls the morphology and size of gold nanoparticles is established by pulse deposition. The kinetics of sulphite oxidation on gold macroelectrodes and gold nanoparticle modified substrates are examined, and experimental voltammetry and simulation for both cases are combined to confirm the mechanism.

Chapter 4 extends the electrodeposition methods for gold nanoparticles to investigate the electrocatalytic activity towards nitrite oxidation. Two electrochemical techniques including cyclic voltammetry and pulse depositions for gold deposits are used. The resulting modified electrodes are compared and optimised for electroanalytical detection of nitrite, and herein the relationship between gold particles and the analytical performance are correlated.

Chapter 5 analyses the hydrogen peroxide electro-reduction mechanism on silver nanoparticle modified boron doped diamond electrodes. The disproportionation of hydrogen peroxide and the role of oxygen reduction during the process are examined, and

a mechanism is proposed and confirmed by voltammetric analysis plus full mechanistic simulation.

Chapter 6 further develops the previous established mechanism project to explore different effects on the electrocatalytic performance for hydrogen peroxide reduction. A number of factors including nanoparticle loading, size, and electrode decoration methods are investigated to provide implication insights for nanoparticle based electroanalysis.

Finally, Chapter 7 draws overall conclusions.

Acknowledgements

First and foremost, I would like to express my sincere and deep gratitude to my supervisors, Professor John S. Foord and Professor Richard G. Compton for accepting me as a DPhil student in both groups. Thank them for the great support and encouragements for the past less than three years in the Department of Chemistry. I am very grateful for John's endless patience, kindness and wisdom, giving me the freedom to explore the science. My enormous thanks go to Richard for his open-door policy, constructive advice, and supervision, leading me how to do the academic research. This thesis would not have been possible with their guidance and help.

I would like to thank Dr. Emina Hadzifejzovic, Dr. Mailis Lounasvuori, Dr. Luyun Jiang, Dr. Martin Martin Rosillo-Lopez, Johanna Svanberg-Larsson, Chenbo Wang, Thomas Hiu-Ming Lau, Ella Bentin, Yifan Wang, and Yue Ma in the Foord group for their help and bringing fun to the daily lab life. Great thanks go to Dr. Eden E. L. Tanner for her patience, kindness and advising when I stepped into the fundamental electrochemistry area at the very tough time. Special thanks to Dr. Chuhong Lin for her suggestion and help with the simulations. Thanks to all the members of the Compton Group past and present for their support and accompaniment no matter in the lab or even in the pub, sharing cultures and exchanging viewpoints on ranges of topics over a pint of beer or more.

Finally, I would like to give my heartfelt thanks to my parents and siblings for their never-ending support, care, and love. I could not achieve my current achievements without the selfless dedication of my parents.

Publications

1. Cai, X.; Lin, C.; Foord, J. S.; Compton, R. G., The Electrochemical Oxidation of Sulphite on Gold Electrodes. *Electroanal* **2019,** *31* (9), 1783-1796.

2. Cai, X.; Tanner, E. E. L.; Lin, C.; Ngamchuea, K.; Foord, J. S.; Compton, R. G., The mechanism of electrochemical reduction of hydrogen peroxide on silver nanoparticles. *Phys Chem Chem Phys* **2018,** *20* (3), 1608-1614.

3. Cai, X.; Foord, J. S., Influence of the gold particle electrodeposition methods on nitrite detection, in preparation.

Contents

Abstract i
Acknowledgements iii
Publications iv
Contents v
Glossary viii
Chapter 1 Introduction 1
1.1 Allotropes of carbon 1
1.2 Synthesis 5
1.2.1 High pressure high temperature technique 5
1.2.2 Chemical vapour deposition technique 6
1.3 Material structure, property and characterization 9
1.3.1 Surface morphology 12
1.3.2 Boron dopant density 13
1.3.3 Surface termination 16
1.3.4 Non-diamond carbon presence 19
1.3.5 Electrochemical properties 20
1.4 Surface modification 25
1.4.1 Surface grafting by chemical reactions 26
1.4.2 Ion implantation 27
1.4.3 Electrodeposition 27
1.5 Applications 28
1.5.1 Electroanalysis 29
1.5.2 Electrosynthesis 32
1.5.3 Electrochemical degradation 33
1.5.4 Electrocatalysis 34
1.5.5 Electrochemical energy storage 35
1.6 Aims and scope of the thesis 36
References 38
Chapter 2 Experimental techniques and the theory behind them 55
2.1 Fundamentals of electrochemistry 55
2.1.1 Equilibrium electrochemistry 55
2.1.2 Dynamic electrochemistry 57

2.1.3 Electrode kinetics 59
2.1.4 Mass transport 61
2.1.5 Faradaic and non-Faradaic processes 65
2.1.6 Electrochemical techniques 67
2.1.7 Electrochemical instrumentation and experimental set-up 76
2.2 X-ray photoelectron spectroscopy 77
2.2.1 XPS fundamentals 77
2.2.2 XPS instrumentation 79
2.3 Scanning electron microscopy 80
References 83
Chapter 3 The electrochemical oxidation of sulphite on gold electrodes 87
3.1 Introduction 87
3.2 Experimental 91
3.2.1 Chemical reagents 91
3.2.2 Electrochemical apparatus and experiments 92
3.2.3 Characterisation 93
3.2.4 Simulation 93
3.3 Results and discussion 94
3.3.1 Electro-oxidation of sulphite at a gold macroelectrode 94
3.3.2 Electrodeposition of gold particles and characterisation 100
3.3.3 Electrochemical oxidation of sulphite on gold particle modified boron doped diamond electrodes 114
3.4 Conclusions 131
References 132
Chapter 4 Electrodeposition of gold nanoparticles for nitrite detection 140
4.1 Introduction 140
4.2 Experimental 142
4.2.1 Chemicals and apparatus 142
4.2.2 Electrode modification and electrochemical measurement 143
4.2.3 Characterisation of gold particles 144
4.2.4 Detection of nitrite 145
4.3 Results and discussion 145
4.3.1 Au electrodeposition 145
4.3.2 Characterisation of gold particles modified electrodes 147
4.3.3 Electrochemical behaviour of nitrite at different electrodes 155

4.3.4 Electrochemical detection of nitrite 159
4.4 Conclusions 163
References 165
Chapter 5 The mechanism of electrochemical reduction of hydrogen peroxide on silver nanoparticles 170
5.1 Introduction 170
5.2 Theory and Simulation 172
5.3 Experimental 177
5.3.1 Chemical reagents 177
5.3.2 Apparatus and electrochemical measurements 177
5.3.3 Electrode modification 178
5.4 Results and Discussion 178
5.5 Conclusions 192
References 193
Chapter 6 Investigating the effects on hydrogen peroxide electro-reduction at silver nanoparticle modified boron doped diamond electrodes 198
6.1 Introduction 198
6.2 Experimental 200
6.2.1 Chemical reagents 200
6.2.2 Apparatus and electrochemical measurements 200
6.2.3 Electrode modification 200
6.3 Results and Discussion 201
6.3.1 Effect of silver nanoparticle loading 201
6.3.2 Effect of silver nanoparticle size 206
6.3.3 Comparison of electrodeposition and drop-casting methods 207
6.3.4 Amperometric determination of H_2O_2 211
6.4 Conclusions 212
References 214
Chapter 7 Conclusions 217

Glossary

Roman symbols

Symbol	Meaning	Units
A	electrode area	m^2
c	concentration	mol m^{-3}
C	Capacitance	F
D	diffusion coefficient	m^2 s^{-1}
E	electrode potential	V
E^0	standard electrode potential	V
E_f^0	formal electrode potential	V
F	Faraday constant (≈ 96485)	C mol^{-1}
i	Current	A
i_0	standard exchange current	A
$i_{a/c}$	anodic/cathodic current	A
i_p	peak current	A
i_f	Faradaic current	A
i_c	capacitative charging current	A
j	Flux	mol m^{-2} s^{-1}
k^0	standard electrochemical rate constant	m s^{-1}
$k_{c/a}$	rate constants for the cathodic/anodic reactions	m s^{-1}
m	Mass	g
M	molar mass	g mol^{-1}
n	number of electrons transferred	unitless
Q	Charge	C

R	universal gas constant (8.314)	J mol^{-1} K^{-1}
R_{ct}	charge-transfer resistance	Ω
R_{Ω}	solution resistance	Ω
t	Time	s
T	Temperature	K
u	mobility of ion	m^2 V^{-1} s^{-1}
v	scan rate	V s^{-1}
z	charge of the ion	C
Z_f	Faradaic impedance	Ω
Z_{Im}	imaginary part of impedance	Ω
Z_{Re}	real part of impedance	Ω
Z_w	Warburg impedance	Ω

Greek symbols

Symbol	Meaning	Unit
α, β	transfer coefficients	unitless
γ	activity coefficient	unitless
η	Overpotential	V
ϕ	electrical potential	V
ω	Frequency	s^{-1}

Abbreviations

Abbreviation	Meaning
AFM	atomic force microscopy
BDD	boron doped diamond
CE	chemical process preceding heterogeneous electron transfer
CV	cyclic voltammetry
CVD	chemical vapour deposition
DPV	differential pulse voltammetry
EC_2	heterogeneous electron transfer followed by homogeneous chemical reaction of second order
EIS	electrochemical impedance spectroscopy
HPHT	high-pressure high-temperature
IHP	inner Helmholtz plane
LOD	limit of detection
LSV	linear sweep voltammetry
MCD	microcrystalline diamond
NCD	nanocrystalline diamond
NPs	Nanoparticles
OHP	outer Helmholtz plane
ORR	oxygen reduction reaction
PBS	phosphate buffer solution
SEM	scanning electron microscopy
UNCD	ultra-nanocrystalline diamond
XPS	X-ray photoelectron spectroscopy

Chapter 1 Introduction

This introductory chapter gives a brief background of the carbon family, and emphasises the diamond allotrope. The developments of boron doped diamond in the electrochemistry area are reviewed, which are driven by understanding the relationship among material synthesis, structure, property, and characterisation. As a designer material, further surface modification of the boron doped diamond with the required function to improve the electrochemical performance of the electrode enables its applications of interest, ranging from electroanalysis, electrosynthesis, electrochemical degradation, electrocatalysis, and electrochemical energy storage. The chapter ends with a concise outline of subsequent chapters in this thesis.

1.1 Allotropes of carbon

Carbon with an atomic number of six in the periodic table is an extraordinary element, which is abundant on the Earth and serves as an essential element for all known living systems. The most well-known forms of carbon are graphite and diamond. In graphite the carbon atoms are sp^2 orbital hybridised with a C-C bond of 0.142 nm length within a plane and an interplanar distance of 0.335 nm in Figure 1.1. In diamond the atoms are sp^3 hybridised and tetrahedrally bonded with a carbon-carbon bond length of 0.154 nm in Figure 1.2.[1] Recently many other allotropes have been discovered, including buckminsterfullerene (C_{60}), carbon nanotubes (CNTs), and graphene. C_{60} has a football-like shape and is a type of fullerene discovered in the 1980s by Robert F. Curl, Harry W. Kroto, and Richard E. Smalley, who were awarded the Nobel Prize in Chemistry for 1996. CNTs are cylindrical in shape and were found in the 1990s.[2] The name implies a tube diameter of a few nanometres while the length can be up to the order of several centimetres. Thanks to its nanostructure owning such large ratio of length to diameter and also to the

bond strength, CNTs have excellent properties including strong mechanical strength, high thermal and electrical conductivity, etc.[3] Graphene, a single layer of carbon atoms in a honeycomb lattice of two-dimension, is a basic structural block of other allotropes of other dimensionalities, and was unveiled in the 2000s by Andre K. Geim and Konstantin S. Novoselov, the laureates for the Nobel Prize in Physics for 2010.[4] Thanks to its extraordinary properties in terms of mechanical, thermal, optical, and electronic perspectives, graphene has been extensively studied despite its short history, and shows numerous potential applications.[5] Table 1.1 lists some basic properties of the common carbon allotropes.[6]

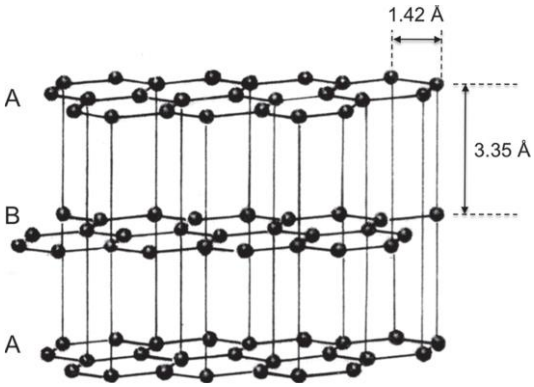


Figure 1.1 The graphite structure. Reproduced from Ref. 1 with permission. Copyright 2011, John Wiley and Sons.

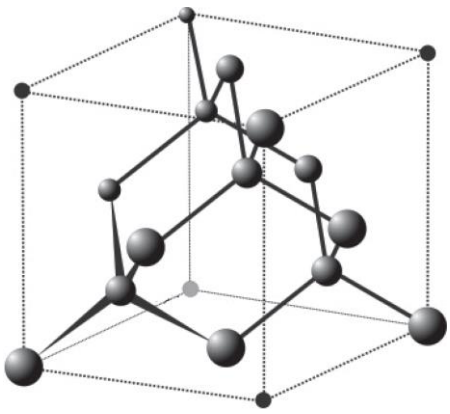
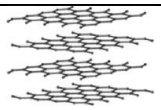
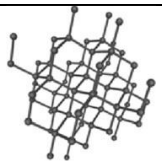
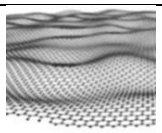
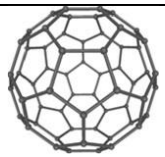


Figure 1.2 The diamond structure. Reproduced from Ref. 1 with permission. Copyright 2011, John Wiley and Sons.

Table 1.1 Properties of the carbon family. Reproduced from Ref. 6 with permission. Copyright 2016, John Wiley and Sons.

	Graphite	Diamond	Graphene	CNT	Fullerene
Structure					
Dimension	3	3	2	1	0
Hybridisation	sp^2	sp^3	sp^2	mostly sp^2	mostly sp^2
Electrical conductivity / S cm^{-1}	structure-dependent	doping-dependent	~ 2000	structure-dependent	10^{-10}
Thermal conductivity / W m^{-1} K^{-1}	structure-dependent	22-33.2	4840-5300	3500	0.4
Hardness	high	high	highest (for single layer)	high	high

These carbon allotropes can exhibit very different properties depending on their carbon-carbon covalent bonding, atom arrangement and structures despite the same atom, C, composition. Diamond, a well-known precious material, was first mined in India in about the fourth century BC, and was first industrially used originating from its supreme hardness by the Chinese in the second century BC.[7] Other than its mechanical hardness (1×10^4 kg mm^{-2}),[8] diamond has the highest thermal conductivity (2200 W m^{-1} K^{-1}) among natural

materials, enabling its application in the cutting and polishing industries. The general performances of diamond are displayed in Table 1.2.[9, 10]

Table 1.2 Fundamental properties of diamond. Adapted from Ref. 9, 10 with permission.

Property	Values
Density	3.52 g cm^{-3}
Specific heat	6.195 J mol^{-1} at 300 K
Thermal conductivity	2200 W m^{-1} K^{-1} at 25 °C
Thermal expansion	$0.8 \times 10^{-6} – 1.2 \times 10^{-6}$/°C at 25-200 °C
Refractive index	2.42 at 546 nm
Optical transparency (undoped)	λ = 2.5 μm to 230 nm
Large electronic bandgap (undoped)	5.45 eV
Electrical resistivity	10^{16} Ω cm
Dielectric constant	5.6
Dielectric strength	ca. 10^{8} to 10^{9} V m^{-1}
Electron mobility	2200 cm^2 V^{-1} s^{-1}
Hole mobility	1600 cm^2 V^{-1} s^{-1}
Extremely high hardness (Vickers)	ca. 10000 kg m^{-2}
Young's modulus	910 – 1250 GPa
Compressive strength	8.68 – 16.53 GPa
Poisson's ratio	0.1 – 0.16
Coefficient of friction in air	0.05 – 0.15
Melting point	4027 K
Chemically inert surface	Up to 850 K in air
	Up to 2000 K in vacuum

With a large bandbap of 5.45 eV, the diamond is an electronic insulator with a high electrical resistivity unless doped with heterogeneous atoms to improve the electronic conductivity, as a key parameter for any electrochemical applications. Boron is the most commonly used dopant to prepare conducting diamond, resulting in boron-doped diamond (BDD). In addition, nitrogen-doped diamond and phosphorus-doped diamond have been studied over the past several decades in various areas.

1.2 Synthesis

1.2.1 High pressure high temperature technique

High-pressure high-temperature (HPHT) and chemical vapour deposition (CVD) techniques are the two major synthesis approaches to prepare (doped) diamond materials. Artificial diamond was prepared in the first industrialised process by the HPHT technique in 1955 at the General Electric Company where diamond was converted from graphite.[11] In this HPHT method, graphite is mixed with transition metal catalysts including Fe, Ni or Co, and the resulting mixture is exposed to tens of thousands of atmosphere (~ 80-300 kbar) and heated at high temperature (~ 1900-3000 ^{o}C),[7] where the conditions are similar to that for the natural diamond production. The molten metals used acting as "solvent-catalysts" may dissolve the graphite-like carbon and decrease the activation energy needed for the conversion from sp^2 graphite to sp^3 diamond. Although this approach has been employed to produce single crystalline (sc) diamond, the resulting products are usually physically small in size in the range of micron to millimetre.[12]

The HPHT method has been utilised to grow doped diamond as well. Pleskov *et al.* reported the synthesis of sc BDD grown from a boron-containing (ferroboron, FeB) Ni-Fe-C melt.[13] Bormashov *et al*[14] synthesized the uniformly boron-doped sc diamonds without any extended structure defects by the HPHT method, which showed a high carrier mobility

of 2200 cm^2 V^{-1} s^{-1} at 300 K, and 7200 cm^2 V^{-1} s^{-1} at 180 K. However, limited BDDs with metallic conductivity can be made by the HPHT method.[15] Meanwhile, the small size and complicated synthesis process restricts its application.

1.2.2 Chemical vapour deposition technique

CVD is the most widely used to grow diamond films. It is carried out at a much lower pressure in comparison to the HPHT technique. The CVD is usually applied in the semiconductor industry for thin film production. Typically, volatile precursors carried by a gas, react to deposit on a substrate surface. A typical diamond film CVD growth process involves three main steps: (1) the activation of the mixture of gases; (2) gas phase reaction; (3) the gas species diffusion to the substrate surface.[7]

In 1962, Eversole and Kenmore[16] developed the cyclic pyrolysis process and demonstrated that diamond could be prepared onto a wafer from a hydrocarbon gas precursor or mixture of CO/CO_2 under low pressures via CVD. In 1968, this research was further developed by Angus *et al*[17] at Case Western Reserve University, and Deryagin *et al.*[18] at Institute of Physical Chemistry, Academy of Sciences of the Soviet Union. The growth rates in these reports were, however, slow despite the attraction of low-pressure synthesis. In 1982, a big breakthrough in diamond CVD technology was made by Matsumoto *et al*[19, 20] in Japan using a mixture of hydrocarbon such as methane, and hydrogen (H_2) gases via a hot filament in order to activate the gas phage for deposition onto diamond and non-diamond substrates including silica, silicon, molybdenum, resulting in an increase of diamond growth rate to the range of micron per hour. The presence of hydrogen is of significance for the growth, helping to abstract H from methane to produce the radical precursor $CH_3\cdot$ and from H-terminated surface sites to provide reactive radical sites for carbon radical addition.[21] In addition, hydrogen is responsible for supressing the formation of sp^2 bonds and increasing the content of sp^3 carbon.[10] Subsequently various techniques for diamond

growth have been developed in terms of gas phase activation divided into two cetrogories: (1) thermal-assisted CVD processes, including hot-filament CVD,[19, 20] the oxygen-acetylene (C_2H_2) torch method;[22] (2) plasma-assisted CVD processes, including microwave plasma CVD,[23] direct current plasma CVD,[24] radio frequency plasma CVD,[25, 26] and electron cyclotron resonance microwave plasma CVD.[27, 28]

With the activation and dissociation of carbon-containing precursor gases, diamond grows at a moderate wafer temperature. The supporting wafer can be either bulk diamond (in the synthetic or natural format) or non-diamond supporting, resulting in homo-epitaxial (single crystalline) or hetero- (polycrystalline) deposition of diamond films, respectively. Single crystal diamond has no grain boundaries, while polycrystalline diamond films contains diamond crystals with different orientations or grain boundaries. Satisfactory substrates can be silicon (Si, both single crystalline and polycrystalline), titanium (Ti), niobium (Nb), molybdenum (Mo), tantalum (Ta) and tungsten (W).[8, 29] The resulting grain size is dependent on various deposition conditions such as pressure, time, temperature, and gas component, which can be adjusted by the ratio of hydrogen to carbon or the introduction of argon gas shown in the early works in the Argonne National Laboratory.[30, 31]

To achieve sufficient conductivity (< 0.1 Ω cm or > 10 S cm^{-1}) for electrochemical applications, controlled doping is an alternative approach using the addition of hetero-elements during CVD growth. The substitution of non-carbon atoms enables an increase in electrical conductivity, depending on the dopant and doping amount. Generally, when the doping levels is lower than 10^{19} atoms cm^{-3}, the diamond acts as a semiconductor. When the doping level of more than 10^{20} atoms cm^{-3} is obtained, the diamond can act as a semimetal due to higher electrical conductivity.[27]

Many dopants has been demonstrated for diamond, including boron, nitrogen,[32] and phosphorus.[33] In 1973, Poferl *et al*[34] used CVD to grow boron-doped diamond for the first time to achieve p-type semiconducting diamond; the boron atom has one less electron than carbon, so it can act as a charge acceptor. By substitution of carbon atoms by boron atoms, an acceptor level 0.37 eV above the valence band in the diamond appears as shown in Figure 1.3.[8] Subsequently many studies of doped diamond have been carried out. The boron source for the synthesis of BDD by CVD is usually diborane (B_2H_6), trimethylboron ($B(CH_3)_3$), or organic borates like trimethoxyborane ($B(OCH_3)_3$).[35, 36] The boron doping level can be from 10^{18} to 10^{21} atoms cm^{-3}, corresponding to a boron-to-carbon ratio of about 10^{-5} to 10^{-3}. Metallic conductivity is achieved at about 3×10^{20} atoms cm^{-3}, while the doping level of 10^{21} atoms cm^{-3} can endow an electrical resistivity of as low as 0.001 Ω cm.[37] It should be mentioned that superconductivity was discovered in the very heavily boron-doped diamond at 4 K by Ekimov *et al* in 2004.[38]

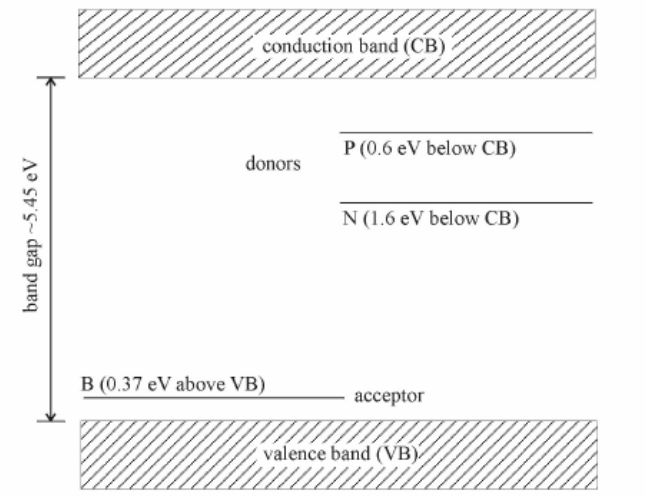


Figure 1.3 The energy diagram of selected states in the bandgap of diamond. Reproduced from Ref. 8.

Other doped diamond films have been investigated. The hetero-atom substitutional doping can be nitrogen (N), phosphorus (P), or sulphur (S) for n-type doping. The elements are

doped by adding appropriate gases to the atmosphere during CVD synthesis, such as N_2[39] for nitrogen doping (1.6 eV below the conduction band), phosphine (PH_3)[33] for phosphorus doping (0.6 eV below the conduction band), and hydrogen sulphide (H_2S) for sulphur doping.[40] For example, nitrogen-doped diamond films were grown using microwave plasma CVD and their conducting behaviour transits from "poor conductor" (1.6×10^{10} Ω cm) to metal-like (3.3×10^{-3} Ω cm) with an increase of nitrogen (from 0 to 25%) as reported by Pleskov *et al*.[41] A phosphorus-doped diamond film with a phosphorus concentration of 7.35×10^{18} cm^{-3} and a conductivity of 1.3×10^{3} Ω cm was grown on a single crystalline diamond substrate by microwave plasma CVD using source gas mixtures of CH_4/H_2 (0.05%) and PH_3/CH_4 (20%).[42]

Today synthetic (doped) diamond is an outstanding material for various application areas including electroanalysis, organic electrosynthesis, electrochemical degradation for water treatment, electrocatalysis, electrochemical energy storage, etc, which will be introduced below. Ahead of that, the following section will firstly focus on BDD in terms of its structure, property and characterisation relevant to its application, as BDD has been one of the most favoured materials in the artificial diamond series since its introduction, despite other common foreign atom doped diamonds.

1.3 Material structure, property and characterization

Today diamond is an important electrode material. However, in comparison to other carbonaceous materials which have been applied for a long time, diamond for the electrochemical study emerged in 1983 by Iwaki *et al*, who introduced ion-implanted diamonds for electrochemical sensing electrodes.[43] In 1987, Pleskov et al found the photoelectrochemistry of CVD polycrystalline diamond electrode deposition on a tungsten wafer for the first time,[44] which triggered later studies over the following three decades

with the establishment of a new branch subject of diamond electrochemistry in the semiconductor electrochemistry.[45] Later the photochemical behaviour of BDD electrodes synthesised by filament-assist CVD were investigated by Patel et al.[46] In 1996, Martin *et al*[47] reported a very wide potential range (-1.25 to 2.3 V versus standard hydrogen electrode) without significant water splitting on BDD electrodes containing about 10^{21} boron atom cm^{-3}. Numerous investigations have sprung up since.

The research related to BDD electrodes has been analysed via Web of Science data collected on July 25, 2018 by Nidheesh *et al*[48] shown in Figure 1.4. 3202 records were found using the term "boron doped diamond electrodes", and the majority of them (89.6%) were published in journal articles with research output reaching a summit at the record of 307 in 2016. Among the subject categories, the two top areas are chemistry and electrochemistry while China and Japan are the top two countries. Most of the articles are published in journals of electrochemistry such as Electrochimica Acta, Electroanalysis, Journal of Electroanalytical Chemistry, and Journal of the Electrochemical Society. The exception is Diamond and Related Materials in the second ranking position. Importantly, diamond electrochemical research has been promoted greatly through efforts of the following research groups: (1) in Japan, Yasuaki Einaga at Keio University, and Akira Fujishima at Tokyo University of Science; (2) in United States, Greg M. Swain at Michigan State University, John C. Angus at Case Western University, John A. Carlisle at Advanced Diamond Technologies, and Robert J. Hamers at University of Wisconsin-Madison; (3) in United Kingdom, Richard G. Compton, and John S. Foord at University of Oxford, Julie V. Macpherson, and Patrick R. Unwin at University of Warwick, Frank Marken at University of Bath, Paul W. May at University of Bristol, and Katherine Holt at University College London; (4) in Spain, Enric Brillas, and Ignasi Sirés at University of Barcelona; (5) in Germany, Christoph E. Nebel at Fraunhofer Institute for Applied Solid State Physics,

and Nianjun Yang at University of Siegen; (6) in France, Mehmet A. Oturan at University of Paris-Est; (7) in Brazil, Romeu C. Rocha-Filho at Federal University of São Carlos; (8) in Russia, Yu. V. Pleskov at Frumkin Institute of Physical Chemistry and Electrochemistry of Russian Academy of Sciences.

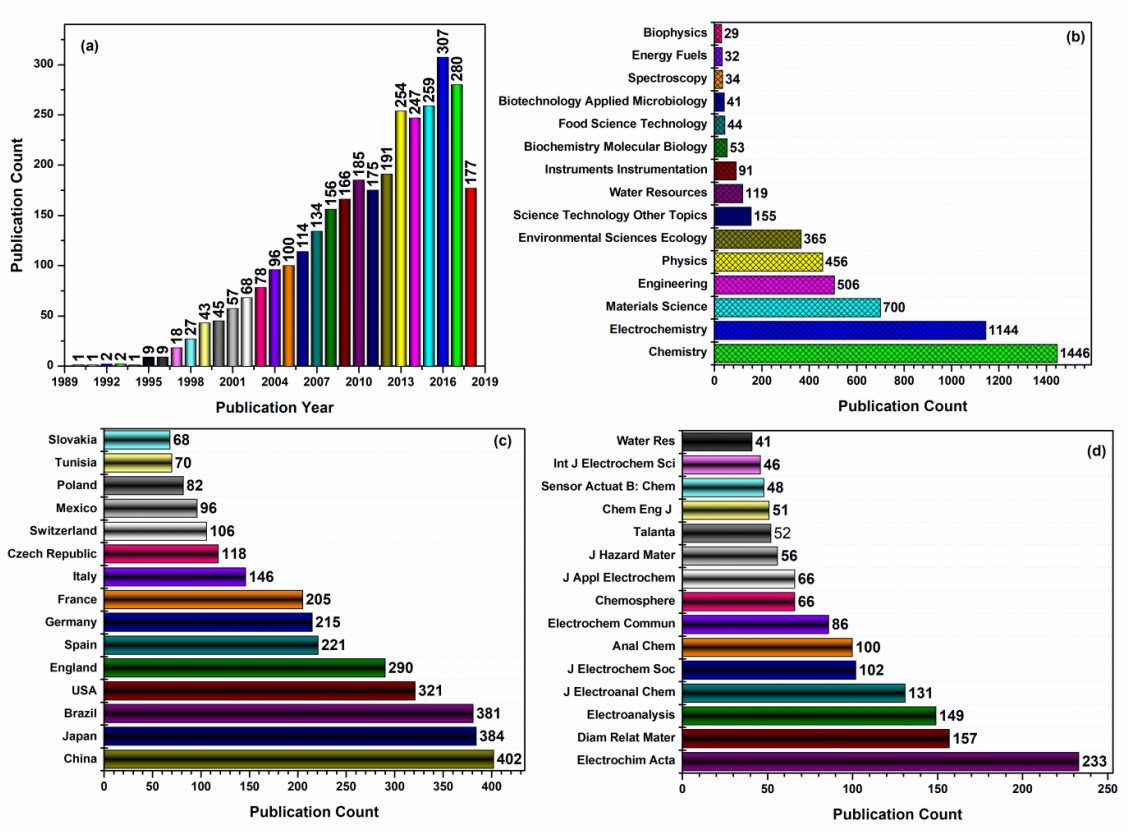


Figure 1.4 Publication details of papers on BDD electrodes. (a) the number of publications per year over the years 1990-2018, (b) the first fifteen application fields, (c) the first fifteen countries and their corresponding publication numbers, (d) the first fifteen journals. Reproduced from Ref. 48 with permission. Copyright 2019, John Wiley and Sons.

Compared with other carbon electrodes, BDDs have excellent chemical and physical properties including wide potential windows, great resistance to chemical corrosion, stable and robust, etc,[15, 27] and therefore BDDs are widely used electrode materials in the electrochemistry areas. When elucidating the electrochemical behaviour using BDDs, some significant considerations should be included as following, surface morphology of

BDDs, boron doping level, surface termination, presence of non-diamond carbon (qualitatively considered as an indicator of sp^2 to sp^3 ratio), and electrochemical properties. These will be reviewed with the corresponding surface characterisation in this section.

1.3.1 Surface morphology

Depending on the crystallite or grain size, polycrystalline BDDs can be divided into the following categories: microcrystalline diamond (MCD), when grain size is of micron scale; nanocrystalline diamond (NCD), if grain size is 10 nm-1 μm; and ultra-nanocrystalline diamond (UNCD), when grain size < 10 nm as shown in Figure 1.5.[49] Scanning electron microscopy (SEM), and atomic force microscopy (AFM) are generally powerful techniques to characterise the surface morphology of different forms of synthesised BDDs and their surface roughness. For MCD, especially after polishing, SEM can distinguish the different areas of boron dopant levels on the BDD surface, with darker regions corresponding to more heavily doped areas.[50] UNCD films in Figure 1.5 are composed of carbon particles of quasi-spherical shape of nanometre size, which are aggregates of diamond grains while NCD consists of larger crystal clusters. Figure 1.6 shows how AFM can characterise surface roughness.[51]

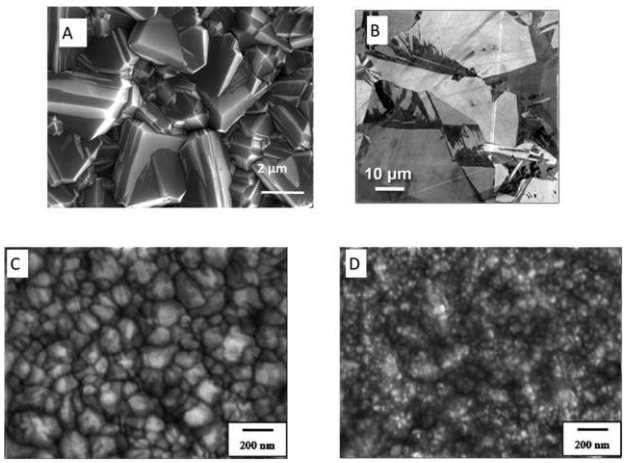


Figure 1.5 SEM images of (A) as-prepared MCD, (B) a polished MCD surface, (C) NCD, and (D) UNCD. Reproduced from Ref. 29 with permission.

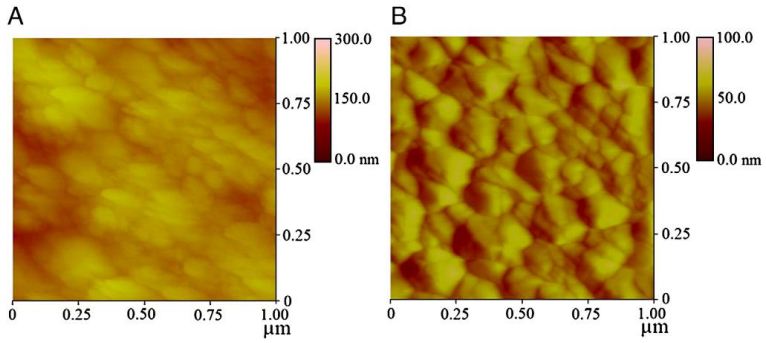


Figure 1.6 AFM images of (A) UNCD, and (B) NCD electrodes. Reprinted from Ref. 51, Copyright (2009), with permission from Elsevier.

1.3.2 Boron dopant density

Substitution of carbon with boron atom introduces p-type holes to the crystalline lattice, resulting in a higher conductivity since diamond is a wide bandgap insulator. The resistivity of BDD exhibits a dependence on the boron doping density as shown in Figure 1.7.[52] The resistivity of undoped diamond (containing ~ 2×10^{23} C atoms cm^{-3} in the lattice) film is about 10^{13} Ω cm.[52] After doping with boron, the resistivity, ρ, decreases dramatically by eight orders of magnitude. As doping density increases, more charge carriers are available. When the doping level becomes above 4-5 × 10^{20} cm^{-3} (a critical transition point of metal-insulator,[53] also typically ~ 1 B in 1000 C atoms), BDD shows metallic conduction behaviour as a semi-metal possessing a lower number of charge carriers or density of states compared with traditional metals; the resistivity of platinum and gold at 20 °C is 1.06 × 10^{-5}, and 2.2 × 10^{-6} Ω cm, respectively.[29]

The boron dopant density is also affected by the different diamond crystal planes. For defected single crystals or polycrystalline materials, different diamond crystal orientations take up boron differently with the order of (111) > (110) > (100). The (111) face incorporates boron about ten times more than the (100) orientation.[15, 29]

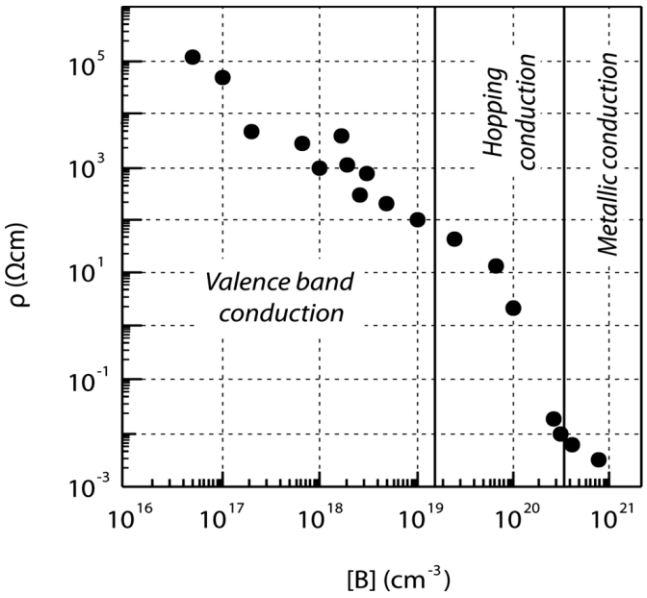


Figure 1.7 The boron doping density effect on the resistivity at room temperature. Reprinted from Ref. 52, Copyright (1998), with permission from Elsevier.

To quantitatively characterise the amount of boron dopants, techniques including secondary ion mass spectrometry (SIMS) and Raman spectrometry are utilised generally. The thickness and boron dopant concentration can be measured by the SIMS technique, which is carried out by sputtering a sample surface using a primary ion beam (such as a $^{16}O_2^+$ or $^{133}Cs^+$ primary beam) and analysing the emitted secondary ions based on mass/charge ratios via a mass spectrometer. Figure 1.8 shows the distribution of the boron and carbon elements with some traces of hydrogen and oxygen by SIMS in a direct image mode, with the homogeneous distribution of C and H and heterogeneous scattering of B and O, and the boron concentration is quantified via ion implanted standards.[54-57] However, this method is destructive, which makes the development of other methods necessary.

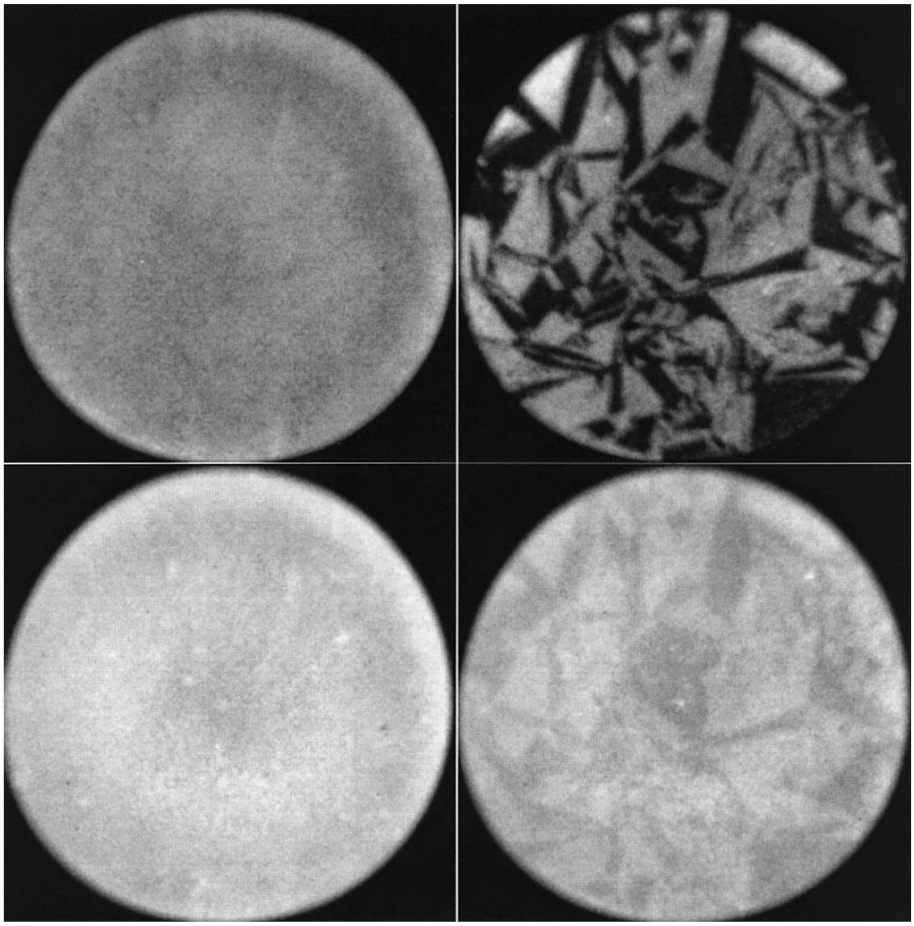


Figure 1.8 SIMS images of a BDD layer: (a) ^{1}H), (b) ^{11}B, (c) ^{12}C), and (d) ^{16}O. Reprinted by permission from Ref. 54, Copyright (1999), Springer Nature.

Raman spectra is a powerful technique to determinate the boron atom amount in boron-doped diamond electrodes. There are two broad peaks at 500 and 1220 cm^{-1} in Figure 1.9, which are connected with boron. Although some explanation have been proposed for the origin of the two peaks, such as disorder and intraband optical transitions,[58] maxima of phonon density of states,[59] boron dimer vibration and symmetry breaking of diamond lattice[60], it remains unclear. In particular, the 500 cm^{-1} peak downshifts significantly with an increase in boron,[58] and is the basis of quantitative evaluation approach of the boron in the range of 2×10^{20} to 10^{22} atoms cm^{-3}. Alternatively, the boron concentration may be approximated by the Fano-resonance due to the incorporation of boron.[60]

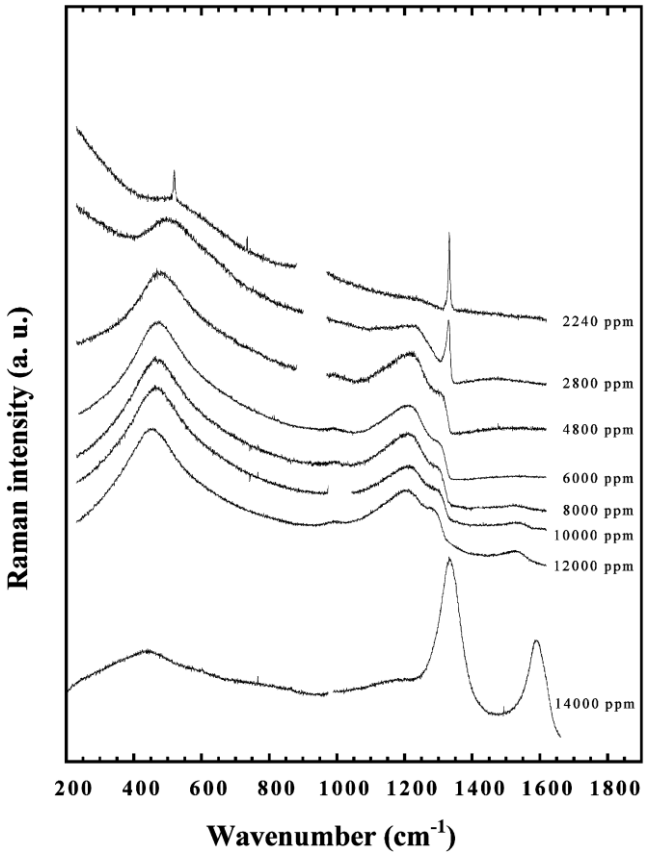


Figure 1.9 Raman spectra of BDD films for different ratios of boron to carbon in the range of 2240-14000 ppm in the gas phase. Reprinted from Ref. 58, Copyright (2004), with permission from Elsevier.

1.3.3 Surface termination

The boron doped diamond surface may be terminated in different ways due to its enriched carbon chemistry and it is of importance to understand the termination since it can have an impact on the wetting properties and resulting electrochemistry, such as inner sphere electron transfer (ET) process, etc. When the BDD surface is bonded with hydrogen, it is called hydrogen-terminated (or hydrogenated) with a hydrophobic property feature where the water contact angle is as high as about 90^{o} as shown in Figure 1.10(a). It is generally believed reliable to hydrogen terminate via a hydrogen plasma. However, as an comparable alternative, the electrochemical hydrogen termination of BDD can be obtained via a severe

cathodic electrochemical treatment by applying an extremely high negative voltage (-35 V) in acidic solutions (2 M hydrochloric acid) for 1-5 min, generating a clean surface of almost no C-O bonds.[61] Although a hydrogen terminated BDD is usually stable in the air for several months, it will slowly oxidise over time and become hydrophilic.

In contrast to hydrogen-terminated BDDs, oxygen-terminated (or oxygenated) BDDs exhibit an opposite feature of hydrophilicity as shown in Figure 1.10(a) with the water contact angle of < 65°. Numerous termination methods have been developed, including oxygen plasma, boiling in acids, mechanical alumina polishing, photochemical oxidation, oxygen treatment at high temperatures, and electrochemical anodic process, etc.[27] The oxygen functional groups are commonly introduced as a species mixture of -OH, -C-O-C- and C=O on the O-terminated BDDs, with different ratios of groups depending on the speciation oxidation processes.[29] A lower amount of C=O functionality group are all introduced on oxygen-terminated BDDs by electrochemical oxidation via anodic polarisation, oxygen plasma, and photochemical oxidation via a ultraviolet (UV)/ozone lamp techniques, but the largest percentage of C-O groups (ether -C-O-C-, or hydroxyl C-OH) at about 286 eV is produced by photochemical oxidation in comparison with the other two methods.[62]

Halogen (F, Cl, etc) termination can be realised on the diamond surface of hydrophobic features via activation of a halogen gas with the formation of free radicals. For instance, Miller reported a mild and versatile approach via employing UV photochemical reactions to produce amine-, methylamine-, chlorine-, thiol-termination diamond.[63]

To assess the surface chemistry of diamond, X-ray photoelectron spectroscopy (XPS), and contact angle assessments are commonly applied. Different carbon bonds such as oxygen functionalities (C=O, C-O-C, C-OH, COOH), C-F, C-Cl, and C-N can be distinguished

from the binding energies by XPS for semi-quantitative surface characterisation. Nevertheless, hydrogen-terminated BDD surface information cannot be acquired by XPS, which may be indicated by the water contact angle technique as a reference for a H- or O-terminated surface. Figure 1.10 shows that the major component in the C 1s of XPS spectra for H-termination BDD is sp^3 carbon-carbon bond at ~ 284.6 eV as the reference position in the bulk diamond. The sp^2 C-C bonds are at the lower position (-1 to -2.1 eV) with reference to the sp^3 bonds. After electrochemical oxidation to form O-terminated BDD, the C/O functionalities increase. In terms of the binding energies, the absorbed hydrocarbons (+0.6 to 0.9 eV) and other oxygen functionalities such as ether (C-O-C)/alcohol (C-OH) (+1-2 eV), carbonyl (C=O, +2.9-3.8 eV), and carboxyl (COOH, +3.7-4.3 eV) are located at different postions.[12]

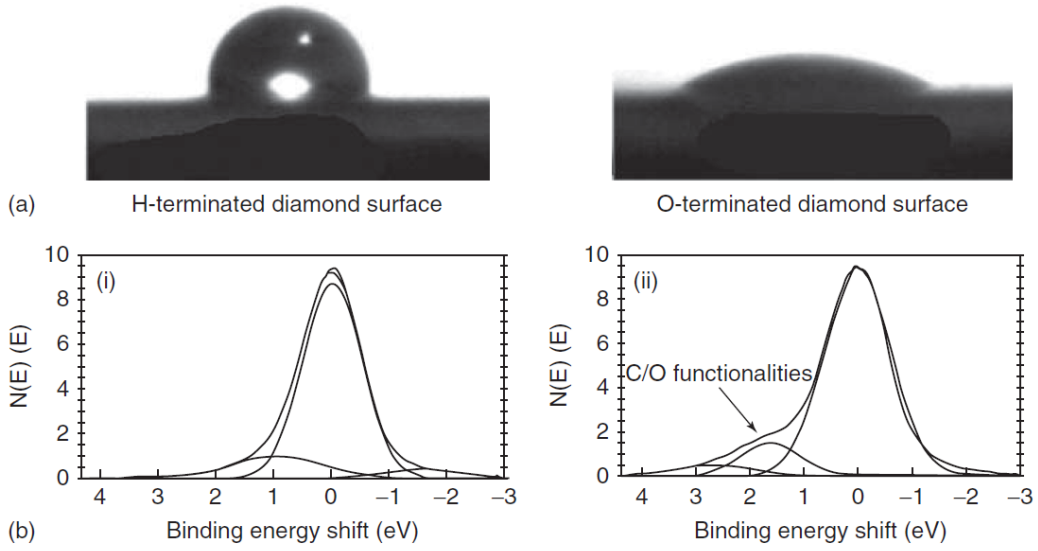


Figure 1.10 (a) The contact angle measurements on the surfaces of H-terminated and O-terminated BDDs, (b) C_{1s} spectra of XPS for H-termination BDD (i) before and (ii) after oxidation by applying +1.5 V for 10 min in the electrolyte of 0.1 M KH_2PO_4. Reproduced from Ref. 12 with permission.

1.3.4 Non-diamond carbon presence

BDD may be viewed as a composite material composed of "non-active" crystalline sp^3 diamond carbon and amorphous sp^2 non-diamond carbon.[64] The synthesis of a pure sp^3 phase diamond with a remarkable boron doping level is challenging. When the doping level increases, it is very difficult to keep crystallinity and manage the quantity of adventitious non-diamond carbon (NDC) impurities of sp^2 hybridisation incorporation within crystalline defects and grain boundaries. Although NDC may improve the conductivity, the widely distinguished electrochemical properties of BDD including low background currents and wide potential range resulting from sp^3 nature along with the weak molecular adsorption, would be compromised to become more similar to glassy carbon.[37, 57, 65] In addition, sp^2 carbon impurities have an effect on the electron transfer kinetics for some redox processes.[66, 67] For example, the presence of a carbon impurity improves the heterogeneous ET rate for oxygen reduction reaction due to the available catalytically binding sites for oxygen provided by NDC.[57]

Raman spectroscopy is utilised to evaluate the sp^2 carbon impurity levels in BDDs. There is only sp^3 carbon (σ bond) in the pure diamond which leads to a single phonon peak at 1332 cm^{-1} in Raman spectroscopy.[29] The line width suggests qualitatively the crystal quality. The more defects there are in the diamond, the broader the line width.[65] NDC (π bonds of sp^2 carbon) produces two peaks labelled D and G. The D peak is due to the breathing mode of sp^2 rings while G peak is assigned to the stretching of pairs of sp^2 sites (chains and rings).[29] The disordered D and G peaks occur at 1355 and 1575 cm^{-1}, respectively, in crystalline graphite. The relative intensity ratio of the sp^3 peak to the sp^2 G peak is usually employed as a qualitative evaluation for diamond quality as shown in Figure 1.11(a). Note that a Fano resonance due to interference between a continuum of electronic excitations and a discrete zone centre optical photon is observed,[57] indicating

the onset of metallic conductivity for B concentrations > 10^{20} atoms cm^{-3}. The Raman spectrum becomes more complex to explain when the crystallite size decreases to the nanoscale as shown in Figure 1.11(b). A peak of 1150 cm^{-1} as a signature feature of NCD is considered to come from transpolyacetylene oligomer molecules (C-C sp^2 vibrations) at the surfaces and grain boundaries.[68] The broadening of sp^3 peak due to the decreased crystallite size overlaps with the D peak related with disordered sp^2 NDC, and the broad peaks of 1470 cm^{-1} and 1550 cm^{-1} are attributed to non-diamond carbon at the grain boundaries.[69]

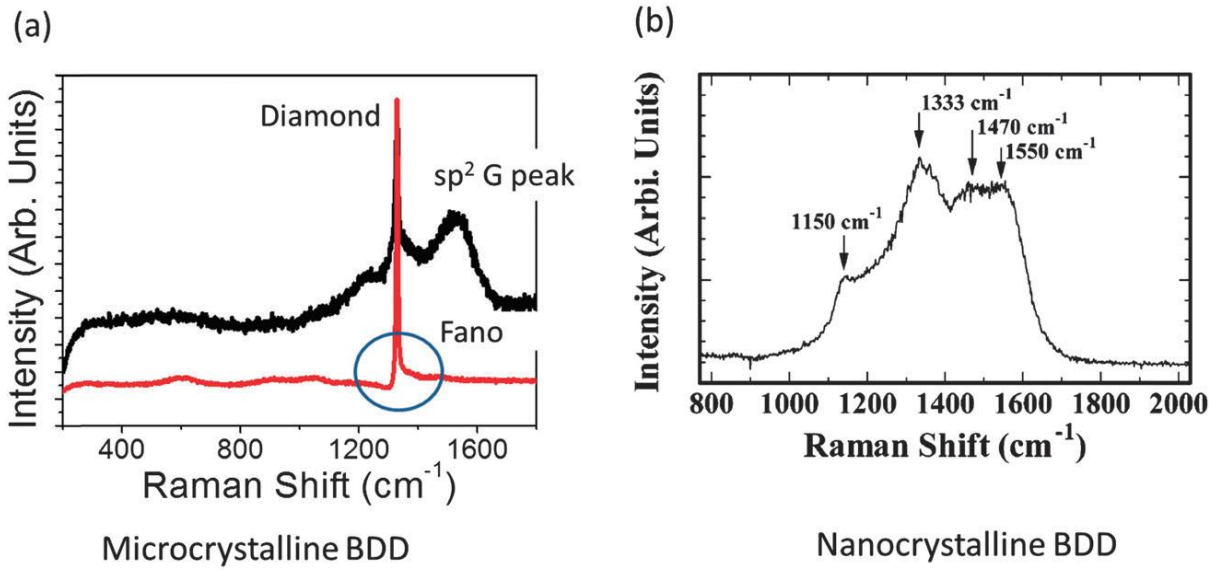


Figure 1.11 (a) Raman spectra of a microcrystalline BDD. The red and black lines are taken in a lower and higher doped surface region, respectively. (b) Raman spectrum of a nanocrystalline BDD. Reproduced from Ref. 29 with permission.

1.3.5 Electrochemical properties

For electrochemical applications, BDD presents distinctive performances and has various advantages over traditional metal electrodes and sp^2 carbon electrodes due to its sp^3 nature, including a very wide potential range, a low background current, mechanical robustness, good chemical stability, resistance to fouling, and excellent bio-compatibility etc.[15, 27, 70]

BDD shows a very wide electrochemical potential range. When defining the potential window, the anodic and cathodic current density should be stated. As shown in Figure 1.12, where a current density of 1.0 mA cm^{-2} is chosen, the potential window of ~ 3 V for BDD is much larger than those of glass carbon electrode, and metal electrodes including Au and Pt.[70] This results from the high overpotentials for decomposition of solvents such as water, as sp^3 carbon is catalytically inert and BDD is a poor adsorbent whereas water splitting needs catalytic sites on the electrode surface.

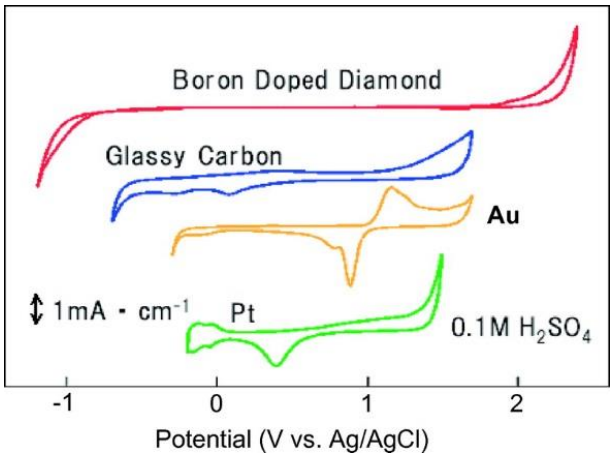


Figure 1.12 Potential windows of platinum, gold, glassy carbon, and BDD electrodes. Reproduced from Ref. 70 with permission.

The background current of BDD is very low in aqueous and non-aqueous solutions. As shown in Figure 1.12, compared with sp^2 carbon electrodes such as glassy carbon, the lower background current and capacitance of BDD is accredited to the lower density of surface electronic states near Fermi level, and the relative absence of electroactive surface groups of carbon-oxygen functionalities.[71, 72] This feature is beneficial for improving signal to background ratio in electroanalytical applications.

The mechanically robust nature of BDD enables its application in the sonoelectrochemical or sonoelectroanalysis process. The mass transport rate can be improved by acoustic streaming and micro-jetting, and BDD is suitable for ultrasonically improved deposition

since the BDD surface can withstand the impact of cavitation without damage.[73] The high chemical inertness or resistance of BDD endows corrosion stability even in extreme conditions such as strong acid solutions. Its weak adsorption property is favourable to avoid electrode fouling and important, as fouling is an issue in terms of decreasing the electrochemical signals when developing sensors.[27, 74] In addition, BDD can be used for *in vitro* and *in vivo* detection of neuronal neurotransmitters (*e.g.* adenosine, norepinephrine, serotonin) and drugs (*e.g.* a diuretic of bumetanide, an antiepileptic reagent of lamotrigine and an anticancer drug of doxorubicin) because of its biocompatibility.[69, 75]

Some typical redox probes are utilised to characterise the electrochemical behaviour of BDD electrodes, including aqueous couples such as $Fe(CN)_6^{3-/4-}$, $IrCl_6^{2-/3-}$, $Ru(NH_3)_6^{2+/3+}$, and methyl viologen ($MV^{+/2+}$), and non-aqueous couples such as ferrocene. The detailed composition of BDD electrodes can affect the electrochemical responses, such as potential window, background current, redox activity, for a specific choice of redox probe including: (1) the dopant type, doping level and distribution, (2) the surface termination, (3) the presence of non-diamond carbon, (4) the crystal structure, such as single crystal or polycrystalline, and different diamond crystal planes.

With an increase of boron dopant concentration, the potential window is becoming narrower as shown in Figure 1.13 from BDD-A of (2×10^{21} atoms cm^{-3}), to BDD-C (5.5×10^{21} atoms cm^{-3}).[76] In terms of redox response in Figure 1.14, when the doping level is below ~ 10^{20} atoms cm^{-3}, the redox probe of $Ru(NH_3)_6^{2+/3+}$ exhibits irreversible behaviour on three BDD electrodes at different boron doping levels of 9.2×10^{16} atoms cm^{-3}, 2×10^{18} atoms cm^{-3}, and mid 10^{19} atoms cm^{-3}, reflective of sluggish electron transfer kinetics, while BDDs of above metallic doping level at 1.9×10^{20} atoms cm^{-3} and 3×10^{20} atoms cm^{-3} display an electrochemically reversible behaviour. The lowest doped electrode shows the largest difference between anodic and cathodic peak potentials (ΔEp). With an

enhancement of the boron doping level, the kinetics of electron transfer increase, leading to the decrease of ΔEp. Therefore $Ru(NH_3)_6^{2+/3+}$ can be a powerful couple to distinguish between semi-conducting and conducting BDDs of different boron doping levels. This is because the kinetics for $Ru(NH_3)_6^{2+/3+}$ are sensitive to the electronic properties of electrode surface, in particular the density of electronic states near the standard redox potential of the probe. Similarly, methyl viologen and $IrCl_6^{2-/3-}$ redox systems are influenced by the BDD electrode electronic structure as $Ru(NH_3)_6^{2+/3+}$.[69]

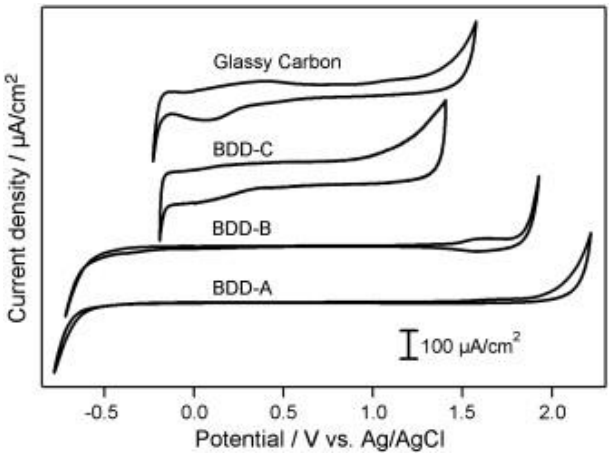


Figure 1.13 Background voltammogram curves for BDD-A (2×10^{21} atoms cm^{-3}), BDD-B (4×10^{21} atoms cm^{-3}), BDD-C (5.5×10^{21} atoms cm^{-3}), and glassy carbon electrodes in 0.5 M H_2SO_4 at 100 mV s^{-1}. Reprinted from Ref. 76, Copyright (2010), with permission from Elsevier.

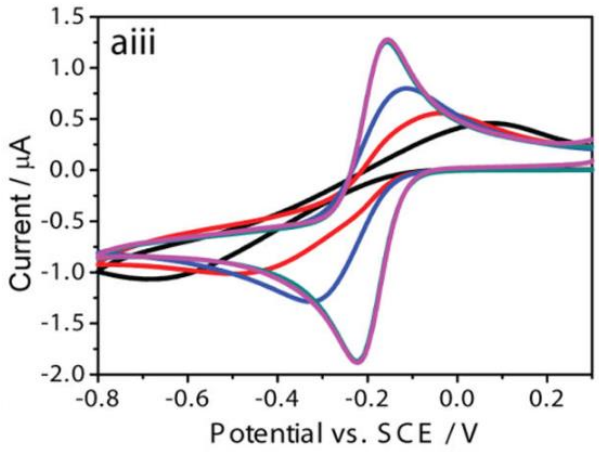


Figure 1.14 Cyclic voltammograms using polycrystalline BDD electrodes A (9.2×10^{16} atoms cm^{-3}, black), B (2×10^{18} atoms cm^{-3}, red), C (mid 10^{19} atoms cm^{-3}, blue), D (1.9×10^{20} atoms cm^{-3}, pink), and E (3×10^{20} atoms cm^{-3}, green) of 1 mm diameter for the reduction of 1 mM $Ru(NH_3)_6^{3+}$ in the electrolyte of 0.1 M KNO_3 at 0.1 V s^{-1}. Adapted with permission from Ref. 57. Copyright (2013) American Chemical Society.

The BDD electrode surface termination can influence the electrochemical response. The background current is lower for a H-terminated BDD than for an O-terminated one, and the termination difference can affect the electron transfer kinetics for sensitive redox probes since it changes the wetting properties of the electrode-electrolyte interface.[27] For instance, the kinetics of $Fe(CN)_6^{3-/4-}$ redox couple are much affected by the surface termination. A smaller ΔEp can be observed at hydrogen-terminated BDD while ΔEp increases after oxygen termination, indicating faster electron transfer rate on the hydrogen terminated surface.[69] This origin of surface dependent electrochemical behaviour is that the adsorption of the intermediate species of the redox probe is inhibited by the oxygen functional group compared with hydrogen termination BDD via in situ attenuated total reflection-infrared spectroscopy.[77]

Non-diamond carbon impurities can have an impact on BDD electrochemical responses in terms of potential window, capacitance current and redox probes. As shown in Figure 1.13

the capacitance of BDD-C (214 μF/cm^2) is more than 20 times larger than that of BDD-B (8 μF/cm^2), indicating that the difference is from the NDC atoms instead of the boron amount.[76] Surface insensitive redox systems such as $Ru(NH_3)_6^{2+/3+}$ are mostly uninfluenced by sp^2 carbon impurities at the BDD surface while others such as $Fe^{2+/3+}$ and 4-*tert*-butylcatechol are affected, as ΔEp decreases with the enhancement of the sp^2 carbon amount.[66]

It is far more challenging to grow single crystal BDD electrodes than their polycrystalline counterparts, and thus the number of electrochemical investigations on single crystal BDDs is much less compared to that on polycrystalline electrodes. Kondo *et al.*[78] suggested that (111) faces are more active than (100) planes using homo-epitaxial single crystal BDD electrodes. However, comparisons taken between these two crystal planes need caution since some studies reveals that there is an ca. ten times higher amount of boron taken up by the (111) plane than the (100) surface when using the same ratio of boron to carbon precursors.[79] Recently a remarkable study shows that under similar level of boron doping of 10^{20} atoms cm^{-3}, polycrystalline BDD is the most active electrode, whilst for the homo-epitaxial single crystalline BDDs, the (111) facet is more active than the (100) plane using outer- and inner-sphere redox probes of $Ru(NH_3)_6^{2+/3+}$ and $Fe(CN)_6^{4-/3-}$ at both hydrogen- and oxygen-terminated electrode surfaces.[80]

1.4 Surface modification

BDD electrodes possess desirable electrochemical performances, including a wide potential range, a high signal-to-background current ratio, good chemical stability, excellent mechanical hardness, and bio-compatibility, and thus have been added to the essential toolbox in the electrochemistry community. Nevertheless, an unfavourable characteristic is that it is not sufficiently electrocatalytic to promote the redox reactions of

interest for many molecules compared with other carbon electrodes, which motivates the research to impart and improve the catalytic activity on the BDD electrode via diverse schemes. Note that the inert feature without surface corrosion and the formation of oxide layer makes it an ideal supporting substrate for catalyst deposition for electrocatalysis studies. In order to modify the BDD surface, common methods have been developed, including surface grafting by chemical reactions, ion implantation, and electrodeposition of metal nanoparticles (NPs).

1.4.1 Surface grafting by chemical reactions

Surface functionalisation of BDD electrodes with organic molecules have been investigated by various methods, including chemical, electrochemical, and photochemical grafting. Surface chemical modifications of oxygen-terminated BDD surfaces using different oxygen functional groups were carried out with 2,4-dinitrophenylhydrazine and 3-aminopropyltriethoxysilane molecules. The latter in particular has potential for application in biology areas since its terminal amino group can be further covalently bonded to biomolecules such as DNA and enzymes.[81] For the first time, electrochemical modification was demonstrated in 1999 by Kuo et al via electrochemical reduction of a phenyl diazonium salt to covalently bond aromatic groups to the sp^3 diamond carbon surface, which motivated subsequent research.[82] Similarly, single crystalline (100) boron-doped homoepitaxial diamond has been surface functionalised via electrochemical reduction of 4-nitrobenzene diazonium tetrafluoroborate for covalent bonding of 4-nitrophenyl groups, which further serve for DNA immobilization.[83] Photochemical modification grafting of organic alkenes to hydrogen-terminated single crystal BDD has been achieved under UV light illumination at 250 nm, and the resultant diamond surface is reacted with crosslinker to attach DNA.[84]

1.4.2 Ion implantation

Ion implantation is a complex process, where the boron doped diamond substrate undergoes the metal ion bombardment via an accelerator, leading to the implantation of metal species into the BDD wafers with change of electrical properties, and enhancing the electrocatalytic activity. During the ion implantation process, the modified BDD needs to be annealed at a high temperature in a hydrogen atmosphere in order to recover the metastable transition structure between sp^3 diamond carbon and graphitic sp^2 carbon induced by the ion bombardment.[85, 86] To date, this approach have been developed to implant nickel (Ni)[85, 87] and Copper (Cu),[85] iridium (Ir),[88] and platinum (Pt)[89], etc, into BDDs for determination of glucose, arsenite (As(III)), and hydrogen peroxide (H_2O_2), respectively. The resulting metal ion implanted BDD electrodes are stable up to 5 months even with ultrasonication since the metal ions are partly buried into the BDD wafers.[85]

1.4.3 Electrodeposition

The electrochemical modification of electrodes with metals, metal oxides, and metal alloys is a convenient way for increasing the electrocatalytic and electroanalytical activity of the electrodes. Nanoparticle modified electrodes have many advantages. Materials at the nanoscale may show some properties which are not observed in the bulk format. A high surface area can be obtained, resulting in the increase of catalytic activity and a saving of the amount of costs especially when using notable metals such as silver, platinum, and gold. Signal to noise ratios can be improved as well due to the increase of active sites.[90] The electron transfer process can be promoted after modification with reducing the overpotential for some analytes.[86]

According to the chemical aims, different materials including metals, metal oxides, and metal alloys can be deposited for various chemical application systems. A variety of metals

have been used to modify BDD electrodes, including iron (Fe), cobalt (Co), nickel (Ni), copper (Cu), palladium (Pd), silver (Ag), Tin (Sn), antimony (Sb), Iridium (Ir), platinum (Pt), gold (Au), lead (Pb), and bismuth (Bi), etc.[86, 91] Metal oxides include TiO_2, $Ni(OH)_2$, Cu_2O, IrO_x, and PbO_2, etc.[91] Metal alloys such as bimetallic alloys exhibit some excellent performances compared with their individual metal counterparts, including Pd-Ni,[92] Pd-Sn, Pt-Cu, Pt-Ru, and Pt-Au, etc.[91]

Electrodeposition is a facile approach for electrode modification. The procedure is easy, fast and reproducible, and it may take place at room temperature. This methodology generally involves reducing the corresponding salts to form metals at the electrode surface by applying an appropriate potential. In all, the deposition is controlled by various voltammetric parameters and the nature of the electrolyte solution. The detailed voltammetric methods and their theory behind them are illustrated in the experiment technique chapter. On one hand for voltammetric technique, nanoparticles with different shapes or morphologies can be deposited by controlling the potential as the most import parameter. For example, flower-like and convex polyhedron Au nanoparticles (AuNPs) onto BDDs can be fabricated by changing the deposition potential from 0.5 V to -0.1 V vs. KCl-saturated Ag/AgCl.[93] On the other hand for the solution, nanoparticle size and coverage can be controlled by the concentration and the pH. For instance, the higher the metal salt concentration, eg. Cu^{2+},[94] the larger the NPs are. The coverage of AuNPs onto amine-terminated BDD surfaces via the electrostatic interaction between amine groups and AuNPs is adjusted by the pH of the solution.[95]

1.5 Applications

BDD presents advantages over conventional metal and other sp^2 carbon electrodes, which encourages its various electrochemistry application areas as shown in Figure 1.15,

including electroanalysis, electrosynthesis, electrocatalysts, electrochemical degradation, electrochemical energy storage, etc.

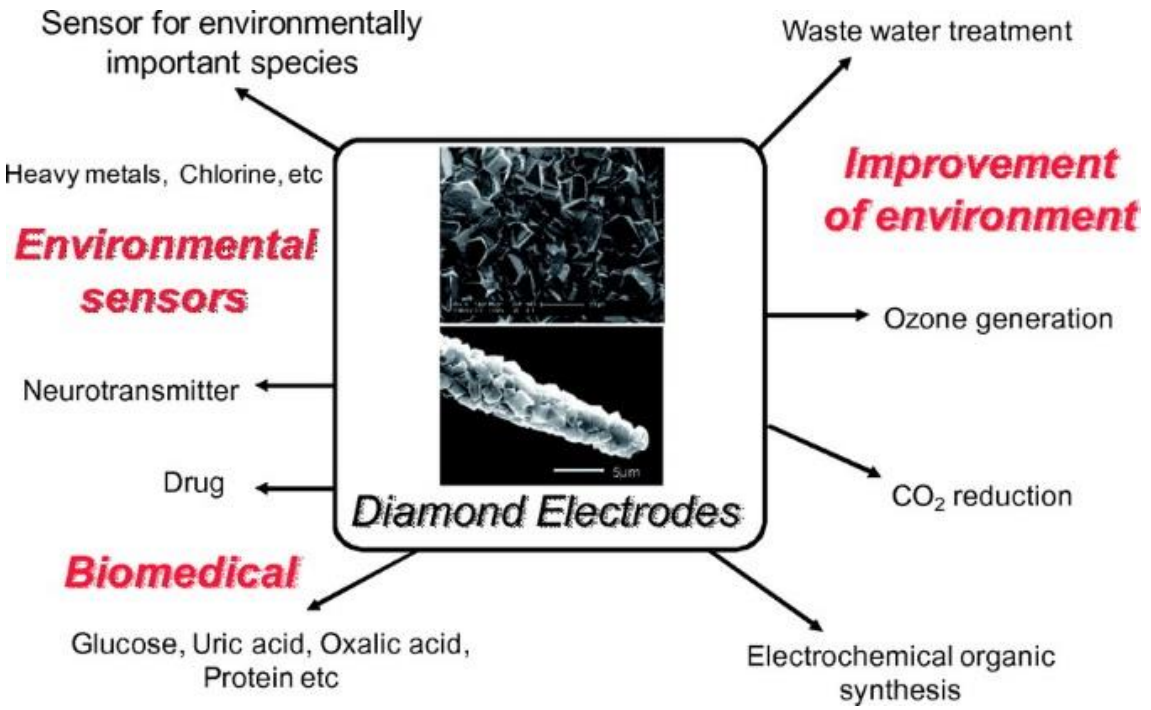


Figure 1.15 The electrochemical applications of diamond electrodes. Reproduced from Ref. 70 with permission.

1.5.1 Electroanalysis

BDD is widely utilised as an electrode in electroanalytical areas, since it can enhance signal to noise ratio with a wide potential window in terms of its low background current mentioned above for electrochemical or bioelectrochemical sensors. A great number of chemicals have been electroanalytically examined by virtue of BDD-based electrodes including pharmaceuticals, biomolecules or biological compounds (such as neurotransmitters, proteins, and DNA/RNA), organic pollutant compounds, and inorganic heave metals, etc.[27, 96]

Bare or modified BDD electrodes have been employed as a useful tool for determination of pharmaceutical compounds. Carisoprodol as a muscle relaxant has a high oxidation

potential at 2.03 V versus Ag/AgCl (3.0 M KCl), making BDD a suitable electrode for determination instead of common carbon electrodes in terms of a high potential window.[97] Similarly, Feier et al.[98] and Hanko et al.[99] have detected the cephalexin for upper respiratory infection cure, and 6-mercaptopurine for maintain remission in leukemia, both using bare BDDs at a high potential of about +1.6 V, and +1.63 V *versus* Ag/AgCl (3M KCl) with a LOD of 34.74 ng mL^{-1}, and 0.51 μM, respectively. Paracetamol for treatment of pain and fever has been determined using a bare BDD electrode without modification in the range of 0.065-32 μM with a limit of detection (LOD) of 0.430 μM, using an optimised pH 7.0.[100] BDD electrodes modified by AuNPs by pulse deposition have been used to detect the antibiotic chloramphenicol used for the treatment of respiratory tract and nervous system infections with a LOD of 5 μM.[101] Other pharmaceutical compounds can be electroanalytically measured on BDD electrodes including antihypertensive, anti-inflammatories, and antibiotics, etc, and the above are examples. The detailed electroanalysis of pharmaceutical compounds on BDD electrodes has been reviewed thoroughly by Sousa et al.[102]

The use of BDD electrodes to determine biomolecules has been investigated partly due to their bio-compatibility and their inertness. Neurotransmitters such as dopamine are important substances for brain function, which are known to foul severely at other electrode surfaces, have been studied. An unmodified BDD as a simple and fast method can be used to determine dopamine using DPV with a LOD of 1.87×10^{-8} M and applied in real urine samples.[103] Enzymatic sensors and non-enzymatic sensors including modifications by noble metals (Pd, Ag, Pt, Au) and cheaper transition metals (Co, Ni, Cu) have been developed to measure glucose.[104, 105] Other biomolecules including proteins, and DNA/RNA can also be electrochemically detected via the BDD electrodes. In order to improve sensitivity and selectivity, biosensors based on the surface modification of BDDs

by attachment of organic linker groups and biomolecules as discussed in the previous section have been investigated both *in vitro* and *in vivo*. The range of biological applications is broad and it has been reviewed by Dong et al. in 2011 (particularly for BDD nano/microelectrodes),[69] Svitkova et al. in 2016,[104] and recently by Baluchova et al in 2019.[96]

Organic pollutant compounds can be detected using bare BDD electrodes such as benzene, toluene and xylenes.[106] Phenolic pollutants (phenol, hydroquinone, 4-nitrophenol) can be feasibly and simultaneously determined with their oxidative peak potential separations of higher than 0.35 V despite of structural analogues.[107] Other organic pollutant species have been electroanalytically investigated using unmodified BDD electrodes including pesticides such as parathion, and the carbamate family (aldicarb, carbaryl, carbofuran, methomyl, and propoxur), as well as herbicides (atrazine, triclopyr, bentazone), to name but a few.[108, 109]

Heavy metals are a concern in environmental systems and biological processes. Due to the toxicity of mercury electrodes in stripping voltammetry, BDDs have been explored for alternative heavy metal sensors exploiting the wide potential window. The anodic stripping voltammetric detection of heavy metal ions (Cu^{2+}, Zn^{2+}, Ag^{+}, Cd^{2+}, Pb^{2+}) has been performed using BDDs with the minimum detectable concentration in the range of mid to low ppb, showing superior analytical merits over Hg-coated glassy carbon.[110] Metal nanoparticle modified BDD electrodes have been extensively reported for the analysis of inorganic species, especially by the Compton Group. For example, Toghill et al. have demonstrated the simultaneous electroanalytical detection of lead (Pb^{2+}) and cadmium (Cd^{2+}) using Bi-BDD and Sb-BDD electrodes by anodic stripping methods with square-wave voltammetry and linear sweep voltammetry, respectively.[111, 112] Other inorganic metals such as arsenic and manganese can be analysed as well.[86]

BDD sensors are not only applied in the above major applications, but also attractive in many other areas, such as the food industry. Numerous species have been investigated, including hydrogen peroxide, sulphite,[113] nitrite, to name but a few, and other situations applied in pH and dissolved O_2.[109, 114]

1.5.2 Electrosynthesis

BDD electrodes can be applied in the electrochemical synthesis area thanks to the extremely large potential window. High overpotentials are present in aqueous solutions for the evolution of hydrogen and oxygen, and active species such as hydroxyl radicals (·OH) and ozone can be electrochemically generated in aqueous solutions,[115] while in solutions containing methanol, methoxyl radicals can be produced.[116] These species may either serve as strong oxidants transforming the reactants or act as radicals, which are incorporated into the reaction products, leading to the occurrence of electrochemical reactions for electro-organic synthesis as shown in Figure 1.16 using a simplified scheme.[117] The electrochemical syntheses can be subdivided into anodic oxidation and cathodic reduction processes.[116]

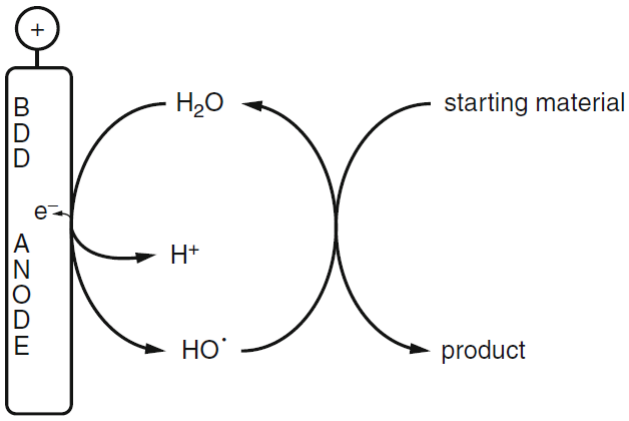


Figure 1.16 A simplified scheme of BDD anode action for electroorganic synthesis. Reprinted by permission from Ref. 117, Copyright (2014), Springer Nature.

Hydroxyl radicals (·OH) generated at BDD electrodes react with the starting reactants, leading to the formation of reactive oxyl radicals (RO·), which triggers various continuing reactions.[15] Alkoxylation reactions of hydrocarbons can be achieved allowing the introduction of oxygenated functionalities as a significant exemplification of investigation without using halogenations.[118] For instance, trimethoxymethane can be electro-organic synthesised by the anodic methoxylation of dimethoxymethane without using cyanhydric acid at BDD anodes.[117] In addition, other anodic conversions includes phenol coupling reaction,[118] C-H amination,[119] cyanation and fluorination reactions[118] driven by these oxyl radicals produced on BDD electrodes.

Compared with anodic electrochemical synthesis, cathodic synthesis on BDD electrodes is more limited. However, the high overpotential of hydrogen evolution is beneficial for the cathodic conversion. Common cathodic transformations involve reduction of oximes to prepare amines, reduction of nitro arenes to synthesize nitrones, and the reductive dimerization of cinnamic acid derivatives (such as methyl cinnamates).[119]

Electro-organic synthesis using BDD electrodes is a vivid research area. In particular, the Waldvogel group in the Johannes Gutenberg University Mainz, have contributed much to this area. Further details are accessible in the reviews in 2012,[118] and updated in 2019.[119, 120]

1.5.3 Electrochemical degradation

Many electrochemical systems using BDD have been applied for the abatement of organic pollutants in wastewater. BDD electrodes serve as anodes to degrade pollutants due to the formation of hydroxyl radicals of a strong oxidizing ability during so called "electrochemical advanced oxidation process", also referred to as electrochemical

"combustion" or "incineration". The organic contaminants are converted into nontoxic compounds or carbon dioxide during the process.[115]

Hydroxyl radicals are thought to be physically adsorbed on the "non-active" BDD electrodes as a result of a weak interaction between the electrode surface and the radical species,[48, 115] and organic pollutants react with these electro-generated hydroxyl radicals on the anode surface. Many organic pollutants have been investigated for degradation, including phenols, pesticides, herbicides, and dyes.[48, 121] The anodic oxidation of organics on BDDs can occur with the aid of other electro-generated oxidants. These agents include chlorine, ozone, and peroxydisulfuric acid ($H_2S_2O_8$), sulphate radical, etc.[122, 123] The NDC impurities, doping level, and surface nanostructures of the BDD anodes can play a notable role in the degradation performance.[27] For example, more hydroxyl radicals are produced by increasing the sp^3/sp^2 ratio of BDD electrodes, promoting mineralisation and degradation of aniline.[124]

1.5.4 Electrocatalysis

BDDs can be exploited as electrodes or as catalyst supporting substrates for electrocatalytic applications, involving carbon dioxide reduction, oxygen reduction reaction, and oxidation of alcohols in fuel cells.[27]

As a "hotspot" in the electrocatalysis area in the recent years, the electro-reduction of carbon dioxide (CO_2) has drawn many researchers' attention as a means to convert CO_2 to useful products such as fuels. A series of investigations on the performance of BDD electrodes have been conducted by the Einaga group, including the effect of alkali-metal cations[125] and anions[126] in the supporting electrolytes on the Faradaic efficiency, and selectivity of the products, respectively, the boron doping level on the efficiency,[127] and the demonstration of a highly stable and efficient conversion of CO_2 to formic acid.[128, 129]

Moreover, modification of BDD electrodes with different metal catalysts has been investigated and the products may vary. For instance, at copper modified BDD electrodes, carbon-carbon bond containing compounds with longer carbon chain including C_2 species of ethanol and acetaldehyde, and C_3 species of acetone can be produced at -1.0 V *vs.* Ag/AgCl,[130] while at palladium modified BDD electrodes, the main reduction product is carbon monoxide at a potential of -1.6 V *vs.* Ag/AgCl.[131]

With different electrocatalysts loaded on BDD electrodes, the catalytic performance has been explored towards other applications, including the oxygen reduction reaction, and fuel cells.[27] For instance, platinum-based catalysts supported on BDDs have been investigated for alcohol oxidation, such as Pt, Pt/Ru,[132] Pt/Sn, Pt/Ru/Sn, Pt/RuO_x.[8, 133]

1.5.5 Electrochemical energy storage

BDD electrode materials are used for electrochemical energy storage systems such as supercapacitors (electric double layer capacitors and pseudocapacitors), and batteries.

Various nanostructures such as porous constructions, foams, nanowires, and nanoparticle forms using BDDs have been applied for supercapacitor electrodes.[134] In particular, the preparation of BDD electrodes with a large surface area is a practical strategy to increase capacitance. To achieve this, a nano-porous honeycomb structure BDD with 200 times increase in the capacitance at 1.97×10^{-3} F cm^{-2} was produced in comparison with the as-deposited surface film.[135] Furthermore, a productive method for obtaining high capacitance is to combine BDD with active pseudo-capacitive species such as metal oxides (for example manganese dioxide, ruthenium oxide, or nickel hydroxide), and conducting polymers (such as polyaniline, or polypyrrole).[134]

The use of BDD has been attempted in lithium batteries and solar cells. For instance, BDD films of different doping levels (10^{18}-10^{21} B cm^{-3}) deposited on carbon felt substrates have

been obtained as lithium intercalation electrodes with a resulting capacity of up to 370 mAh g^{-1} when doped with 10^{21} atoms cm^{-1} for lithium ion batteries.[136] A p-type dye-sensitized solar cell has been tested using a BDD foam electrode, and the cathodic photocurrent is about three times higher than that of flat BDD film, which is due to the augmentation of the foam electrode surface area.[137]

1.6 Aims and scope of the thesis

This thesis aims to investigate the electrochemical behaviour using boron doped diamond electrodes modified by metal nanoparticles in fundamental research, especially the underlying mechanism behind the voltammetry behaviour.

Chapter 2 introduces the experimental techniques and the theory behind them. It explains basic concepts and methodologies involved in the electrochemical processes, and the fundamental principles of the measurement techniques used in this thesis.

Chapter 3 explores the electro-oxidation of sulphite in acid media on gold macroelectrodes and gold particle array modified boron doped diamond electrodes. The arrays of different morphologies, sizes, densities are obtained by controlling electrodeposition parameters. More importantly, the goal of this chapter is to disclose the electro-oxidation mechanism of sulphite via comparison of on both gold substrate and gold particle modified diamond electrodes by experimental voltammetry and digital simulation.

Chapter 4 extends the previous chapter about gold and further examines the effect of gold electrodeposition methods for nitrite detection. This work compares pulse and cyclic voltammetry depositions of gold particles on boron doped diamond electrodes, and analyses the corresponding deposits with the intention of optimisation of as-prepared electrodes with high electrocatalytic activity for electrochemical oxidation of nitrite.

Chapter 5 investigates the reduction of hydrogen peroxide on silver nanoparticle modified boron doped diamond electrodes in neutral media. It reveals the electro-reduction mechanism of hydrogen peroxide in this context via the cyclic voltammetric analysis and full mechanistic simulation.

Chapter 6 develops the above work using silver nanoparticles deposited onto boron doped diamond electrodes by drop casting and electrodeposition for hydrogen peroxide determination. The object is to explore a number of factors, such as the silver loadings, nanoparticle sizes, and deposition methods to compare and optimise the silver modified electrodes towards the hydrogen peroxide detection by cyclic voltammetry and amperometry.

Chapter 7 summarises briefly the key results and conclusions in this thesis.

References

1. Quiroz, M. A.; Bandala, E. R., Types of Conducting Diamond Materials and their Properties. In *Synthetic Diamond Films: Preparation, Electrochemistry, Characterization and Applications*, Brillas, E.; Martinez-Huitle, C. A., Eds. John Willey & Sons: Hoboken, 2011; pp 57-75.

2. Iijima, S., Helical Microtubules of Graphitic Carbon. *Nature* **1991,** *354* (6348), 56-58.

3. Baughman, R. H.; Zakhidov, A. A.; de Heer, W. A., Carbon nanotubes - the route toward applications. *Science* **2002,** *297* (5582), 787-792.

4. Novoselov, K. S.; Geim, A. K.; Morozov, S. V.; Jiang, D.; Zhang, Y.; Dubonos, S. V.; Grigorieva, I. V.; Firsov, A. A., Electric field effect in atomically thin carbon films. *Science* **2004,** *306* (5696), 666-669.

5. Geim, A. K.; Novoselov, K. S., The rise of graphene. *Nat Mater* **2007,** *6* (3), 183-191.

6. Yang, N. J.; Swain, G. M.; Jiang, X., Nanocarbon Electrochemistry and Electroanalysis: Current Status and Future Perspectives. *Electroanal* **2016,** *28* (1), 27-34.

7. Srikanth, V. V.; Jiang, X., Synthesis of Diamond Films. In *Synthetic Diamond Films: Preparation, Electrochemistry, Characterization and Applications*, Brillas, E.; Martinez-Huitle, C. A., Eds. John Willey & Sons: Hoboken, 2011; pp 21-55.

8. Kraft, A., Doped diamond: A compact review on a new, versatile electrode material. *Int J Electrochem Sc* **2007,** *2* (5), 355-385.

9. Compton, R. G.; Foord, J. S.; Marken, F., Electroanalysis at diamond-like and doped-diamond electrodes. *Electroanal* **2003,** *15* (17), 1349-1363.

10. Luong, J. H. T.; Male, K. B.; Glennon, J. D., Boron-doped diamond electrode: synthesis, characterization, functionalization and analytical applications. *Analyst* **2009,** *134* (10), 1965-1979.

11. Bundy, F. P.; Hall, H. T.; Strong, H. M.; Wentorf, R. H., Man-Made Diamonds. *Nature* **1955,** *176* (4471), 51-55.

12. Macpherson, J. V., The Use of Conducting Diamond in Electrochemistry. In *Electrochemistry of Carbon Electrodes*, Alkire, R. C.; Bartlett, P. N.; Lipkowski, J., Eds. Wiley-VCH: Weinheim, 2015; pp 163-210.

13. Pleskov, Y. V.; Evstefeeva, Y. E.; Krotova, M.; Mishuk, V. Y.; Laptev, V.; Palyanov, Y. N.; Borzdov, Y. M., Effect of Crystal Structure on the Behavior of Diamond Electrodes Electrochemical Characteristics of Individual Crystal Faces. *J Electrochem Soc* **2002,** *149* (7), E260-E264.

14. Bormashov, V. S.; Tarelkin, S. A.; Buga, S. G.; Kuznetsov, M. S.; Terentiev, S. A.; Semenov, A. N.; Blank, V. D., Electrical properties of the high quality boron-doped synthetic single-crystal diamonds grown by the temperature gradient method. *Diam Relat Mater* **2013,** *35*, 19-23.

15. Cobb, S. J.; Ayres, Z. J.; Macpherson, J. V., Boron Doped Diamond: A Designer Electrode Material for the Twenty-First Century. *Annual Review of Analytical Chemistry* **2018,** *11*, 463-484.

16. Eversole, W. G.; Kenmore, N. Y. Synthesis of diamond. US Patents 3030187 and 3030188, 1962.

17. Angus, J. C.; Will, H. A.; Stanko, W. S., Growth of Diamond Seed Crystals by Vapor Deposition. *J Appl Phys* **1968,** *39* (6), 2915-2922.

18. Deryagin, B. V.; Builov, L. L.; Zubkov, V. M.; Kochergi.Aa; Fedoseev, D. V., Filamentary Diamond Crystals. *Sov Phys Crystallogr* **1969,** *14* (3), 449-450.

19. Matsumoto, S.; Sato, Y.; Kamo, M.; Setaka, N., Vapor-Deposition of Diamond Particles from Methane. *Jpn J Appl Phys* **1982,** *21* (4), L183-L185.

20. Matsumoto, S.; Sato, Y.; Tsutsumi, M.; Setaka, N., Growth of Diamond Particles from Methane-Hydrogen Gas. *J Mater Sci* **1982,** *17* (11), 3106-3112.

21. Angus, J. C., Diamond synthesis by chemical vapor deposition: The early years. *Diam Relat Mater* **2014,** *49*, 77-86.

22. Hirose, Y.; Kondo, N. In *Program and Book of Abstracts*, Japan Applied Physics 1988 Spring meeting, March 29; 1988; p 434.

23. Kamo, M.; Sato, Y.; Matsumoto, S.; Setaka, N., Diamond Synthesis from Gas-Phase in Microwave Plasma. *J Cryst Growth* **1983,** *62* (3), 642-644.

24. Suzuki, K.; Sawabe, A.; Yasuda, H.; Inuzuka, T., Growth of Diamond Thin-Films by Dc Plasma Chemical Vapor-Deposition. *Appl Phys Lett* **1987,** *50* (12), 728-729.

25. Matsumoto, S., Chemical Vapor-Deposition of Diamond in Rf Glow-Discharge. *J Mater Sci Lett* **1985,** *4* (5), 600-602.

26. Matsumoto, S.; Hino, M.; Kobayashi, T., Synthesis of Diamond Films in a Rf Induction Thermal Plasma. *Appl Phys Lett* **1987,** *51* (10), 737-739.

27. Yang, N. J.; Yu, S. Y.; Macpherson, J. V.; Einaga, Y.; Zhao, H. Y.; Zhao, G. H.; Swain, G. M.; Jiang, X., Conductive diamond: synthesis, properties, and electrochemical applications. *Chem Soc Rev* **2019,** *48* (1), 157-204.

28. Lee, S. T.; Lin, Z. D.; Jiang, X., CVD diamond films: nucleation and growth. *Mat Sci Eng R* **1999,** *25* (4), 123-154.

29. Macpherson, J. V., A practical guide to using boron doped diamond in electrochemical research. *Phys Chem Chem Phys* **2015,** *17* (5), 2935-2949.

30. Zhou, D.; Gruen, D. M.; Qin, L. C.; McCauley, T. G.; Krauss, A. R., Control of diamond film microstructure by Ar additions to CH_4/H_2 microwave plasmas. *J Appl Phys* **1998,** *84* (4), 1981-1989.

31. Gruen, D. M., Nanocrystalline diamond films. *Annu Rev Mater Sci* **1999,** *29*, 211-259.

32. Liu, Y. M.; Zhang, Y. J.; Cheng, K.; Quan, X.; Fan, X. F.; Su, Y.; Chen, S.; Zhao, H. M.; Zhang, Y. B.; Yu, H. T.; Hoffmann, M. R., Selective Electrochemical Reduction of Carbon Dioxide to Ethanol on a Boron- and Nitrogen-Co-doped Nanodiamond. *Angew Chem Int Edit* **2017,** *56* (49), 15607-15611.

33. Haenen, K.; Meykens, K.; Nesladek, M.; Knuyt, G.; Stals, L. M.; Teraji, T.; Koizumi, S.; Gheeraert, E., Phonon-assisted electronic transitions in phosphorus-doped n-type chemical vapor deposition diamond films. *Diam Relat Mater* **2001,** *10* (3-7), 439-443.

34. Poferl, D. J.; Gardner, N. C.; Angus, J. C., Growth of Boron-Doped Diamond Seed Crystals by Vapor-Deposition. *J Appl Phys* **1973,** *44* (4), 1428-1434.

35. Morooka, S.; Fukui, T.; Semoto, K.; Tsubota, T.; Saito, T.; Kusakabe, K.; Maeda, H.; Hayashi, Y.; Asano, T., Electrical properties of homoepitaxial boron-doped diamond thin films grown by chemical vapor deposition using trimethylboron as dopant. *Diam Relat Mater* **1999,** *8* (1), 42-47.

36. Watanabe, T.; Yoshioka, S.; Yamamoto, T.; Sepehri-Amin, H.; Ohkubo, T.; Matsumura, S.; Einaga, Y., The local structure in heavily boron-doped diamond and the effect this has on its electrochemical properties. *Carbon* **2018,** *137*, 333-342.

37. Einaga, Y.; Foord, J. S.; Swain, G. M., Diamond electrodes: Diversity and maturity. *Mrs Bull* **2014,** *39* (6), 525-532.

38. Ekimov, E. A.; Sidorov, V. A.; Bauer, E. D.; Mel'nik, N. N.; Curro, N. J.; Thompson, J. D.; Stishov, S. M., Superconductivity in diamond. *Nature* **2004,** *428* (6982), 542-545.

39. Chen, Q. Y.; Gruen, D. M.; Krauss, A. R.; Corrigan, T. D.; Witek, M.; Swain, G. M., The structure and electrochemical behavior of nitrogen-containing nanocrystalline diamond films deposited from CH_4/N_2/Ar mixtures. *J Electrochem Soc* **2001,** *148* (1), E44-E51.

40. Sakaguchi, I.; Gamo, M. N.; Kikuchi, Y.; Yasu, E.; Haneda, H.; Suzuki, T.; Ando, T., Sulfur: A donor dopant for n-type diamond semiconductors. *Phys Rev B* **1999,** *60* (4), R2139-R2141.

41. Pleskov, Y. V.; Krotova, M. D.; Saveliev, A. V.; Ralchenko, V. G., The effects of nitrogenation on the electrochemical properties of nanocrystalline diamond films. *Diam Relat Mater* **2007,** *16* (12), 2114-2117.

42. Mukuda, Y.; Watanabe, T.; Ueda, A.; Nishibayashi, Y.; Einaga, Y., Electrochemical properties of phosphorus doped diamond. *Electrochim Acta* **2015,** *179*, 599-603.

43. Iwaki, M.; Sato, S.; Takahashi, K.; Sakairi, H., Electrical conductivity of nitrogen and argon implanted diamond. *Nucl Instrum Methods Phys Res* **1983,** *209-210*, 1129-1133.

44. Pleskov, Y. V.; Sakharova, A. Y.; Krotova, M. D.; Bouilov, L. L.; Spitsyn, B. V., Photoelectrochemical Properties of Semiconductor Diamond. *J Electroanal Chem* **1987,** *228* (1-2), 19-27.

45. Fujishima, A.; Einaga, Y.; Rao, T. N.; Tryk, D. A., *Diamond electrochemistry*. Elsevier: Amsterdam, 2005.

46. Patel, K.; Hashimoto, K.; Fujishima, A., Photoelectrochemical Investigations on Boron-Doped Chemically Vapor-Deposited Diamond Electrodes. *J Photoch Photobio A* **1992,** *65* (3), 419-429.

47. Martin, H. B.; Argoitia, A.; Landau, U.; Anderson, A. B.; Angus, J. C., Hydrogen and oxygen evolution on boron-doped diamond electrodes. *J Electrochem Soc* **1996,** *143* (6), L133-L136.

48. Nidheesh, P. V.; Divyapriya, G.; Oturan, N.; Trellu, C.; Oturan, M. A., Environmental Applications of Boron-Doped Diamond Electrodes: 1. Applications in Water and Wastewater Treatment. *ChemElectroChem* **2019,** *6* (8), 2124-2142.

49. Williams, O. A., Nanocrystalline diamond. *Diam Relat Mater* **2011,** *20* (5-6), 621-640.

50. Patten, H. V.; Meadows, K. E.; Hutton, L. A.; Iacobini, J. G.; Battistel, D.; McKelvey, K.; Colburn, A. W.; Newton, M. E.; Macpherson, J. V.; Unwin, P. R., Electrochemical Mapping Reveals Direct Correlation between Heterogeneous Electron-Transfer Kinetics and Local Density of States in Diamond Electrodes. *Angew Chem Int Edit* **2012,** *51* (28), 7002-7006.

51. Wang, S.; Swope, V. M.; Bulter, J. E.; Feygelson, T.; Swain, G. M., The structural and electrochemical properties of boron-doped nanocrystalline diamond thin-film electrodes grown from Ar-rich and H_2-rich source gases. *Diam Relat Mater* **2009,** *18* (4), 669-677.

52. Lagrange, J. P.; Deneuville, A.; Gheeraert, E., Activation energy in low compensated homoepitaxial boron-doped diamond films. *Diam Relat Mater* **1998,** *7* (9), 1390-1393.

53. Watanabe, T.; Honda, Y.; Kanda, K.; Einaga, Y., Tailored design of boron-doped diamond electrodes for various electrochemical applications with boron-doping level and sp^2-bonded carbon impurities. *Phys Status Solidi A* **2014,** *211* (12), 2709-2717.

54. Kolber, T.; Piplits, K.; Haubner, R.; Hutter, H., Quantitative investigation of boron incorporation in polycrystalline CVD diamond films by SIMS. *Fresen J Anal Chem* **1999,** *365* (8), 636-641.

55. Habka, N.; Pinault, M. A.; Mer, C.; Jomard, F.; Barjon, J.; Nesladek, M.; Bergonzo, P., Substrate influence on MPCVD boron-doped homoepitaxial diamond. *Phys Status Solidi A* **2008,** *205* (9), 2169-2172.

56. Chen, C. F.; Chen, S. H.; Hong, T. M.; Wang, T. C., Characterization of Boron-Doped Diamond Films Using (CH_4-CO_2) Gas-Mixtures with $B(OCH_3)_3$ as a Dopant Source by Mpcvd. *Thin Solid Films* **1994,** *248* (2), 149-155.

57. Hutton, L. A.; Iacobini, J. G.; Bitziou, E.; Channon, R. B.; Newton, M. E.; Macpherson, J. V., Examination of the Factors Affecting the Electrochemical Performance of Oxygen-Terminated Polycrystalline Boron-Doped Diamond Electrodes. *Anal Chem* **2013,** *85* (15), 7230-7240.

58. Bernard, M.; Deneuville, A.; Muret, P., Non-destructive determination of the boron concentration of heavily doped metallic diamond thin films from Raman spectroscopy. *Diam Relat Mater* **2004,** *13* (2), 282-286.

59. Mortet, V.; Zivcova, Z. V.; Taylor, A.; Davydova, M.; Frank, O.; Hubik, P.; Lorincik, J.; Aleshin, M., Determination of atomic boron concentration in heavily boron-doped diamond by Raman spectroscopy. *Diam Relat Mater* **2019,** *93*, 54-58.

60. Knittel, P.; Stach, R.; Yoshikawa, T.; Kirste, L.; Mizaikoff, B.; Kranz, C.; Nebel, C. E., Characterisation of thin boron-doped diamond films using Raman spectroscopy and chemometrics. *Anal Methods* **2019,** *11* (5), 582-586.

61. Hoffmann, R.; Kriele, A.; Obloh, H.; Hees, J.; Wolfer, M.; Smirnov, W.; Yang, N.; Nebel, C. E., Electrochemical hydrogen termination of boron-doped diamond. *Appl Phys Lett* **2010,** *97* (5).

62. Wang, M.; Simon, N.; Decorse-Pascanut, C.; Bouttemy, M.; Etcheberry, A.; Li, M. S.; Boukherroub, R.; Szunerits, S., Comparison of the chemical composition of boron-doped diamond surfaces upon different oxidation processes. *Electrochim Acta* **2009,** *54* (24), 5818-5824.

63. Miller, J. B., Amines and thiols on diamond surfaces. *Surf Sci* **1999,** *439* (1-3), 21-33.

64. Muzyka, K.; Sun, J. R.; Fereja, T. H.; Lan, Y. X.; Zhang, W.; Xu, G. B., Boron-doped diamond: current progress and challenges in view of electroanalytical applications. *Anal Methods* **2019,** *11* (4), 397-414.

65. Granger, M. C.; Witek, M.; Xu, J. S.; Wang, J.; Hupert, M.; Hanks, A.; Koppang, M. D.; Butler, J. E.; Lucazeau, G.; Mermoux, M.; Strojek, J. W.; Swain, G. M., Standard electrochemical behavior of high-quality, boron-doped polycrystalline diamond thin-film electrodes. *Anal Chem* **2000,** *72* (16), 3793-3804.

66. Bennett, J. A.; Wang, J. A.; Show, Y.; Swain, G. M., Effect of sp^2-bonded nondiamond carbon impurity on the response of boron-doped polycrystalline diamond thin-film electrodes. *J Electrochem Soc* **2004,** *151* (9), E306-E313.

67. Garcia-Segura, S.; dos Santos, E. V.; Martinez-Huitle, C. A., Role of sp^3/sp^2 ratio on the electrocatalytic properties of boron-doped diamond electrodes: A mini review. *Electrochem Commun* **2015,** *59*, 52-55.

68. Ferrari, A. C.; Robertson, J., Origin of the 1150-cm^{-1} Raman mode in nanocrystalline diamond. *Phys Rev B* **2001,** *63* (12).

69. Dong, H.; Wang, S.; Galligan, J. J.; Swain, G. M., Boron-doped diamond nano/microelectrodes for bio-sensing and in vitro measurements. *Front Biosci (Schol Ed)* **2011,** *3*, 518-540.

70. Einaga, Y., Development of Electrochemical Applications of Boron-Doped Diamond Electrodes. *B Chem Soc Jpn* **2018,** *91* (12), 1752-1762.

71. Lucio, A. J.; Shaw, S. K.; Zhang, J.; Bond, A. M., Double-Layer Capacitance at Ionic Liquid-Boron-Doped Diamond Electrode Interfaces Studied by Fourier Transformed Alternating Current Voltammetry. *J Phys Chem C* **2018,** *122* (22), 11777-11788.

72. Xu, J. S.; Granger, M. C.; Chen, Q. Y.; Strojek, J. W.; Lister, T. E.; Swain, G. M., Boron-doped diamond thin-film electrodes. *Anal Chem* **1997,** *69* (19), A591-A597.

73. Jones, S. E. W.; Compton, R. G., Stripping analysis using boron-doped diamond electrodes. *Curr Anal Chem* **2008,** *4* (3), 170-176.

74. Hanssen, B. L.; Siraj, S.; Wong, D. K. Y., Recent strategies to minimise fouling in electrochemical detection systems. *Rev Anal Chem* **2016,** *35* (1), 1-28.

75. Ogata, G.; Ishii, Y.; Asai, K.; Sano, Y.; Nin, F.; Yoshida, T.; Higuchi, T.; Sawamura, S.; Ota, T.; Hori, K.; Maeda, K.; Komune, S.; Doi, K.; Takai, M.; Findlay, I.; Kusuhara, H.; Einaga, Y.; Hibino, H., A microsensing system for the in vivo real-time detection of local drug kinetics. *Nat Biomed Eng* **2017,** *1* (8), 654-666.

76. Watanabe, T.; Shimizu, T. K.; Tateyama, Y.; Kim, Y.; Kawai, M.; Einaga, Y., Giant electric double-layer capacitance of heavily boron-doped diamond electrode. *Diam Relat Mater* **2010,** *19* (7-9), 772-777.

77. Kamoshida, N.; Kasahara, S.; Ikemiya, N.; Hoshi, N.; Nakamura, M.; Einaga, Y., In situ ATR-IR study of $Fe(CN)_6^{3-}/Fe(CN)_6^{4-}$ redox system on boron-doped diamond electrode. *Diam Relat Mater* **2019,** *93*, 50-53.

78. Kondo, T.; Einaga, Y.; Sarada, B. V.; Rao, T. N.; Tryk, D. A.; Fujishima, A., Homoepitaxial single-crystal boron-doped diamond electrodes for electroanalysis. *J Electrochem Soc* **2002,** *149* (6), E179-E184.

79. Ushizawa, K.; Watanabe, K.; Ando, T.; Sakaguchi, I.; Nishitani-Gamo, M.; Sato, Y.; Kanda, H., Boron concentration dependence of Raman spectra on {100} and {111} facets of B-doped CVD diamond. *Diam Relat Mater* **1998,** *7* (11-12), 1719-1722.

80. Ivandini, T. A.; Watanabe, T.; Matsui, T.; Ootani, Y.; Iizuka, S.; Toyoshima, R.; Kodama, H.; Kondoh, H.; Tateyama, Y.; Einaga, Y., Influence of Surface Orientation on Electrochemical Properties of Boron-Doped Diamond. *J Phys Chem C* **2019,** *123* (9), 5336-5344.

81. Kondo, T.; Honda, K.; Tryk, D. A.; Fujishimad, A., Covalent modification of single-crystal diamond electrode surfaces. *J Electrochem Soc* **2005,** *152* (1), E18-E23.

82. Kuo, T. C.; McCreery, R. L.; Swain, G. M., Electrochemical modification of boron-doped chemical vapor deposited diamond surfaces with covalently bonded monolayers. *Electrochem Solid St* **1999,** *2* (6), 288-290.

83. Shin, D. C.; Tokuda, N.; Rezek, B.; Nebel, C. E., Periodically arranged benzene-linker molecules on boron-doped single-crystalline diamond films for DNA sensing. *Electrochem Commun* **2006,** *8* (5), 844-850.

84. Shin, D.; Rezek, B.; Tokuda, N.; Takeuchi, D.; Watanabe, H.; Nakamura, T.; Yamamoto, T.; Nebel, C. E., Photo- and electrochemical bonding of DNA to single crystalline CVD diamond. *Phys Status Solidi A* **2006,** *203* (13), 3245-3272.

85. Ivandini, T. A.; Sato, R.; Makide, Y.; Fujishima, A.; Einaga, Y., Electroanalytical application of modified diamond electrodes. *Diam Relat Mater* **2004,** *13* (11-12), 2003-2008.

86. Toghill, K. E.; Compton, R. G., Metal Nanoparticle Modified Boron Doped Diamond Electrodes for Use in Electroanalysis. *Electroanal* **2010,** *22* (17-18), 1947-1956.

87. Ohnishi, K.; Einaga, Y.; Notsu, H.; Terashima, C.; Rao, T. N.; Park, S. G.; Fujishima, A., Electrochemical glucose detection using nickel-implanted boron-doped diamond electrodes. *Electrochem Solid St* **2002,** *5* (3), D1-D3.

88. Ivandini, T. A.; Sato, R.; Makide, Y.; Fujishima, A.; Einaga, Y., Electrochemical detection of arsenic(III) using iridium-implanted boron-doped diamond electrodes. *Anal Chem* **2006,** *78* (18), 6291-6298.

89. Ivandini, T. A.; Sato, R.; Makide, Y.; Fujishima, A.; Einaga, Y., Pt-implanted boron-doped diamond electrodes and the application for electrochemical detection of hydrogen peroxide. *Diam Relat Mater* **2005,** *14* (11-12), 2133-2138.

90. Welch, C. M.; Compton, R. G., The use of nanoparticles in electroanalysis: a review. *Anal Bioanal Chem* **2006,** *384* (3), 601-619.

91. Lounasvuori, M. M.; Nelson, G. W.; Foord, J. S., Nanoparticle-Based Diamond Electrodes. In *Novel Aspects of Diamond: From Growth to Applications*, Second ed.; Yang, N., Ed. Springer: Cham, 2019; pp 257-312.

92. Mavrokefalos, C. K.; Hasan, M.; Rohan, J. F.; Foord, J. S., Enhanced Mass Activity and Stability of Bimetallic Pd-Ni Nanoparticles on Boron-Doped Diamond for Direct Ethanol Fuel Cell Applications. *ChemElectroChem* **2018,** *5* (3), 455-463.

93. Li, M. F.; Zhao, G. H.; Geng, R.; Hu, H. K., Facile electrocatalytic redox of hemoglobin by flower-like gold nanoparticles on boron-doped diamond surface. *Bioelectrochemistry* **2008,** *74* (1), 217-221.

94. Welch, C. M.; Simm, A. O.; Compton, R. G., Oxidation of electrodeposited copper on Boron Doped Diamond in acidic solution: Manipulating the size of copper nanoparticles using voltammetry. *Electroanal* **2006,** *18* (10), 965-970.

95. Tian, R. H.; Rao, T. N.; Einaga, Y.; Zhi, J. F., Construction of two-dimensional arrays gold nanoparticles monolayer onto boron-doped diamond electrode surfaces. *Chem Mater* **2006,** *18* (4), 939-945.

96. Baluchova, S.; Danhel, A.; Dejmkova, H.; Ostatna, V.; Fojta, M.; Schwarzova-Peckova, K., Recent progress in the applications of boron doped diamond electrodes in electroanalysis of organic compounds and biomolecules - A review. *Anal Chim Acta* **2019,** *1077*, 30-66.

97. Eisele, A. P. P.; Valezi, C. F.; Sartori, E. R., Exploiting the high oxidation potential of carisoprodol on a boron-doped diamond electrode: an improved method for its simultaneous determination with acetaminophen and caffeine. *Analyst* **2017,** *142* (18), 3514-3521.

98. Feier, B.; Gui, A.; Cristea, C.; Sandulescu, R., Electrochemical determination of cephalosporins using a bare boron-doped diamond electrode. *Anal Chim Acta* **2017,** *976*, 25-34.

99. Hanko, M.; Svorc, L.; Plankova, A.; Mikus, P., Novel electrochemical strategy for determination of 6-mercaptopurine using anodically pretreated boron-doped diamond electrode. *J Electroanal Chem* **2019,** *840*, 295-304.

100. Niedzialkowski, P.; Cebula, Z.; Malinowska, N.; Bialobrzeska, W.; Sobaszek, M.; Ficek, M.; Bogdanowicz, R.; Anand, J. S.; Ossowski, T., Comparison of the paracetamol electrochemical determination using boron-doped diamond electrode and boron-doped carbon nanowalls. *Biosens Bioelectron* **2019,** *126*, 308-314.

101. Bottari, F.; De Wael, K., Electrodeposition of gold nanoparticles on boron doped diamond electrodes for the enhanced reduction of small organic molecules. *J Electroanal Chem* **2017,** *801*, 521-526.

102. Sousa, C. P.; Ribeiro, F. W. P.; Oliveira, T. M. B. F.; Salazar-Banda, G. R.; de Lima-Neto, P.; Morais, S.; Correia, A. N., Electroanalysis of Pharmaceuticals on Boron-Doped Diamond Electrodes: A Review. *ChemElectroChem* **2019,** *6* (9), 2350-2378.

103. Tyszczuk-Rotko, K.; Jaworska, I.; Jedruchniewicz, K., Application of unmodified boron-doped diamond electrode for determination of dopamine and paracetamol. *Microchem J* **2019,** *146*, 664-672.

104. Svitkova, J.; Ignat, T.; Svorc, L.; Labuda, J.; Barek, J., Chemical Modification of Boron-Doped Diamond Electrodes for Applications to Biosensors and Biosensing. *Crit Rev Anal Chem* **2016,** *46* (3), 248-256.

105. Gong, Z.; Hu, N.; Ye, W.; Zheng, K.; Li, C.; Ma, L.; Wei, Q.; Yu, Z.; Zhou, K.; Huang, N.; Lin, C.-T.; Luo, J., High-performance non-enzymatic glucose sensor based on Ni/Cu/boron-doped diamond electrode. *J Electroanal Chem* **2019,** *841*, 135-141.

106. de Freitas, G. G.; Florencio, T. M.; Mendonca, R. J.; Salazar-Banda, G. R.; Oliveira, R. T. S., Simultaneous Voltammetric Determination of Benzene, Toluene and Xylenes (BTX) in Water Using a Cathodically Pre-treated Boron-doped Diamond Electrode. *Electroanal* **2019,** *31* (3), 554-559.

107. Lei, Y. Z.; Zhao, G. H.; Liu, M. C.; Xiao, X.; Tang, Y. T.; Li, D. M., Simple and feasible simultaneous determination of three phenolic pollutants on boron-doped diamond film electrode. *Electroanal* **2007,** *19* (18), 1933-1938.

108. Jevtic, S.; Stefanovic, A.; Stankovic, D. M.; Pergal, M. V.; Ivanovic, A. T.; Jokic, A.; Petkovic, B. B., Boron-doped diamond electrode - A prestigious unmodified carbon electrode for simple and fast determination of bentazone in river water samples. *Diam Relat Mater* **2018,** *81*, 133-137.

109. Trellu, C.; Chakraborty, S.; Nidheesh, P. V.; Oturan, M. A., Environmental Applications of Boron-Doped Diamond Electrodes: 2. Soil Remediation and Sensing Applications. *ChemElectroChem* **2019,** *6* (8), 2143-2156.

110. Mcgaw, E. A.; Swain, G. M., A comparison of boron-doped diamond thin-film and Hg-coated glassy carbon electrodes for anodic stripping voltammetric determination of heavy metal ions in aqueous media. *Anal Chim Acta* **2006,** *575* (2), 180-189.

111. Toghill, K. E.; Wildgoose, G. G.; Moshar, A.; Mulcahy, C.; Compton, R. G., The fabrication and characterization of a bismuth nanoparticle modified boron doped diamond electrode and its application to the simultaneous determination of cadmium(II) and lead(II). *Electroanal* **2008,** *20* (16), 1731-1737.

112. Toghill, K. E.; Xiao, L.; Wildgoose, G. G.; Compton, R. G., Electroanalytical Determination of Cadmium(II) and Lead(II) Using an Antimony Nanoparticle Modified Boron-Doped Diamond Electrode. *Electroanal* **2009,** *21* (10), 1113-1118.

113. Chinvongamorn, C.; Pinwattana, K.; Praphairaksit, N.; Imato, T.; Chailapakul, O., Amperometric determination of sulfite by gas diffusion-sequential injection with boron-doped diamond electrode. *Sensors* **2008,** *8* (3), 1846-1857.

114. Read, T. L.; Cobb, S. J.; Macpherson, J. V., An sp^2 Patterned Boron Doped Diamond Electrode for the Simultaneous Detection of Dissolved Oxygen and pH. *Acs Sensors* **2019,** *4* (3), 756-763.

115. He, Y. P.; Lin, H. B.; Guo, Z. C.; Zhang, W. L.; Li, H. D.; Huang, W. M., Recent developments and advances in boron-doped diamond electrodes for electrochemical oxidation of organic pollutants. *Sep Purif Technol* **2019,** *212*, 802-821.

116. Ivandini, T. A.; Einaga, Y., Polycrystalline boron-doped diamond electrodes for electrocatalytic and electrosynthetic applications. *Chem Commun* **2017,** *53* (8), 1338-1347.

117. Waldvogel, S. R.; Elsler, B., Boron-Doped Diamond for Green Electro-Organic Synthesis. In *Encyclopedia of Applied Electrochemistry*, Kreysa, G.; Ota, K.-i.; Savinell, R. F., Eds. Springer: New York, 2014; pp 143-148.

118. Waldvogel, S. R.; Elsler, B., Electrochemical synthesis on boron-doped diamond. *Electrochim Acta* **2012,** *82*, 434-443.

119. Martínez-Huitle, C. A.; Waldvogel, S. R., Trends of Organic Electrosynthesis by Using Boron-Doped Diamond Electrodes. In *Novel Aspects of Diamond*, Yang, N., Ed. Springer International Publishing: Cham, 2019; pp 173-197.

120. Lips, S.; Waldvogel, S. R., Use of Boron-Doped Diamond Electrodes in Electro-Organic Synthesis. *ChemElectroChem* **2019,** *6* (6), 1649-1660.

121. Zhang, Y. N.; Niu, Q.; Gu, X.; Yang, N.; Zhao, G., Recent progress on carbon nanomaterials for the electrochemical detection and removal of environmental pollutants. *Nanoscale* **2019,** *11* (25), 11992-12014.

122. Scialdone, O.; Galia, A., Modeling of Electrochemical Process for Water Treatment Using Diamond Films. In *Synthetic Diamond Films: Preparation, Electrochemistry, Characterization and Applications*, Brillas, E.; Martinez-Huitle, C. A., Eds. John Willey & Sons: Hoboken, 2011; pp 261-280.

123. Ganiyu, S. O.; Martinez-Huitle, C. A., Nature, Mechanisms and Reactivity of Electrogenerated Reactive Species at Thin-Film Boron-Doped Diamond (BDD) Electrodes During Electrochemical Wastewater Treatment. *ChemElectroChem* **2019,** *6* (9), 2379-2392.

124. Espinoza, L. C.; Henriquez, A.; Contreras, D.; Salazar, R., Evidence for the production of hydroxyl radicals at boron-doped diamond electrodes with different sp^3/sp^2 ratios and its relationship with the anodic oxidation of aniline. *Electrochem Commun* **2018,** *90*, 30-33.

125. Ikemiya, N.; Natsui, K.; Nakata, K.; Einaga, Y., Effect of alkali-metal cations on the electrochemical reduction of carbon dioxide to formic acid using boron-doped diamond electrodes. *RSC Adv* **2017,** *7* (36), 22510-22514.

126. Tomisaki, M.; Kasahara, S.; Natsui, K.; Ikemiya, N.; Einaga, Y., Switchable Product Selectivity in the Electrochemical Reduction of Carbon Dioxide Using Boron-Doped Diamond Electrodes. *J Am Chem Soc* **2019,** *141* (18), 7414-7420.

127. Xu, J.; Natsui, K.; Naoi, S.; Nakata, K.; Einaga, Y., Effect of doping level on the electrochemical reduction of CO_2 on boron-doped diamond electrodes. *Diam Relat Mater* **2018,** *86*, 167-172.

128. Natsui, K.; Iwakawa, H.; Ikemiya, N.; Nakata, K.; Einaga, Y., Stable and Highly Efficient Electrochemical Production of Formic Acid from Carbon Dioxide Using Diamond Electrodes. *Angew Chem Int Edit* **2018,** *57* (10), 2639-2643.

129. Ikemiya, N.; Natsui, K.; Nakata, K.; Einaga, Y., Long-Term Continuous Conversion of CO_2 to Formic Acid Using Boron-Doped Diamond Electrodes. *Acs Sustain Chem Eng* **2018,** *6* (7), 8108-8112.

130. Jiwanti, P. K.; Natsui, K.; Nakata, K.; Einaga, Y., The electrochemical production of C_2/C_3 species from carbon dioxide on copper-modified boron-doped diamond electrodes. *Electrochim Acta* **2018,** *266*, 414-419.

131. Jiwanti, P. K.; Einaga, Y., Electrochemical reduction of CO_2 using palladium modified boron-doped diamond electrodes: enhancing the production of CO. *Phys Chem Chem Phys* **2019,** *21* (28), 15297-15301.

132. Campbell, F. W.; Compton, R. G., The use of nanoparticles in electroanalysis: an updated review. *Anal Bioanal Chem* **2010,** *396* (1), 241-259.

133. Eguiluz, K. I. B.; Peralta-Hernández, J. M.; Hernández-Ramírez, A.; Guzmán-Mar, J. L.; Hinojosa-Reyes, L.; Martínez-Huitle, C. A.; Salazar-Banda, G. R., The Use of

Diamond for Energy Conversion System Applications: A Review. *International Journal of Electrochemistry* **2012,** *2012*, 1-20.

134. Yang, N. J.; Foord, J. S.; Jiang, X., Diamond electrochemistry at the nanoscale: A review. *Carbon* **2016,** *99*, 90-110.

135. Honda, K.; Rao, T. N.; Tryk, D. A.; Fujishima, A.; Watanabe, M.; Yasui, K.; Masuda, H., Electrochemical characterization of the nanoporous honeycomb diamond electrode as an electrical double-layer capacitor. *J Electrochem Soc* **2000,** *147* (2), 659-664.

136. Almeida, E. C.; Trava-Airoldi, V. J.; Ferreira, N. G.; Rosolen, J. M., Electrochemical insertion of lithium into a doped diamond film grown on carbon felt substrates. *Diam Relat Mater* **2005,** *14* (10), 1673-1677.

137. Krysova, H.; Kavan, L.; Zivcova, Z. V.; Yeap, W. S.; Verstappen, P.; Maes, W.; Haenen, K.; Gao, F.; Nebel, C. E., Dye-sensitization of boron-doped diamond foam: champion photoelectrochemical performance of diamond electrodes under solar light illumination. *RSC Adv* **2015,** *5* (99), 81069-81077.

Chapter 2 Experimental techniques and the theory behind them

This chapter aims to offer a general sight of the theory underpinning the work in this thesis, in particular electrochemistry. Fundamentals of electrochemistry are described, including equilibrium electrochemistry, Faradaic and non-Faradaic processes, mass transfer, and electrode reaction kinetics. Electrochemical methods including linear sweep voltammetry, cyclic voltammetry, differential pulse voltammetry, and electrochemical impedance spectroscopy with electrochemical instrumentation and experimental set-up are introduced. Characterisation techniques including X-ray photoelectron spectroscopy (XPS) and scanning electron microscopy (SEM) are also covered.

2.1 Fundamentals of electrochemistry

2.1.1 Equilibrium electrochemistry

Electrochemistry focuses on the study of the charge transfer across the interface between an ionic conductor (an electrolyte) and an electronic conductor (an electrode).[1] This process is heterogeneous in essence. A simple charge transfer process can be expressed by the following equation:

$$O + n\,e^- \rightleftarrows R \quad (2.1)$$

where an oxidised species *O* in solution accepts n electrons from an electrode to become the reduced species *R* in solution. As a paradigm case, an electrochemical equilibrium can be established by inserting a platinum wire "electrode" into a solution containing potassium ferrocyanide $K_4Fe(CN)_6$, and potassium ferricyanide $K_3Fe(CN)_6$ as shown in Figure 2.1.[2] The establishment of an equilibrium indicates that the electron-donating rate from $Fe(CN)_6^{4-}$ to the metal wire is balanced to the electron transfer from the metal wire

to $Fe(CN)_6^{3-}$. As the reaction involves electron transfer, there would be a net electrical charge on each phase once the equilibrium is obtained. Accordingly, a difference in electrical potential between the metal electrode and the solution phase will be established, being referred as an electrode potential.

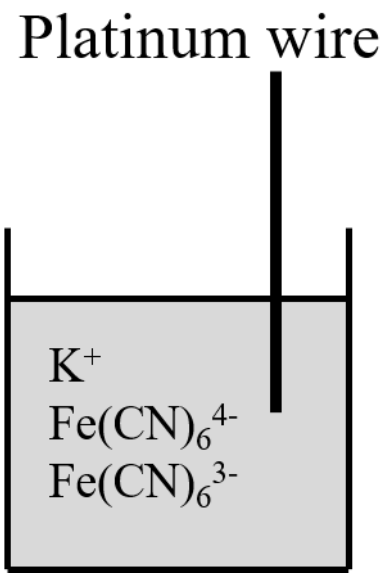


Figure 2.1 A Pt wire immersed into an aqueous solution containing $K_4Fe(CN)_6$ and $K_3Fe(CN)_6$.

Nevertheless, it is impossible to measure an absolute value individually for the interfacial potential difference relating to a single electrode-solution interface. The electrochemical potential can, however, be measured by the introduction of another second electrode acting as a reference electrode against which the potential is measured. The equilibrium potential is given by the Nernst equation:

$$E = E^0 + \frac{RT}{nF} \ln \frac{\alpha_O}{\alpha_R} \quad (2.2)$$

where E^0 is the standard electrode potential (V) using the standard hydrogen electrode as a reference electrode, R is the universal gas constant (8.314 J K^{-1} mol^{-1}), T is the temperature (K), n is the number of electrons transferred, F is the Faraday constant (96485

C mol^{-1}), α_O and α_R are the activities of oxidised species O and reduced species R, respectively.

The activities of species are related to the concentrations as follows:

$$\alpha_O = \gamma_O C_O \quad (2.3)$$

$$\alpha_R = \gamma_R C_R \quad (2.4)$$

where γ_O and γ_R are the activity coefficients of species O and R, respectively, C_O and C_R are the corresponding species concentrations. Since the concentration is a much more important quantity in electrochemical experiments while the activity coefficient are generally unknown, it is not convenient to deal with activities. To avoid this the formal potential E_f^0 is introduced, resulting in a simplified Nernst form using the electroactive species concentrations:

$$E = E_f^0 + \frac{RT}{nF} \ln \frac{C_O}{C_R} \quad (2.5)$$

where

$$E_f^0 = E^0 + \frac{RT}{nF} \ln \frac{\gamma_O}{\gamma_R} \quad (2.6)$$

2.1.2 Dynamic electrochemistry

Electrochemical reactions can be examined under either equilibrium or non-equilibrium context. Under equilibrium conditions, there is no net charge flow and the overall reaction rate is zero.[3] Under non-equilibrium circumstances, the electrode process proceeds by the application of a potential enabling the exchange of electrons, resulting in reactants being depleted and products being formed.[4] Cyclic voltammetry, amperometry, and electrochemical impedance spectroscopy, etc, are categorised into this topic, as it generally

involves the introduction of a potential or current program, leading to an electrical current flow.[5]

For an electrode reaction at the electrode-solution interface, the current or electrode reaction rate is affected by several factors: mass transfer, such as the transportation of reactants from bulk solution to the electrode surface, and the products away from it; the electron transfer at the surface of the electrode; coupled chemical reactions before or after the electron transfer, which could be protonation, dimerization, or catalytic decomposition; and other surface reactions including adsorption and desorption.[1] The complex process involving a series of steps is shown in Figure 2.2. The overall reaction rate is limited by the most sluggish reaction, the rate determining step.

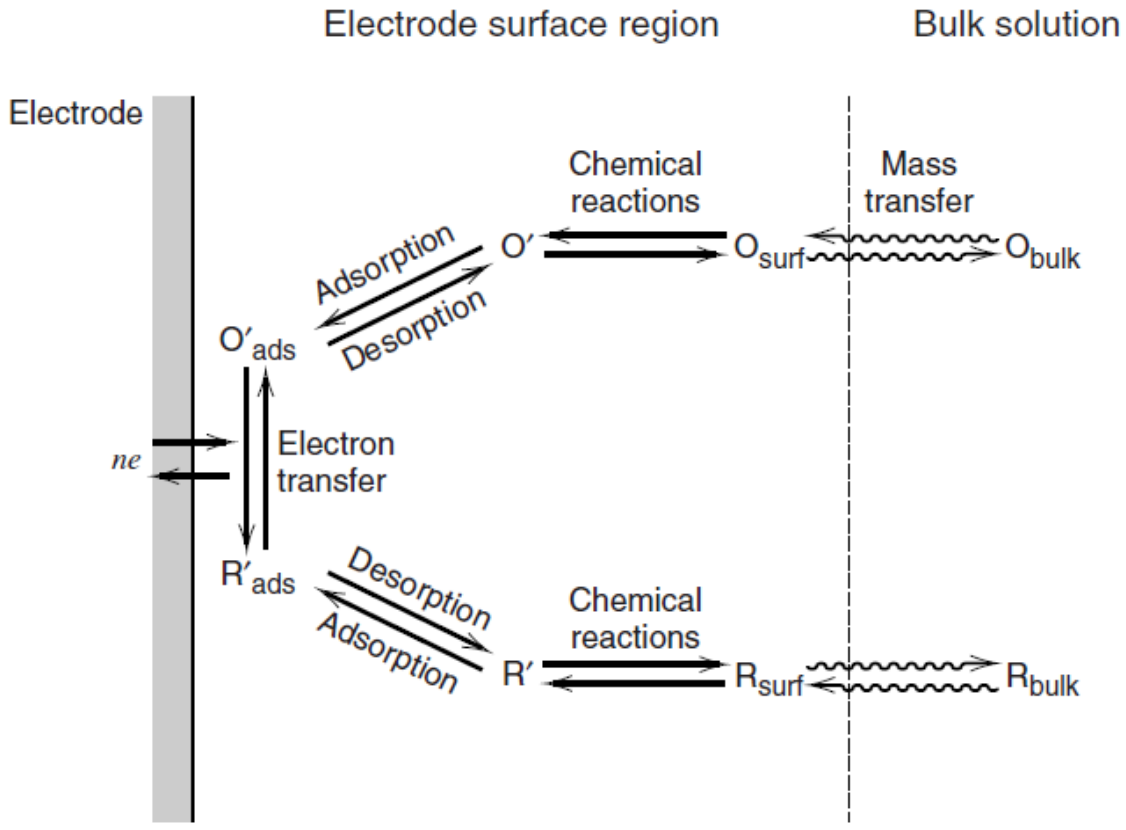


Figure 2.2 An electrode reaction pathway. Reproduced from Ref. 1 with permission. Copyright 2001, John Wiley and Sons.

2.1.3 Electrode kinetics

For an electrode reaction, the electrode kinetics are strongly affected by the potential. In order to describe the charge transfer dynamics between the electrode-solution interfaces accurately, the potential-dependence of the heterogeneous rate constants for the electron transfer reaction is required quantitatively. As a typical example, the simplest electrode process, a one-step and one-electron transfer process without involvement of any other chemical reactions, is considered for equation 2.1 when *n* is equal to one. The current response can be predicted as follows:

$$i_c = -FAk_c[O]_0 \quad (2.7)$$

$$i_a = FAk_a[R]_0 \quad (2.8)$$

where i_c and i_a are the cathodic current and the anodic current, respectively, k_c and k_a are the heterogeneous rate constants for the forward cathodic and backward anodic reactions, respectively, and A is the electrode area. The net current flow is given by the contributions of oxidative and reductive components for the reaction:

$$i = i_a + i_c = FA(k_a[R]_0 - k_c[O]_0) \quad (2.9)$$

Based on the transition state theory where an energy barrier is overcome enabling the reactants to become products,[6] and the practical experimental purposes where a reference electrode is required in any circuit, the electrochemical rate constant depending on the applied potential is written in the following useful form:

$$k_c = k^0 e^{\frac{-\alpha F\left(E-E_f^0\right)}{RT}} \quad (2.10)$$

$$k_a = k^0 e^{\frac{\beta F\left(E-E_f^0\right)}{RT}} \quad (2.11)$$

where k^0 is the standard electrochemical rate constant, α and β are the cathodic and anodic transfer coefficients, respectively, and β is equal to $1-\alpha$, with both being in the range of zero to unity.[7, 8] E is the applied potential while E_f^0 measures the formal potential, defining the overpotential η as follows to drive the electrode process:

$$\eta = E - E_f^0 \quad (2.12)$$

According to the above equations, the net current flow can be given by the following form:

$$i = FAk^0\left[[R]_0 e^{\frac{\beta F\eta}{RT}} - [O]_0 e^{\frac{-\alpha F\eta}{RT}}\right] \quad (2.13)$$

where [ ]$_0$ means the species surface concentration. This is the Butler-Volmer equation named after pioneering works. [9, 10] This equation describes how the current can be predicted as a function of the overpotential, the transfer coefficients, and the reactant concentrations at the electrode surface. If the solution is well stirred without limitation of transporting, the surface concentrations approximate to the bulk concentrations. Mass transport effects are elucidated in the following section. When the standard electrochemical rate constant k^0 is large, a negligible overpotential to drive the electrode reaction is required, which is termed a reversible system. Conversely, when k^0 is very small, a large activation overpotenial is needed to promote the current flow, being regarded as an irreversible process. These are two important limits, and under different sets of experiment conditions, any electrochemistry system may be reversible, quasireversible, or irreversible depending on charge transfer kinetics.[1]

When the overpotential is large for driving the anodic (or cathodic) process, the cathodic (or anodic) current is extremely small, and the corresponding term can be neglected in the Butler-Volmer equation, and upon taking natural logarithms of both sides the equation becomes:

$$\ln i_a = \frac{\beta F \eta}{RT} + \ln i_0 \quad (2.14)$$

$$\ln|i_c| = -\frac{\alpha F \eta}{RT} + \ln i_0 \quad (2.15)$$

where i_0 is the standard exchange current. These two equation shows how the transfer coefficients, α and β, can be obtained from plots of $\ln|i|$ vs. η, known as Tafel plots, a powerful tool for assessing kinetic parameters as shown in Figure 2.3.[1, 2, 4, 11]

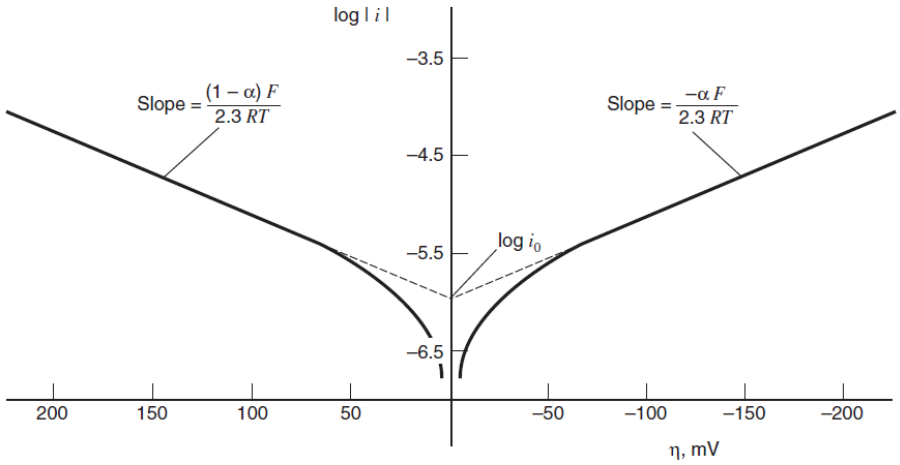


Figure 2.3 Tafel plots if taking common logarithms of base 10 for α = 0.5, T = 298 K, and the exchange current density is 10^{-6} A cm^{-2}. Reproduced from Ref. 1 with permission. Copyright 2001, John Wiley and Sons.

2.1.4 Mass transport

Besides the electron transfer reaction rate mentioned before, mass transport can have an effect on the overall kinetics for a specific electrode process, which recognises the transporting of species for reactants and products between the bulk solution and the electrode surface. Mass transport arises by the following processes: diffusion, convection and migration in solution.

Diffusion is a spontaneous phenomenon where the species diffuse from high to low concentrations. For a simple one-dimensional case of linear diffusion to a planar surface,

it has been described by Fick[12] that a diffusion flux *j*, the number of species moles passing through a unit area in a unite time, is quantified by the following:

$$j = -D\frac{\partial c}{\partial x} \quad (2.16)$$

where *D* is the diffusion coefficient as a characteristic feature of the diffusing species, *c* is the species concentration. This equation is known as Fick's first law of diffusion and shows the dependence of the flux on the concentration gradient $\frac{\partial c}{\partial x}$.[12]

Moreover, the concentration variation at a given location *x* as a function of time *t* may be considered in practice as well, which is given by the Fick's second law:

$$\frac{\partial c}{\partial t} = D\frac{\partial^2 c}{\partial x^2} \quad (2.17)$$

This is the differential equation for diffusion in one dimension. In three dimensions using Cartesian coordinates (*x*, *y*, *z*), this becomes:

$$\frac{\partial c}{\partial t} = D\left(\frac{\partial^2 c}{\partial x^2} + \frac{\partial^2 c}{\partial y^2} + \frac{\partial^2 c}{\partial z^2}\right) \quad (2.18)$$

All in all, Fick's laws describe how the species flux and concentration vary with position and time.

Due to the electrical potential drop between the electrode and solution interface the resulting electric field can drive the movement of charged species in the interfacial area from or to electrode via an electrostatic force.[4] This is mass transport of charged ions in solution by migration. The migratory flux j_m is given by the following equation[2]:

$$j_m = -uc\frac{\partial \phi}{\partial x} = -\frac{|z|FD}{RT}c\frac{\partial \phi}{\partial x} \quad (2.19)$$

where *u* is the ionic mobility, *z* is the charge of the ion, ϕ is the electrical potential, and the other terms are defined above. The electrolysis in an electrochemical reaction may result

in the change of ion concentrations at the electrode, which further changes the electrical potential in the solution and the resultant electric field variation can affect the mass transport of electroactive species in turn. This makes it difficult to model and interpret experiment data. Therefore to neglect the migration effect a large quantity of electrochemically inert supporting or background electrolyte at the potentials of interest is usually added into the solution in a two orders of magnitude excess relative to the redox of interest, so that the migration contribution to the current is limited to less than 1%. Generally the typical concentration required is around or more than 0.1 M. The electrical neutrality in the interfacial region is almost maintained by the supporting ions without building up of electric fields except for a tiny region where the interfacial potential drop is compressed to a distance of 10-20 Å adjacent to the electrode.[2, 4] In addition, a high concentration of supporting electrolyte is advantageous in terms of the increase of solution conductivity and maintenance of constant ionic strength.[4]

Convection arises when there is an imbalance of forces in the solution.[1] Two forms of convection may be discerned, which are natural and forced ones.

Natural convection occurs resulting from density gradients in the solution and thermal differences. The density differences may be result from the occurrence of electrolysis which builds up the local density gradients in the solution owing to density differences between reactants and products.[1] The thermal variations can be due to the endo- or exo-thermic nature of the process, imperfect thermostatting or resulting from solvent evaporation.[2, 4] Natural convection is typically irreproducible and undesirable in practical electrochemistry experiments.

Forced convection is realised with the help of external forces via various mechanical means to agitate the solution by bubbling, pumping or stirring, etc.[4] It is usually deliberately

introduced to the electrochemical system. In particular, hydrodynamic voltammetry is often studied on the basis of controlled convective mass transport. A quantitative description of the concentration variations due to the solution movement is given as follows in one dimension by[2]:

$$\frac{\partial c}{\partial t} = -v_x \frac{\partial c}{\partial x} \quad (2.20)$$

where v_x is the local fluid velocity in the x direction. Two typical systems for controlled convective mass transport are rotating disc electrodes and channel electrodes which can give kinetic and mechanistic information by controlling the rotation speed or the solution flow rate, respectively.[2]

To summarise, the total mass transfer of the electroactive materials is governed by the diffusion, migration, and convection. The Nernst-Planck equation describes all the contributions. In one dimension this is:

$$J = -D \frac{\partial c}{\partial x} - \frac{zF}{RT} Dc \frac{\partial \phi}{\partial x} + cv_x \quad (2.21)$$

where J is the total flux, $\frac{\partial \phi}{\partial x}$ is the electrical field or potential gradient, and the other physical quantities has been described before. On the right side of the equation, the three terms show the independent contributions by diffusion, migration, and convection due to the effect of concentration difference, electric field, and hydrodynamic velocity from the first, second, and third terms, respectively. These three modes if present simultaneously in the same experiment may make the study complex, and thus the electrochemical experiments may be designed in order to remove the effects of the electric field and hydrodynamic transport by the addition of supporting electrolyte and using still conditions without stirring, limiting the mass transfer to the diffusion contribution, which is the main focus of this thesis unless stated otherwise.

2.1.5 Faradaic and non-Faradaic processes

There are two kinds of processes taking place at electrodes. One type are the Faradaic processes as discussed above, where electrons are transferred across the interface between the metal electrode and solution, triggering the occurrence of oxidation and reduction. These reactions follow Faraday's laws of electrolysis as follows[13, 14]:

$$m = \frac{QM}{Fz} \quad (2.22)$$

where *m* is the substance mass produced at an electrode, *Q* is the electric charge passed, *F* is the Faraday constant with a value of 96485 C mol^{-1}, *M* is the molar mass of the substance, *z* is the valency number of the substance ion. The Faradaic process is generally of key interest for an electrode reaction in analytical electrochemistry and its rate can be influenced by the electrode reaction kinetics and mass transfer behaviour, which has been reviewed above.

In the above discussion of electron transfer, the nature of the electrode or the electrolyte interface has been neglected, but is still capable of affecting electrode behaviour. The non-Faradaic processes include adsorption, desorption, the change of structure of the electrode and solution interface due to variation of electrode potential.[1] An electrical double layer model is required to explain these effects.

The metal electrode possesses a charge density at the electrode surface, which causes a charge imbalance. The opposite charged species are electrostatically allocated from solution in order to maintain interfacial electrical neutrality. This can be thought of an analogy to two plates of a capacitor governed by the equation:[1]

$$\frac{q}{E} = C \quad (2.23)$$

where q is the charge in coulomb on the capacitor, E is the potential in volt across the capacitor, and C is the capacitance in farad. Whenever the applied potential at the electrode varies, charge will accumulate and flow on the metal electrode accompanied by ion migration in solution from or to the interface for compensation subject to the above equation, during which a current named the charging (or capacitive) current flows.[3] This capacitor model is an approximation as C is typically potential dependent.

There are several layers on the solution side in the structure of double layer as shown in Figure 2.4. The inner or compact layer closet to the electrode comprises solvent molecules and ion species "specifically adsorbed" to the electrode surface, also called the Helmholtz or Stern layer. The centre of the specifically adsorbed species defines the Inner Helmholtz Plane (IHP), at which ϕ_1 is the potential with respect to bulk solution. The solvated ions are non-specifically adsorbed and interact with the charged metal electrode only via long-range electrostatic forces. The plane drawn through the centre of these nearest solvated ions away from the electrode surface defines the Outer Helmholtz Plane (OHP), at which ϕ_2 is the potential relative to bulk solution. Beyond OHP these solvated ions are distributed within the diffuse layer, which extends into the bulk solution.

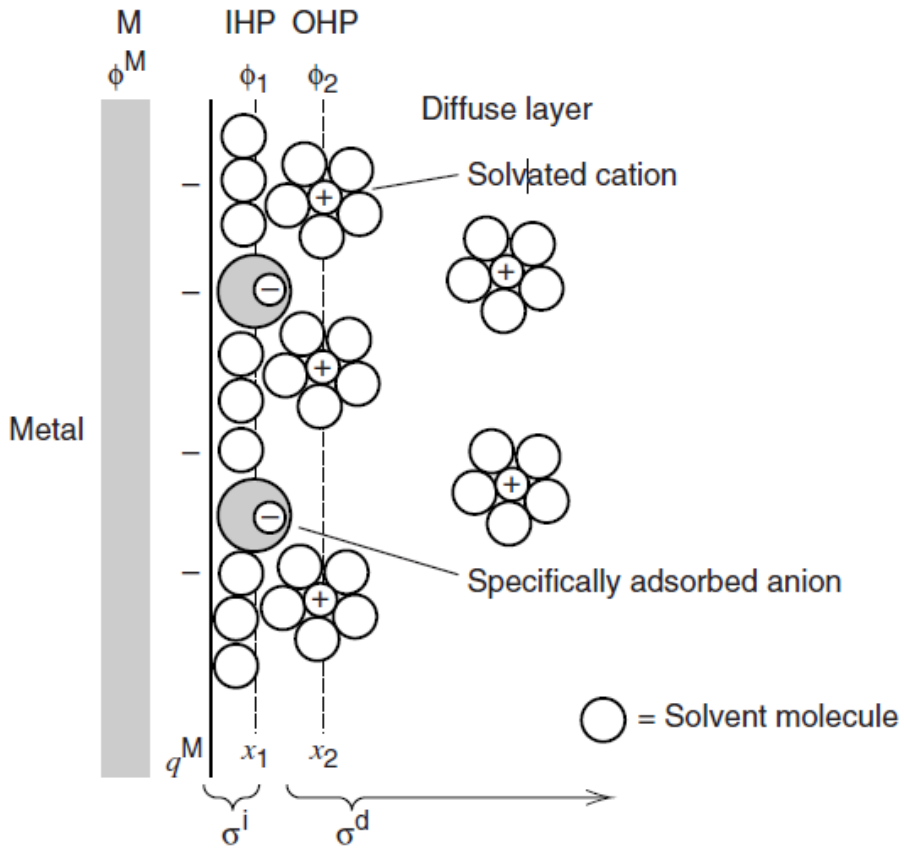


Figure 2.4 Electrical double layer model. Reproduced from Ref. 1 with permission. Copyright 2001, John Wiley and Sons.

2.1.6 Electrochemical techniques

Most of electrochemical techniques measure current as a function of the applied potential in an electrochemical cell. This section will outline the common voltammetric methods: potential step methods such as chronoamperometry, potential sweep methods including linear sweep voltammetry (LSV), cyclic voltammetry (CV), differential pulse voltammetry (DPV), and electrochemical impedance spectroscopy (EIS).

2.1.6.1 Chronoamperometry

Potential step methods involve stepping the potential of working electrode instantaneously from a value where no Faradaic process occurs to another one in which the electroactive species are completely converted via oxidation or reduction at the electrode surface. One

of the most frequent used methods is chronoamperometry, which records the current response passing as a function of time at a constant potential. A large current is observed once upon changing the potential. As the reactant species depletes with time, the diffusion layer enlarges and the current drops as shown in Figure 2.5. The current response of a macroelectrode as a function of time *t* is predicted by the Cottrell equation:[2]

$$i = \frac{nFAD^{1/2}c}{\pi^{1/2}t^{1/2}} \quad (2.24)$$

where A is the electrode area. This equation indicates that potential step methods can be utilised to obtain diffusion coefficient or electrode area if the other parameters are known.

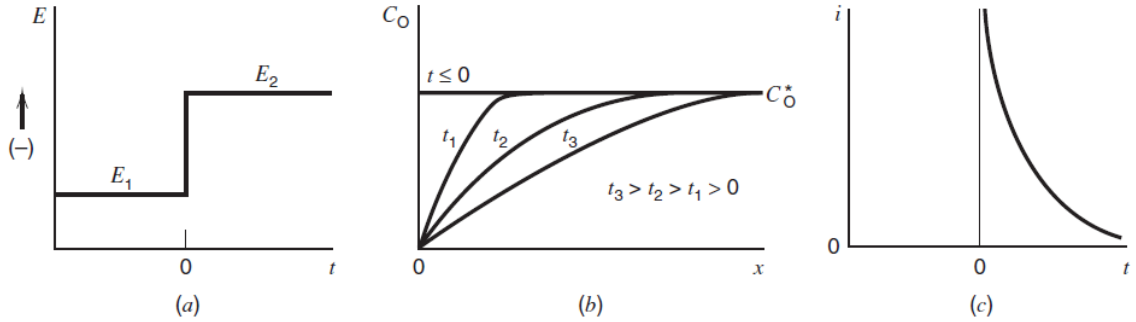


Figure 2.5 (a) For a potential step experiment the variation of applied potential with time. (b) Concentration profiles for different experiment time. (c) The current response with time. Reproduced from Ref. 1 with permission. Copyright 2001, John Wiley and Sons.

2.1.6.2 Linear sweep voltammetry

Potential sweep methods apply potentials which change with time in a predetermined manner and record the current as a function of potential.[15] The common potential sweep techniques are linear sweep voltammetry, cyclic voltammetry, and differential pulse voltammetry.

Linear sweep voltammetry is the simplest potential sweep technique for study of electrochemical systems. The electrode potential is swept from an initial value where no

Faradaic process takes place to another one at a constant rate during which electron transfer occurs with the flowing Faradaic current.[4] The rate where the potential is swept referred as the scan rate (v) in V s^{-1} is of extreme importance. Figure 2.6 shows the linear potential sweep and the corresponding current response. As the potential increases, the surface concentration of reactive species decreases, and flux to the surface with the current augments. When the surface concentration is near completely consumed, the mass transfer from the bulk solution to the surface for the reactant reaches a maximum, and it drops then as depicted in the peak current-potential curve.

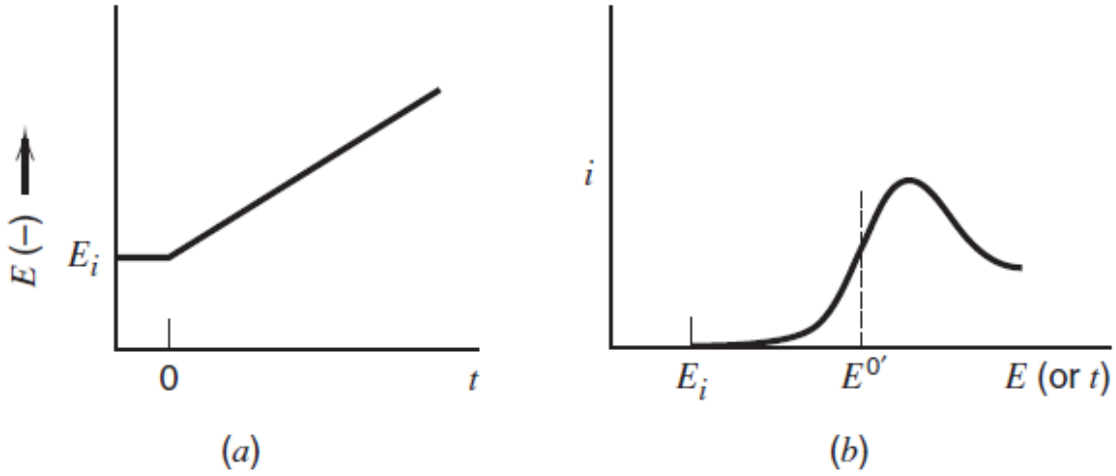


Figure 2.6 (a) The potential sweep and (b) the current-potential curve where $E^{0'}$ is E_f^0. Reproduced from Ref. 1 with permission. Copyright 2001, John Wiley and Sons.

2.1.6.3 Cyclic voltammetry

Cyclic voltammetry is a close relative of LSV, which is the scan direction is reversed after the potential reaches a peak at the switching time, and then the potential is swept back to the initial value, and thus LSV is the first part of the triangular waveform of the corresponding CV. CV is a powerful tool to gain extensive information about electrode reactions and is used predominantly in this thesis.

Figure 2.7 shows a typical potential scan and the corresponding cyclic voltammogram. The voltammogram shape for the forward scan is similar to that illustrated above for the LSV case. Once the potential is reversely scanned, since a large concentration of the reduced products exists in the vicinity of the electrode formed during the forward scan, these species becomes re-oxidised with flowing of an anodic current.

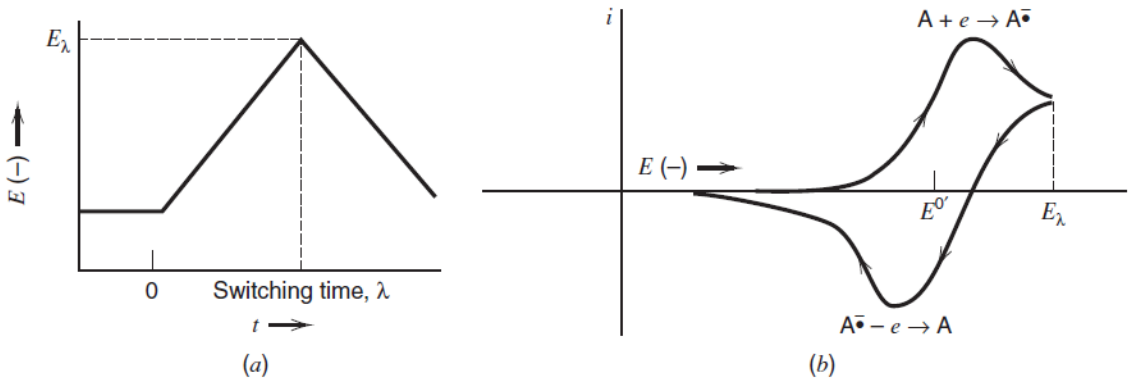


Figure 2.7 (a) Cyclic potential scan and (b) cyclic voltammogram. Reproduced from Ref. 1 with permission. Copyright 2001, John Wiley and Sons.

There are three kinds of electrochemical systems: reversible, quasi-reversible and irreversible systems. The two extreme cases of electrochemically reversible and irreversible correspond to fast and slow electrode kinetics with large and small values of the standard electrochemical rate constant, respectively, while the intermediate case of quasi-reversible behaviour exists.

For a reversible system, the electrode reaction is so fast compared with the mass transfer rate that the establishment of the equilibrium ratio of reactants and products at the electrode surface is as predicted by Nernst equation above. The potential separation of the forward and backward peaks is independent of voltage scan rate, as one diagnostic of the nature of the reversible case. On the other hand, the peak current i_p is given by the following Randles-Sevcik equation for a reversible system:[16, 17]

$$i_p = 0.4463nFAc\left(\frac{nFDv}{RT}\right)^{1/2} \quad (2.25)$$

where all the symbols are defined as before. At 25 ^{o}C, it becomes:

$$i_p = 2.69 \times 10^5 n^{3/2} AD^{1/2} cv^{1/2} \quad (2.26)$$

It is noteworthy that the peak current is proportional to the concentration and the square root of scan rate, and this equation may be used to calculate the area of electrode or the diffusion coefficient of the species.

For an irreversible system, there is no or almost no reverse peak, and the peak potentials depend on the scan rate. The peak current is predicted by the irreversible Randles-Sevcik equation:[2]

$$i_p = 0.496(n' + \alpha)^{1/2} nFAc\left(\frac{FDv}{RT}\right)^{1/2} \quad (2.27)$$

where *n'* is the number of electrons transferred before the rate determining step. At room temperature the equation is given as follows:[18]

$$i_p = 2.99 \times 10^5 n(n' + \alpha)^{1/2} AD^{1/2} cv^{1/2} \quad (2.28)$$

Most electrochemical redox systems lay somewhere in between these two extremes and show intermediate quasi-reversible behaviour.[19]

2.1.6.4 Differential pulse voltammetry

To detect small concentrations of a species, the voltammetric techniques are further modified, and thus potential pulse techniques are widely used in analytical electrochemistry such as differential pulse voltammetry and square wave voltammetry. They are used to improve the sensitivity in electrochemical sensing applications.[2]

The enhanced sensitivity of these techniques originate from the increased response to the Faradaic current relative to the suppressed capacitive or charging current.[2] The current response to a potential step is characterised in chronoamperometry, where a pulse of current decays with time as the electroactive species is consumed near the electrode surface. A capacitative contribution because of the double layer charging is superimposed on this response. The charging current decays far more quickly, often within 1~2 ms, than the Faradaic response. After the diminishment of the capacitative constitution, the current is given by the Cottrell equation suggested before. Thus in pulse techniques the current is generally sampled after the dying away of the capacitative current. Meanwhile the techniques are parameterised to make sure that time is not allowed for natural convection to disturb the response.[2, 15]

The applied potential profile of differential pulse voltammetry is shown in Figure 2.8. The duration of the staircase waveform is at least longer than the pulse period, and the timescales of these two parameters are about ~ 0.5-4 s, and 5-100 ms, respectively.[2, 20] Two current samples are taken. One is sampled just before the applied pulse, and another one is sampled before each pulse ending as shown in Figure 2.9. The difference between these two currents is plotted versus the staircase potential, resulting in a peak-shaped waveform. DPV decreases the contribution of non-Faradaic, mainly capacitative current to the recorded signal by the subtraction to achieve better limits of detection of analytes for trace analysis.

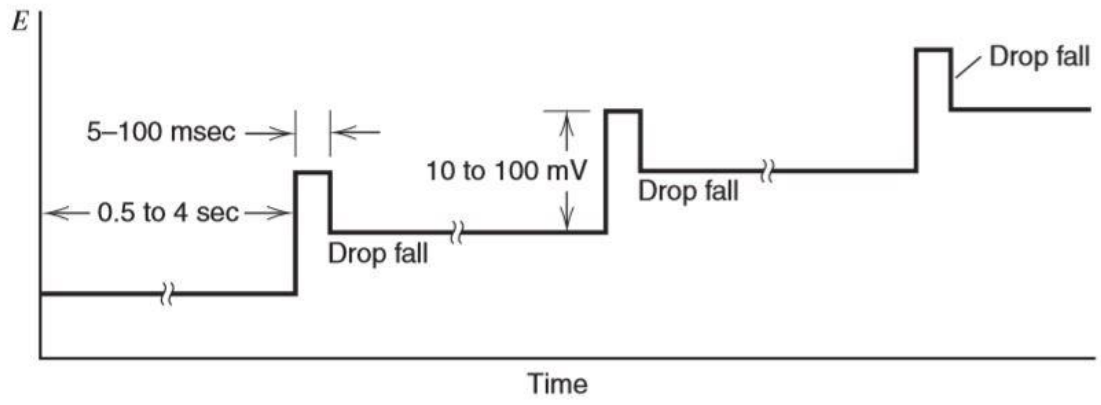


Figure 2.8 Schematic waveform of the applied potential for a DPV experiment. Reproduced from Ref. 1 with permission. Copyright 2001, John Wiley and Sons.

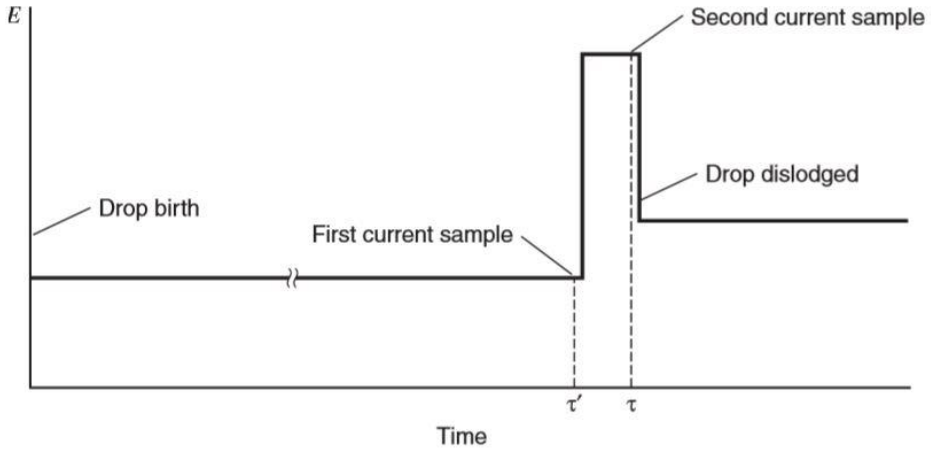


Figure 2.9 A single drop event of a DPV scan. Reproduced from Ref. 1 with permission. Copyright 2001, John Wiley and Sons.

2.1.6.5 Electrochemical impedance spectroscopy

Electrical impedance, coined by Oliver Heaviside in 1880s,[21, 22] measures the ability of an electrical circuit to resist the passage of an alternating current by applying an alternating voltage to an electrochemical system.[14, 23] Unlike potential sweep or step techniques which drive the electrode far away from equilibrium, a small alternating signal perturbation is applied to observe how the system responses to the perturbation near steady state. The perturbation form is often a small sinusoidal wave over a broad frequency spectrum

ranging from 10 mHz to 100 kHz.[23] Thus the impedance is evaluated with the change of the frequency of the alternating current source, where this technique is called electrochemical impedance spectroscopy.[1]

Generally, the performance of an electrochemical cell can be simplified as an equivalent circuit of resistors and capacitors. A Randles equivalent circuit for a simplest electrode process is frequently employed.[24] As shown in Figure 2.10, the total current is the sum of Faradaic current, i_f, and the capacitative charging current, i_c. Since the entire current passes through the solution resistance, R_Ω represents this effect as a series element. The double-layer constitution is a pure capacitor exemplified by the capacitance parameter of C_d in the equivalent circuit while the Faradaic process is regarded as a general impedance Z_f, with a dependence on frequency, which is considered in one of two ways. The first one consists of a series resistance R_s and a pseudocapacity C_s as a series combination. A more common, second, way is a combination element comprising the charge-transfer resistance R_{ct} to model the Faradaic charge transfer reaction, and the Warburg impedance Z_w depicting the resistance to mass transfer.[1] Thus EIS analysis allows the revelation of characteristic information about the electric resistance of the solution, the interfacial capacitance between the electrode and solution phases, and the electrochemical rate constant of the electrode reaction with the coupled diffusion process.[23]

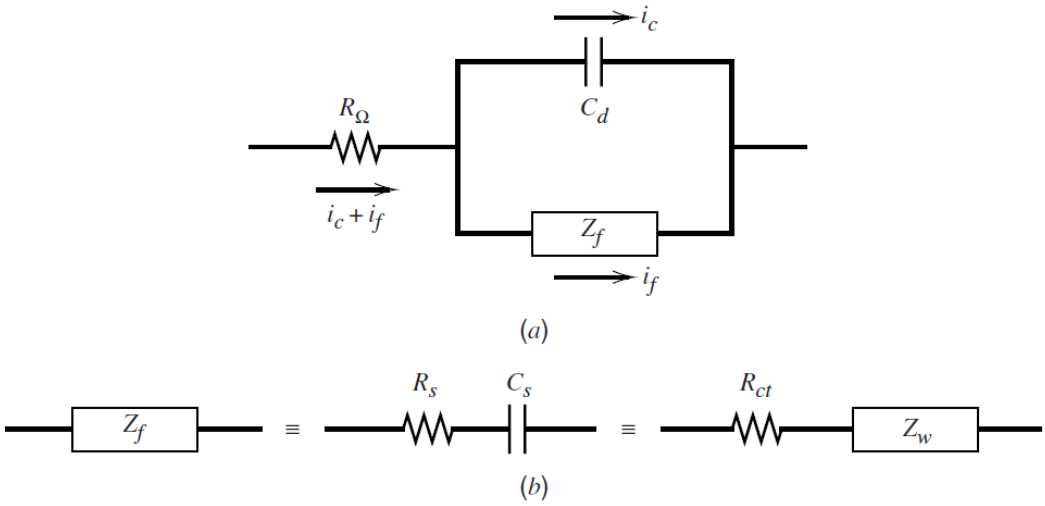


Figure 2.10 (a) The equivalent Randles and (b) two equivalences for the Faradaic impedance. Reproduced from Ref. 1 with permission. Copyright 2001, John Wiley and Sons.

Importantly, the impedance variation with the change of frequency is of significance and interest with various ways in which two can be displayed. A regular presentation manner is the plot of imaginary part of the impedance, Z_{Im}, versus real part of the impedance, Z_{Re}, for different values of frequency, ω, called a Nyquist plot as shown in Figure 2.11. Therefore every point on the plot is the impedance at one frequency. It is noteworthy that from the left side of the plot to the right on the x-axis, the frequency is from high to low. The high frequency intercept yields R_Ω as a value of the electrolyte resistance, while a quantity of $R_\Omega + R_{ct}$ is generated by the low frequency intercept, indicating the semicircle diameter of the plot is the charge electron transfer resistance for controlling the electron transfer kinetics.[1] As lower frequencies are reached, in the impedance plot a large augmentation, modelled by the Warburg impedance,[25] provides possible insight into the governing mass transport behaviour for the species.

In summary, EIS is a powerful tool and has been applied to various systems, including solid state devices like solid electrolyte chemical sensors, and photoelectrochemical solar

cells, electrochemical power sources like batteries, supercapacitors, and fuel cells, and the study of corrosion phenomena, etc.[22]

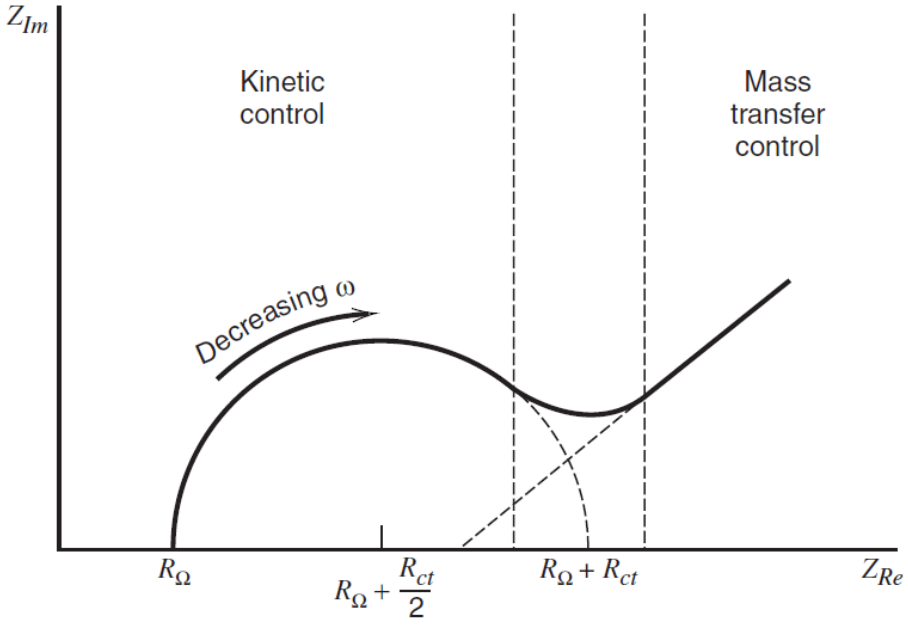


Figure 2.11 Nyquist plot. Reproduced from Ref. 1 with permission. Copyright 2001, John Wiley and Sons.

2.1.7 Electrochemical instrumentation and experimental set-up

The electrochemical measurements in this thesis are performed using electrochemical instrumentation consisting of a potentiostat/galvanostat PGSTAT128N (Metrohm Autolab, Utrecht, Netherlands) which is connected to a computer for recording signals of potential, current and time. As a crucial component, the software package NOVA 2.1.4 is used to control the Autolab instrument with an "intuitive" user interface.

The electrochemical cell is set up with a standard three-electrode configuration, which consists of a working electrode, a platinum coil counter electrode, and a Ag/AgCl (1M KCl) reference electrode. All the potentials are reported against the Ag/AgCl reference electrode unless stated otherwise. A boron doped diamond electrode is used usually either in a bare form or decorated by materials of interest as the working electrode, which is mounted in a

home-built polytetrafluoroethylene holder with an exposed circular area of 0.37 cm^2 to the electrolyte. All aqueous solutions are prepared with ultrapure water with a resistivity of 18.2 MΩ cm, and all electrochemical experiments are conducted at room temperature unless stated otherwise. Other specific experimental conditions and details of study will be described in the corresponding experimental sections of the respective chapters.

2.2 X-ray photoelectron spectroscopy

2.2.1 XPS fundamentals

X-ray photoelectron spectroscopy, also known as electron spectroscopy for surface chemical analysis, is a quantitative technique, which can determine the composition, chemical and electronic states of elements, and empirical formula at the surface of a material. The material is irradiated with an energetic beam of X-rays, and the resulting photoelectrons escape from the top 0-10 nm of the solid material surface. The kinetic energy and number of electrons are measured to collect XPS spectra.[26] XPS was developed by Kai Siegbahn and his co-workers in the 1940-1950s at the University of Uppsala in Sweden and he was awarded the Nobel Prize in 1981 for this invention.[26] Overall XPS is a surface-sensitive spectroscopic technique providing the chemical composition and speciation information over the surface region.[27]

XPS works on the basis of the photoelectric effect.[28, 29] Soft X-rays of Mg Kα and Al Kα are commonly used as the exciting photon source, which interact with a core level electron initially bound to an atom with the occurrence of the photon energy transfer, leading to the emission of the electron. The kinetic energy of emitted photoelectrons (E_K) is measured, which is a distribution of discrete peaks relative to the electron binding energies (E_B), with these, in turn, being element and chemical composition specific. The relationship can be expressed as the following equation:[30]

$$E_K = hv - E_B - \phi \quad (2.29)$$

where *h* is the Plank's constant, *v* is the X-ray frequency, and the product *hv* represents the energy of X-ray photons, and ϕ is the work function of the instrument's spectrometer at a typical value of 3-5 eV.[31] Therefore XPS spectra are produced as the plots of the intensity of emitted electrons versus their binding energies. Because the electron binding energy in a specific atom shell is distinctive for each element, elements and relative chemical composition can be identified except hydrogen and helium.

In addition, the atom is in a highly excited core ionized state after the photoemission event. It can further decay radiatively in the fluorescence process or non-radiatively in the Auger emission. The relative probabilities of these two competing mechanisms depend on the elemental atomic number while Auger process is dominant for low atomic numbers of less than 30.[26, 32] The two de-excitation processes are shown in Figure 2.12. After the photoelectron emission, an electron from a higher level drops into the core level vacancy, resulting in the energy release in the form of the photon emission. This process is X-ray fluorescence measured by other analytical techniques. Another relaxation process of the excited ion is the Auger electron emission, where the energy previously released from the filling of the core level hole is transferred to a third electron, causing the ejection of such electron from the atom. Therefore peaks from Auger electrons and photoelectrons can be both observed in XPS. However, Auger emission does not depend on the photon energy and therefore the X-ray source, and thus a dual source of Al/Mg X-ray in conjunction can help to distinguish between Auger and photoelectric peaks.[26]

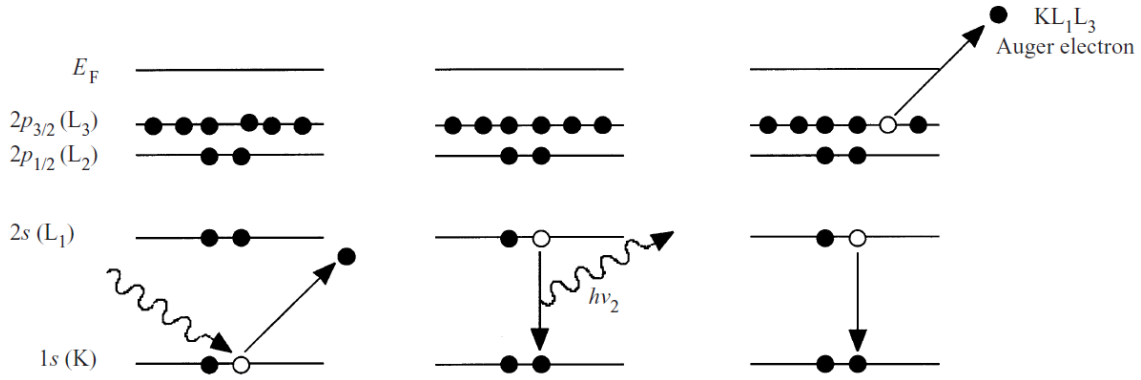


Figure 2.12 Schematic energy level diagram for the process of photoelectron emission and the relaxation processes by X-ray fluorescence or Auger electron emission from left to right. Reprinted from Ref. 31, Copyright (2001), with permission from Elsevier.

2.2.2 XPS instrumentation

An XPS instrument primarily comprises an X-ray source, electron energy analyser, and detector in a high vacuum environment as show in Figure 2.13. Although moderate vacuum of about 1×10^{-3} Pa is at least needed, most instruments operate in an ultrahigh vacuum region (< 10^{-7} Pa) in order to avoid the gaseous species adsorption and prevent surface reactions/contaminations.[31] X-rays are produced by bombarding a metallic solid anode such as magnesium (Mg) or aluminum (Al) with sufficiently energetic electrons from a cathode, based on thermionic sources such as a tungsten filament. The X-ray source line width has a great influence on the energy resolution in XPS, and it can be enhanced to below 0.3 eV using quartz crystal monochromators.[31] Currently Mg Kα (1253.6 eV) and Al Kα (1486.6 eV) are the most common X-rays sources. Then the energy spectrum of the photoelectron flux emitted from the solid sample is measured by the electron energy analyser. Only the electrons with the proper kinetic energies can pass through the energy filter configurations and thus will be counted by the detection system. Two configurations are used including cylindrical mirror analyser and concentric hemispherical analyser, and the latter is more prevalent due to its enhanced energy resolution of 0.01 eV accessible.[27]

The number of electrons recorded by the detection system is as important as the energy of electron emissions measured by the energy analyser, and the transmitted electrons are counted by the detector of electron multiplier.

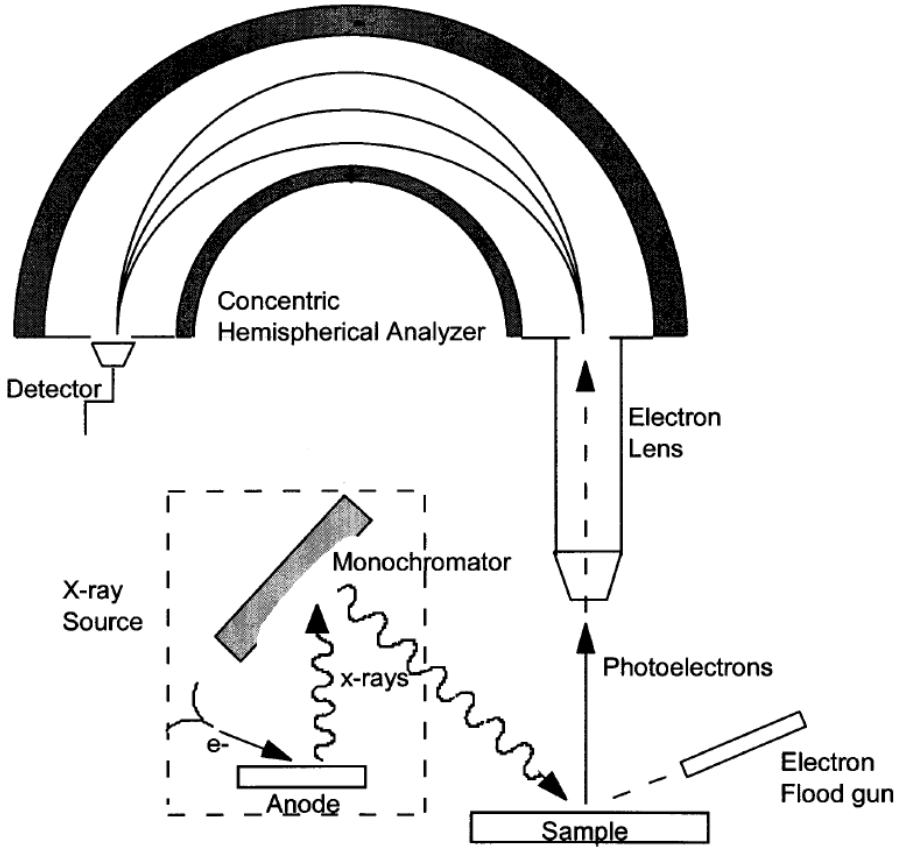


Figure 2.13 Schematic diagram of an XPS instrument. Reprinted from Ref. 31, Copyright (2001), with permission from Elsevier.

2.3 Scanning electron microscopy

Scanning electron microscopy (SEM) has been a widely used technique to observe and characterise materials from micrometre to nanometre scale providing surface topography and composition since the development of first commercial microscope "Stereoscan" by Cambridge Scientific Instruments at Cambridge in 1965.[33] It takes advantage of an electron beam to form images instead of light in the traditional optical microscopes, and the resolution can be as low as 1-10 nm.[34] In principal, the sample is irradiated with a focused

electron beams of high energy with the resulting signals due to the interactions between electron beam and the atoms at various depths within the specimen. Various kinds of signals, including secondary electrons, backscattered electrons, and characteristic X-rays, etc., are collected to acquire images and chemical information about the sample surface.[34]

The major components of the SEM are the electron column, and the computer control console system as shown in Figure 2.14. The SEM instrumentation may incorporate secondary and backscattered electron detectors, electron backscattered diffraction detector, energy-dispersive X-ray spectrometer, etc. Although it is rare for a sole instrument to have all the detectors for all the signals, secondary electron detectors are the standard configuration in all SEMs.

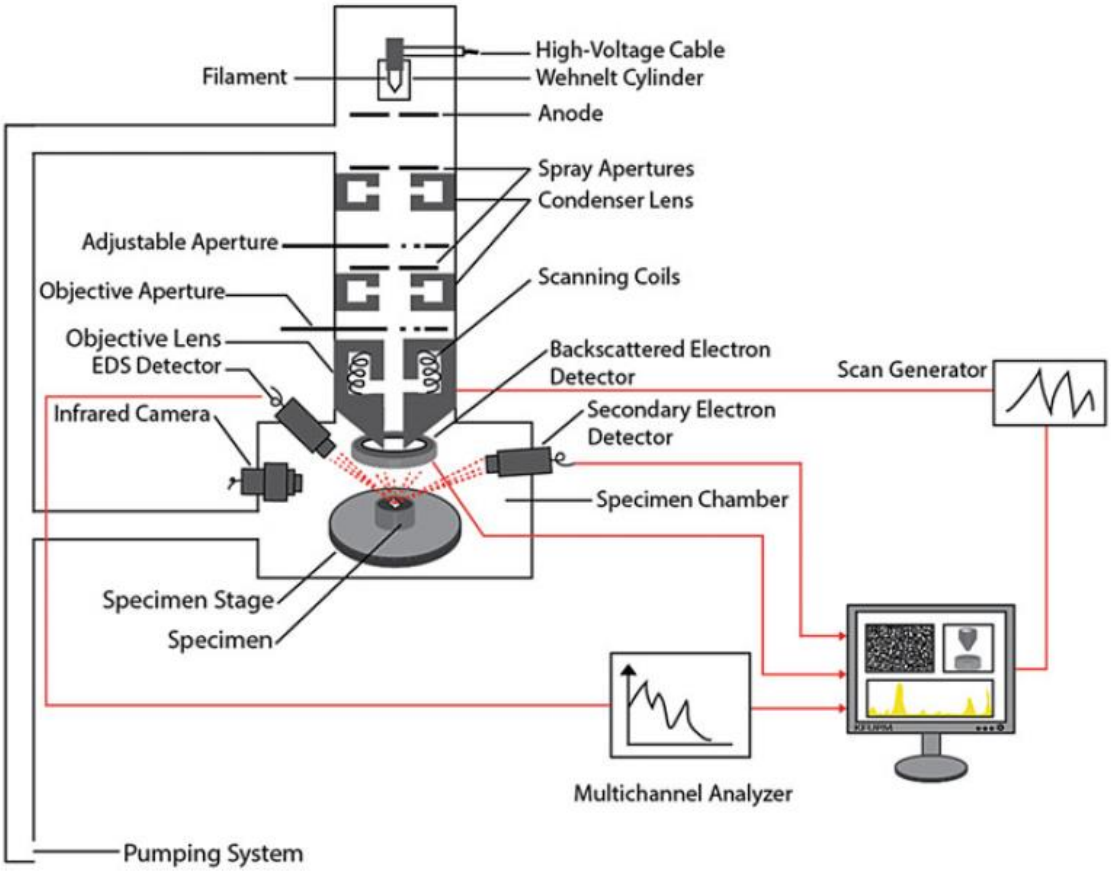


Figure 2.14 A schematic diagram of a scanning electron microscope instrument. Reprinted by permission from Ref. 34, Copyright (2018), Springer Nature.

The electron column contains an electron gun, two or more electron lenses and other accessories. The electron gun at the top of the column is to generate electrons and accelerate them downward through the cylindrical body in the range of 0.1-30 keV.[35] The traditional electron guns are thermionic emitters such as tungsten filament or lanthanum hexaboride (LaB_6) while new microscopes may be equipped with Schottky, or cold field emission gun.[35] The spot size of the beam is too large, and thus it is de-magnified or focused to be a probe size of 10 nm by the electron optical system.[34] The demagnification is performed by electromagnetic lenses, which is initiated by typically two condenser lenses and followed by final lens termed as objective lens. After traveling down the vacuum tube, the fine electron probe strikes the surface of materials in the specimen chamber located at the base of the column. Many kinds of signals are produced due to the beam and specimen interactions including secondary electrons (SE) and backscattered electrons (BSE), and characteristic X-rays. The topographic and compositional contrast images are generated by virtue of the two types of electrons signals while the elemental constitution of the material are achieved with the help of X-rays using energy dispersive X-ray spectrometry detector.[34] When the electron beam hits the sample, it is deflected in two modes. If the electrons are deflected without losing any kinetic energy, it is called elastic scattering, and those electrons deflected through large angles and finally leaving out of the material are known as backscattered electrons. In contrast, inelastic scattering involves the loss or transfer of kinetic energy from the incident electrons during the beam-specimen interaction. In an inelastic event, loosely bound outer shell electrons belonging to the specimen are knocked out of the material, which are termed as secondary electrons typically with < 50 eV kinetic energy.[34] All these electrons are then collected and converted by the detector with the resulting intensity distribution mapping of electron signals to form an image as shown on the screen.

References

1. Bard, A. J.; Faulkner, L. R., *Electrochemical methods : fundamentals and applications*. Second ed.; John Wiley & Sons: New York, 2001.

2. Compton, R. G.; Banks, C. E., *Understanding voltammetry*. Third ed.; World Scientific Publishing: London, 2018.

3. Banica, F., Dynamic Electrochemistry Transduction Methods. In *Chemical Sensors and Biosensors: Fundamentals and Applications*, Banica, F., Ed. John Wiley & Sons: Chichester, 2012; pp 258-313.

4. Fisher, A. C., *Electrode dynamics*. Oxford University Press: Oxford, 1996.

5. Anderson, J. L.; Coury, L. A.; Leddy, J., Dynamic electrochemistry: Methodology and application. *Anal Chem* **2000,** *72* (18), 4497-4520.

6. Cox, B. G., *Modern liquid phase kinetics*. Oxford University Press: Oxford, 1994.

7. Guidelli, R.; Compton, R. G.; Feliu, J. M.; Gileadi, E.; Lipkowski, J.; Schmickler, W.; Trasatti, S., Defining the transfer coefficient in electrochemistry: An assessment (IUPAC Technical Report). *Pure Appl Chem* **2014,** *86* (2), 245-258.

8. Guidelli, R.; Compton, R. G.; Feliu, J. M.; Gileadi, E.; Lipkowski, J.; Schmickler, W.; Trasatti, S., Definition of the transfer coefficient in electrochemistry (IUPAC Recommendations 2014). *Pure Appl Chem* **2014,** *86* (2), 259-262.

9. Butler, J. A. V., Studies in heterogeneous equilibria. Part III. A kinetic theory of reversible oxidation potentials at inert electrodes. *Transactions of the Faraday Society* **1924,** *19*, 734-739.

10. Erdey-Grúz, T.; Volmer, M., Zur theorie der wasserstoff überspannung. *Zeitschrift für physikalische Chemie* **1930,** *150A* (1), 203-213.

11. Li, D. L.; Lin, C. H.; Batchelor-McAuley, C.; Chen, L. F.; Compton, R. G., Tafel analysis in practice. *J Electroanal Chem* **2018,** *826*, 117-124.

12. Fick, A., V. On liquid diffusion. *The London, Edinburgh, and Dublin Philosophical Magazine and Journal of Science* **1855,** *10* (63), 30-39.

13. Jensen, W. B., Faraday's Laws or Faraday's Law? *J Chem Educ* **2012,** *89* (9), 1208-1209.

14. Bhattacharyya, B., Electrochemical Machining: Macro to Micro. In *Electrochemical Micromachining for Nanofabrication, MEMS and Nanotechnology*, Bhattacharyya, B., Ed. William Andrew: Oxford, 2015; pp 25-52.

15. Brett, C. M. A.; Brett, A. M. O., *Electroanalysis*. Oxford University Press: Oxford, 1998.

16. Randles, J. E. B., A cathode ray polarograph. Part II.—The current-voltage curves. *Transactions of the Faraday Society* **1948,** *44*, 327-338.

17. Ševčik, A., Oscillographic polarography with periodical triangular voltage. *Collection of Czechoslovak Chemical Communications* **1948,** *13*, 349-377.

18. Batchelor-McAuley, C.; Compton, R. G., Voltammetry of multi-electron electrode processes of organic species. *J Electroanal Chem* **2012,** *669*, 73-81.

19. Matsuda, H.; Ayabe, Y., The theory of Randles-Sevcik's cathode-ray polarography. *Z. Elektrochem.* **1955,** *59* (6), 494-503.

20. Compton, R. G.; Batchelor-McAuley, C.; Dickinson, E. J. F., *Understanding Voltammetry: Problems and Solutions*. Imperial College Press: London, 2012.

21. Macdonald, D. D., Reflections on the history of electrochemical impedance spectroscopy. *Electrochim Acta* **2006,** *51* (8-9), 1376-1388.

22. Barsoukov, E.; Macdonald, J. R., *Impedance spectroscopy: theory, experiment, and applications*. Third ed.; John Wiley & Sons: Hoboken, 2018.

23. Banica, F., Electrical Impedance-Based Sensors. In *Chemical Sensors and Biosensors: Fundamentals and Applications*, Banica, F., Ed. John Wiley & Sons: Chichester, 2012; pp 367-403.

24. Randles, J. E. B., Kinetics of rapid electrode reactions. *Discussions of the Faraday Society* **1947,** *1*, 11-19.

25. Warburg, E., About the behaviour of so-called "impolarizable electrodes" in the present of alternating current. *Ann. Phys. Chem.* **1899,** *67* (3), 493-499.

26. Wagner, J. M., *X-Ray Photoelectron Spectroscopy*. Nova Science Publishers, Incorporated: New York, 2011.

27. van der Heide, P., *X-ray Photoelectron Spectroscopy : An introduction to Principles and Practices*. John Wiley & Sons: Hoboken, 2012.

28. Hertz, H., Ueber einen Einfluss des ultravioletten Lichtes auf die electrische Entladung. *Ann. Phys. Chem.* **1887,** *267* (8), 983-1000.

29. Einstein, A., Über einen die Erzeugung und Verwandlung des Lichtes betreffenden heuristischen Gesichtspunkt. *Ann. Phys.* **1905,** *322* (6), 132-148.

30. Konno, H., Chapter 8 - X-ray Photoelectron Spectroscopy. In *Materials Science and Engineering of Carbon: Characterization*, Inagaki, M.; Kang, F., Eds. Butterworth-Heinemann: Amsterdam, 2016; pp 153-171.

31. Burrell, M. C., Chemical Analysis, Electron Spectroscopy. In *Encyclopedia of Materials: Science and Technology*, Buschow, K. H. J.; Cahn, R. W.; Flemings, M. C.; Ilschner, B.; Kramer, E. J.; Mahajan, S.; Veyssière, P., Eds. Elsevier: Oxford, 2001; pp 1142-1149.

32. Carley, A. F., Surface Analysis: X-ray Photoelectron Spectroscopy. In *Encyclopedia of Materials: Science and Technology*, Buschow, K. H. J.; Cahn, R. W.;

Flemings, M. C.; Ilschner, B.; Kramer, E. J.; Mahajan, S.; Veyssière, P., Eds. Elsevier: Oxford, 2001; pp 8991-8996.

33. Oatley, C. W., The Early History of the Scanning Electron-Microscope. *J Appl Phys* **1982,** *53* (2), R1-R13.

34. Ul-Hamid, A., *A Beginners' Guide to Scanning Electron Microscopy*. Springer: Cham, Switzerland, 2018.

35. Goldstein, J.; Newbury, D. E.; Michael, J. R.; Ritchie, N. W. M.; Scott, J. H. J.; Joy, D. C., *Scanning electron microscopy and x-ray microanalysis*. Fourth ed.; Springer: New York, 2018.

Chapter 3 The electrochemical oxidation of sulphite on gold electrodes

The electro-oxidation of sulphite is studied in acid media on gold macroelectrodes and Au particle array modified boron doped diamond electrodes. Hydrated sulphur dioxide is the main electroactive species at low pH (< 2), and its oxidation proceeds through a one-electron transfer process followed by a chemical step of second order (EC_2 mechanism), as evidenced by experimental voltammetry and digital simulation for both gold macroelectrodes and gold particle modified substrates. The diffusion coefficient of sulphite is calculated consistently for both cases at about 4×10^{-9} m^2 s^{-1}, with the reverse peak behaviour concentration dependent. The arrays are made by electrodeposition and show a morphological transition from a quasi-spherical to a star shape as the growth time of the particles increases. Kinetic parameters inferred from the electro-oxidation at the macroelectrode can be successfully applied to model the gold particle modified electrode data to confirm the EC_2 mechanism, whilst recognising the overlapping diffusion layers of adjacent gold particles.

The work presented in this chapter has been published in *Electroanalysis*.[1]

3.1 Introduction

The electrochemical oxidation of aqueous sulphite solutions has attracted attention because of the wide application of sulphite in industry as preservatives in foods like alcoholic beverages (such as beer and wine), soft drinks, and dried fruits.[2] However levels need to be controlled since excessive exposure may have harmful effects such as gastrointestinal problems and respiratory disorders.[3] Hence, its determination is of much importance and interest.[4-5] To provide a platform for robust electroanalytical methods, it is vital to decipher

the electrochemical process in terms of the mechanism of oxidation and reduction, which has been a focus of earlier investigations but remains an open question.[6-18]

The electrochemical reactivity of the sulphite system has been studied in different electrolyte media and at various electrode materials. In particular carbon has been utilised by electrochemists in many forms including activated carbon, graphite, glassy carbon, and carbon black.[19-24] However, the electro-oxidation of sulphite at carbon electrodes usually requires a high overpotential and is a kinetically sluggish process.[22] Hence attention has been paid to metals, which may decrease the overpotential and show catalytic ability towards the sought reaction.[25]

Metal oxides including PbO_2[26-27] have been studied as well as noble metals, such as Pd,[28-29] Pt[6-12, 17] and Au,[12-17] which are recognized as effective electrocatalysts. For the achievement of high reactivity efficiency and the saving of the metal volume, however, construction of nanostructures in the form of small particles deposited on various substrates such as ceramics or boron-doped diamond (BDD) has been utilised.[30-31] Note that BDD electrodes are widely used wafers for electrochemical applications in terms of their wide potential window, low background current, mechanical robustness, good chemical stability and resistance to fouling.[32-34] The improved diffusion based on convergent at nanoparticles can provide a higher local mass transport rate to the electrode surface provided adjacent diffusion fields do not overlap.[35] Meanwhile high effective surface areas and interface-dominated properties can be obtained at the nanoscale along with many active sites and a better signal-to-noise ratio.[36] Furthermore, the excellent electrocatalytic properties of some nanometer-sized particles can endow greater reversibility for redox processes making the processes more kinetically viable compared to the same electrode materials in bulk,[37-38] and the effect of nanoparticle size in electrocatalytic reaction has been reported.[39-40] Last

but not least, the local microenvironment can be controlled via the use of nanoparticles for biomolecule immobilization.[36, 41]

In order to appreciate the following mechanistic discussion, the sulphite speciation must be first recognised. It is known that the aqueous sulphite anion (SO_3^{2-}) equilibrates with bisulphite and sulphur dioxide depending on the solution pH with the following reactions.

$$SO_2 + H_2O \rightleftharpoons HSO_3^- + H^+ \quad (3.1)$$

$$HSO_3^- \rightleftharpoons SO_3^{2-} + H^+ \quad (3.2)$$

Although equilibrium constants reported in the literature vary, the corresponding pKa values (25 ^oC) widely accepted are 1.8 and 7.2 for the above reactions, respectively.[18, 42-44] According to the Henderson-Hasselbalch equation for a weak acid [HA] and its conjugate base [A^-]:

$$pH = pK_a + \log([A^-]/[HA]) \quad (3.3)$$

the equilibrium fractions of sulphite species for hydrated SO_2, HSO_3^-, and SO_3^{2-} are, for example, about 89%, 11%, and 0%, respectively under the experimental solution conditions of pH=0.89. Similarly the equilibrium concentration of sulphite species can be calculated at the other pH values. So the equilibrium concentrations of the three sulphur (IV) species can be determined as a function of the solution pH.[18, 42] The results in Figure 3.1 show that the dominant species is aqueous sulphur dioxide (SO_2) when pH < 1.85. Bisulphite (HSO_3^-) dominates in the range of 1.85 < pH < 7.20 whereas sulphite (SO_3^{2-}) is the major species in the solution of pH > 7.20.[43, 45] Hence, SO_2 is the major species during the experiments in this work since the pH of the supporting electrolyte of 0.10 M H_2SO_4 is far below 2.

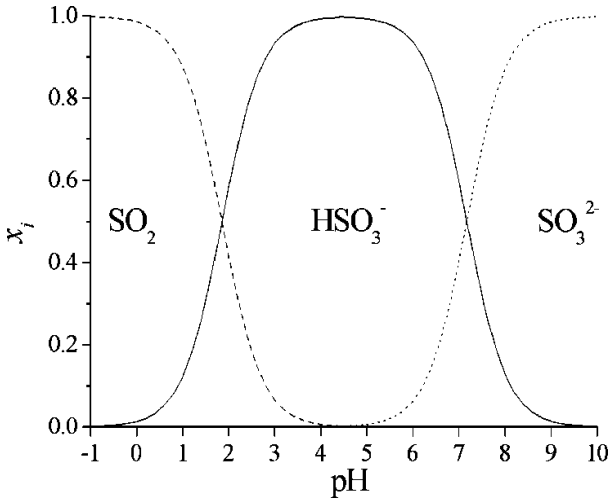


Figure 3.1 Equilibrium concentrations of sulphur (IV) species as the fraction x_i of the total sulphur in aqueous solution versus pH. Reprinted with permission from Ref. 18. Copyright (2005) American Chemical Society.

In terms of the mechanistic aspects of the electro-oxidation of sulphite, there have been numerous well-documented studies using bulk Pt[7-11] as a preferred electrocatalytic electrode but relatively fewer on bulk Au. The latter is the focus of this paper. Several mechanisms have been proposed for the sulphite oxidation. Seo and Sawyer[12] studied the oxidation of sulphite on bulk gold in acidic solutions by means of voltammetric and chronopotentiometric techniques and observed two oxidative processes where the first one was a pure electrochemical charge transfer process while the second one was a chemical reaction between electrochemically generated metal oxide and the sulphite species. Moreover, a two-electron oxidation for the overall reaction of an irreversible nature was indicated. Samec and Weber[13] provided a further insight into the electrochemical behaviour of sulphite on gold macroelectrodes in acidic media, inferring the involvement of "strongly" or "weakly" adsorbed hydrated sulphur dioxide, and a S(VI) intermediate species which reacted with water to form the final product of bisulphate or sulphate. That said, other work[14] using voltammetry and radiotracer studies indicated the formation of both bisulphate/sulphate (HSO_4^-/SO_4^{2-}) and dithionate ($S_2O_6^{2-}$) upon electro-oxidation of

aqueous sulphite solutions on bulk gold. These findings may be conflicting, which reflects the intrinsic complexity of electrochemistry of sulphite in terms of its reactivity and various valence states, and the well-grounded dependence on the corresponding electrochemical context. On the other hand, mechanistic observations of aqueous sulphite oxidation on wafer supported disperse catalysts to compare the behaviour to its bulk metal electrode established decades of years ago are scarce.[46-48] In the light of the reported better intrinsic performance of gold compared with platinum towards sulphite oxidation allied to its much stronger absorption on platinum,[15] the advantages of nanoparticles, and the antecedents mentioned before, in this article we report new findings acquired by cyclic voltammetry (CV) studies of this process using gold particle arrays deposited on BDD in acid media coupled with digital simulation, and in particular offer insight into mechanistic aspects of sulphite oxidation. Importantly, it is shown that the mechanism of sulphite oxidation on gold can be elucidated with simulation of data acquired at Au particle arrays supported on a BDD electrode, whereas for a bulk gold electrode the greater capacitance precludes quantitative analysis.

3.2 Experimental

3.2.1 Chemical reagents

Hydrochloric acid (analytical reagent grade, 37%), nitric acid (analytical reagent grade, 70%), and sodium sulphite anhydrous (laboratory reagent grade) were purchased from Fisher Chemical. Sulphuric acid (ACS reagent, 95.0-97.0%) and gold chloride trihydrate (≥ 99.9%) were obtained from Sigma-Aldrich. Aqua regia was prepared in a volume ratio of 1:3 between HNO_3 and HCl. All the chemicals were used as received without further purification. All aqueous solutions were made with using ultrapure water from Millipore with a resistivity of close to 18.2 MΩ cm at 25 °C.

3.2.2 Electrochemical apparatus and experiments

All the electrochemical measurements were undertaken using a computer controlled Autolab PGSTAT128N potentiostat (Metrohm Autolab, Utrecht, Netherlands) equipped with Nova software. A standard three-electrode system was employed for all electrochemical measurements. A gold macroelectrode of 2.0 mm diameter (CH Instruments, USA) and a boron doped diamond wafer (B ≈ 5×10^{20} atoms cm^{-3}, Element Six) were used as working electrodes. BDD was embedded in a home built polytetrafluoroethylene electrochemical cell with an exposed area of 0.37 cm^2 to the electrolyte, which has been described before.[49] A silver/silver chloride electrode (1.0 M KCl) was used as a reference electrode and a platinum coil served as a counter electrode. All the potentials reported in this work were with respect to this reference electrode, unless specified.

Prior to use, the BDD electrode was cleaned in a vial containing aqua regia overnight to remove the previous gold residuals between experiments and immersed in 0.10 M HNO_3 for voltammetric cycles between -1.7 to 2.5 V at 0.1 V s^{-1}. Before use, the gold electrode was polished sequentially on lapping pads with aqueous slurries of 1 µm, 0.3 µm, 0.05 µm alumina powder (Buehler, USA), followed by rinsing and sonicating with water to remove the slurry residues.

The electrochemical deposition of gold on the BDD surface was undertaken in 0.10 M H_2SO_4 containing 1.0 mM $HAuCl_4$ according to the literature.[50-51] The method included one nucleation-growing pulse. The nucleation pulse was applied at -0.7 V for 2 s, followed by growth pulses at 0 V for different times of 10 s, 50 s, or 150 s to form Au particles herein referred to as Au (10), Au (50), Au (150), respectively. The particles without the growing stage were studied for comparison, and were labelled as Au (0).

The sulphite measurements were carried out by cyclic voltammetry in 0.10 M H_2SO_4 (pH=0.89) containing different analyte concentrations of 10 µM – 2.0 mM at different scan rates using Au particle modified BDDs and Au macroelectrodes.

3.2.3 Characterisation

The gold particles were characterised using Scanning Electron Microscope (SEM, Hitachi S-4300, Japan) with an acceleration voltage of 10 kV. Microscopy images were analysed for particle size and separation using ImageJ (National Institute of Health, USA). The bar in the SEM images was used for scale calibration. The "Analyze Particles" function from the "Analyze" toolbox was used to count the number of particles and measure the size. The areas of interest were selected and marked "by hand" via the user interface, and the "Measure" function from the "Analyze" toolkit was utilised to determine the chosen areas.

3.2.4 Simulation

The simulation program DigiSim (Version 3.03b, Bioanalytical Systems, Inc., West Lafayette, IN, USA) developed by Rudolph[52] was employed to model the cyclic voltammograms for sulphite oxidation. A simplified reaction mechanism was entered into the simulator:

$$A \xrightarrow{E^0,\alpha,k_s} B + e \tag{3.4}$$

$$B + B \xrightarrow{K_{eq},k_f,k_b} C \tag{3.5}$$

where A is the sulphite, B is a reaction intermediate, and C is a dimer. The following parameters were used: E^0 is the formal potential, α is the charge transfer coefficient, and k_s is the heterogeneous electron transfer rate constant with the Butler-Volmer model assumed to apply; k_f and k_b are the forward (second order) and backward (first order) rate constants of the chemical step, respectively, with their ratio corresponding to the equilibrium

constant K_{eq}. Semi-infinite linear diffusion system was assumed and pre-equilibration was enabled for all the fittings.

3.3 Results and discussion

3.3.1 Electro-oxidation of sulphite at a gold macroelectrode

The focus of this work is the oxidation at gold electrodes of sulphite in aqueous solution. Initially the voltammetric response was studied using a gold macroelectrode of 2.0 mm diameter. Figure 3.2 shows cyclic voltammograms of 1.0 mM Na_2SO_3 in 0.10 M H_2SO_4 at different scan rates. It is clear that all CV curves have well-defined anodic peaks. The peak potentials of sulphite oxidation lie between 0.4 and 0.5 V *vs.* Ag/AgCl. This feature is consistent with the reported work earlier in terms of shape and potential.[17] The peak potential shifts negatively with the decrease of scan rate. This will be discussed later in this chapter. The plot of peak current of sulphite oxidation versus the square root of scan rate is linear, indicating that the electrochemical oxidation of sulphite is diffusion controlled. The slope (5.2×10^{-5} A $V^{-0.5}$ $s^{0.5}$) of the plot is used to calculate the diffusion coefficient of sulphite, yielding the values of 3.8×10^{-9} m^2 s^{-1} and 4.8×10^{-10} m^2 s^{-1}, respectively, based on one- and two-electron processes, according to the Randles-Sevcik equation for an electrochemically reversible reaction at 25 ^oC (discussed later):

$$I_p = 2.69 \times 10^5 A D^{0.5} C v^{0.5} n^{1.5} \quad (3.6)$$

where I_p is the peak current, A is the electrode area, D is the diffusion coefficient of reactant species, C is the bulk concentration of species, v is the scan rate, n is the total number of electrons. Note that a previous literature report assumed a two-electron process in contrast to the conclusion below.[12]

The voltammograms were further analysed in order to characterise the electron transfer process. As shown in Figure 3.3, the Tafel analysis region were taken from the initial part

of the ascending profile of the anodic peak. From the forward scan a plot of ln *I versus E* was drawn with the linear fitting shown in the inset. The slope of the resulting plot was used to calculate the anodic transfer coefficient (β) via the equation $slope = \frac{\beta F}{RT}$ where F is the Faraday constant, R is the universal gas constant, and T is the temperature.[53] The calculated value of transfer coefficient was 0.88 ± 0.09 for the range of scan rates in Table 3.1. This apparent value is close to unity, indicating that the process is seemingly likely a one-electron transfer reversible reaction at first glance.[54] However, the positive shift of potential with the increase of scan rate suggests a more complex process since for a simple pure reversible reaction the peak potential would be independent of scan rate.[55]

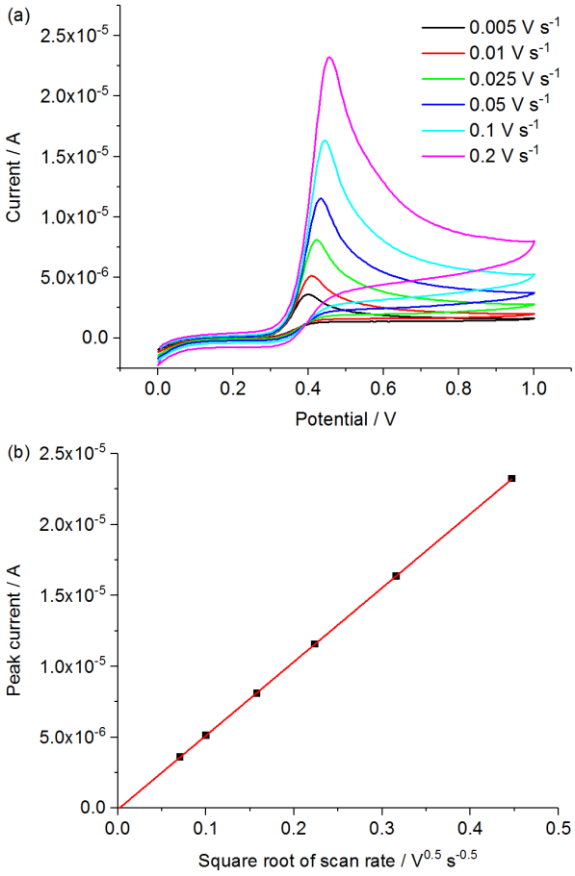


Figure 3.2 (a) CV of Au macroelectrode in 0.10 M H_2SO_4 containing 1.0 mM Na_2SO_3 recorded at different scan rates. (b) Plot of peak current as a function of the square root of scan rate from 0.005 to 0.2 V s^{-1}.

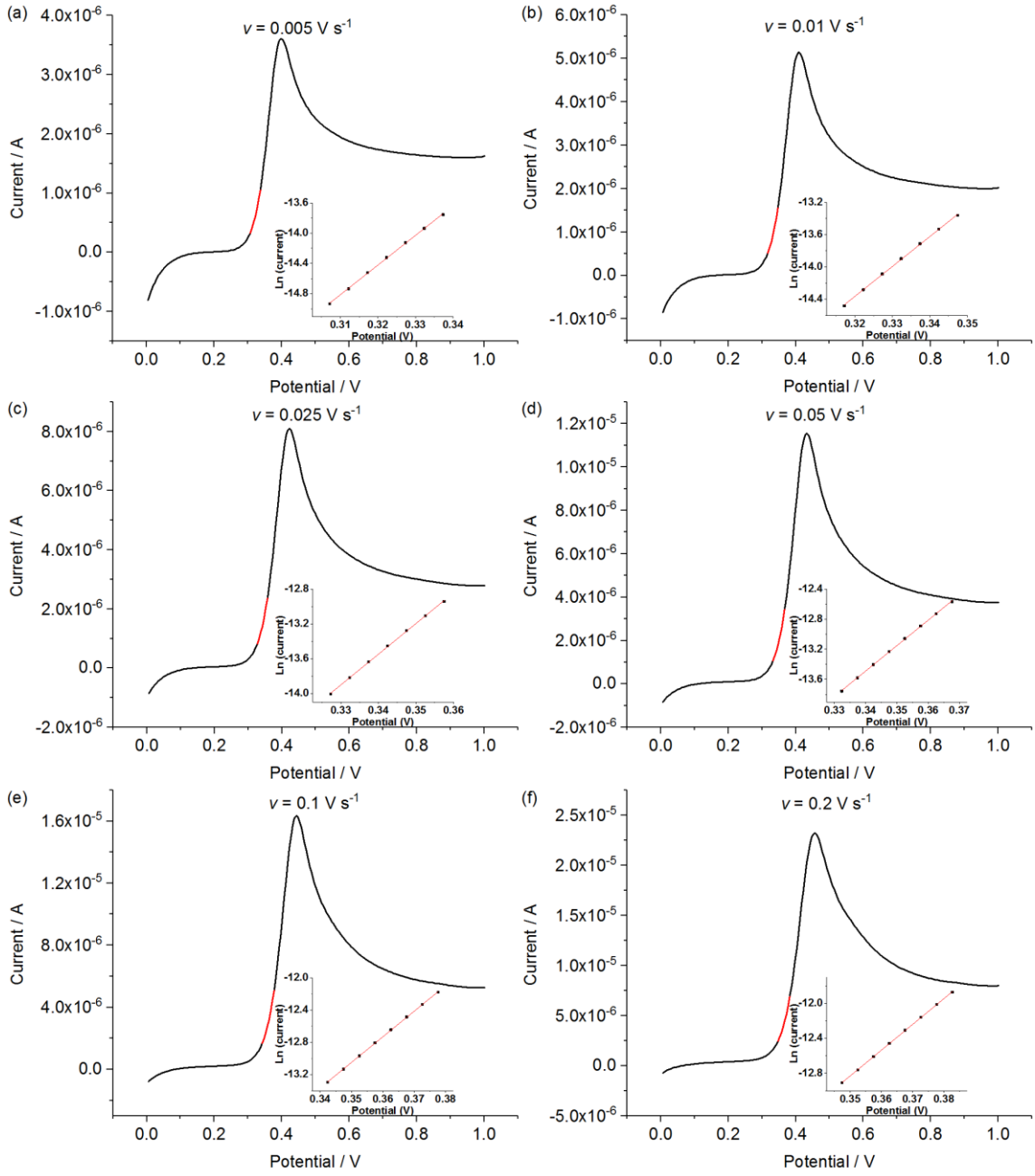


Figure 3.3 The forward CV of Au macroelectrode in 0.10 M H_2SO_4 containing 1.0 mM Na_2SO_3 at different scan rates of (a) 0.005 V s^{-1}, (b) 0.01 V s^{-1}, (c) 0.025 V s^{-1}, (d) 0.05 V s^{-1}, (e) 0.1 V s^{-1}, and (f) 0.2 V s^{-1}, with the highlighted Tafel analysis region in red. Insets are the corresponding Tafel plots.

Table 3.1 The calculated anodic transfer coefficient for a gold macroelectrode

Scan rate (V s^{-1})	Tafel slope	β	β (average)
0.005	39.2	1.01	0.88 ± 0.09
0.01	37.1	0.95	
0.025	35.2	0.91	
0.05	33.8	0.87	
0.1	31.7	0.81	
0.2	29.6	0.76	

The electro-oxidation of sulphite was then studied at different concentrations of 10, 100, and 1000 µM. The CVs of sulphite oxidation at these three concentrations measured using a gold macroelectrode are shown at a scan rate of 0.05 V s^{-1} in Figure 3.4. To enable observation of the changing voltammogram shape, the currents were normalized to the oxidation peak current. From Figure 3.4 it is noteworthy that as the concentration decreases to 10 µM, a backward peak appears, and the wave moves to more positive potential. This likely suggests a change of concentration affecting the mechanism. We focus on the data obtained at 1.0 mM concentration which has well defined signal background characteristics. Given that the Tafel analysis above is suggestive of an electrochemically reversible oxidation the observed behaviour could be due to a following chemical reaction in particular.[56] The idea of an EC type scheme was considered first, where E represents the electrochemical reaction and C denotes a first order chemical reaction using the Testa and Reinmuth notation.[57] The lack of any back peak in the 1.0 mM data is consistent with a fast following reaction and, in the case of a reversible electron transfer, the shift of the oxidation wave with potential. On the other hand, the emergence of a back peak in the lower concentration data suggests that the homogeneous kinetics are likely not first order.

Therefore alternatively an EC_2 (the electrochemical reaction followed by a chemical step of second order) mechanism can be proposed,[58] since the presence of a back peak depends on both the scan rate and the concentration of the analyte in an EC_2 process. We next simulated this hypothesis and the scan rate dependence of the 1.0 mM data using DigiSim software described in the simulation section using the following scheme.

$$A \xrightarrow{E^0,\alpha,k_s} B + e \tag{3.7}$$

$$B + B \xrightarrow{K_{eq},k_f,k_b} C \tag{3.8}$$

The parameters are given as following: E^0 = 0.4 V, α = 0.5, k_s = 0.01 cm s^{-1}, K_{eq} = 1×10^6, k_f = 1×10^4 M^{-1} s^{-1}, $D_A = D_B = D_C = 4\times10^{-9}$ m^2 s^{-1}, working electrode area A = 3.14×10^{-6} m^2. In order to optimize the fit across various voltage scan rates, the transfer coefficient was assumed to be 0.5 which with a fast k_s value would give reversible behaviour, and the diffusion coefficients of the species were presumed to be equal. The simulated diffusion coefficient of electroactive species is close to the calculated experiment value above on the basis of the one electron transfer assumption. Figure 3.5 shows the overlaid experimental and simulated voltammograms at different scan rates of from 0.005 to 0.2 V s^{-1}. There is a good fit across the full range of scan rates in terms of voltammogram shapes as well as peak currents and peak potentials. The mismatches in the reverse scan reflect the background capacitance but capture exactly the lack of a back peak. The presence or absence of a reverse peak is dependent on a dimensionless kinetic rate constant $K_2 = \frac{k_f}{v}\left(\frac{RT}{F}\right)[A]_{bulk}$, which is proportional to the analyte concentration ($[A]_{bulk}$) and inversely proportional to the scan rate (v) for an EC_2 as mentioned before.[55] From Figure 3.5 at a such high concentration of 1.0 mM sulphite the loss of a back peak occurs for large K_2. Returning to Figure 3.4 the data shown for 100 μM shows two forward peaks and the possible emergence of a back peak. This suggests the “turn off” of the following chemical

step as the product is diluted with the two waves suggestive of a split wave where the chemical step is partially completed.[59]

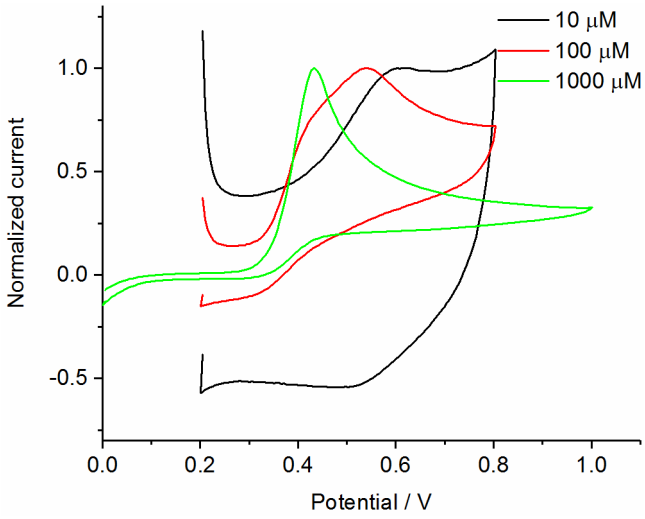


Figure 3.4 Normalized CV of sulphite at different concentrations of 10 μM, 100 μM and 1000 μM on the gold macroelectrode at 0.05 V s^{-1}.

From the above general approach the possible chemical reaction pathway can next be discussed further. A previous electrochemical study[60] indicated that the oxidation of SO_2 on platinum in sulphuric acid may involve a chemical step via the formation of the dithionate ($S_2O_6^{2-}$) accredited by spectroscopic study,[61] which is consistent with the above discussion combining the fitting of EC_2 model with the speciation via the following reactions:

$$SO_2 + H_2O \rightarrow H_2SO_3^+ + e^- \quad (3.9)$$

$$2\ H_2SO_3^+ \rightarrow H_2S_2O_6 + 2H^+ \quad (3.10)$$

Although dithionic acid ($H_2S_2O_6$) may decompose via a disproportionation step, dilute solutions of the acid are known to be stable with the occurrence of decomposition on concentration only above 50 ^oC.[62]

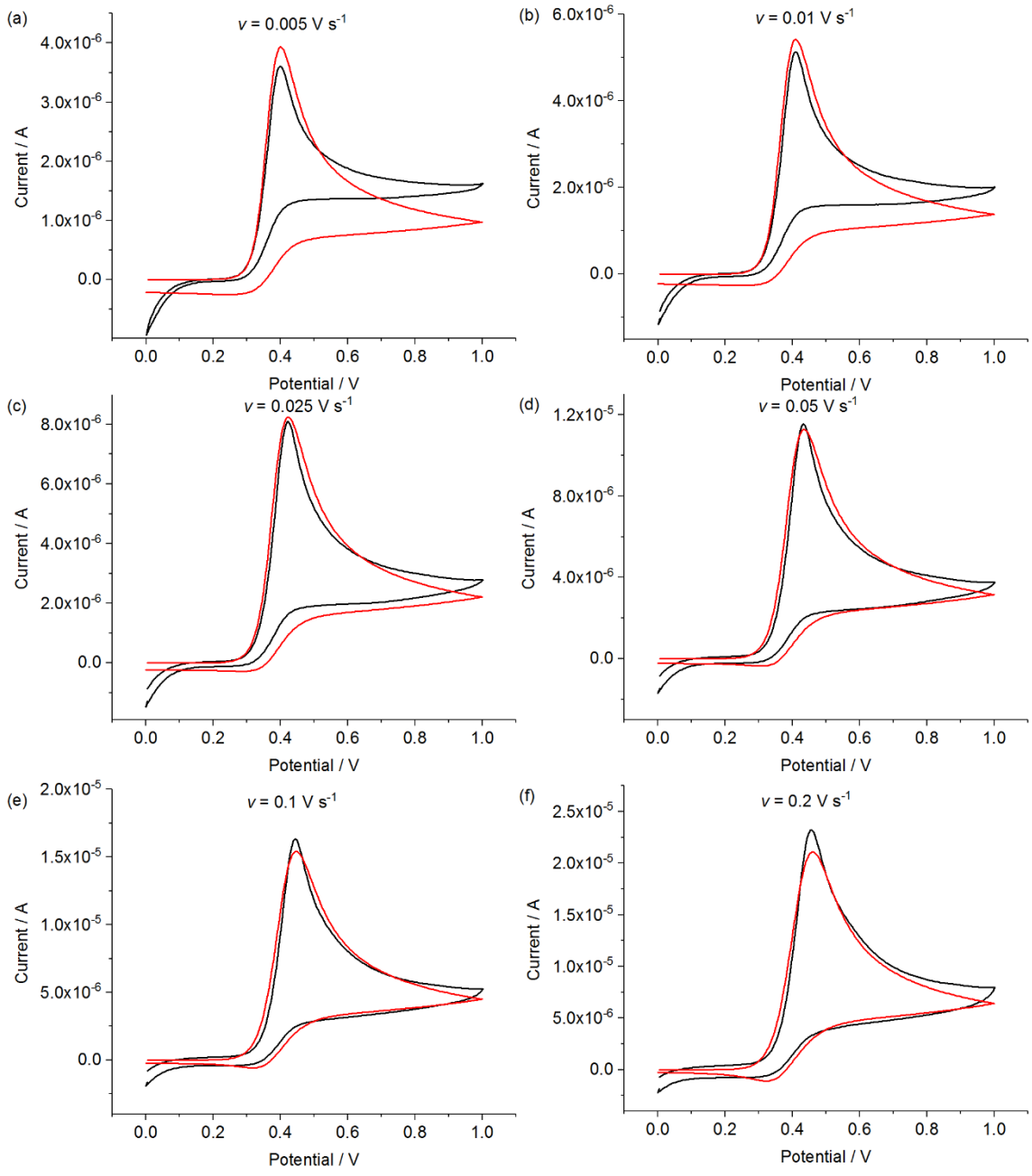


Figure 3.5 CV from experiment (black) and simulation (red) at different scan rates of (a) 0.005 V s^{-1}, (b) 0.01 V s^{-1}, (c) 0.025 V s^{-1}, (d) 0.05 V s^{-1}, (e) 0.1 V s^{-1}, and (f) 0.2 V s^{-1}.

3.3.2 Electrodeposition of gold particles and characterisation

Having established an electrochemical mechanism using a gold macroelectrode, the behaviour of gold particles dispersed on supporting electrodes for electro-oxidation of sulphite was next studied. First, a facile preparation method of Au deposition onto boron

doped diamond was developed. A nucleation-growth pulse protocol was applied for gold particles deposition on BDD in 1.0 mM $HAuCl_4$ solution. The potential and current versus time curves are shown in Figure 3.6. A nucleation pulse was applied at -0.7 V versus Ag/AgCl for 2 s; these parameters were chosen to enable the fast electrodeposition of gold nuclei and to avoid hydrogen evolution.[50-51] A growth pulse was applied at 0 V for different times and utilised to maintain a small cathodic current observed in Figure 3.6(d, f, h) during the growth stage. The durations of growth pulses were changed to be 0, 10, 50, and 150 s for different depositions. Au particle deposition onto the BDD electrode surface was confirmed by SEM analysis.

The SEM images of gold particles on the BDDs under different deposition conditions are shown in Figure 3.7 at three different magnifications. It is apparent that the deposition pulse without any growth step yields quasi-spherical gold nanoparticles (AuNPs) as shown in Figure 3.7(i) under high magnification. Traces of lower aspect ratio protrusions can be observed on branched gold nuclei structures for the 10 s growth pulse. The branched geometry tendency becomes more obvious for 50 s growth in Figure 3.7(k) while growth deposition for 150 s yields star-like structures consisting of a few branches around a gold centre in Figure 3.7(l). This result demonstrates that the Au particle morphology transition from quasi-spherical to star shaped can be easily controlled via the duration of the growth pulse.

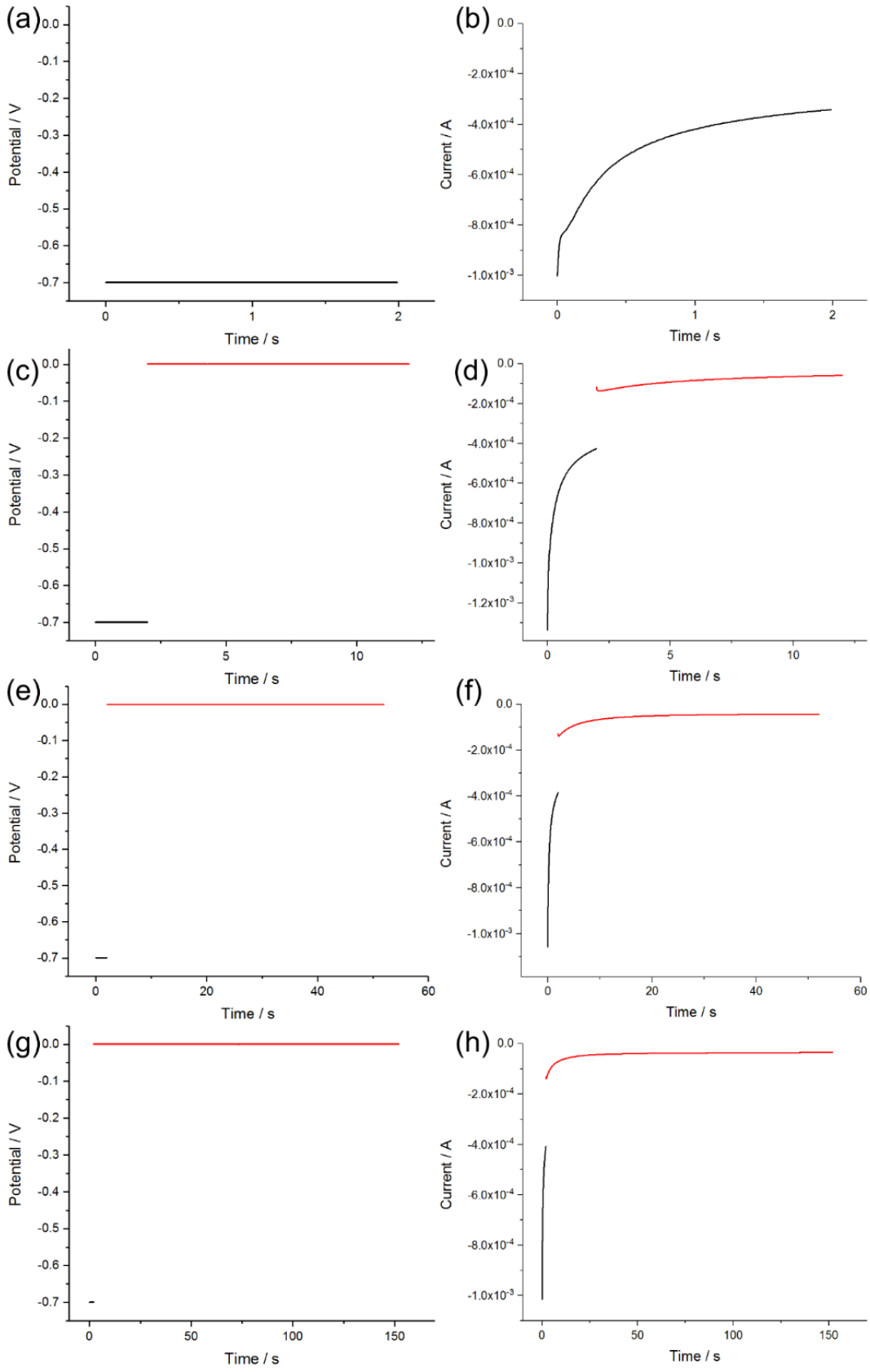


Figure 3.6 (a, c, e, g) The potential-time and (b, d, f, h) current-time curves for deposition Au (0), Au (10) Au (50), and Au (150), respectively.

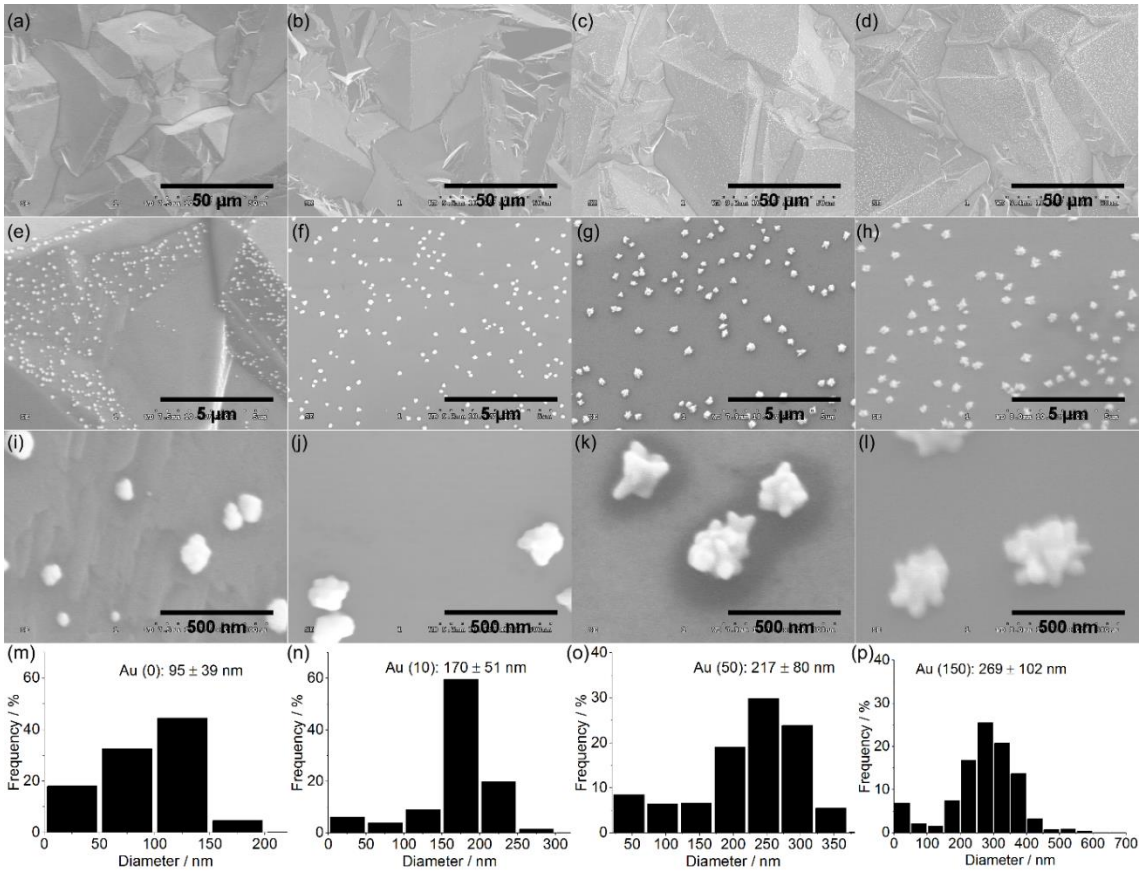


Figure 3.7 SEM images of (a, e, i) Au (0), (b, f, j) Au (10), (c, g, k) Au (50), (d, h, l) Au (150) particles after different growth times deposition at three different magnifications of (a-d) 1000×, (e-h) 10000×, and (i-l) 100000×. The size distributions of the (m) Au (0), (n) Au (10), (o) Au (50), and (p) Au (150) particles.

A statistical analysis of particle sizes was carried out based on the SEM images of Au particles using ImageJ. To provide the information of the particle diameter, hundreds of particles of 450, 698, 436, and 1279 were analysed for each deposition of Au (0), Au (10), Au (50), and Au (150), respectively, with the number notation in the bracket being the growth pulse time defined in the experiment section above. The size-based histograms of the gold particles were generated as shown in Figure 3.7(m-p). The average diameter of Au (0) is 95 ± 39 nm and 44% of them are within the range of 105-145 nm. The size of Au (10) is 170 ± 51 nm, and 60% of the particles are 155-195 nm. With longer growth times,

the average sizes increase to be 217 ± 80 nm, and 269 ± 102 nm for Au (50) and Au (150), respectively, with the corresponding maximum percentage of 30% and 25% in the size range of 225-265 and 255-295 nm. The results show that it is feasible to tune the particles of different size from the nanometer to the submicron scale via the growth time.

For particle arrays on a supported inert substrate, the electrochemical response of the electrode depends on the size and morphology of particles, the diffusion coefficient of analyte, *D*, and the interparticle distance (nanoparticle surface coverage), *d*, assuming that electrolysis is confined to the particles and not the support.[63] A further but key parameter is the timescale of the experiment, *t*, controlled by varying scan rate, so that if $d \gg \sqrt{Dt}$, the particles are diffusional isolated but at larger times, the diffusion fields of individual particle overlap. Accordingly, the diffusional regime may be divided into the five cases as shown in Figure 3.8.[64] Case 1 corresponds to the diffusion field at isolated particles being linear at very short times where $r_p > \sqrt{Dt}$ (r_p is the radius of particle). Case 2 describes the diffusion to the each particle is convergent over a longer timescale when $r_p < \sqrt{Dt}$. In both cases of 1 and 2, adjacent particles are far enough that they are diffusionally independent on the time scale of the experiment. Case 3 is seen when the diffusional fields of neighbouring particles partially overlap where the diffusion layer thickness of each particle is comparable to the interparticle separation. When the diffusion layers of adjacent particles overlap heavily, such that the diffusion to the whole electrode surface is linear in nature, it is categorised as case 4. The above four cases are realized assuming the substrate is macroscopic in size.[65-66] In case 5, convergent diffusion to the whole substrate is achieved in the very long experimental timescale, giving sigmoidal shaped voltammograms when the substrate is of the microscale.

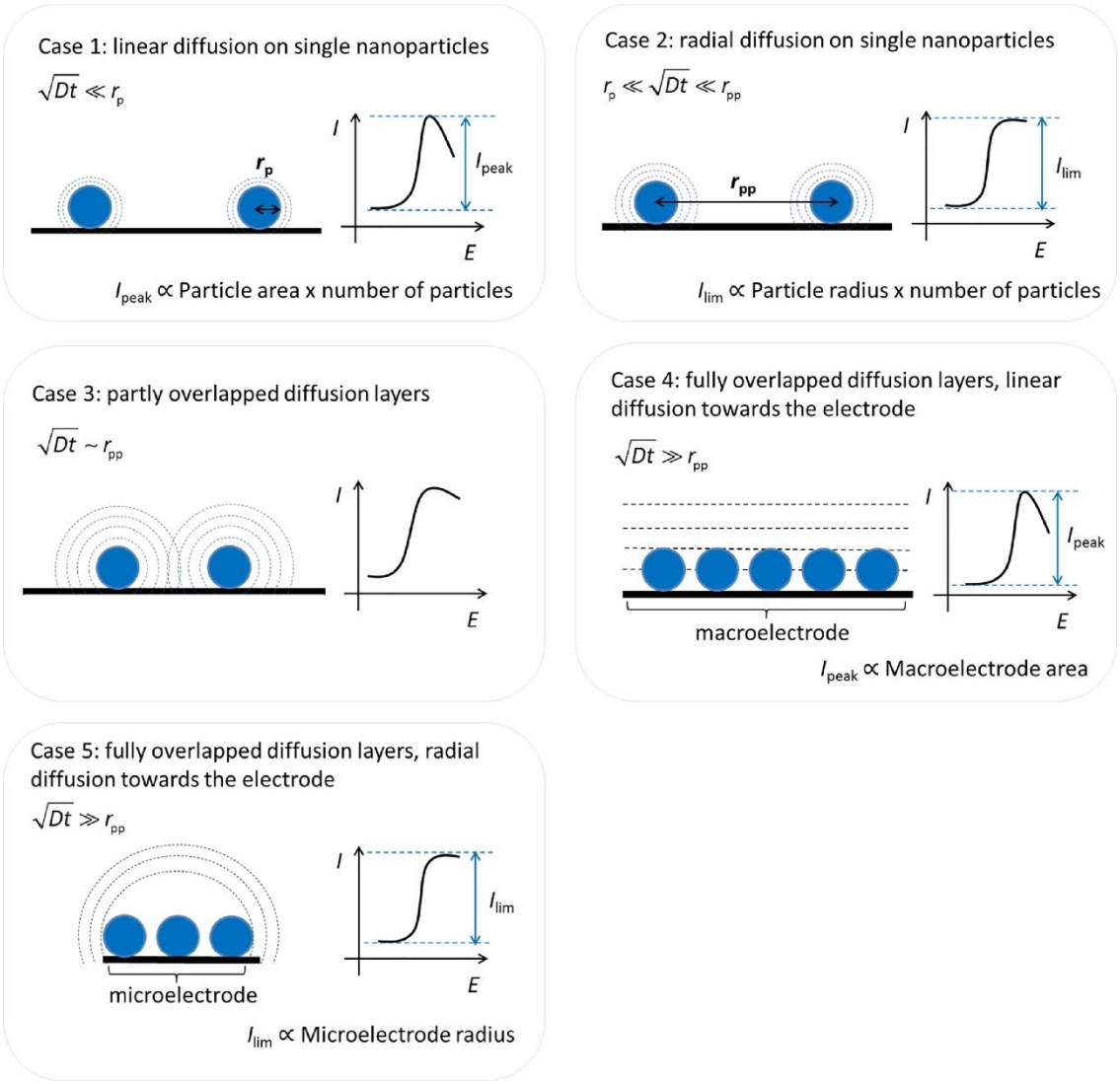


Figure 3.8 The five cases of diffusion regimes for nanoparticle modified substrate electrode. The spheres are nanoparticles and the dash lines are the diffusion fields. Reprinted from Ref. 64, Copyright (2019), with permission from Elsevier.

The images in Figure 3.7(a-d) show that the particle coverage increases with longer deposition time. Next we analyse the interparticle separation in more detail. For Au (0), the nanoparticles are located mostly at the BDD edge areas from Figure 3.7(a) although there are a few nanoparticles are on the basal planes. This may be due to the local heterogeneities in terms of differential boron dopant level.[67] The AuNPs may nucleate at the high conductivity regions where there is a higher boron concentration within the

domains during the very short nucleation pulse while only a few nanoparticles are formed on the low boron-doped facets.

In order to know the interparticle distance for Au (0) and the resulting diffusion category correspondingly, we simplified the Au (0) deposition model described below via the following assumptions. First within the edge domains, the AuNPs are very close to each other and these edge domains can be simply assumed from a diffusional perspective as the individual bigger Au "arrays/blocks" highlighted in the Figure 3.9 as irregular shapes. Simultaneously, to simplify the calculation to know the block distance, the basal planes are further assumed to be "blank" areas "without" AuNPs. Hence the entire BDD can be viewed as several randomly distributed Au arrays of flat discs of a few microns in diameter, which are separated by the "blank" BDD domains.

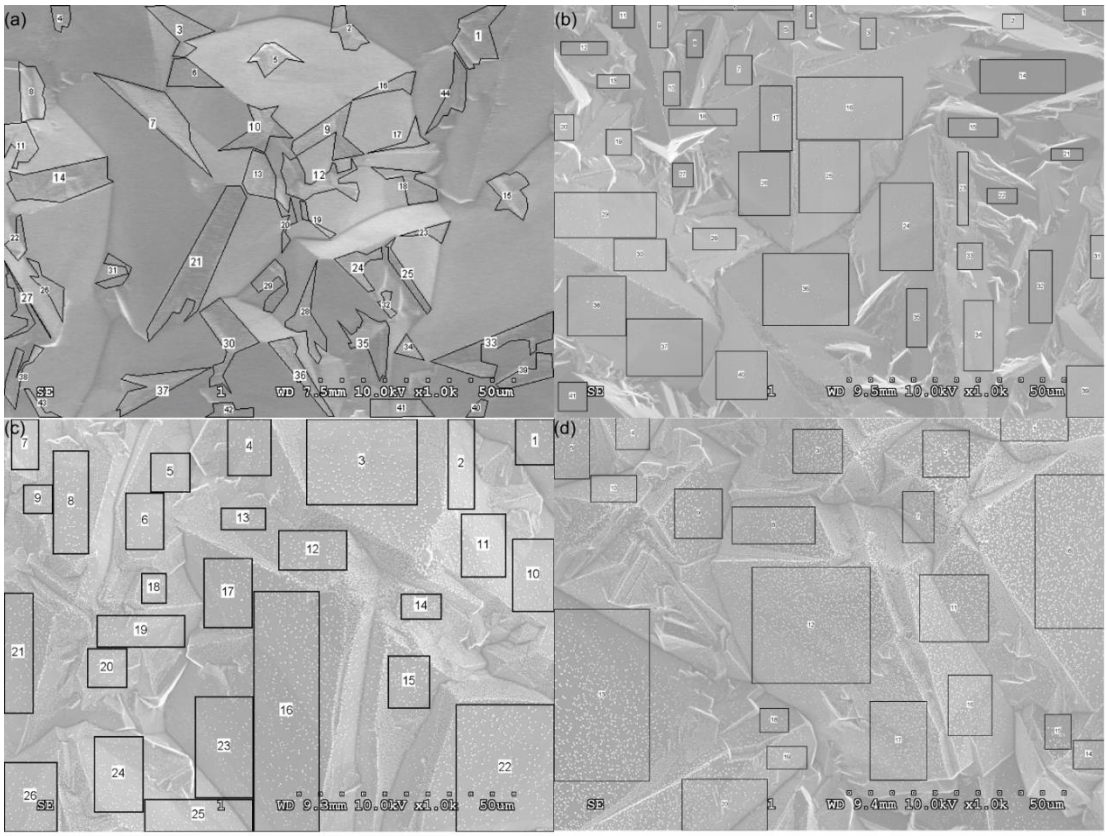


Figure 3.9 The highlight analysed areas for (a) Au (0), (b) Au (10), (c) Au (50), and (d) Au (150).

For Au (0), the area of each circled Au block in Figure 3.9 was measured by ImageJ. Each Au block with the area (*S*) is approximated as a disc, such that $S = \pi d_{eff}^2/4$. Therefore the effective diameter of each Au block can be calculated as shown in Table 3.2. Then a mean diameter for these Au blocks can be further approximated, which is 7.9 ± 2.9 μm. Assuming that the Au particle blocks compactly occupy the whole electrode in the pattern of square grid each with the same side length, the centre-to-centre distance between two neighbouring blocks is the value of the side length, which is given by:

the average interblock distance = $\sqrt{\frac{area}{number\ of\ blocks}}$ = 16.4 μm.

Table 3.2 The effective diameter of Au (0) blocks

Area	d_{eff}: μm	Area	d_{eff}: μm	Average d_{eff} : μm
1	11.30	23	4.94	7.9 ± 2.9
2	7.38	24	7.31	
3	9.36	25	6.07	
4	5.09	26	6.47	
5	7.30	27	6.32	
6	8.09	28	9.27	
7	13.34	29	7.57	
8	8.98	30	11.41	
9	10.05	31	5.17	
10	9.20	32	3.88	
11	8.04	33	12.59	
12	10.62	34	4.68	

13	8.73	35	9.78
14	13.90	36	8.47
15	8.83	37	10.24
16	6.08	38	7.25
17	5.27	39	7.76
18	7.96	40	3.88
19	3.83	41	8.18
20	4.78	42	5.66
21	16.83	43	4.04
22	5.49	44	8.11

For Au (10), Au (50) and Au (150), more gold particles were deposited onto the flat facets. The assumption of "blank" basal planes was not taken for these cases, as it is especially notable that gold submicron-particles are distributed quite uniformly forming a monolayer on the BDD surface in two dimensions for Au (150) from Figure 3.9(d). Therefore the detailed interparticle distances in these basal planes circled in the Figure 3.9(b-d) for these three Au deposits are analysed individually below.

To calculate the interparticle spacing it was assumed that the particles are homogeneously distributed on each of the highlighted areas for Au (10), Au (50) and Au (150). For these Au deposits, at least 20 areas in the each SEM were chosen randomly for analysis in order to get good statistics. The interparticle separation was calculated assuming a regular square lattice. The chosen area was assumed to be split into square cells each of equal area. Each Au particle was considered to be at the centre of a unit cell featuring an identical side length of square. Accordingly, with this approximation the centre-to-centre distance between adjacent particles was also equal to the side length as following:

the average interparticle distance = $\sqrt{\frac{rectangle\ area}{number\ of\ particles}}$

The rectangle area and particle statistics required for the calculation were measured and counted via the image analysis software ImageJ. The interparticle separation was obtained via the above equation for each highlighted area as shown in Table 3.3, Table 3.4, and Table 3.5 for three Au deposits. Furthermore, the mean interparticle distance for each gold deposit is estimated by averaging the corresponding values in these analysis rectangle areas. Accordingly, with longer deposition time, the mean interparticle distances for Au (10), Au (50) and Au (150) are 1.43 ± 0.26, 1.19 ± 0.12, and 0.83 ± 0.12 μm, respectively.

Table 3.3 The interparticle distance for Au (10) deposition

Area	Area size: μm^2	AuNPs number	Interparticle distance: μm	Average interparticle distance : μm
1	33.06	26	1.13	1.43 ± 0.26
2	15.82	8	1.41	
3	25.46	18	1.19	
4	11.87	9	1.15	
5	14.65	11	1.15	
6	30.56	13	1.53	
7	40.58	23	1.33	
8	23.06	7	1.81	
9	39.18	17	1.52	
10	29.06	17	1.31	
11	26.84	7	1.96	

12	31.62	31	1.01
13	22.36	8	1.67
14	149.27	40	1.93
15	48.35	34	1.19
16	342.23	213	1.27
17	108.94	89	1.11
18	57.94	33	1.32
19	33.26	14	1.54
20	25.87	16	1.27
21	19.22	9	1.46
22	23.75	12	1.41
23	40.85	32	1.13
24	240.15	220	1.04
25	225.55	81	1.67
26	169.70	66	1.60
27	25.19	10	1.59
28	48.50	21	1.52
29	239.42	118	1.42
30	85.56	41	1.44
31	30.10	19	1.26
32	86.40	30	1.70
33	34.36	19	1.34
34	107.67	40	1.64
35	62.38	31	1.42
36	320.11	109	1.71

37	224.51	58	1.97
38	179.99	95	1.38
39	100.33	35	1.69
40	127.89	121	1.03
41	43.21	18	1.55

Table 3.4 The interparticle distance for Au (50) deposition

Area	Area size: μm^2	AuNPs number	Interparticle distance: μm	Average interparticle distance : μm
1	91.34	48	1.38	1.19 ± 0.12
2	122.06	91	1.16	
3	489.65	326	1.23	
4	126.68	79	1.27	
5	78.41	48	1.28	
6	110.37	60	1.36	
7	70.57	43	1.28	
8	187.63	135	1.18	
9	42.34	41	1.02	
10	156.02	134	1.08	
11	143.98	112	1.13	
12	139.17	138	1.00	
13	49.31	42	1.08	
14	51.64	58	0.94	

15	111.21	90	1.11
16	813.49	511	1.26
17	172.64	104	1.29
18	37.66	37	1.01
19	142.58	100	1.19
20	78.41	62	1.12
21	178.97	130	1.17
22	646.14	405	1.26
23	301.49	147	1.43
24	189.33	117	1.27
25	180.23	114	1.26
26	189.60	117	1.27

Table 3.5 The interparticle distance for Au (150) deposition

Area	Area size: μm^2	AuNPs number	Interparticle distance: μm	Average interparticle distance: μm
1	80.26	149	0.73	0.83 ± 0.12
2	113.01	164	0.83	
3	112.57	246	0.68	
4	55.13	78	0.84	
5	111.26	139	0.89	
6	549.22	886	0.79	
7	83.36	214	0.62	

8	158.60	242	0.81
9	121.44	130	0.97
10	63.39	106	0.77
11	239.25	426	0.75
12	709.49	1576	0.67
13	848.52	837	1.01
14	46.10	66	0.84
15	46.92	50	0.97
16	136.94	253	0.74
17	231.45	393	0.77
18	35.53	37	0.98
19	46.65	46	1.01
20	226.66	266	0.92

The results of the above analysis are summarised in the Table 3.6. The Au (0) blocks of micron size are separated by 16 μm while for the other three gold deposits the interparticle distance is about 1 μm. From Table 3.6, the interparticle separation decreases with longer deposition time, which reflects the increasing particle density observed from Figure 3.7(a-d). In essence, the system can be viewed as gold (sub)microelectrode arrays with inter-array separation of micrometre size on the BDD substrate. According to the above results, and four categories of the diffusional behaviour at a nanoparticle array depending on the particle size, interparticle distance, and $\sqrt{Dt}$ (estimated as 200-1265 μm by approximating $D = 4 \times 10^{-9}$ m^2 s^{-1} and t = 10-400 s via various scan rates of 0.005-0.2 V s^{-1}), it is case 4 for this present study, which is the diffusion domains of neighbouring particles heavily overlap such that diffusion to the whole electrode surface is linear.[63] To this end, the current

results show that the nucleation-growth pulse deposition strategy is a facile and powerful method to construct metal particle arrays of controllable nano- and submicron- structures in terms of size and shape onto boron-doped diamond electrode surfaces, resulting in mass transport to the surface, which is planar diffusional, and hence expected to give voltammetric signals reflecting the geometric area of the BDD substrate.

Table 3.6 The approximation of gold size and separation

	Au (0)	Au (10)	Au (50)	Au (150)
Block/particle diameter (μm)	7.94	0.17	0.217	0.269
Interblock/interparticle separation (μm)	16.4	1.43	1.19	0.83

3.3.3 Electrochemical oxidation of sulphite on gold particle modified boron doped diamond electrodes

Having established the successful fabrication of Au arrays on BDD substrates, the next step was to evaluate the electrochemical response of the as-prepared BDD electrode interfaces for sulphite oxidation in H_2SO_4 electrolyte solution using CV technique. The comparison between Au (0), Au (10), Au (50), and Au (150) modified BDD electrodes was first carried out in 1.0 mM Na_2SO_3. Simultaneously, it is also of significance to evaluate the nature of the sulphite oxidation process to distinguish between surface bound or diffusional behaviour. For this purpose a scan rate dependence study was run at the same time for each Au modification. Figure 3.10 shows the experimentally recorded voltammograms for several Au particle modified BDD electrodes with variable scan rates towards the oxidation of sulphite. The peak currents of sulphite oxidation increase along

with the increase of scan rates and all the curves show the peak from 0.4 to 0.6 V with similar waveshapes. There is a potential shift to more positive position for each gold deposit, which is in agreement with the findings using the gold macroelectrode above. The good linearity in the plot of the peak current versus the square root of scan rate is observed for all the cases, indicating that this behaviour is a diffusional controlled process instead of an absorption confined one where peak currents are proportional to the scan rate.

To attain the further insights about the electrode transfer behaviour for the sulphite oxidation process, Tafel analysis was examined again for the several gold particles modified electrodes. The Tafel plots for Au (0), Au (10), Au (50), and Au (150) modified electrodes are charted in Figure 3.11-3.14, respectively. The corresponding effective anodic transfer coefficient (β) is calculated via the Tafel equation mentioned before in the Tables 5.7-5.10. The results are summarized in Table 3.11. It shows an increasing trend for charge transfer coefficient from 0.84 to 0.95. The β value for Au (150) modified BDD is close to unity, indicating again a one-electron transfer electrochemically reversible process as seen for the gold macroelectrode. This corresponds to case 4 where diffusion fields of neighbouring gold particles overlap heavily for sulphite oxidation resulting in the planar diffusion toward the whole electrode. The voltammetry response is almost equivalent to that of a macroelectrode of the same geometric area as the modified electrode using much less gold particles acting as two-dimensional monolayer arrays with reducing the cost simultaneously. Hence the geometric area of 0.37 cm^2 can be used for calculation of diffusion coefficient of sulphite via the Randles-Sevcik equation for electrochemically reversible process with one electron transfer involved for Au (150). With the plot slope (6.51×10^{-4} A $V^{-0.5}$ $s^{0.5}$) of the peak current versus the square root of scan rate for Au (150) in Figure 3.10(e), the diffusion coefficient value is 4.28×10^{-9} m^2 s^{-1}, confirming the above result achieved by a gold macroelectrode. Figure 3.10(e) shows that the electrodes found

by electrodeposition for 0, 10, 50 s second lower gradients in the Randles-Sevcik plot of I_p versus $v^{0.5}$ as compared to Au (150) with the slopes being the evaluation of electrochemical reversibility. This reflects an increased level of electrochemical irreversibility as the deposition time shortens:

$$I_p = 2.99 \times 10^5 A D^{0.5} C v^{0.5} n(n' + \beta)^{0.5} \quad (3.11)$$

where the above physical quantities have their general meanings as stated before except that n' is the number of electrons transferred before the rate determining step at 25 ^{o}C. This in turn suggests that the morphology of the nanoparticles influences the electron transfer rate. Moreover, the slope of I_p versus $v^{0.5}$ was predicted using $D = 4.28 \times 10^{-9}$ m^2 s^{-1}, $n' = 0$, and the measured β values in Table 3.11. Although the interparticle spacing is as estimated above for Au (0), Au (10), and Au (50), small compared to diffusion layer thickness associated with the voltammetry at the particle, it should be noticed that the prediction of peak currents using equation (3.11) is inappropriate for the present situation since the process at each particle involves following second order kinetics. As we move "up" the wave towards the peak current the following reaction occurs to a greater extent as the reaction is second order. Accordingly, the extent of "chemically promoted electrochemical irreversibility" at the peak current drops below that estimated from equation (3.11) in Figure 3.10.[68]

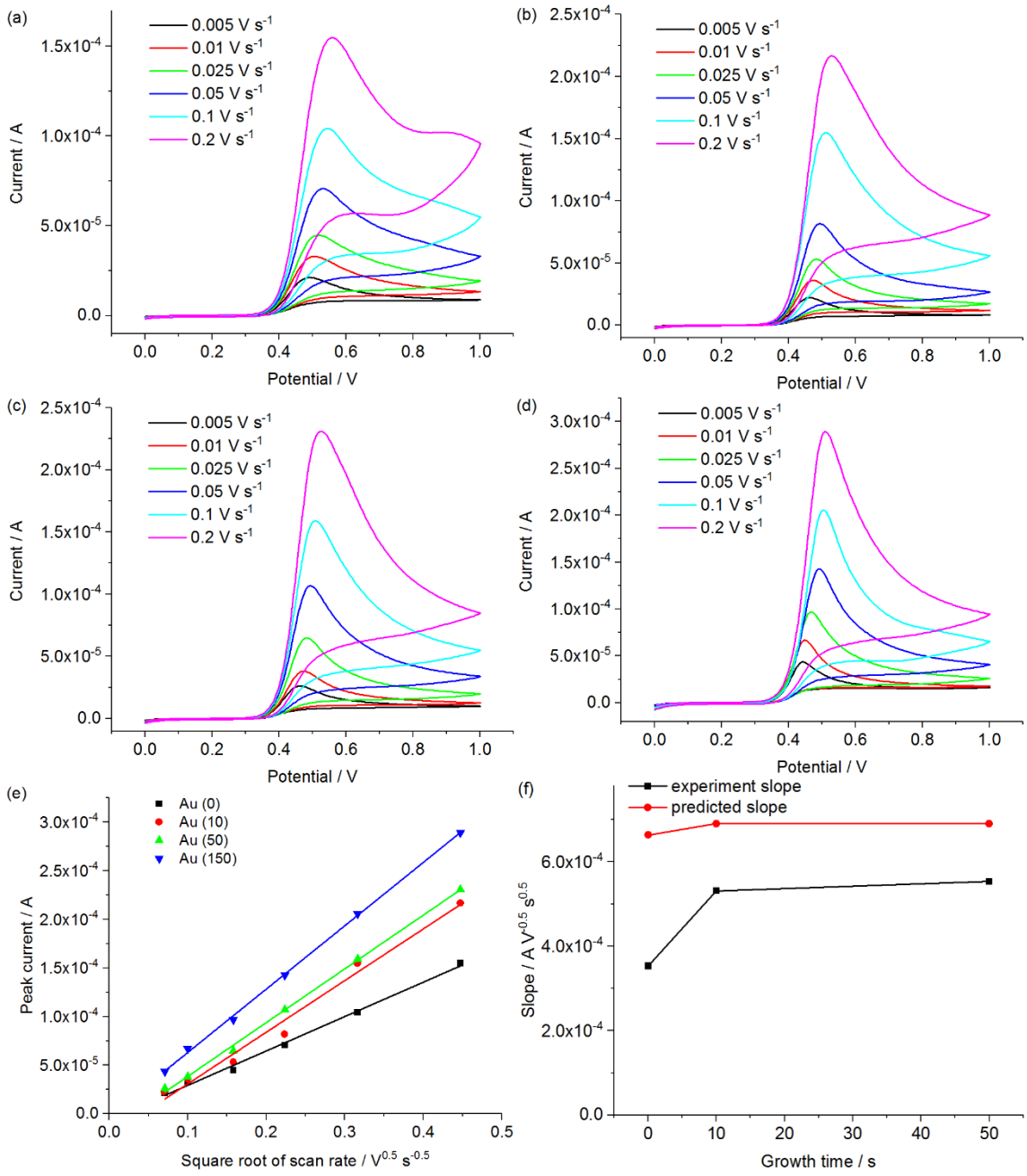


Figure 3.10 CV of (a) Au (0), (b) Au (10), (c) Au (50), and (d) Au (150) particles modified BDD electrodes in 1.0 mM Na_2SO_3/0.10 M H_2SO_4 at different scan rates. (e) Plot of peak current as a function of the square root of scan rate from 0.005 to 0.2 V s^{-1} for the corresponding gold modified BDDs. (f) The comparison of experimental (black) and predicted (red) slope of the plot.

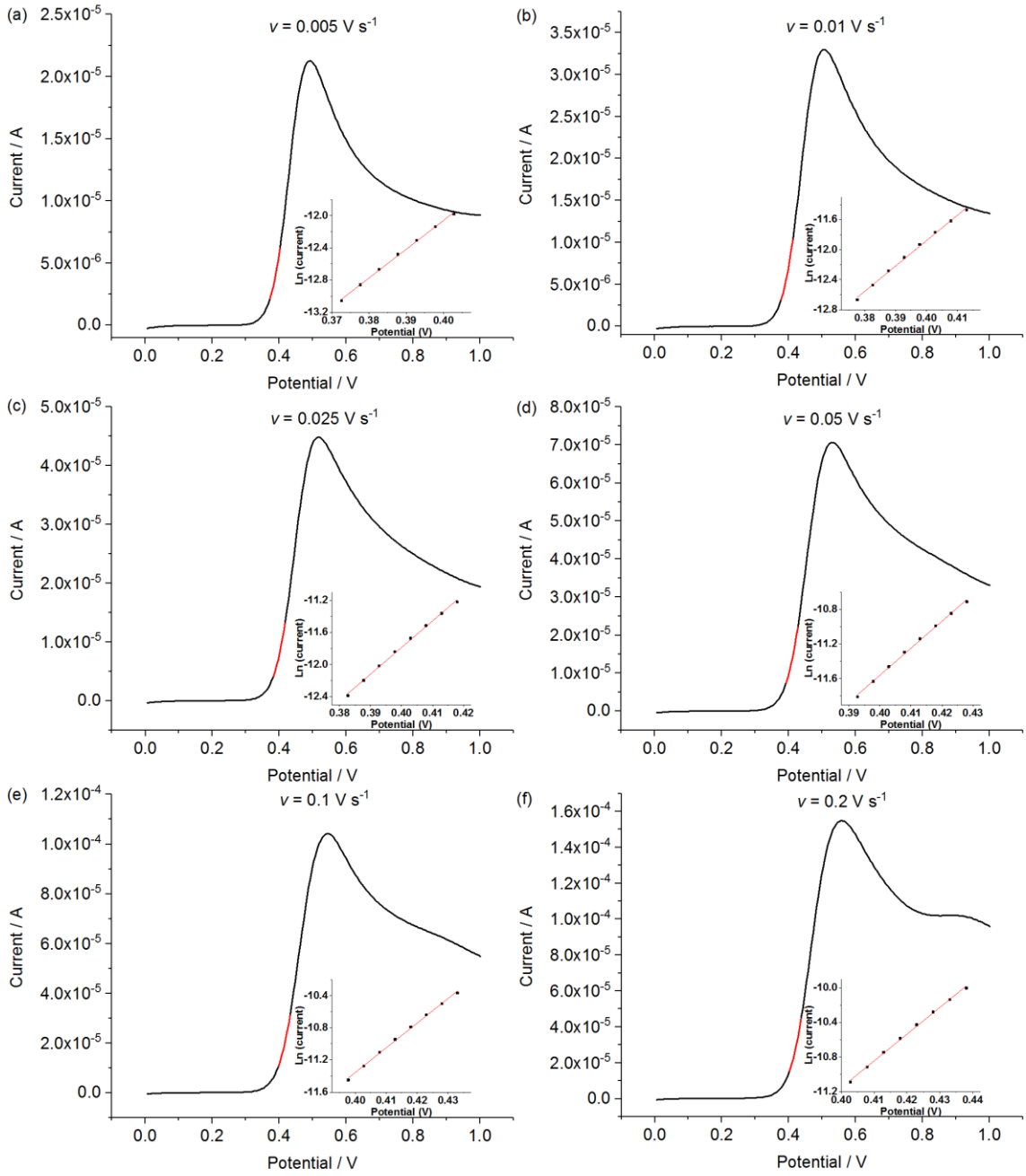


Figure 3.11 The forward CV of Au (0) modified BDD in 0.10 M H_2SO_4 containing 1.0 mM Na_2SO_3 at different scan rates of (a) 0.005 V s^{-1}, (b) 0.01 V s^{-1}, (c) 0.025 V s^{-1}, (d) 0.05 V s^{-1}, (e) 0.1 V s^{-1}, and (f) 0.2 V s^{-1}, with the highlighted Tafel analysis region in red. Insets are the corresponding Tafel plots.

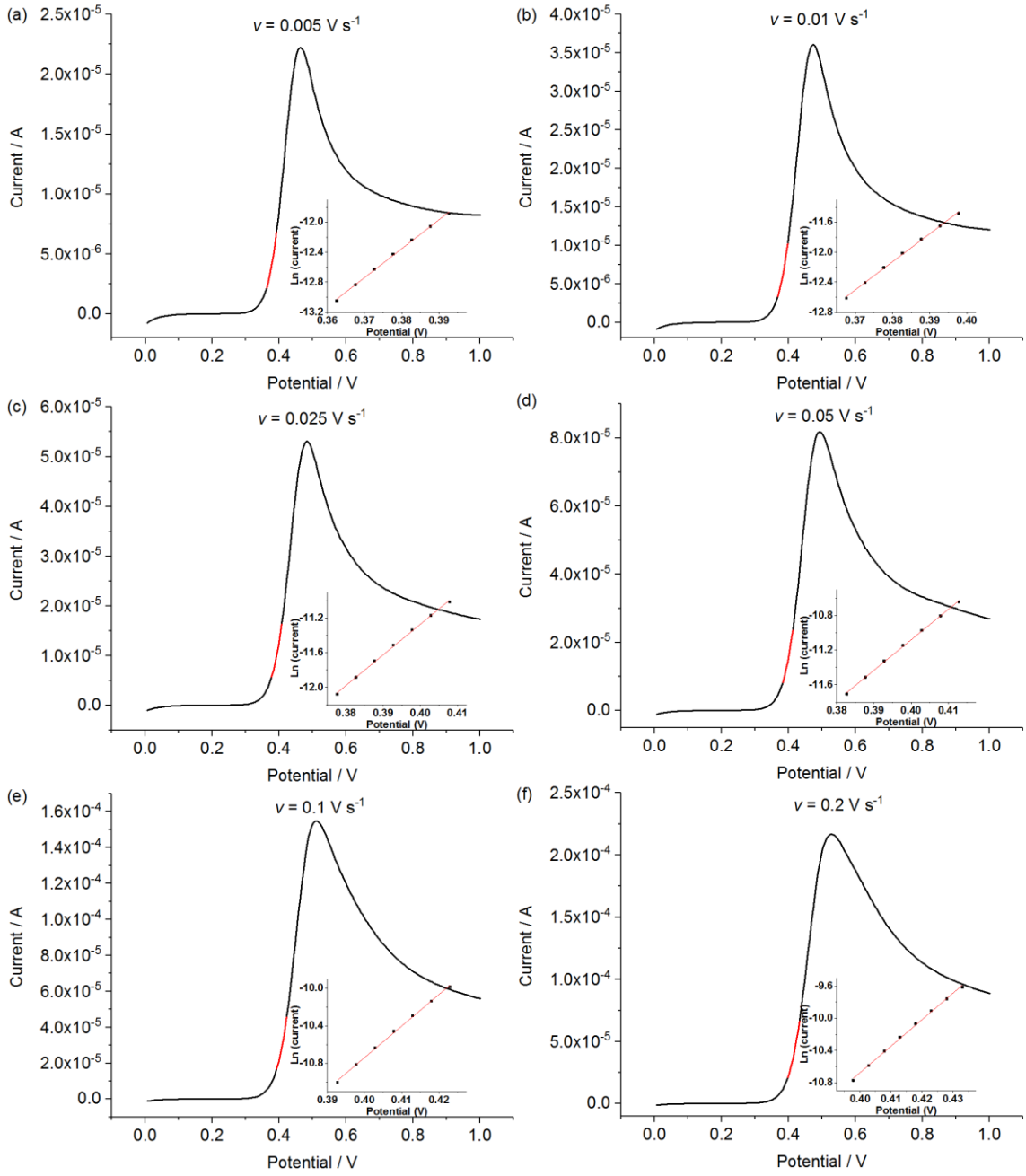


Figure 3.12 The forward CV of Au (10) modified BDD in 0.10 M H_2SO_4 containing 1.0 mM Na_2SO_3 at different scan rates of (a) 0.005 V s^{-1}, (b) 0.01 V s^{-1}, (c) 0.025 V s^{-1}, (d) 0.05 V s^{-1}, (e) 0.1 V s^{-1}, and (f) 0.2 V s^{-1}, with the highlighted Tafel analysis region in red. Insets are the corresponding Tafel plots.

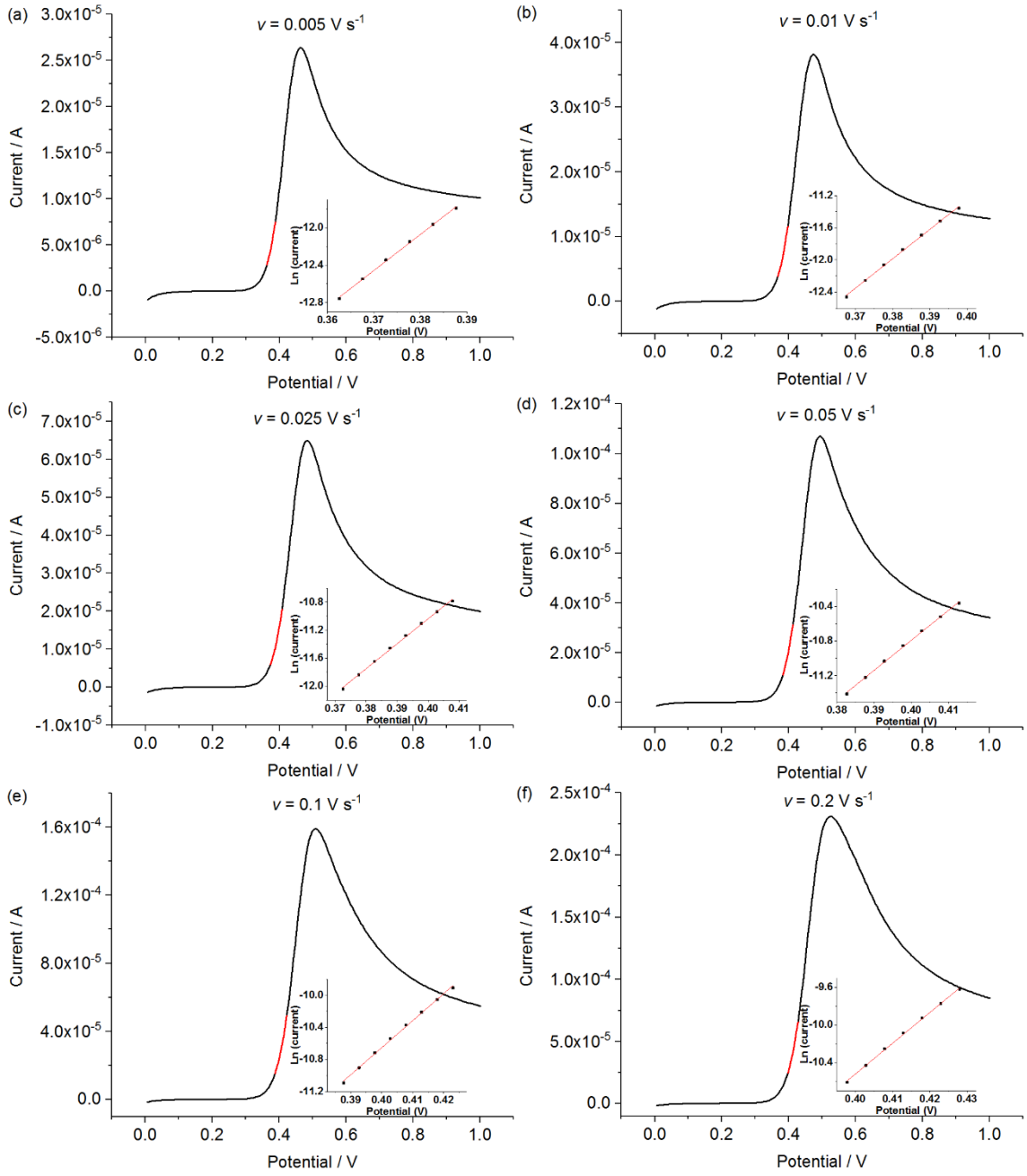


Figure 3.13 The forward CV of Au (50) modified BDD in 0.10 M H_2SO_4 containing 1.0 mM Na_2SO_3 at different scan rates of (a) 0.005 V s^{-1}, (b) 0.01 V s^{-1}, (c) 0.025 V s^{-1}, (d) 0.05 V s^{-1}, (e) 0.1 V s^{-1}, and (f) 0.2 V s^{-1}, with the highlighted Tafel analysis region in red. Insets are the corresponding Tafel plots.

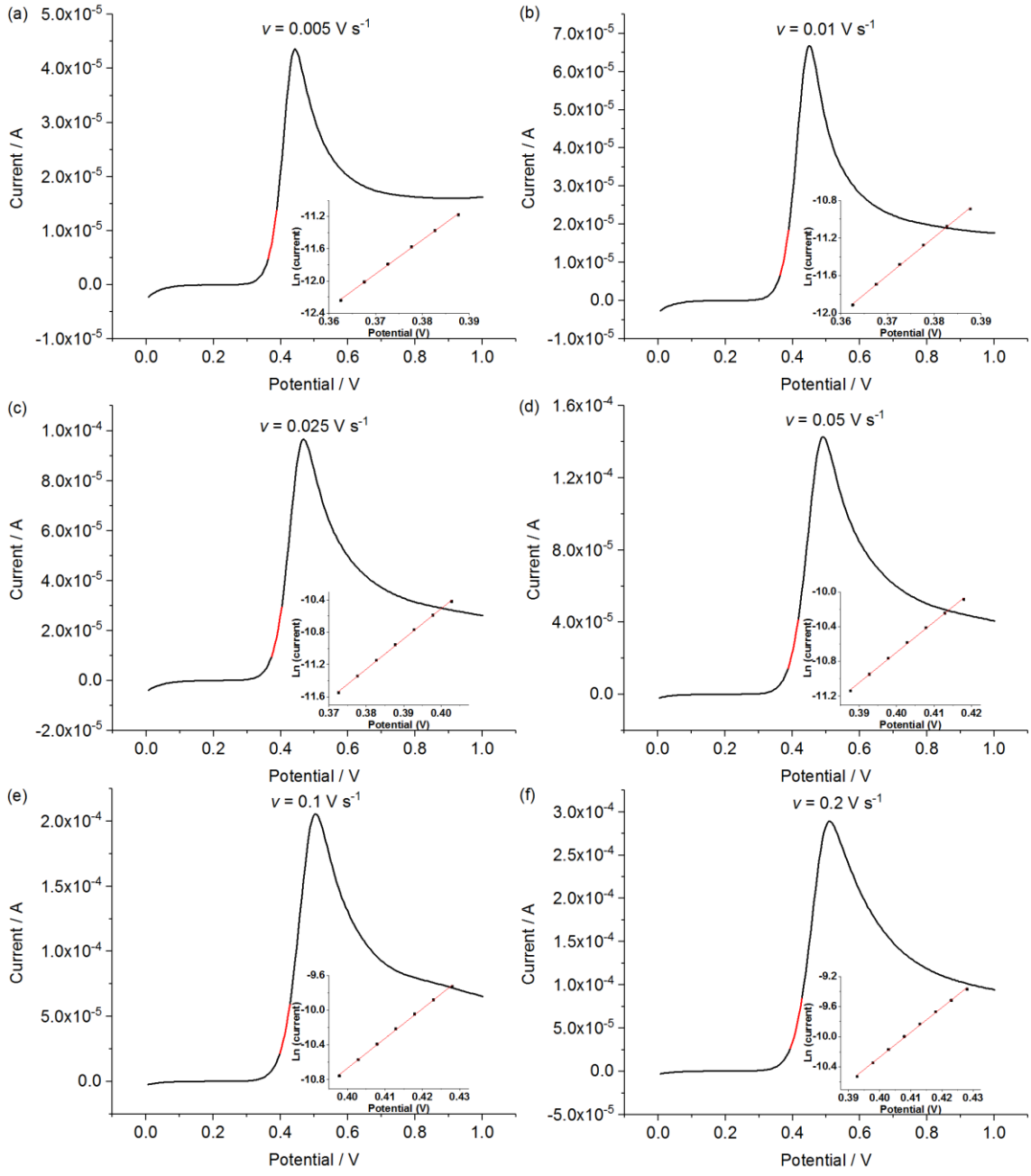


Figure 3.14 The forward CV of Au (150) modified BDD in 0.10 M H_2SO_4 containing 1.0 mM Na_2SO_3 at different scan rates of (a) 0.005 V s^{-1}, (b) 0.01 V s^{-1}, (c) 0.025 V s^{-1}, (d) 0.05 V s^{-1}, (e) 0.1 V s^{-1}, and (f) 0.2 V s^{-1}, with the highlighted Tafel analysis region in red. Insets are the corresponding Tafel plots.

Table 3.7 The calculated anodic transfer coefficient for Au (0) modified BDD

Scan rate (V s^{-1})	Tafel slope	β	β (average)
0.005	35.8	0.92	0.84 ± 0.052
0.01	33.9	0.87	
0.025	33.1	0.85	
0.05	31.2	0.80	
0.1	30.8	0.79	
0.2	30.8	0.79	

Table 3.8 The calculated anodic transfer coefficient for Au (10) modified BDD

Scan rate (V s^{-1})	Tafel slope	β	β (average)
0.005	38.6	0.99	0.91 ± 0.055
0.01	37.5	0.96	
0.025	35.4	0.91	
0.05	35.2	0.90	
0.1	33.6	0.86	
0.2	33.0	0.85	

Table 3.9 The calculated anodic transfer coefficient for Au (50) modified BDD

Scan rate (V s^{-1})	Tafel slope	β	β (average)
0.005	38.6	0.99	0.91 ± 0.054
0.01	36.6	0.94	
0.025	35.6	0.91	
0.05	34.7	0.89	
0.1	33.7	0.86	
0.2	32.8	0.84	

Table 3.10 The calculated anodic transfer coefficient for Au (150) modified BDD

Scan rate (V s^{-1})	Tafel slope	β	β (average)
0.005	42.3	1.09	0.95 ± 0.097
0.01	40.7	1.05	
0.025	37.4	0.96	
0.05	34.9	0.90	
0.1	34.1	0.88	
0.2	32.9	0.85	

Table 3.11 Transfer coefficient values of sulphite oxidation for gold particle modified electrodes

	Au (0)	Au (10)	Au (50)	Au (150)
Anodic transfer coefficient	0.84 ± 0.052	0.91 ± 0.055	0.91 ± 0.054	0.95 ± 0.10

As noted above for the Au (150) modified electrode and its electrochemical response, and with the recognition that it behaves as a gold macroelectrode, a sulphite concentration study was made. Different concentrations of sulphite were chosen for Au (150) particle modified BDD at 10, 20, 200 μM, 1.0 mM, and 2.0 mM at a fixed scan rate of 0.05 V s^{-1} as shown in Figure 3.15. At high concentrations of 1.0 mM and 2.0 mM, there is only a forward oxidation peak without back peaks. A very tiny reversal peak rises with sulphite being a moderate concentration of 200 μM. On decreasing the concentration to 20 and 10 μM, there are obvious backward peaks at 0.38 V, indicating that the presence of back peaks is relevant to the sulphite concentration. As mentioned before that EC_2 scheme has a dependence on the bulk concentration of analyte, these results using gold particle modified electrodes show a similar electrochemical oxidation behaviour to that on the gold macroelectrode, further providing evidence for the EC_2 hypothesis. Furthermore, Figure 3.15(f) shows that the anodic peak currents increase linearly with the concentration of sulphite with the slope value of 1.4×10^{-4} A mol^{-1} m^3, with which the electrochemically reversible Randles-Sevcik equation was applied at a scan rate of 0.05 V s^{-1} for achieving the diffusion coefficient value of sulphite of 3.8×10^{-9} m^2 s^{-1}. This is also consistent with the above values via the linear dependence of peak current versus square root of scan rate on both gold macroelectrode and BDD decorated by Au (150) at 1.0 mM sulphite.

Next the simulation was carried out again to examine the above model across the concentration range. The fitting parameters were as follows: E^0 = 0.44 V, α = 0.5, k_s = 0.007 cm s^{-1}, $K_{eq} = 1\times10^6$, $k_f = 1\times10^4$ M^{-1} s^{-1}, $D_A = D_B = D_C = 4\times10^{-9}$ m^2 s^{-1}, v = 0.05 V s^{-1}, the geometric area $A = 3.7\times10^{-5}$ m^2 of the substrate electrode as approximated for planar diffusion. The kinetic parameters for the second order chemical step are the same as those used for the gold macroelectrode while the kinetics of the electrochemical step are close to those seen on the macro-gold substrates. The simulation fits well across the full range of

concentrations differing by more than two orders of magnitude regarding the voltammetric shapes with peak currents and potentials in the Figure 3.16. Note that the region below 0.2 V may additionally reflect double-layer charging capacitance behaviour since large gold particles are decorated onto the BDD substrate likely overcoming its own low background capacitance and there is still such reduction current in the CV scan without sulphite as shown in the Figure 3.17.

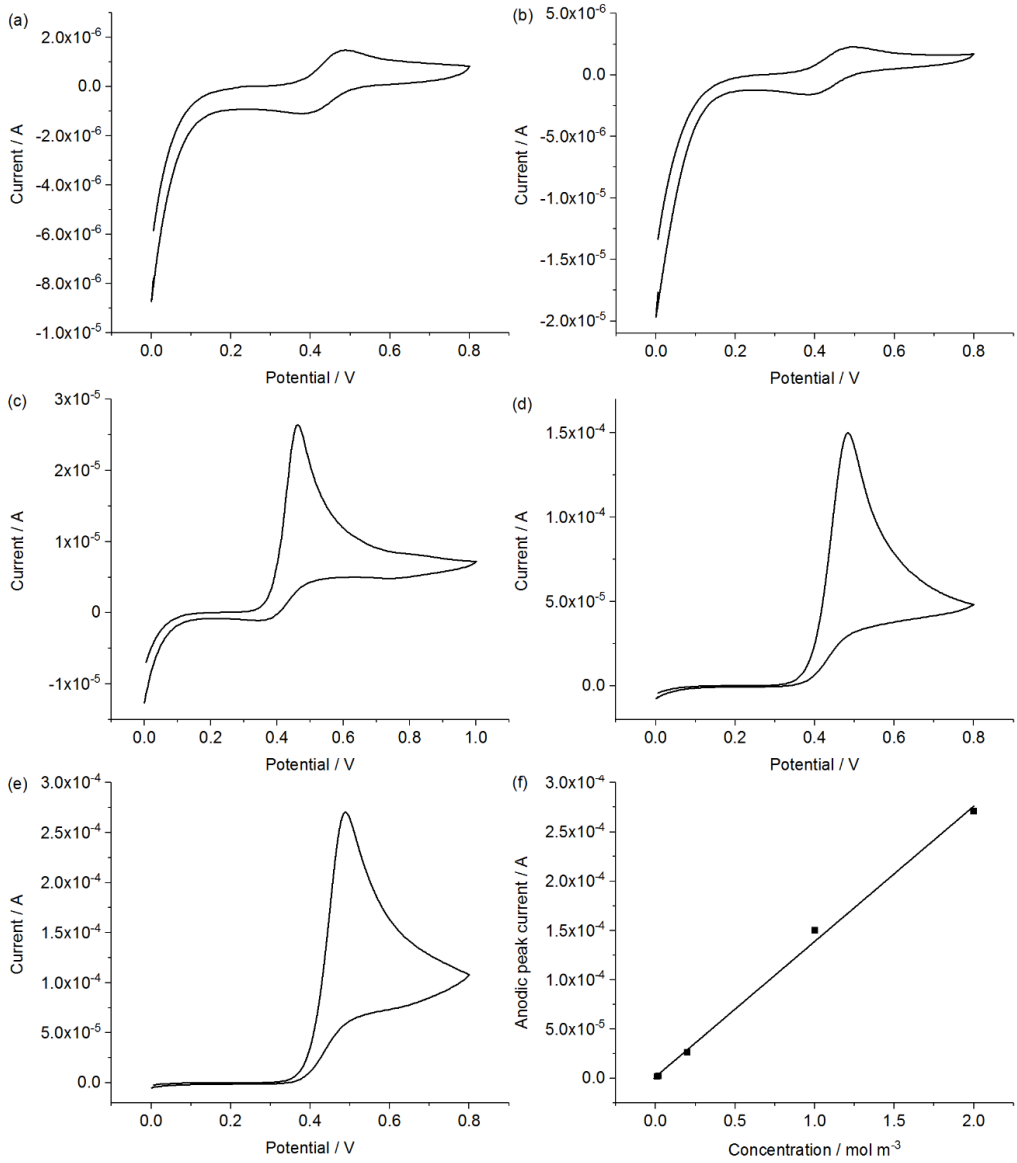


Figure 3.15 CV of sulphite at different concentrations of (a) 10 µM, (b) 20 µM, (c) 200 µM, (d) 1.0 mM, and (e) 2.0 mM at the Au (150)-BDD electrode at 0.05 V s^{-1}. (f) Plot of anodic peak currents versus the concentration of sulphite.

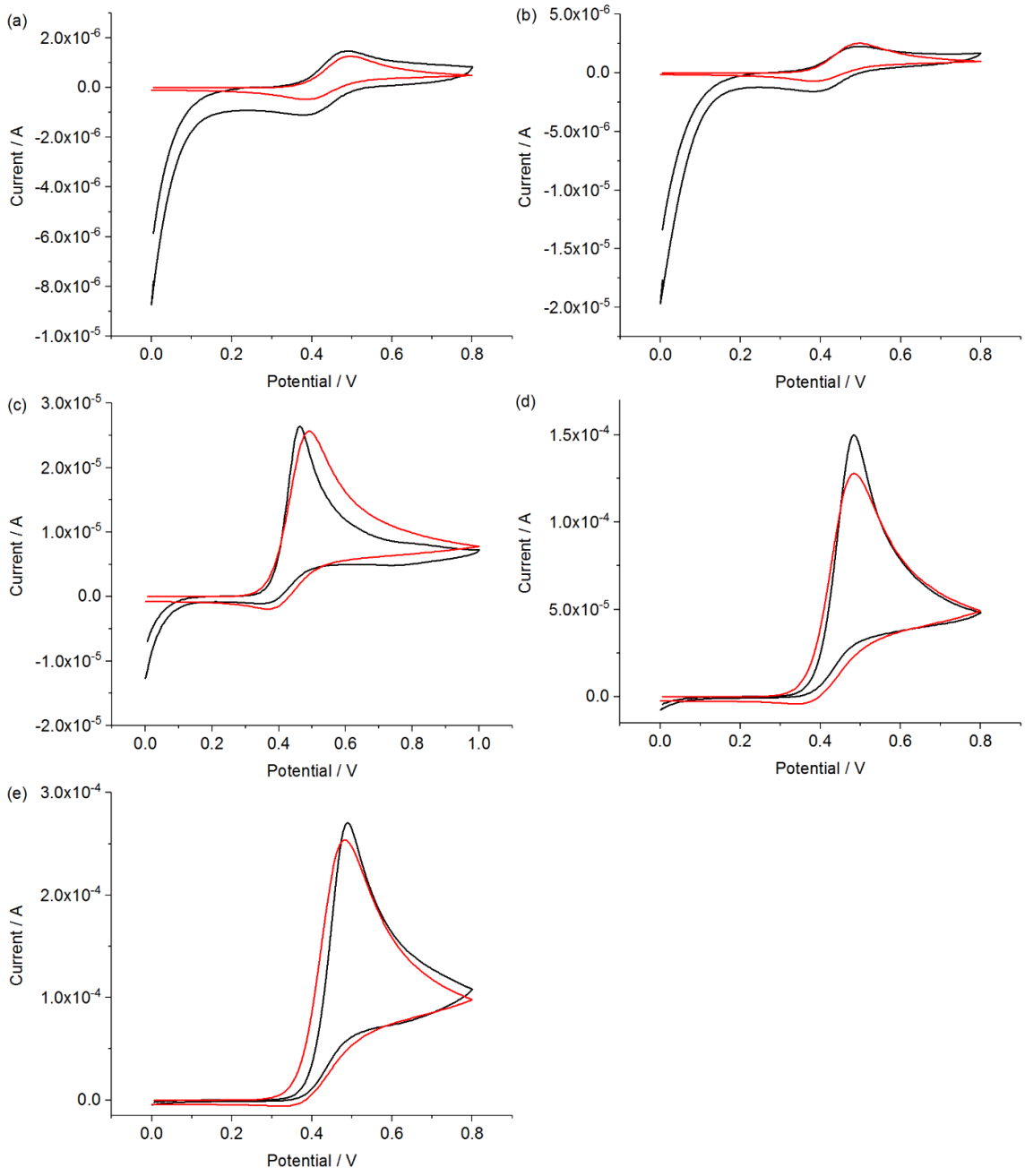


Figure 3.16 CV from experiment (black) and simulation (red) at different sulphite concentrations of (a) 10 µM, (b) 20 µM, (c) 200 µM, (d) 1.0 mM, and (e) 2.0 mM at the Au (150)-BDD electrode at a scan rate of 0.05 V s^{-1}.

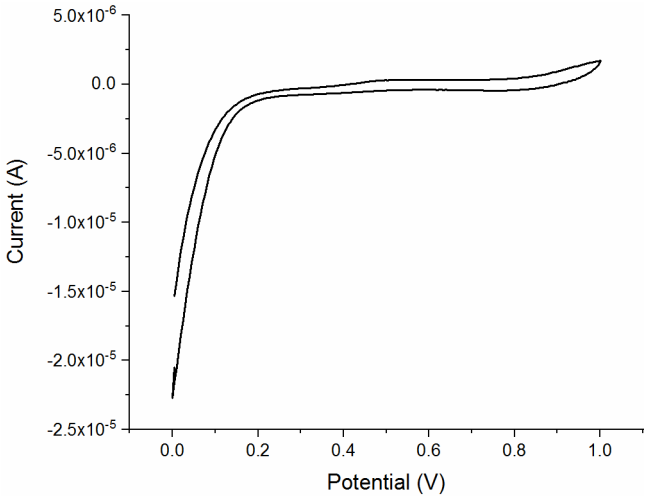


Figure 3.17 CV at the Au (150)-BDD electrode in 0.10 M H_2SO_4 without sulphite at 0.05 V s^{-1}.

The transport characteristics of the electrode were investigated with voltammetry at different scan rates. Two extremes are considered; one is at a high concentration of 2.0 mM and the other is at a low concentration of 10 µM. Figure 3.18 displays CV data of the sulphite redox process varying scan rates of 0.005 - 0.05 V s^{-1}. At 10 µM, reverse peaks show at 0.38 V while no such peaks are seen at 2.0 mM, indicating that an enhanced concentration promotes the follow-up second order chemical kinetics and therefore, the loss of the reverse peak within the EC_2 scheme. Besides, not only the anodic but also cathodic peak currents have a linear fitting as a function of square root of scan rate in 10 µM sulphite in Figure 3.18(b), suggesting the sulphite redox process is diffusion limited. So does the anodic process in the high concentration of 2.0 mM sulphite.

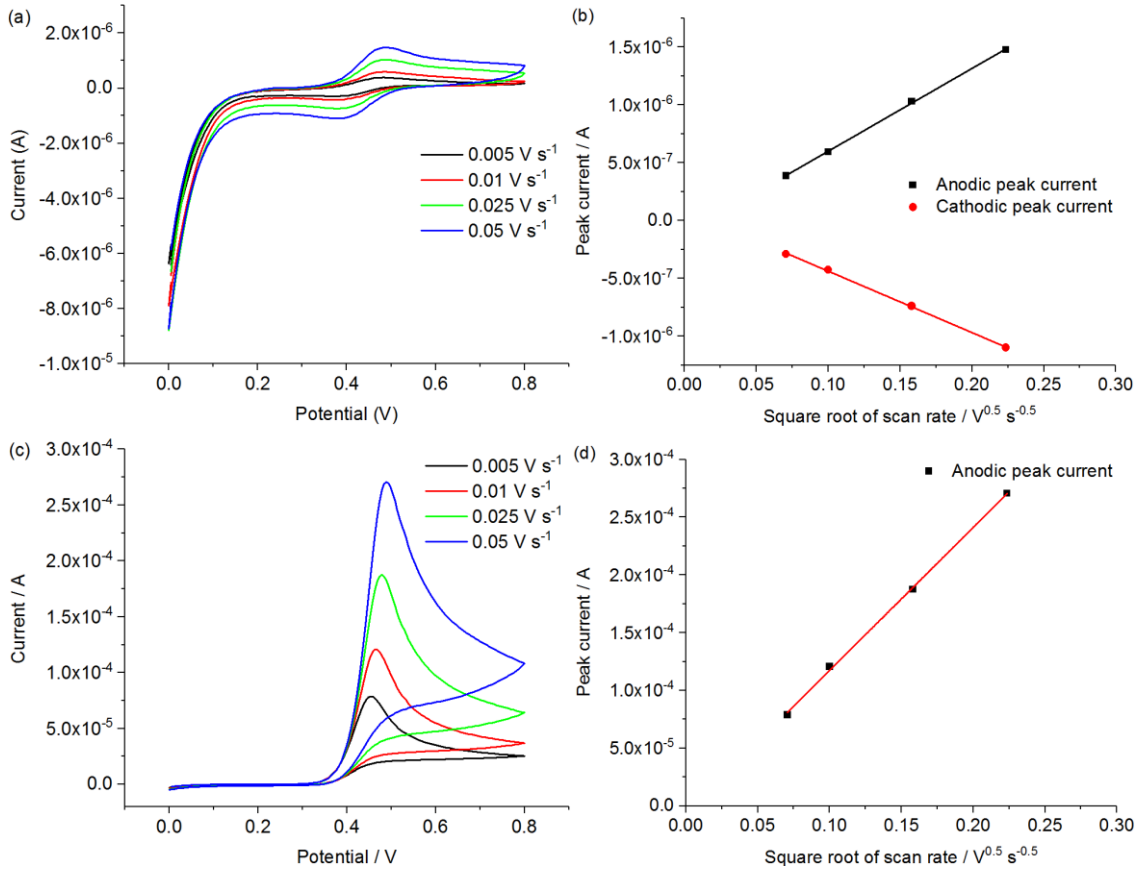


Figure 3.18 CV of sulphite in the concentrations of (a) 10 µM, and (c) 2.0 mM at different scan rates of 0.005-0.05 V s^{-1} at Au (150)-BDD electrode. Plot of anodic and cathodic peak currents versus the square root of scan rate in (b) 10 µM, and (d) 2.0 mM sulphite.

The EC_2 model was employed again for simulation using the same parameters as for the Au (150) modified BDD. Data obtained at scan rates ranging from 0.005 to 0.05 V s^{-1} were fitted. Figure 3.19 shows the overlaid experimental and simulated voltammograms for two extreme concentrations of 10 µM and 2.0 mM sulphite. The fitting is good in the peak potential and current across both concentrates and scan rates. The reasonable fitting (particularly for the oxidation process) over these wide ranges matches the general trend in the experimental CVs, and supports the indication of a one-electron oxidation process with a follow-up dimerization reaction (EC_2 mechanism).

Note that the improved data in terms of signal to noise between the gold macroelectrode and the Au particle decorated BDD reflects the lower capacitance of the latter. This diffusional response relating to gold macroelectrodes can be attained for the heavily decorated BDD electrodes but with a reduced capacitance facilitating modelling which is challenging on the macroelectrode.

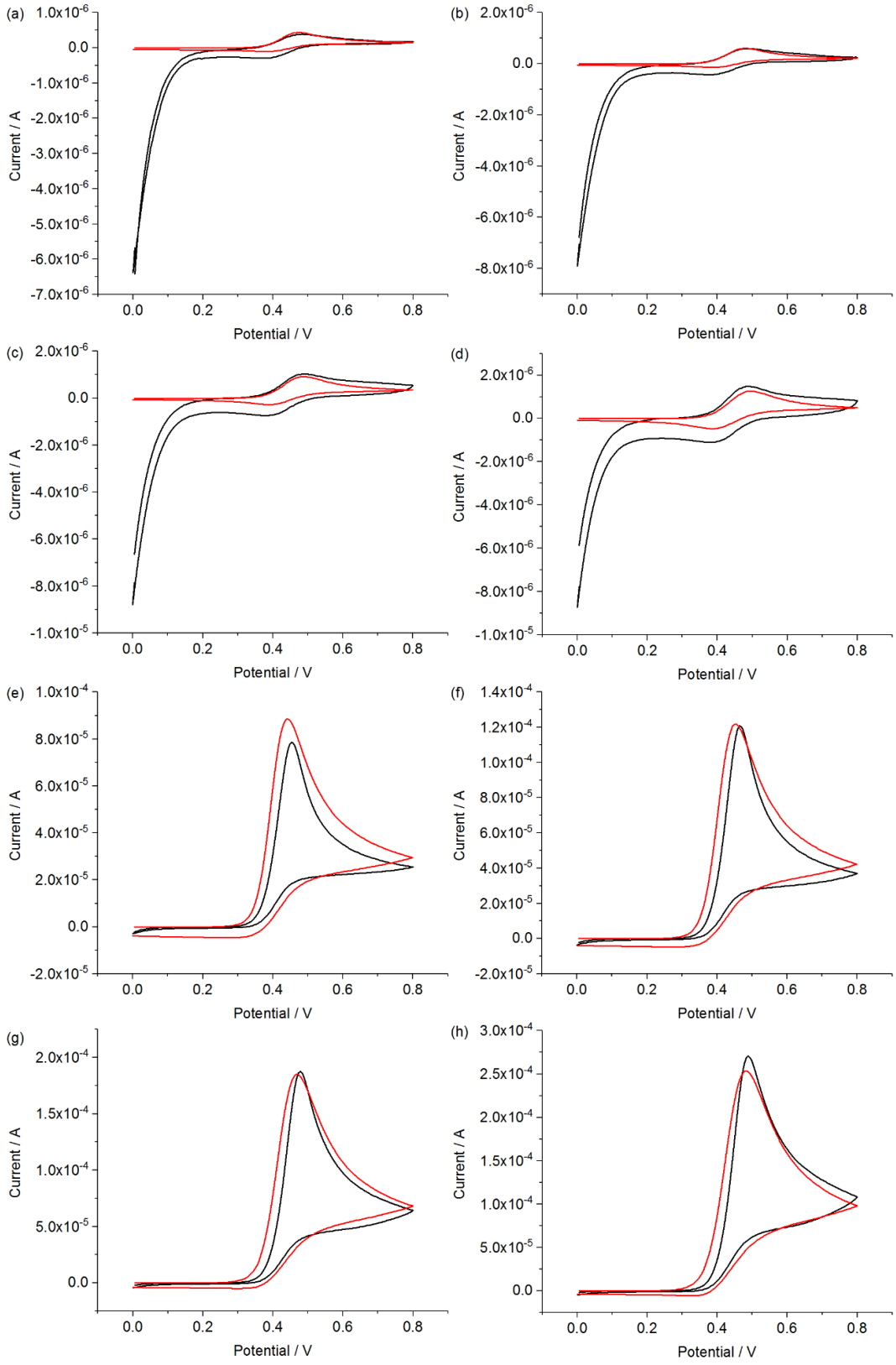


Figure 3.19 The comparison of experimental (black) and simulated (red) voltammograms for the oxidation of (a-d) 10 µM, and (e-h) 2.0 mM sulphite at scan rates of (a, e) 0.005 V s^{-1}, (b, f) 0.01 V s^{-1}, (c, g) 0.025 V s^{-1}, and (d, h) 0.05 V s^{-1} at the Au (150)-BDD electrode.

3.4 Conclusions

The main finding of this chapter is shown via a scheme in Figure 3.20 in a visual format. To summarise, the electro-oxidation of sulphite has been investigated in sulphuric acid solution on Au macroelectrode and particles modified BDDs. Electrodeposition of gold particles was realized via a nucleation-growth pulse strategy. The approach enables the fabrication of gold of various sizes from nanometer to submicron-scale, and different morphologies of quasi-spherical and star-shape, with varying surface coverages. The sulphite oxidation proceeds via a one-electron transfer process followed by a second order chemical reaction, EC_2 mechanism, which was supported by the interpretation of the experiment and digital simulation for both macroscopic gold electrode and the as-prepared gold particle modified BDDs. We confirm that the AuNPs deposited electrode is a good alternative for the Au macroelectrode for sulphite oxidation. The knowledge of the electro-oxidation mechanism of sulphite in acid media is of significance for various applications when using electrochemical methods to monitor sulphite wherever present such as in the food industry.

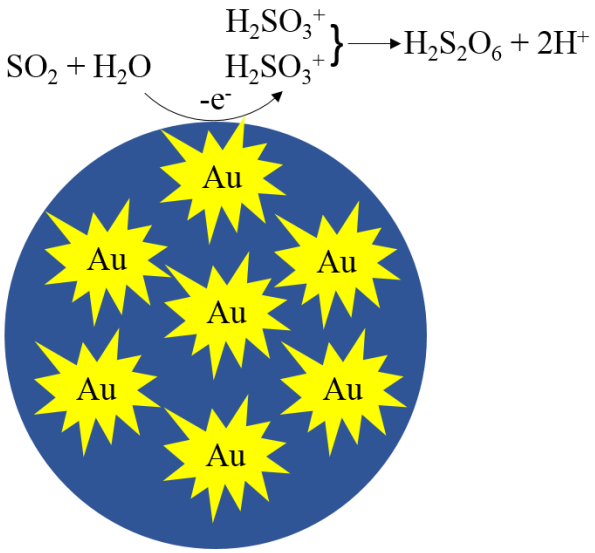


Figure 3.20 A scheme of the EC_2 mechanism

References

1. Cai, X.; Lin, C.; Foord, J. S.; Compton, R. G., The Electrochemical Oxidation of Sulphite on Gold Electrodes. *Electroanal* **2019,** *31* (9), 1783-1796.

2. Winiarski, J. P.; de Barros, M. R.; Magosso, H. A.; Jost, C. L., Electrochemical reduction of sulfite based on gold nanoparticles/silsesquioxane-modified electrode. *Electrochim Acta* **2017,** *251*, 522-531.

3. Satienperakul, S.; Phongdong, P.; Liawruangrath, S., Pervaporation flow injection analysis for the determination of sulphite in food samples utilising potassium permanganate-rhodamine B chemiluminescence detection. *Food Chem* **2010,** *121* (3), 893-898.

4. Garcia, T.; Casero, E.; Lorenzo, E.; Pariente, F., Electrochemical sensor for sulfite determination based on iron hexacyanoferrate film modified electrodes. *Sensor Actuat B-Chem* **2005,** *106* (2), 803-809.

5. Manikandan, V. S.; Adhikari, B.; Chen, A. C., Nanomaterial based electrochemical sensors for the safety and quality control of food and beverages. *Analyst* **2018,** *143* (19), 4537-4554.

6. Glasstone, S.; Hickling, A., Studies in electrolytic oxidation. Part III. The formation of dithionate by the electrolytic oxidation of potassium sulphite. *Journal of the Chemical Society* **1933,** (0), 829-836.

7. Rozenthal, K. I.; Veselovsky, V. I., *Zh. Fiz. Khim.* **1953,** *27*, 1163.

8. Quijada, C.; Rodes, A.; Vazquez, J. L.; Perez, J. M.; Aldaz, A., Electrochemical Behaviour of Aqueous SO_2 at Pt Electrodes in Acidic Medium - a Voltammetric and in-Situ Fourier Transform IR Study .1. Oxidation of SO_2 on Pt Electrodes with Sulphur-Oxygen Adsorbed Species. *J Electroanal Chem* **1995,** *394* (1-2), 217-227.

9. Quijada, C.; Rodes, A.; Vazquez, J. L.; Perez, J. M.; Aldaz, A., Electrochemical Behaviour of Aqueous Sulphur Dioxide at Polycrystalline Pt Electrodes in Acidic Medium - a Voltammetric and in-Situ FT-IR Study .2. Promoted Oxidation of Sulphur Dioxide - Reduction of Sulphur Dioxide. *J Electroanal Chem* **1995,** *398* (1-2), 105-115.

10. Quijada, C.; Vazquez, J. L.; Aldaz, A., Study of sulphur adlayers on polyoriented platinum electrodes: Influence on the electrocatalysis of the SO_2 oxidation reaction. *J Electroanal Chem* **1996,** *414* (2), 229-233.

11. O'Brien, J. A.; Hinkley, J. T.; Donne, S. W., The Electrochemical Oxidation of Aqueous Sulfur Dioxide I. Experimental Parameter Influences on Electrode Behavior. *J Electrochem Soc* **2010,** *157* (9), F111-F115.

12. Seo, E. T.; Sawyer, D. T., Electrochemical oxidation of dissolved sulphur dioxide at platinum and gold electrodes. *Electrochim Acta* **1965,** *10* (3), 239-252.

13. Samec, Z.; Weber, J., Study of the oxidation of SO_2 dissolved in 0.5 M H_2SO_4 on a gold electrode—I stationary electrode. *Electrochim Acta* **1975,** *20* (6), 403-412.

14. Varga, K.; Baradlai, P.; Vertes, A., In-situ radiotracer studies of sorption processes in solutions containing (bi)sulfite ions .1. Polycrystalline gold. *Electrochim Acta* **1997,** *42* (7), 1143-1155.

15. Quijada, C.; Morallon, E.; Vazquez, J. L.; Berlouis, L. E. A., Electrochemical behaviour of aqueous SO_2 at polycrystalline gold electrodes in acidic media. A voltammetric and in-situ vibrational study. Part II. Oxidation of SO_2 on bare and sulphur-modified electrodes. *Electrochim Acta* **2000,** *46* (5), 651-659.

16. Tolmachev, Y. V.; Scherson, D. A., The electrochemical oxidation of sulfite on gold: UV-Vis reflectance spectroscopy at a rotating disk electrode. *Electrochim Acta* **2004,** *49* (8), 1315-1319.

17. O'Brien, J. A.; Hinkley, J. T.; Donne, S. W., Electrochemical Oxidation of Aqueous Sulfur Dioxide II. Comparative Studies on Platinum and Gold Electrodes. *J Electrochem Soc* **2012,** *159* (9), F585-F593.

18. Streeter, I.; Wain, A. J.; Davis, J.; Compton, R. G., Cathodic reduction of bisulfite and sulfur dioxide in aqueous solutions on copper electrodes: An electrochemical ESR study. *J Phys Chem B* **2005,** *109* (39), 18500-18506.

19. Dribinskii, A. V.; Tarasevich, M. R.; Kazarinov, V. E., Electrocatalysis on Carbon Materials. *Mater Chem Phys* **1989,** *22* (3-4), 377-400.

20. Urisson, N. A.; Schteinberg, G. V.; Tarasevich, M. R.; Bagotsky, V. S.; Zagudaeva, N. M., Electrochemical oxidation of sulfur dioxide on activated carbon. *Electrokhimiya* **1983,** *19*, 275-281.

21. Hunger, T.; Lapicque, F.; Storck, A., Electrochemical oxidation of sulphite ions at graphite electrodes. *J Appl Electrochem* **1991,** *21* (7), 588-596.

22. Hunger, T.; Lapicque, F., Electrochemistry of the Oxidation of Sulfite and Bisulfite Ions at a Graphite Surface - an Overall Approach. *Electrochim Acta* **1991,** *36* (5-6), 1073-1082.

23. Lu, J.; Dreisinger, D. B.; Cooper, W. C., Anodic oxidation of sulphite ions on graphite anodes in alkaline solution. *J Appl Electrochem* **1999,** *29* (10), 1161-1170.

24. Quijada, C.; Vazquez, J. L., Electrochemical reactivity of aqueous SO_2 on glassy carbon electrodes in acidic media. *Electrochim Acta* **2005,** *50* (27), 5449-5457.

25. Mu, C.; Hou, M.; Xiao, Y.; Zhang, H. J.; Hong, S. J.; Shao, Z. G., Electrochemical Oxidation of Sulfur Dioxide on Nitrogen-Doped Graphite in Acidic Media. *Electrochim Acta* **2015,** *171*, 29-34.

26. Brevett, C. A. S.; Johnson, D. C., Anodic Oxidations of Sulfite, Thiosulfate, and Dithionite at Doped PbO_2-Film Electrodes. *J Electrochem Soc* **1992,** *139* (5), 1314-1319.

27. Scott, K.; Taama, W. M., An investigation of anode materials in the anodic oxidation of sulphur dioxide in sulphuric acid solutions. *Electrochim Acta* **1999,** *44* (19), 3421-3427.

28. Lu, P. W. T.; Ammon, R. L., An Investigation of Electrode Materials for the Anodic-Oxidation of Sulfur-Dioxide in Concentrated Sulfuric-Acid. *J Electrochem Soc* **1980,** *127* (12), 2610-2616.

29. Quijada, C.; Vazquez, J. L., Electrochemical reactivity of aqueous sulphur dioxide at polycrystalline noble metal electrodes in acidic media. *Recent Res. Dev. Electrochem.* **2000,** *3* (Pt. 1), 137-181.

30. Chu, S. Z.; Kawamura, H.; Mori, M., Fabrication and characteristics of Pd nanoparticles/nanofilms on ceramics toward catalytic electrodes. *Electrochim Acta* **2007,** *53* (1), 92-99.

31. Toghill, K. E.; Compton, R. G., Metal Nanoparticle Modified Boron Doped Diamond Electrodes for Use in Electroanalysis. *Electroanal* **2010,** *22* (17-18), 1947-1956.

32. Yang, N. J.; Yu, S. Y.; Macpherson, J. V.; Einaga, Y.; Zhao, H. Y.; Zhao, G. H.; Swain, G. M.; Jiang, X., Conductive diamond: synthesis, properties, and electrochemical applications. *Chem Soc Rev* **2019,** *48* (1), 157-204.

33. Muzyka, K.; Sun, J. R.; Fereja, T. H.; Lan, Y. X.; Zhang, W.; Xu, G. B., Boron-doped diamond: current progress and challenges in view of electroanalytical applications. *Anal Methods* **2019,** *11* (4), 397-414.

34. Cobb, S. J.; Ayres, Z. J.; Macpherson, J. V., Boron Doped Diamond: A Designer Electrode Material for the Twenty-First Century. *Annual Review of Analytical Chemistry* **2018,** *11*, 463-484.

35. Campbell, F. W.; Compton, R. G., The use of nanoparticles in electroanalysis: an updated review. *Anal Bioanal Chem* **2010,** *396* (1), 241-259.

36. Welch, C. M.; Compton, R. G., The use of nanoparticles in electroanalysis: a review. *Anal Bioanal Chem* **2006,** *384* (3), 601-619.

37. Raj, C. R.; Okajima, T.; Ohsaka, T., Gold nanoparticle arrays for the voltammetric sensing of dopamine. *J Electroanal Chem* **2003,** *543* (2), 127-133.

38. Katz, E.; Willner, I.; Wang, J., Electroanalytical and bioelectroanalytical systems based on metal and semiconductor nanoparticles. *Electroanal* **2004,** *16* (1-2), 19-44.

39. Kizling, M.; Dzwonek, M.; Wieckowska, A.; Bilewicz, R., Gold nanoparticles in bioelectrocatalysis - The role of nanoparticle size. *Curr Opin Electroche* **2018,** *12*, 113-120.

40. Peng, Y. Y.; Guo, D.; Ma, W.; Long, Y. T., Intrinsic Electrocatalytic Activity of Gold Nanoparticles Measured by Single Entity Electrochemistry. *ChemElectroChem* **2018,** *5* (20), 2982-2985.

41. Jiang, J. J.; Fan, W. J.; Du, X. Z., Nitrite electrochemical biosensing based on coupled graphene and gold nanoparticles. *Biosens Bioelectron* **2014,** *51*, 343-348.

42. Siddiqi, M. A.; Krissmann, J.; PetersGerth, P.; Luckas, M.; Lucas, K., Spectrophotometric measurement of the vapour-liquid equilibria of (sulphur dioxide plus water). *J Chem Thermodyn* **1996,** *28* (7), 685-700.

43. O'Brien, J. A.; Hinkley, J. T.; Donne, S. W.; Lindquist, S. E., The electrochemical oxidation of aqueous sulfur dioxide: A critical review of work with respect to the hybrid sulfur cycle. *Electrochim Acta* **2010,** *55* (3), 573-591.

44. Iwasaki, C.; Ohsaka, T.; Kitamura, F., The pH Dependence of the Oxidation Reaction of SO_2 at a Platinum Electrode Studied by Voltammetric and In Situ Infrared Spectroscopic Measurements. *ECS Transactions* **2009,** *25* (1), 671-679.

45. Zelinsky, A. G.; Pirogov, B. Y., Electrochemical oxidation of sulfite and sulfur dioxide at a renewable graphite electrode. *Electrochim Acta* **2017,** *231*, 371-378.

46. Wiesener, K., The Electrochemical Oxidation of Sulphur Dioxide at Porous Catalyzed Carbon Electrodes in Sulphuric Acid. *Electrochim Acta* **1973,** *18* (2), 185-189.

47. Lyke, S. E.; Langer, S. H., Oxidation of Sulfur Dioxide in Sulfur-Modified Platinum-Graphite Packed Bed Electrodes. *J Electrochem Soc* **1991,** *138* (6), 1682-1687.

48. Tarasevich, M. R.; Dribinskii, A. V.; Shmakov, S. A.; Rylov, V. A., Electrochemical reactions of sulfur dioxide at carbon materials and disperse gold. *Soviet Electrochemistry* **1986,** *22* (7), 911-915.

49. Cai, X. S.; Tanner, E. E. L.; Lin, C. H.; Ngamchuea, K.; Foord, J. S.; Compton, R. G., The mechanism of electrochemical reduction of hydrogen peroxide on silver nanoparticles. *Phys Chem Chem Phys* **2018,** *20* (3), 1608-1614.

50. Izquierdo, J.; Mizaikoff, B.; Kranz, C., Surface-enhanced infrared spectroscopy on boron-doped diamond modified with gold nanoparticles for spectroelectrochemical analysis. *Phys Status Solidi A* **2016,** *213* (8), 2056-2062.

51. Bottari, F.; De Wael, K., Electrodeposition of gold nanoparticles on boron doped diamond electrodes for the enhanced reduction of small organic molecules. *J Electroanal Chem* **2017,** *801*, 521-526.

52. Rudolph, M.; Reddy, D. P.; Feldberg, S. W., A Simulator for Cyclic Voltammetric Responses. *Anal Chem* **1994,** *66* (10), A589-A600.

53. Li, D. L.; Lin, C. H.; Batchelor-McAuley, C.; Chen, L. F.; Compton, R. G., Tafel analysis in practice. *J Electroanal Chem* **2018,** *826*, 117-124.

54. Albery, W. J., *Electrode kinetics*. Clarendon Press: Oxford, 1975.

55. Compton, R. G.; Banks, C. E., *Understanding voltammetry*. Third ed.; World Scientific Publishing: London, 2018.

56. Pletcher, D.; Greff, R.; Peat, R.; Peter, L. M.; Robinson, J., *Instrumental Methods in Electrochemistry*. Woodhead Publishing Limited: Cambridge, 2011.

57. Testa, A. C.; Reinmuth, W. H., Stepwise Reactions in Chronopotentiometry. *Anal Chem* **1961,** *33* (10), 1320-1324.

58. Kang, C.; Lee, J.; Silvester, D. S., Electroreduction of 2,4,6-Trinitrotoluene in Room Temperature Ionic Liquids: Evidence of an EC2 Mechanism. *J Phys Chem C* **2016,** *120* (20), 10997-11005.

59. Ward, K. R.; Lawrence, N. S.; Hartshorne, R. S.; Compton, R. G., Cyclic Voltammetry of the EC' Mechanism at Hemispherical Particles and Their Arrays: The Split Wave. *J Phys Chem C* **2011,** *115* (22), 11204-11215.

60. Appleby, A. J.; Pichon, B., The Mechanism of the Electrochemical Oxidation of Sulfur Dioxide in Sulfuric Acid Solutions. *J Electroanal Chem* **1979,** *95* (1), 59-71.

61. Korzeniewski, C.; McKenna, W.; Pons, S., An in situ infrared study of the oxidation of sulfur dioxide on platinum electrodes. *Journal of Electroanalytical Chemistry and Interfacial Electrochemistry* **1987,** *235* (1), 361-368.

62. Schmidt, M.; Siebert, W., Sulphur. In *Comprehensive inorganic chemistry*, First ed.; Bailar, J. C.; Emeléus, H. J.; Nyholm, R.; Trotman-Dickenson, A. F., Eds. Pergamon Press: Oxford, 1973; Vol. 2.

63. Batchelor-McAuley, C.; Katelhon, E.; Barnes, E. O.; Compton, R. G.; Laborda, E.; Molina, A., Recent Advances in Voltammetry. *Chemistryopen* **2015,** *4* (3), 224-260.

64. Lin, C.; Compton, R. G., Understanding mass transport influenced electrocatalysis at the nanoscale via numerical simulation. *Curr Opin Electroche* **2019,** *14*, 186-199.

65. Davies, T. J.; Ward-Jones, S.; Banks, C. E.; del Campo, J.; Mas, R.; Munoz, F. X.; Compton, R. G., The cyclic and linear sweep voltammetry of regular arrays of microdisc electrodes: Fitting of experimental data. *J Electroanal Chem* **2005,** *585* (1), 51-62.

66. Davies, T. J.; Compton, R. G., The cyclic and linear sweep voltammetry of regular and random arrays of microdisc electrodes: Theory. *J Electroanal Chem* **2005,** *585* (1), 63-82.

67. Wilson, N. R.; Clewes, S. L.; Newton, M. E.; Unwin, P. R.; Macpherson, J. V., Impact of grain-dependent boron uptake on the electrochemical and electrical properties of polycrystalline boron doped diamond electrodes. *J Phys Chem B* **2006,** *110* (11), 5639-5646.

68. Streeter, I.; Jenkinson, S. F.; Fleet, G. W. J.; Compton, R. G., Chemical instability promotes apparent electrochemical irreversibility: Studies on the electrode kinetics of the one electron reduction of the 2,6-diphenylpyrylium cation in acetonitrile solution. *J Electroanal Chem* **2007,** *600* (2), 285-293.

Chapter 4 Electrodeposition of gold nanoparticles for nitrite detection

Gold particles are deposited on boron doped diamond electrodes by using two electrochemical techniques including cyclic voltammetry (CV), and potentiostatic double pulse. For each electrodeposition method, the resulting gold particle modified electrodes are characterised by CV and SEM. For CV deposition different deposits are obtained during the electro-reduction step, showing a dependence on the number of cyclic potential scan, while pulse deposition can control the morphology from quasi-sphere to "star-shape" via the second pulse growth time. The modified electrodes are used for nitrite detection using CV, differential pulse voltammetry, and amperometry. Au particles prepared by pulse deposition present better amperometric response towards nitrite while involving the lower charge amount consumed in the electro-reduction step. This analytical performance is correlated to high coverage of gold particles with more homogeneous distribution on electrodes, displaying high effective electroactive surface area. In the optimal conditions using growth pulse time of 150 s, the submicron array exhibits a sensitivity of 5.50×10^{-2} $\mu A\ \mu M^{-1}$ with a limit of detection of 0.48 μM.

4.1 Introduction

Nitrite (NO_2^-) has been extensively used in the food industry as a significant preservative and colour former especially for meat product processing.[1, 2] In the research community, 838 journal articles associated with nitrite and nitrate analysis in food were published between 2008 and 2018.[2] Nevertheless, the potential toxicity of nitrite may threaten human health such as gastric and esophageal cancer when a high level exposure is presented in physiological systems.[3] Many countries and organisations have made strict regulations to control the use and dosage of nitrite. For instance, the acceptable daily nitrite intake is

recommended to be 0.06 mg kg^{-1} of body weight by European Union Scientific Committee for Food, while the USA Environmental Protection Agency sets the upper limit of contaminant level to be 1 ppm.[3] Thus nitrite trace detection and quantification is a significant research area, which attracts many researchers to develop the corresponding analytical systems.

Moorcroft *et al.* reviewed the numerous works on various techniques in the literature for detection and determination of nitrite,[4] and recently updated reviews have been presented by Wang *et al.* and by Singh *et al.* in 2017 and 2019, respectively.[5, 6] Spectrophotometric methods are the most popular technique due to their low cost and simplicity, but Griess Assay based spectrophotometry in particularly suffers from poor sensitivity and ionic interferences.[5] Chemiluminescent and chromatographic techniques provide excellent performance. However, the complexity of instrumentation is required for effective implementation.[4]

Comparatively, an electrochemical detection method is a promising alternative, and has become more appealing due to its low-cost, easy operation and miniaturisation, high sensitivity, and low limit of detection.[4, 7] So far, many working electrode materials have been used including glassy carbon and boron doped diamond (BDD) for nitrite detection. However, the slow electron transfer kinetics limit their usages,[1] and a high overpotential at bare electrodes is required for direct electro-oxidation of nitrite.[8] In order to improve the analytical performances, an alternative strategy is to chemically modify electrode surface with electrocatalysts.[9]

Interests have focused on the development of nanoscale materials, including carbon nanomaterial[1] (such as graphene,[3] carbon nanotubes,[10] and carbon nanofibers[11]), and particularly metallic nanoparticles due to their attractive physicochemical properties

including enhanced diffusion of species, improved catalytic property, and larger effective surface area, contributing to a higher signal-to-background ratio.[12] These excellent properties combined to the electrocatalytic oxidation activity of gold for nitrite favour the establishment of modified electrode by gold nanoparticles (AuNPs).[13, 14] Although AuNPs can be directly deposited by means of electrochemical techniques, very few studies have been reported on the effect with respect to nitrite determination. It is well-known that the control of the electrodeposition conditions is of great significance, and in order to investigate this aspect further, the effect of the electrodeposition methods on the electroanalytical performances of Au-BDD electrodes for oxidation of nitrite needs to be considered.

In the present work, the comparison of two different electrochemical deposition methods, namely cyclic voltammetry, and potentiostatic double pulse has been demonstrated. The different gold deposits are characterised by CV and scanning electron microscopy. For individual electrodeposition approach, the analytical performances of the optimised Au-BDD electrodes are examined with respect to nitrite detection.

4.2 Experimental

4.2.1 Chemicals and apparatus

Nitric acid (HNO_3, 70%), and hydrochloric acid (HCl, 37%) of analytical reagent grade were obtained from Fisher Chemical. Sulphuric acid (H_2SO_4, 95.0–97.0%, ACS reagent), tetrachloroauric (III) acid trihydrate ($HAuCl_4 \cdot 3H_2O$, ≥ 99.9%), sodium nitrite (ACS reagent, ≥ 97.0%), potassium chloride (KCl, ≥ 99.0%), and potassium hexacyanoferrate (III) ($K_3Fe(CN)_6$, ACS reagent, ≥ 99.0%) were purchased from Sigma-Aldrich. Aqua regia was mixed using HNO_3 and HCl in a volume ratio of 1 : 3. All the reagents were used

as received without further purification. All the solutions were prepared using ultrapure water (Millipore, USA, 18.2 MΩ cm at 25 ^{o}C).

All the electrochemical measurements except electrochemical impedance spectroscopy experiments were conducted at room temperature using an Autolab PGSTAT128N potentiostat (Metrohm Autolab, Utrecht, Netherlands) connected to a computer and equipped with Nova software package. Electrochemical impedance spectroscopy (EIS) experiments were conducted in a μAutolab type III potentiostat/galvanostat (Eco Chemie B. V., Utrecht, The Netherlands) with frequency response analyser software. A standard three-electrode system was used for all electrochemical measurements. A boron doped diamond substrate (boron doping level of about 5×10^{20} atoms cm^{-3}, Element Six) was used as the working electrode. A silver/silver chloride electrode (1.0 M KCl) and a platinum coil served as reference and counter electrodes. All the potentials reported here were against the Ag/AgCl electrode, unless specified.

4.2.2 Electrode modification and electrochemical measurement

Prior to each use, the gold particle modified BDD electrodes were immersed in the as-prepared fresh aqua regia solution overnight in order to dissolve the gold particles, ensuring that no Au particles remained on the BDD surface from a previous experiment, and providing a reproducible and clean surface before the beginning of each experiment. Then the BDD electrode was immersed in 0.10 M HNO_3 for cyclic potential scans between -1.7 to 2.5 V at 0.1 V s^{-1}.

Gold particles were deposited onto BDD electrodes using CV and pulse deposition. The approach using CV has been demonstrated before.[15, 16] Gold particles were deposited by CV scans from 0.7 V to -0.1 V and back to 0.7 V at 0.1 V s^{-1} in dilute aqua regia (0.1 M HCl and 0.3 M HNO_3) containing 1.0 mM $HAuCl_4 \cdot 3H_2O$ for a given number of scans (*N*)

with the formation of gold particles herein referred to as Au (1 CV), Au (3 CVs), Au (10 CVs), Au (15 CVs), and Au (20 CVs), respectively. The procedure using potentiostatic double pulse has been reported in previous Chapter 3 research.[17] Briefly, the electrodeposition conditions were applied in 0.10 M H_2SO_4 containing 1.0 mM $HAuCl_4 \cdot 3H_2O$ as follows: E_1 = - 0.7 V, t_1 = 2 s for the first nucleation pulse; and E_2 = 0 V, t_2 is from 0 to 150 s for the second growth pulse with the resulting gold deposits herein labelled as Au (0), Au (10), Au (50), and Au (150), respectively, where the number in the brackets indicates the growth time of second pulse. Whatever the electrodeposition method adopted, the as-prepared gold deposits were electrochemically characterised by performing CV experiments in the dilute aqua regia at different scan rates.

Electrochemical performances of gold modified BDD electrodes were investigated by electrochemical techniques including cyclic voltammetry and EIS. CV and EIS measurements were carried out in a 0.10 M KCl solution containing 5.0 mM $K_3Fe(CN)_6$ as a probe. CVs were scanned from -0.3 to 0.6 V at a scan rate of 5 mV s^{-1}, and EIS experiments were conducted at open circuit potential in the frequency range from 0.01 Hz to 100 kHz with 5 mV amplitude.

4.2.3 Characterisation of gold particles

The Au-BDD electrodes were characterized using scanning electron microscopy (SEM) and X-ray photoelectron spectroscopy (XPS). The characterisation of electrode surface was achieved using a field emission scanning electron microscope (Hitachi S-4300, Japan) at an accelerating voltage of 10 kV. Image analysis was conducted for average diameter measurement of particles using ImageJ (National Institute of Health, USA). X-ray photoelectron spectroscopy was performed using a Thermo Scientific K-Alpha instrument equipped with a hemispherical analyser detector and with a monochromated Al X-ray source.

4.2.4 Detection of nitrite

The electro-oxidation behaviour of nitrite at the Au-BDD electrodes was examined using cyclic voltammetry, differential pulse voltammetry, and amperometry. For CV, the electrochemical behaviour of nitrite was performed in 0.10 M phosphate buffer solution (PBS, pH = 7.4) containing 1.0 mM $NaNO_2$ at 0.1 V s^{-1} using Au particle modified BDDs. The differential pulse voltammetry was conducted in 0.10 M PBS containing different analyte concentrations with a step of 0.005 V, a pulse amplitude of 0.025 V, a pulse width of 0.05 s, and a pulse period of 0.1 s.

Chronoamperometry experiments were performed by measuring the current response for each addition of nitrite under constant stirring solution. The amperometric current-time responses for different modified electrodes were recorded for successive injections of different concentrations of nitrite into 0.10 M PBS solution at an applied peak potential of 0.8 V.

4.3 Results and discussion

4.3.1 Au electrodeposition

Figure 4.1 shows two different deposition method curves. Figure 4.1(a) shows there is an obvious cathodic peak at about 0.3 V using one cyclic scan deposition due to the reduction of gold (III), indicating the successful deposition of gold particles onto the BDD electrode surface:[18, 19]

$$Au^{3+} + 3e^{-} \rightarrow Au \quad (4.1)$$

The shape of the first cyclic voltammogram is consistent with previous reported results.[20] For the three cycle deposition, the first voltammogram is similar, while for the second voltammogram, the reduction peak shifts positively, indicating that gold deposition occurs

preferentially on the previous deposited particles during the first scan than a nucleation of new particles on BDD electrode.[20] It is note that the cathodic peak current of the second scan is lower than that of the first scan, which is due to the $AuCl_4^-$ consumption in the diffusion layer. This similar behaviour can be also observed for the third scan. For the following cyclic scans (not shown for N = 10, 15 and 20), the cathodic peak current further decreases and the peak potential moves to more positive values.

For the pulse deposition, it has been revealed in Chapter 3 a nucleation-growing pulse strategy is used through applying -0.7 V for 2 s, and 0 V for different growth times of 0 s, 10 s, 50 s, and 150 s, enabling the fast deposition gold nuclei while maintaining a low current for growth at the two corresponding stages.[17]

The deposition charge (Q_{dep}) associate with the gold formation during the electrodeposition reduction process can be acquired by integration of the area under *I*-*V* or *I*-*t* deposition curves for CV and pulse deposition methods, respectively, which is summarised in Table 4.1 assuming that the Faradaic yield during gold electrodeposition process is 100%. It can be observed that the charges increase with N or t_2, that is, the total amount of electrodeposited gold particles depends on the number of cyclic scans or pulse growth deposition time.

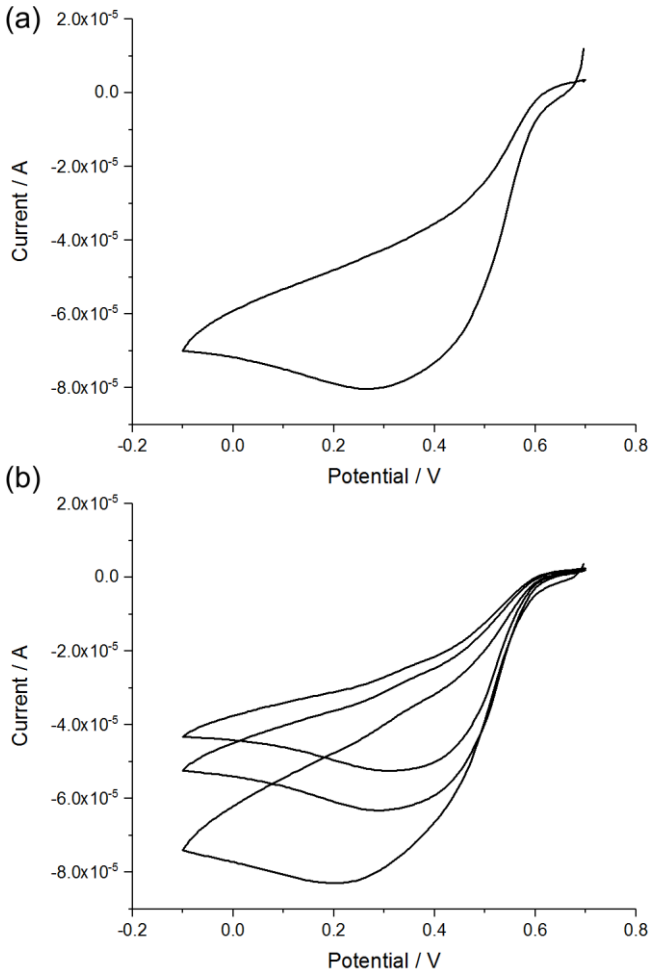


Figure 4.1 The gold electrodeposition using CV scan via (a) one cycle and (b) three cycles.

4.3.2 Characterisation of gold particles modified electrodes

4.3.2.1 Electrochemical characterisation of gold particles

The decoration of Au particle on the BDD electrode surface was confirmed by cyclic voltammetry, XPS and SEM. Gold deposits were first characterised by performing cyclic voltammetric experiments in dilute aqua regia. Figure 4.2 shows the typical electrochemical response behaviour of Au particles using N = 1 and t_2 = 150 s as examples at different scan rates. Both show similar oxidation peaks at 0.9 - 1.0 V, which represents the stripping of gold as follows:[19]

$$Au \rightarrow Au^{3+} + 3e^{-} \quad (4.2)$$

On the backward scan reduction peaks at 0.3 - 0.5 V were observed, which was related with the reduction of the oxides formed during the forward sweep. Whatever the electrodeposition method was utilised, the shape of voltammograms is similar, and a large peak-to-peak separation increases with the scan rate, indicating the irreversible behaviour for the process. Furthermore, the plots of gold anodic and cathodic peak currents versus scan rates are shown in the Figure 4.2, and a linear relationship can be observed over the scan rate range 1 - 150 mV s^{-1}, indicating that it's a surface-controlled process.

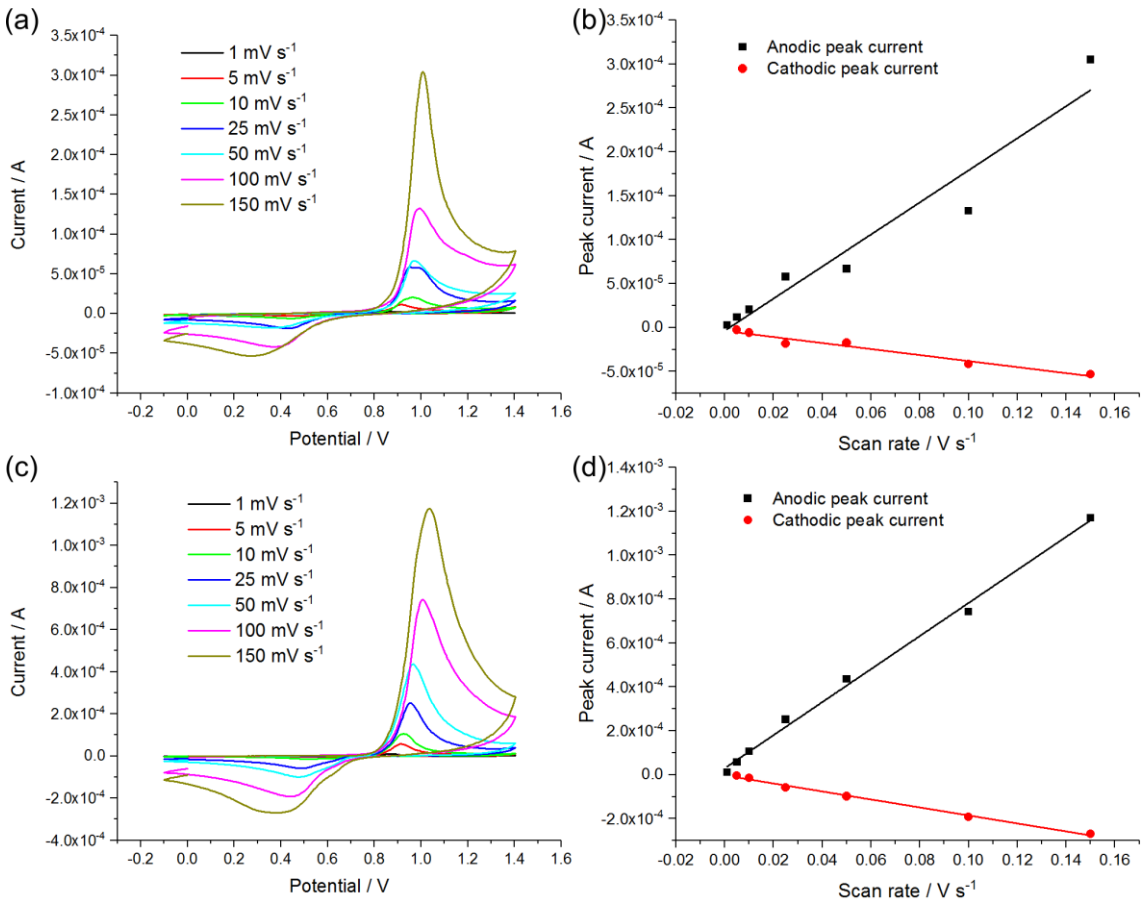


Figure 4.2 CVs recorded at different scan rates in dilute aqua regia using (a) one cycle CV deposition and (c) pulse deposition of 150 s; Plot of anodic and cathodic peak currents versus scan rates for (b) CV deposition and (d) pulse deposition.

4.3.2.2 XPS characterisation

XPS was used to identify the electrode surface chemical composition. The survey spectrum of the Au (150)-BDD electrode as a typical example shows the presence of C_{1s}, O_{1s}, and Au_{4f} peaks in Figure 4.3. The intense C_{1s} peak at 284 eV is attributed to diamond bulk carbon and the O_{1s} peak at 532 eV indicates there is oxygen impurity on the BDD surface.[21] The high resolution spectra of Au_{4f} show two peaks at the binding energy of 84.08 eV (Au $4f_{7/2}$), and 87.78 eV (Au $4f_{5/2}$), which is consistent with zerovalent metallic Au, confirming the successful deposition of gold particles.[22, 23]

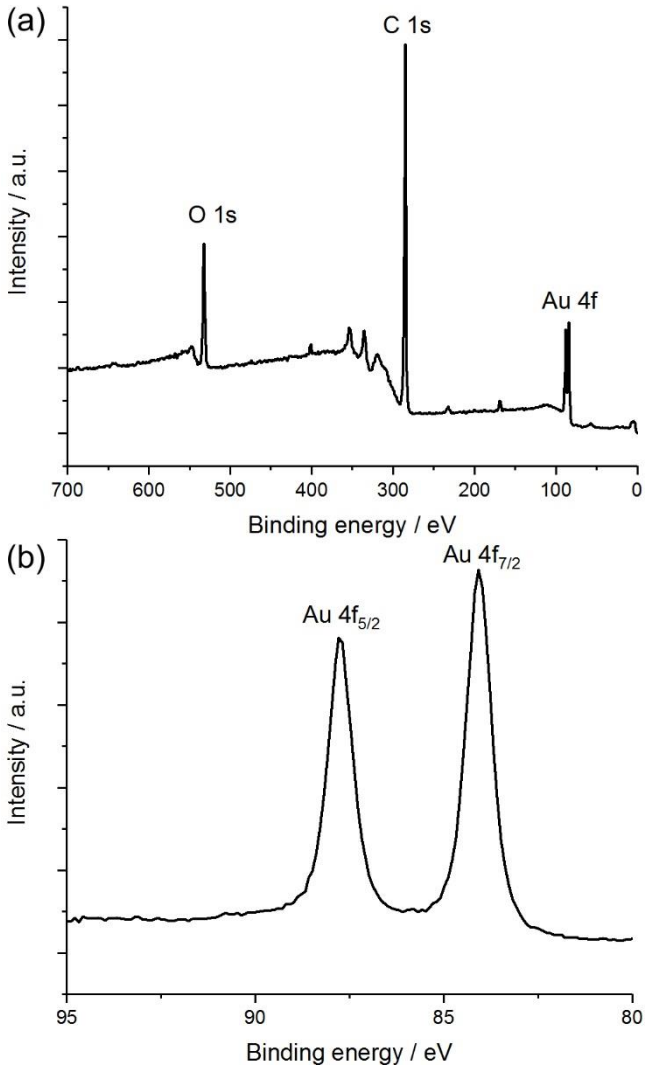


Figure 4.3 (a) XPS spectra of Au (150)-BDD, and (b) high resolution spectra of Au_{4f}.

4.3.2.3 SEM characterisation

In order to characterise the deposits, SEM analyses were performed. Figure 4.4 shows the morphologies of gold particles modified BDD electrodes by CV deposition. It has been checked that after cleaning with aqua regia prior to cyclic voltammograms, there are no gold residue left on the BDDs, confirming the success of the cleaning protocol. Gold nanoparticles with a sphere shape were successfully and relatively homogeneously decorated onto BDD electrodes using CV deposition when N = 1. When increasing the cyclic scans, the morphology tends to become less spherical, and the gold deposits switch to convex polyhedral compact particles with irregular face. It is noteworthy that larger and less homogenously distributed particles form and a preferential location along BDD edges instead of the flat basal planes takes place for multiple cyclic scan deposition. This may be due to the local heterogeneities of boron doping level at different domains.[24] While in the case of pulse deposition, the small quasi-spherical Au nuclei are formed during the short nucleation stage while the morphology transits to star-like shape with more homogeneous distribution of BDD surfaces when increasing of duration of growth pulse as shown in Chapter 3. This demonstrates that different morphologies with favoured particle location and distribution can be electrochemically controlled via different electrodeposition methods with easily varying deposition parameters.

The particle size are analysed by ImageJ and summarised in Table 4.1. For the CV method, the particle diameter is 247 ± 82 nm after one cycle deposition. With the increasing of potential scan cycles, the particle sizes increase to be 285 ± 88, 401 ± 129, 614 ± 243, and 792 ± 260 for N = 3, 10, 15, and 20 respectively. In the case of pulse deposition, the average diameter of Au nanoparticle (AuNPs) is 95 ± 39 nm without the growth stage while with longer growth times of 10, 50 and 150 s, the mean sizes of Au increase to be 170 ± 51 nm, 217 ± 80 nm, and 269 ± 102 nm, respectively. These results illustrate that it is attainable to

control the particle size from the nanometer to the submicron scale by varying the cyclic scans or the growth time.

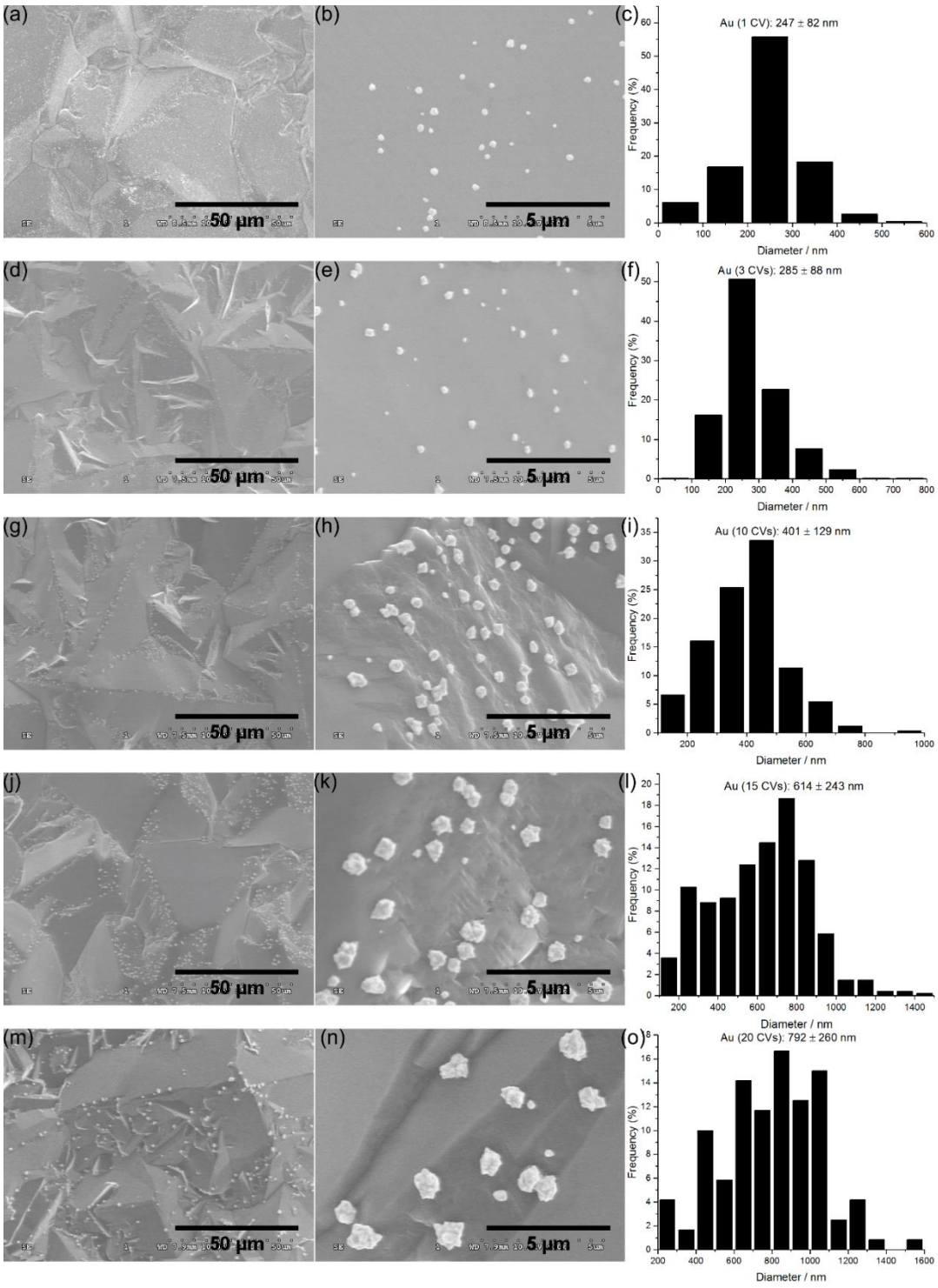


Figure 4.4 SEM images of Au particles and the corresponding size distributions using CV deposition when N = 1 (a-c), 3 (d-f), 10 (g-i), 15 (j-l), and 20 (m-o) at different magnifications.

Table 4.1 Characterisation of gold particles on BDD electrodes using CV deposition for different numbers of scans (*N*), and pulse deposition for different deposition times t_2 during the electrodeposition step.

Method	*N* or t_2	Q_{dep} (mC)	Diameter (nm)	Number of particles analysed
CV	1	0.8 ± 0.03	247 ± 82	570
deposition	3	1.9 ± 0.04	285 ± 88	679
	10	4.7 ± 0.2	401 ± 129	256
	15	6.4 ± 0.09	614 ± 243	477
	20	8.2 ± 0.3	792 ± 260	120
Pulse	0 s	1.0 ± 0.1	95 ± 39	450
deposition	10 s	1.8 ± 0.1	170 ± 51	698
	50 s	3.4 ± 0.4	217 ± 80	436
	150 s	6.9 ± 0.3	269 ± 102	1279

4.3.2.4 Electrochemical characteristics of gold modified electrodes

To compare electrochemical performance, the modified electrodes were characterised by cyclic voltammetry and electrochemical impedance spectroscopy using a probe of $[Fe(CN)_6]^{4-/3-}$. It is known that cyclic voltammetry is a powerful method to demonstrate improved electron transfer rate and high electroactive surface area for modified electrodes, and CV tests were conducted to examine the current response of presented electrodes in 0.10 M KCl solution containing 5.0 mM $K_3Fe(CN)_6$. Figure 4.5 shows cyclic voltammograms for bare BDD and modified electrodes by Au (20 CVs) and Au (150) at a scan rate of 5 mV s^{-1}, both of which are chosen according to the optimised results of modified electrodes for electro-oxidation of nitrite discussed later. It is noteworthy that the Q_{dep}, namely deposition amount, for Au (150) is smaller than that for Au (20 CVs). For

bare BDD, the redox peaks of $[Fe(CN)_6]^{3-/4-}$ are well-defined. After modification by gold particles, the peak currents increase for both cases. Furthermore, Au (150)-BDD shows increased redox peak current response with smaller peak-to-peak separation compared to Au (20 CVs)-BDD, indicating the fastest electrode kinetics for the electrochemical reaction of the redox at the Au (150)-BDD. It has been reported that the apparent rate constant is proportional to the coverage of electrochemically active area.[25] From the comparison of SEM images of Au (150 CVs)-BDD and Au (20 CVs)-BDD, it can be observed that an increasing "active" nanoparticle coverage to decreasing "inactive" blocking BDD domains, that is, greater effective electroactive surface areas available for the reaction to occur. With increasing surface coverage, the diffusion layers overlap heavily, and the diffusion regime may transit from convergent diffusion to planar diffusion as it has been demonstrated for Au (150) in Chapter 3. Having established the preliminary qualitative observation, the electroactive surface area can be estimated according to the Randles-Sevcik equation:[26, 27]

$$I_p = 2.69 \times 10^5 A D^{0.5} C v^{0.5} n^{1.5} \quad (4.3)$$

where I_p is the anodic peak current, A is the effective electroactive surface area, D is diffusion coefficient of the probe (7.6×10^{-10} m^2 s^{-1}),[28-30] C is the molecule concentration, and v is the scan rate, and n is number of electrons involved in the redox reaction (n = 1). The values of the electrochemical active surface area for bare BDD, Au (20 CVs)-BDD, and Au (150)-BDD electrodes are 1.98×10^{-5}, 2.23×10^{-5}, and 2.48×10^{-5} m^2, respectively. The increasing of "active" surface areas from Au (150)-BDD to Au (20 CVs)-BDD are consistent with the visual particle coverages from SEM images, and responsible for the following discussion in terms of analytical performance towards nitrite determination. Therefore, it demonstrates a convinced sign of improved electrocatalytic performance of the as-prepared electrode by pulse deposition method.

The interfacial electron transfer properties of the gold modified BDD electrodes were investigated by using electrochemical impedance spectroscopy. The Nyquist plots are shown in Figure 4.5. The equivalent circuit for fitting the EIS data are shown in the inset where *Rs* is the ohmic solution resistance; R_{ct} represents the charge transfer resistance; C_{dl} is the double layer capacitance resulting from charge rearrangement at the interface between the electrode and the solution; and W represents the impedance to mass transfer, called Warburg impedance.[31, 32] The EIS consists of a semicircle at high frequencies and a nearly 45^{o} line at low frequencies. The linear part corresponds to the diffusion process, while the charge transfer resistance offers information on the electron transfer process kinetics at the BDD electrode interface and is obtained from semicircle diameters. The R_{ct} for the unmodified, Au (20 CVs)-, and Au (150)-BDD electrodes are 1210 Ω, 361 Ω, and 199 Ω, respectively. It is evident that gold modified BDDs increase the electronic transmission of BDD. The R_{ct} of Au (150)-BDD electrode are even lower than that of Au (20 CVs)-BDD, indicating that the AuNPs by pulse deposition can further effectively improve the electron transfer between the surface of BDD electrode and the redox ions, namely faster electron kinetics. Considering that the deposition amount of Au (150) is even lower than that of Au (20 CVs) from Q_{dep}, this may be assigned to higher coverage active "star-shape" nanoparticles arising from exposing larger fractions of electrocatalytic active sites and larger electroactive surface area for the Faradaic redox reaction.

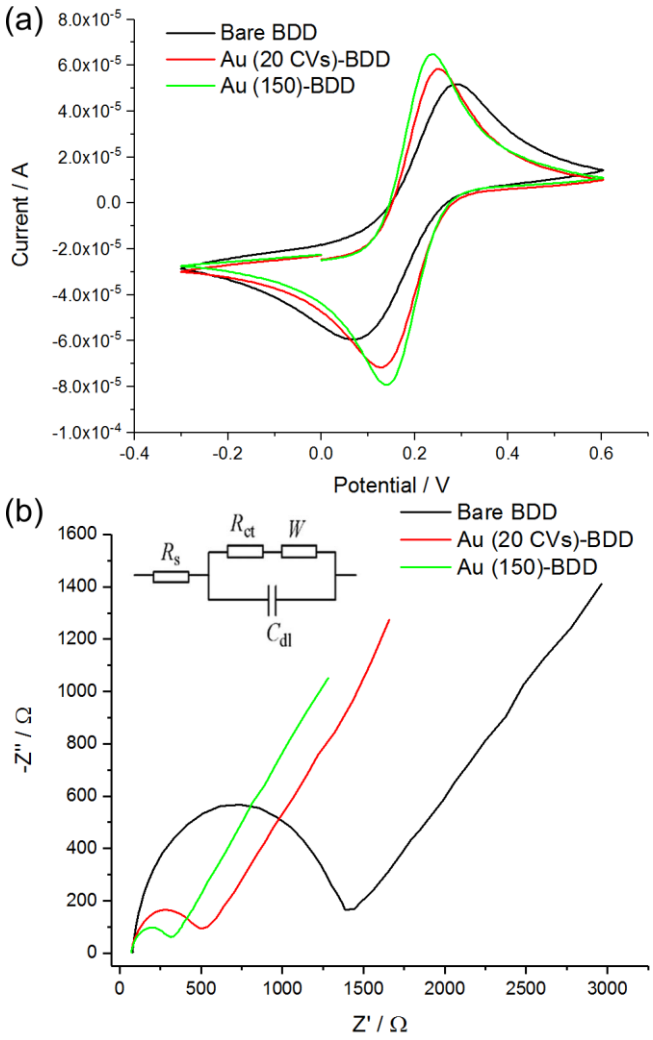


Figure 4.5 (a) CVs and (b) EIS response for bare BDD, Au (20 CVs)-BDD, and Au (150)-BDD in 0.10 M KCl solution containing 5.0 mM $K_3Fe(CN)_6$ at a scan rate of 5 mV s^{-1}. The inset is the equivalent circuit for the impedance spectra.

4.3.3 Electrochemical behaviour of nitrite at different electrodes

4.3.3.1 Electrochemical response and optimisation towards nitrite

In order to test and optimise the electrochemical response of Au-BDD electrodes towards nitrite oxidation, a series of experiments were conducted with different deposits prepared by CV and pulse deposition. The response of nitrite at Au-BDD electrodes was examined using CV in a 0.10 M phosphate buffer solution. For preliminary experiments, a high

concentration of 1.0 mM nitrite was chosen since this value is easily detectable for further optimization of the system.

The effect of both the amount of gold particles deposited and electrodeposition methods was examined using CV in the 1.0 mM nitrite solution. Figure 4.6 shows the typical voltammetric signals recorded at modified BDD electrodes prepared by varying scan numbers and growth pulse time. The voltammograms obtained for both deposition methods exhibit typical sharp and well-defined peaks at 0.83 V, which is associated with the oxidation of nitrite. This indicates gold particles have obviously catalytic activity towards oxidation of nitrite. The oxidation mechanism of NO_2^- on metal nanoparticles are well-documented in previous reports, and accordingly a two-electron oxidation reaction occurs from NO_2^- to NO_3^- at neutral medium as shown in the following equation:[13, 32, 33]

$$NO_2^- + H_2O \rightarrow NO_3^- + 2H^+ + 2e^- \quad (4.4)$$

The peaks at around 0.39 V are the Au reduction peak. Figure 4.6(c) shows the comparison of nitrite oxidation peak current as a function of Q_{dep} for CV and pulse deposition. For both methods, the peak current increases with the Q_{dep} values, indicating that more gold deposits are responsible for the higher electrocatalytic ability towards oxidation of nitrite. In essence, the gold deposits may be view as arrays of quasi-spherical- or star-shaped (sub)microelectrode,[17, 34] and the previous Chapter 3 has demonstrated the Au (150) modified electrode configuration acting as two-dimensional monolayer arrays where diffusion layers of adjacent gold particles overlap strongly leading to the planar diffusion towards the whole BDD electrode surface. This is why Au (150) is taken as the optimised condition for nitrite oxidation and the basis for comparison of electrodeposition method effect study in terms of diffusion behaviour.

For the low electrodepostion charge of about 1.9 mC, the response of both modified electrode for nitrite are similar. Nevertheless, for higher Q_{dep}, the anodic peak current is higher using pulse deposition when the corresponding Q_{dep} = 4.4 or 6.4 mC than that using CV deposition when Q_{dep} = 4.6 or 6.6 mC. From another point of view, pulse deposition provides similar analytical response current (8.0×10^{-5}, 1.2×10^{-4}, 1.6×10^{-4} A) while lower Q_{dep} is consumed during the electrodeposition process. From the comparison of Figure 4.6 with data in Table 4.1 and SEM images, when increasing cyclic scans for CV deposition, it is detrimental on the new nuclei formation but beneficial for growth on the established nuclei instead, resulting in bigger gold particles and probably aggregation and/or coalescence phenomena, and meanwhile preference site of particle growth on BDD edge areas instead of flat facets leads to inhomogeneous distribution. For the pulse deposition, the homo-dispersity of the deposits on the BDD electrode is favoured when increasing the pulse deposition time compared to that of CV deposition. To sum up, although the charges consumed, that is, the total deposit amount, is comparable, smaller star-shape gold particles with higher coverage are more homogeneously distributed on BDDs using pulse deposition, while heterogeneous distribution of larger polygons particles is the case for CV deposition. As a consequence, a maximum peak current is observed for Au (150)-BDD resulting from the increase in the effective electroactive surface area of (sub)microelectrodes and the planar diffusion regime.

To summarise, the pulse deposition method affords more homogeneous deposits of smaller size with higher coverage than CV deposition, and thus the former provide better analytical responses while involving lower Q_{dep}. This result spotlights a correlation between gold deposits characterization (such as gold coverage and effective surface area) and the resulting analytical performance for nitrite detection, when the NPs-based modified electrode is dedicated to an analytical system.

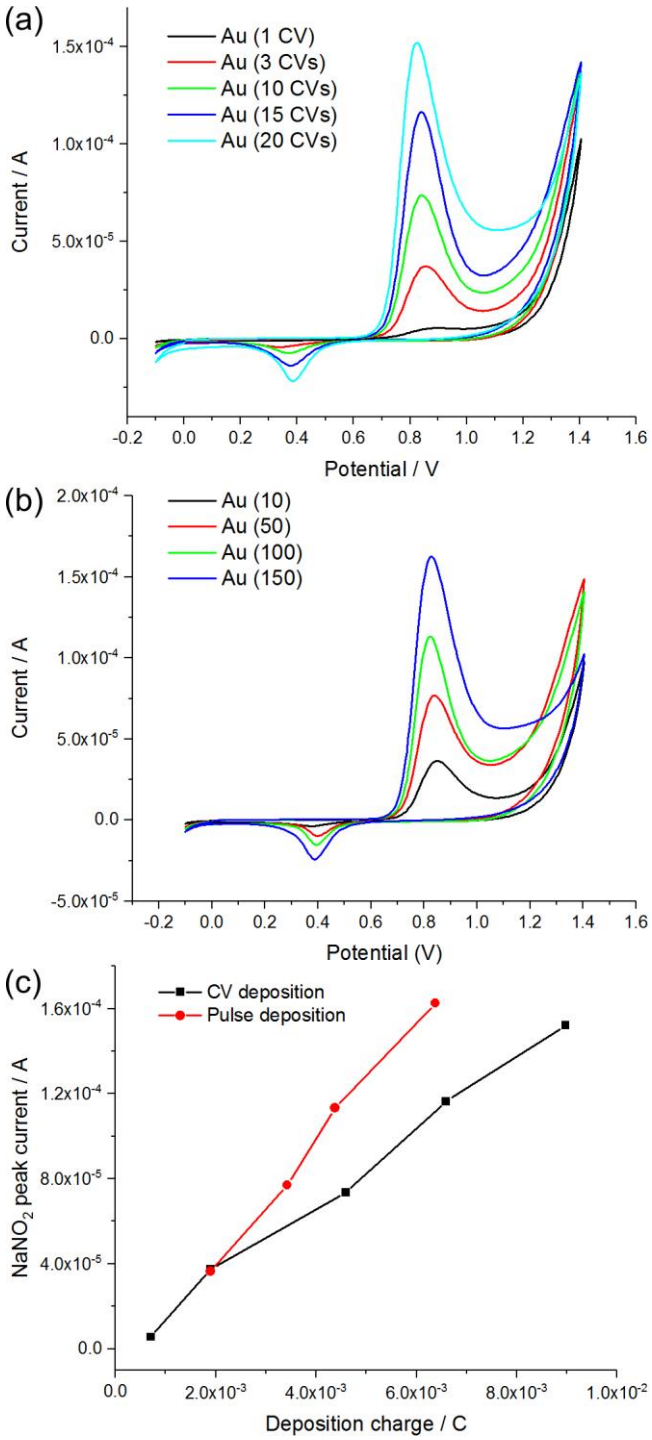


Figure 4.6 CVs of Au-BDD prepared by (a) different scan cycles, and (b) grow deposition time in 0.10 M PBS containing 1.0 mM $NaNO_2$ at 0.1 V s^{-1}; (c) Effect of the corresponding charges consumed during the gold electrodeposition on the nitrite oxidation peak current.

4.3.3.2 Effect of scan rate

Based on the above results, the Au (20 CVs) and Au (150) modified BDD electrodes were chosen for further study. Since it is significant to consider the nature of the electron transfer process to distinguish between diffusion or surface controlled process, a scan rate dependence study was carried out. Figure 4.7 shows the CVs of Au-BDD in 0.10 M PBS solution containing 1.0 mM $NaNO_2$ at various scan rates from 1 to 50 mV s^{-1}. It can be observed that the anodic peak currents increase linearly with the square root of scan rate, indicating that the anodic process of $NaNO_2$ is diffusional limited. In addition, it can be found that the response is higher using Au (150)-BDD than that of Au (20 CVs)-BDD at all scan rates, confirming the better electrocatalytic performance of electrodes modified by the pulse deposition for the oxidation of nitrite due to the higher effective surface area of gold deposits of star-shaped at the Au particle-electrolyte interface.

4.3.4 Electrochemical detection of nitrite

Differential pulse voltammetry (DPV) regularly has higher sensitivity than cyclic voltammetry since the charging current is minimised.[13, 35] Accordingly, the DPV method was conducted for quantitative detection of different concentrations of nitrite on the modified BDD electrodes. Figure 4.8 describes that the DPV curves of Au (20 CVs)- and Au (150)-BDD electrodes in the 0.10 M PBS containing different nitrite concentrations. As shown in Figure 4.8, the anodic peak current of $NaNO_2$ increases linearly with the concentration in the range from 20 to 1000 μM. The linear regression equations are expressed as Ip (A) = 1.69×10^{-8} C (μM) + 2.55×10^{-6}, R^2 =0.99298 for Au (20 CVs)-BDD, and Ip = 5.50×10^{-8} C (μM) + 1.05×10^{-5}, R^2 =0.99432 for Au (150)-BDD, and the corresponding sensitivities of the modified electrodes are 1.69×10^{-2} μA μM^{-1}, and 5.50×10^{-2} μA μM^{-1}, respectively. This confirms that the obtained electrode by the pulse

deposition has better electrochemical activity towards the oxidation of nitrite, which agrees with the above discussion.

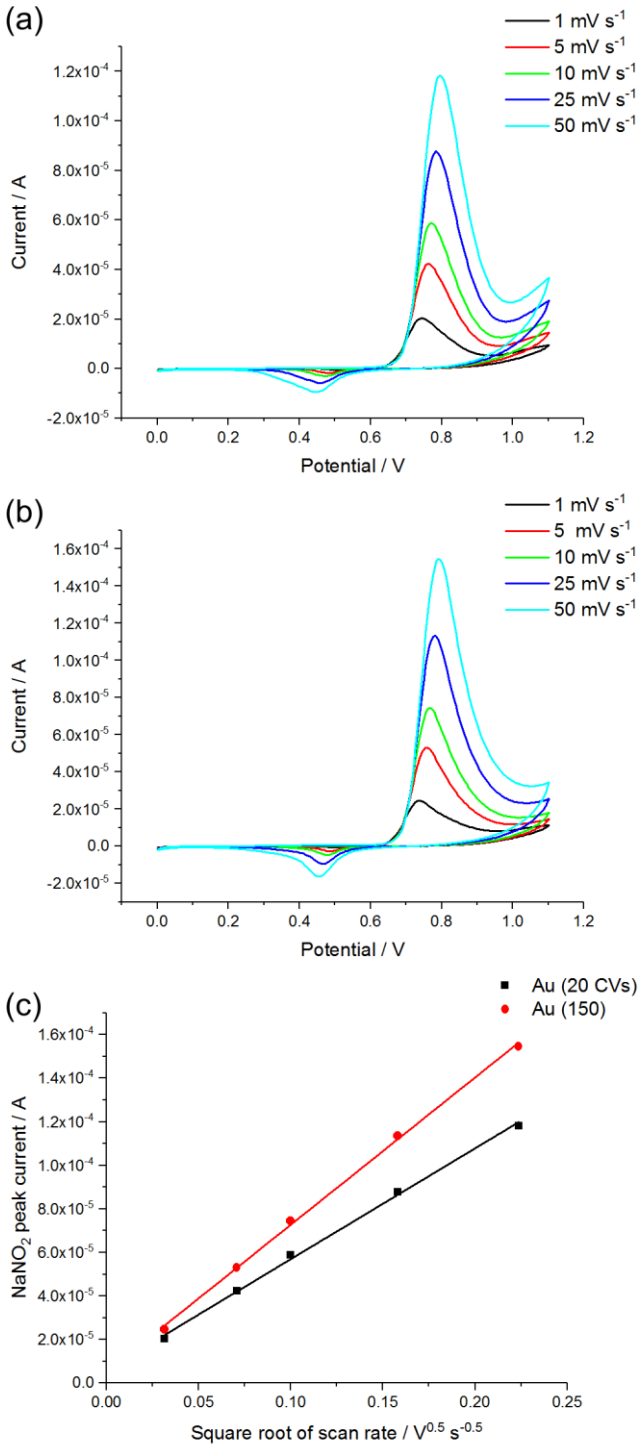


Figure 4.7 CVs of the Au-BDD electrodes in 0.10 M PBS solution containing 1.0 mM $NaNO_2$ at different scan rates from 1 to 50 mV s^{-1} using (a) Au (20 CVs) and (b) Au (150); (c) the plots of anodic peak currents versus square root of scan rates.

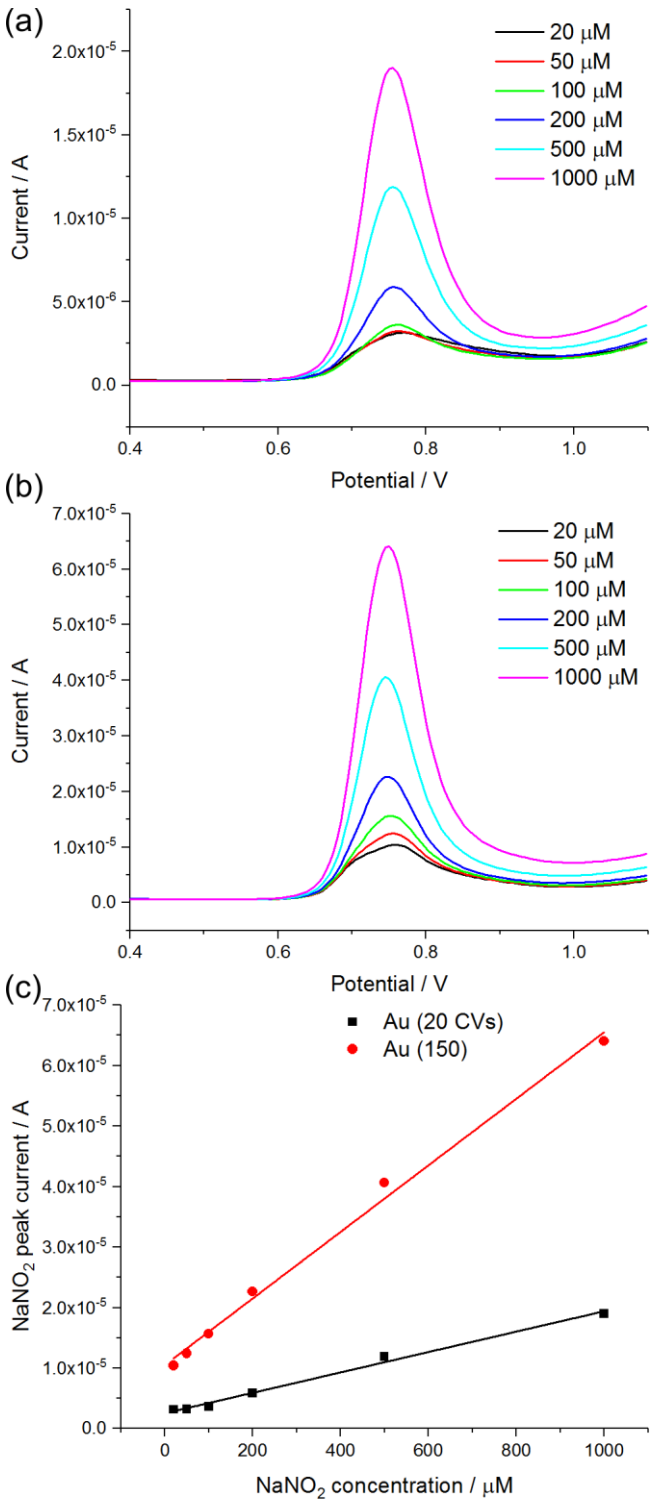


Figure 4.8 DPV of (a) Au (20 CVs) and (b) Au (150) deposition in 0.10 M PBS containing different $NaNO_2$ concentrations from 20 to 1000 μM; (c) Plot of $NaNO_2$ peak current versus different $NaNO_2$ concentrations for the corresponding gold modified BDD electrodes.

It is commonly known that amperometry is a preferred method for trace analyte determination since it offers a fast assessment of the electrodes and main characteristics of sensors such as limit of detection (LOD), and response time. In order to study the performance of the as-prepared Au (20 CVs)- and Au (150)-BDD electrodes, lower concentration of $NaNO_2$ for determination was investigated by amperometry. Figure 4.9 represents the typical amperometric response of modified electrodes upon consecutive addition of different concentrations of $NaNO_2$ in 0.10 M PBS at a fixed potential of 0.8 V. When an aliquot of $NaNO_2$ was added into the stirring solution, both modified electrodes responded rapidly, and the current increased steeply to reach a stable value within 5 s, reflecting a fast amperometric response behaviour. In addition, it is apparent that a gradual boost in the oxidation currents of nitrite was attained with stepwise increasing of the nitrite concentrations. Furthermore, it can be observed that the anodic peak current responses at Au (150)-BDD for the same concentration of nitrite are larger than that at Au (20 CVs)-BDD. The response currents at both modified electrodes are proportional to the nitrite concentration from 1 to 32 μM. Based on calibration plots, and a signal -to-noise of 3, limit of detection (LOD) for Au (20 CVs)-BDD and Au (150)-BDD electrodes is 1.59 μM and 0.48 μM, respectively. All the results confirm that the analytical performance of modified electrode by pulse deposition is better than that of CV deposition, which is consistent with the above findings. In addition, the LOD results are much below the World Health Organization guideline (3 mg L^{-1} or 65.2 μM) for drinking water,[36] and better than those using other Au nanoparticle based sensors reported, including AuNPs modified glassy carbon electrode (GCE, 2.4 μM),[8] AuNPs/poly(3-methylthiophene) composites coated GCE (2.3 μM),[37] Au/TiO_2/carbon nanotube composite modified GCE (3 μM),[38] and Dy_2O_3-AuNPs nanocomposite modified GCE (3.3 μM).[39] It is evident that the present

modified electrodes through facile depositions without further combination with other complex composites provide a good platform for electrochemical detection of nitrite.

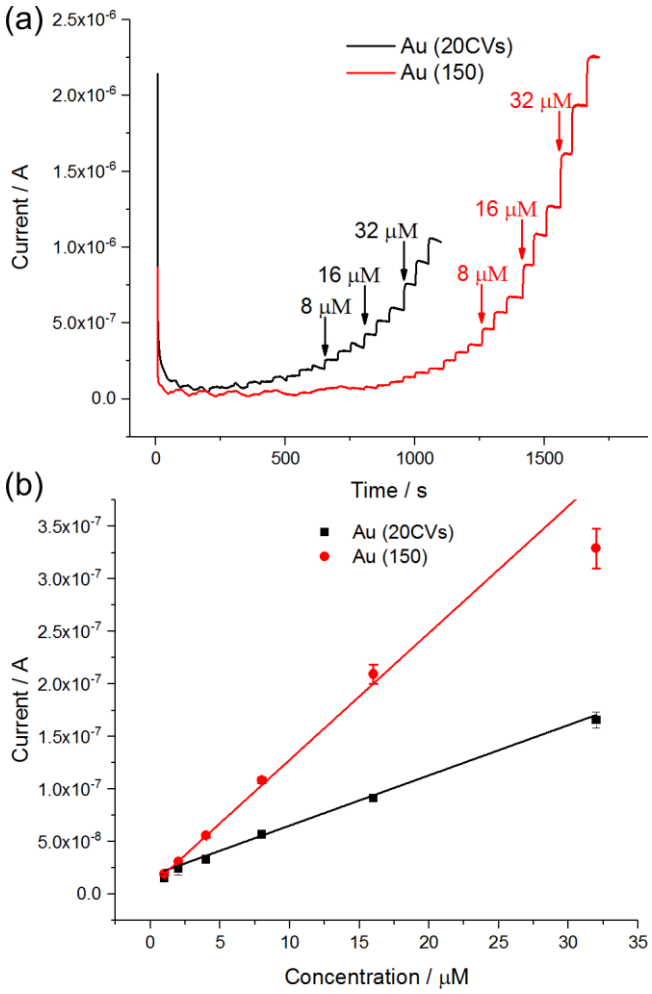


Figure 4.9 (a) Amperometric response on the Au (20 CVs)- and Au (150)-BDD electrodes with successive injection of different concentrations of $NaNO_2$ at the potential of 0.8 V under stirring PBS solution; (b) Plot of peak current versus $NaNO_2$ concentrations.

4.4 Conclusions

In this chapter, two different electrodeposition methods for gold, specifically cyclic voltammetry and pulse depositions, have been compared for nitrite sensing. From the series of results, pulse deposition is shown to afford the better morphological, size, and more homogeneous distribution control of the gold deposits with a higher coverage. Pulse

deposition modified boron doped diamond electrode increases the electrochemical characteristics of the electrode and exhibits better analytical performance towards nitrite detection than cyclic voltammetry deposition. In the optimised conditions, a sensitivity of 5.50×10^{-2} μA μM^{-1} with a limit of detection of 0.48 μM is obtained for gold modified BDD electrode using pulse deposition of 150 s towards nitrite determination. The deposition strategy may be extended to other metal nanoparticles, and the ability to activate boron doped diamond electrodes via the fast, facile and effective deposition procedure for electrocatalysts makes this method cost-effective and promising to promote the development of electrochemical sensors for food analysis.

References

1. Li, X. J.; Ping, J. F.; Ying, Y. B., Recent developments in carbon nanomaterial-enabled electrochemical sensors for nitrite detection. *Trac-Trend Anal Chem* **2019,** *113*, 1-12.

2. Kalaycioglu, Z.; Erim, F. B., Nitrate and Nitrites in Foods: Worldwide Regional Distribution in View of Their Risks and Benefits. *J Agr Food Chem* **2019,** *67* (26), 7205-7222.

3. Li, G.; Xia, Y.; Tian, Y.; Wu, Y.; Liu, J.; He, Q.; Chen, D., Review—Recent Developments on Graphene-Based Electrochemical Sensors toward Nitrite. *J Electrochem Soc* **2019,** *166* (12), B881-B895.

4. Moorcroft, M. J.; Davis, J.; Compton, R. G., Detection and determination of nitrate and nitrite: a review. *Talanta* **2001,** *54* (5), 785-803.

5. Wang, Q. H.; Yu, L. J.; Liu, Y.; Lin, L.; Lu, R. G.; Zhu, J. P.; He, L.; Lu, Z. L., Methods for the detection and determination of nitrite and nitrate: A review. *Talanta* **2017,** *165*, 709-720.

6. Singh, P.; Singh, M. K.; Beg, Y. R.; Nishad, G. R., A review on spectroscopic methods for determination of nitrite and nitrate in environmental samples. *Talanta* **2019,** *191*, 364-381.

7. Afkhami, A.; Soltani-Felehgari, F.; Madrakian, T.; Ghaedi, H., Surface decoration of multi-walled carbon nanotubes modified carbon paste electrode with gold nanoparticles for electro-oxidation and sensitive determination of nitrite. *Biosens Bioelectron* **2014,** *51*, 379-385.

8. Cui, Y. P.; Yang, C. Z.; Zeng, W.; Oyama, M.; Pu, W. H.; Zhang, J. D., Electrochemical determination of nitrite using a gold nanoparticles-modifled glassy carbon

electrode prepared by the seed-inediated growth technique. *Anal Sci* **2007,** *23* (12), 1421-1425.

9. Liu, Y.; Gu, H. Y., Amperometric detection of nitrite using a nanometer-sized gold colloid modified pretreated glassy carbon electrode. *Microchim Acta* **2008,** *162* (1-2), 101-106.

10. Jin, J. X.; Xiao, B.; Yan, J. L.; Liu, B. Z., Electrocatalytic Oxidation and Determination of Nitrite at Multi-Walled Carbon Nanotubes Modified Electrode. *J Nanosci Nanotechno* **2019,** *19* (4), 2124-2129.

11. Li, L. B.; Liu, D.; Wang, K.; Mao, H. P.; You, T. Y., Quantitative detection of nitrite with N-doped graphene quantum dots decorated N-doped carbon nanofibers composite-based electrochemical sensor. *Sensor Actuat B-Chem* **2017,** *252*, 17-23.

12. Welch, C. M.; Compton, R. G., The use of nanoparticles in electroanalysis: a review. *Anal Bioanal Chem* **2006,** *384* (3), 601-619.

13. Zou, C. E.; Yang, B. B.; Bin, D.; Wang, J.; Li, S. M.; Yang, P.; Wang, C. Q.; Shiraishi, Y.; Du, Y. K., Electrochemical synthesis of gold nanoparticles decorated flower-like graphene for high sensitivity detection of nitrite. *J Colloid Interf Sci* **2017,** *488*, 135-141.

14. Zhang, F. H.; Yuan, Y. W.; Zheng, Y. Q.; Wang, H.; Liu, T. H.; Hou, S. F., A glassy carbon electrode modified with gold nanoparticle-encapsulated graphene oxide hollow microspheres for voltammetric sensing of nitrite. *Microchim Acta* **2017,** *184* (6), 1565-1572.

15. Holt, K. B.; Sabin, G.; Compton, R. G.; Foord, J. S.; Marken, F., Reduction of tetrachloroaurate (III) at boron-doped diamond electrodes: Gold deposition versus gold colloid formation. *Electroanal* **2002,** *14* (12), 797-803.

16. Svanberg-Larsson, J.; Nelson, G. W.; Steinvall, S. E.; Leo, B. F.; Brooke, E.; Payne, D. J.; Foord, J. S., A Comparison of Explicitly-terminated Diamond Electrodes Decorated with Gold Nanoparticles. *Electroanal* **2016,** *28* (1), 88-95.

17. Cai, X.; Lin, C.; Foord, J. S.; Compton, R. G., The Electrochemical Oxidation of Sulphite on Gold Electrodes. *Electroanal* **2019,** *31* (9), 1783-1796.

18. Dudin, P. V.; Unwin, P. R.; Macpherson, J. V., Electrochemical Nucleation and Growth of Gold Nanoparticles on Single-Walled Carbon Nanotubes: New Mechanistic Insights. *J Phys Chem C* **2010,** *114* (31), 13241-13248.

19. Bond, A. M.; Kratsis, S.; Mitchell, S.; Mocak, J., Comparison of the gold reduction and stripping processes at platinum, rhodium, iridium, gold and glassy carbon micro- and macrodisk electrodes. *Analyst* **1997,** *122* (10), 1147-1152.

20. Hezard, T.; Fajerwerg, K.; Evrard, D.; Colliere, V.; Behra, P.; Gros, P., Gold nanoparticles electrodeposited on glassy carbon using cyclic voltammetry: Application to Hg(II) trace analysis. *J Electroanal Chem* **2012,** *664*, 46-52.

21. Tian, R. H.; Zhi, J. F., Fabrication and electrochemical properties of boron-doped diamond film-gold nanoparticle array hybrid electrode. *Electrochem Commun* **2007,** *9* (5), 1120-1126.

22. Yu, H.; Feng, X.; Chen, X. X.; Wang, S. S.; Jin, J., A highly sensitive determination of sulfite using a glassy carbon electrode modified with gold nanoparticles-reduced graphene oxide nano-composites. *J Electroanal Chem* **2017,** *801*, 488-495.

23. Crist, B. V., *Handbook of monochromatic XPS spectra*. Wiley: Chichester, 2000.

24. Wilson, N. R.; Clewes, S. L.; Newton, M. E.; Unwin, P. R.; Macpherson, J. V., Impact of grain-dependent boron uptake on the electrochemical and electrical properties of polycrystalline boron doped diamond electrodes. *J Phys Chem B* **2006,** *110* (11), 5639-5646.

25. Zhou, Y. G.; Campbell, F. W.; Belding, S. R.; Compton, R. G., Nanoparticle modified electrodes: Surface coverage effects in voltammetry showing the transition from convergent to linear diffusion. The reduction of aqueous chromium (III) at silver nanoparticle modified electrodes. *Chem Phys Lett* **2010,** *497* (4-6), 200-204.

26. Hrapovic, S.; Liu, Y. L.; Male, K. B.; Luong, J. H. T., Electrochemical biosensing platforms using platinum nanoparticles and carbon nanotubes. *Anal Chem* **2004,** *76* (4), 1083-1088.

27. Huang, B. T.; Liu, J.; Lai, L. F.; Yu, F.; Ying, X.; Ye, B. C.; Li, Y. C., A free-standing electrochemical sensor based on graphene foam-carbon nanotube composite coupled with gold nanoparticles and its sensing application for electrochemical determination of dopamine and uric acid. *J Electroanal Chem* **2017,** *801*, 129-134.

28. Abdel-Raoof, A. M.; El-Shal, M. A.; Said, R. A. M.; Abostate, M. H.; Morshedy, S.; Emara, M. S., Versatile Sensor Modified with Gold Nanoparticles Carbon Paste Electrode for Anodic Stripping Determination of Brexpiprazole: A Voltammetric Study. *J Electrochem Soc* **2019,** *166* (12), B948-B955.

29. Preecharueangrit, S.; Thavarungkul, P.; Kanatharana, P.; Numnuam, A., Amperometric sensing of sulfite using a gold electrode coated with ordered mesoporous carbon modified with nickel hexacyanoferrate. *J Electroanal Chem* **2018,** *808*, 150-159.

30. Kadara, R. O.; Jenkinson, N.; Banks, C. E., Characterisation of commercially available electrochemical sensing platforms. *Sensor Actuat B-Chem* **2009,** *138* (2), 556-562.

31. Winiarski, J. P.; de Barros, M. R.; Magosso, H. A.; Jost, C. L., Electrochemical reduction of sulfite based on gold nanoparticles/silsesquioxane-modified electrode. *Electrochim Acta* **2017,** *251*, 522-531.

32. Li, S. J.; Zhao, G. Y.; Zhang, R. X.; Hou, Y. L.; Liu, L.; Pang, H., A sensitive and selective nitrite sensor based on a glassy carbon electrode modified with gold nanoparticles and sulfonated graphene. *Microchim Acta* **2013,** *180* (9-10), 821-827.

33. Zhang, Y.; Wen, F. F.; Tan, J.; Jiang, C.; Zhu, M.; Chen, Y. J.; Wang, H. G., Highly efficient electrocatalytic oxidation of nitrite by electrodeposition of Au nanoparticles on molybdenum sulfide and multi-walled carbon nanotubes. *J Electroanal Chem* **2017,** *786*, 43-49.

34. Hezard, T.; Fajerwerg, K.; Evrard, D.; Colliere, V.; Behra, P.; Gros, P., Influence of the gold nanoparticles electrodeposition method on Hg(II) trace electrochemical detection. *Electrochim Acta* **2012,** *73*, 15-22.

35. Dai, Y. F.; Wang, C. L.; Chiu, L. Y.; Abbasi, K.; Tolbert, B. S.; Sauve, G.; Yen, Y.; Liu, C. C., Application of bioconjugation chemistry on biosensor fabrication for detection of TAR-DNA binding protein 43. *Biosens Bioelectron* **2018,** *117*, 60-67.

36. Ghanei-Motlagh, M.; Taher, M. A., A novel electrochemical sensor based on silver/halloysite nanotube/molybdenum disulfide nanocomposite for efficient nitrite sensing. *Biosens Bioelectron* **2018,** *109*, 279-285.

37. Huang, X.; Li, Y. X.; Chen, Y. L.; Wang, L., Electrochemical determination of nitrite and iodate by use of gold nanoparticles/poly(3-methylthiophene) composites coated glassy carbon electrode. *Sensor Actuat B-Chem* **2008,** *134* (2), 780-786.

38. Sun, L. P.; Li, H. J.; Li, M. J.; Li, P.; Li, C. P.; Yang, B. H., Simultaneous Determination of Small Biomolecules and Nitrite Using an Au/TiO_2/Carbon Nanotube Composite-Modified Electrode. *J Electrochem Soc* **2016,** *163* (13), B567-B572.

39. Huang, H. P.; Yue, Y. F.; Li, L. L.; Zhu, J. J., Rare Earth Oxide Dy_2O_3-Au Nanocomposite-Based Electrochemical Sensor for Sensitive Determination of Nitrite. *J Electrochem Soc* **2017,** *164* (6), H321-H325.

Chapter 5 The mechanism of electrochemical reduction of hydrogen peroxide on silver nanoparticles

Although the hydrogen peroxide (H_2O_2) reduction on silver electrodes has been widely investigated, it is an open question of great significance and interest to discern the mechanism of this process. In this chapter, the reduction of hydrogen peroxide on a silver nanoparticle modified boron doped diamond electrode in a neutral solution is shown to proceed through a CE mechanism, where the a chemical reaction takes places before the electron transfer reaction using "C" and "E" formalism, respectively. Hydrogen peroxide undergoes a disproportionation reaction to form oxygen (and water) on the silver surface, creating a diffusion layer of oxygen, which, at a sufficiently biased electrode, is then reduced to hydrogen peroxide. Voltammetry and a full mechanistic simulation are undertaken to confirm the mechanism, showing at short times a dependence of the reductive signal on waiting time prior to voltammetric analysis reflecting the extent of the disproportionation step which occurs prior to voltammetric analysis.

The work presented in this chapter has been published in *Physical Chemistry Chemical Physics*.[1]

5.1 Introduction

The reduction of hydrogen peroxide on silver electrodes has been extensively studied, with over 159 papers published on the subject since 2005, when Welch *et al.*[2] reported the electrochemical detection of hydrogen peroxide using a silver nanoparticle modified glassy carbon electrode. A review of hydrogen peroxide detection on metal nanoparticles was published in 2013 by Chen *et al.*,[3] and in the last two years alone a number of papers have

been published on the subject,[4-5] including investigating the effect of modifying the nanoparticles,[6-7] the pH[8-9] and the carbon electrode.[10-15]

Determining the mechanism of this process is an open question with high interest due to the fact that different mechanisms operate depending on the context (for example the electrode material and pH). The most commonly proposed mechanism in acidic and neutral conditions is usually *assumed* to be:

$$H_2O_2 + H^+ + e^- \rightarrow OH_{ads} + H_2O \quad (5.1)$$

$$H^+ + OH_{ads} + e^- \rightarrow H_2O \quad (5.2)$$

The vast majority of studies investigating hydrogen peroxide reduction (including those cited above) are analytically or applications focused and presume the above process holds true. Understanding the mechanism operating is critical to optimising any application that relies on hydrogen peroxide reduction.

In particular, the possible role of oxygen reduction in this process has not yet been examined, despite the fact that oxygen reduction on silver in neutral aqueous media, as studied in detail by Neumann *et al.*,[16] has been shown to proceed through a 2 electron reduction to hydrogen peroxide, and that the latter is known to disproportionate on silver.

Consequently in this chapter we consider an alternative mechanism for hydrogen peroxide reduction – a CE process involving an initial disproportionation of the hydrogen peroxide into oxygen that is followed by an electron transfer:

$$H_2O_2 \rightarrow 1/2O_2 + H_2O \quad (5.3)$$

$$O_2 + 2e^- + 2H^+ \rightarrow H_2O_2 \quad (5.4)$$

This mechanism is herein investigated in the context of silver nanoparticle modified boron doped diamond electrodes (BDDE) and supported by simulations, providing strong evidence that a CE reaction with an oxygen reduction step is the mechanism operating in neutral pH for the reduction of hydrogen peroxide on silver nanoparticle modified electrodes.

5.2 Theory and Simulation

All the simulations presented in this chapter were performed by Dr. Chuhong Lin.

The CE electrode reaction under consideration contains two parts. Before applying the potential to the electrode, the hydrogen peroxide in the solution reacts to form oxygen at the surface of the silver catalyst:

$$H_2O_2 \xrightarrow{k_{het}} H_2O + \frac{1}{2}O_2 \qquad (5.3)$$

where k_{het} is the heterogeneous disproportionation rate constant (m s^{-1}). We assume that the oxidation of the hydrogen peroxide occurs at a time $t = 0$, corresponding to insertion of the electrode into the solution. The working electrode is at open circuit during the waiting time before the voltammetry scan. Subsequently a reductive voltammetric scan is initiated at a time t_{het} (s) leading to the reduction of the product oxygen:

$$O_2 + 2e^- + 2H^+ \xrightarrow{k_0;\alpha} H_2O_2 \qquad (5.4)$$

where k_0 is the electron transfer rate constant (m s^{-1}) and α is the transfer coefficient.[17-18] Note H_2O_2 is assumed not to be active at the potentials required for the reduction of O_2.

Assuming that there is enough amount of electrolyte in the solution and the experimental time is rather short, the influence of the migration and convection can be ignored.[19-20] So that the change of the concentration in the solution is only driven by diffusion. As the

electrode used in the experiments reported below is relatively large compared to the diffusion layer, and the coverages of nanoparticles used are approximately mono-layers,[21-24] we only need to consider diffusion that is perpendicular to the plane of the electrode surface.[25] Therefore, the three-dimensional electrode system can be simplified to a one-dimension problem. Fick's second law for the one-dimensional diffusion equation is:[26]

$$\frac{\partial c(t,x)}{\partial t} = D\frac{\partial^2 c(t,x)}{\partial x^2} \qquad (5.5)$$

where c (t, x) is the concentration (mol m^{-3}, mM), calculated as a function of the reaction time t (s) and the space distance x (m). x represents the dimension perpendicular to the electrode. D is the diffusion coefficient (m^2 s^{-1}).

During the heterogeneous disproportionation reaction ($t < t_{wait}$, t_{wait} is the time of waiting before implementing the linear potential sweep to the electrode), the reaction rate equations of H_2O_2 and O_2 at the electrode surface are expressed as:

$$D_{H_2O_2}\frac{\partial c_{H_2O_2}(t,x)}{\partial x}\Big|_{x=0} = k_{het}c_{H_2O_2}(t, x=0) \qquad (5.6)$$

$$D_{O_2}\frac{\partial c_{O_2}(t,x)}{\partial x}\Big|_{x=0} = -\frac{1}{2}k_{het}c_{H_2O_2}(t, x=0) \qquad (5.7)$$

x = 0 corresponds to the electrode surface where the reactions occur. After the electrochemical reaction starts ($t > t_{wait}$), the rate equations change to:

$$D_{H_2O_2}\frac{\partial c_{H_2O_2}(t,x)}{\partial x}\Big|_{x=0} = k_{het}c_{H_2O_2}(t, x=0) - k_0'\exp\left(\frac{-\alpha F(E-E_f)}{RT}\right)c_{O_2}(t, x=0) \qquad (5.8)$$

$$D_{O_2}\frac{\partial c_{O_2}(t,x)}{\partial x}\Big|_{x=0} = -\frac{1}{2}k_{het}c_{H_2O_2}(t, x=0) + k_0'\exp\left(\frac{-\alpha F(E-E_f)}{RT}\right)c_{O_2}(t, x=0) \qquad (5.9)$$

where E is the applied electrode potential (V), E_f is the formal potential of redox couple H_2O_2/O_2, F is the Faraday constant (96485 C mol^{-1}), T is the room temperature (298 K),

and R is the gas constant (8.314 J·mol^{-1}·K^{-1}). The electron transfer is described by the Butler-Volmer equation,[27-28] assuming that the electron transfer is fully irreversible and k_0' is the effective standard electron transfer rate constant. To simulate the cyclic voltammetry applied in the experiment, the applied potential in the potential window [E_{ini}, E_{rev}] is expressed as a function of electrochemical reaction time t_{el} ($t_{el} = t - t_{wait}$) and the scan rate v (V s^{-1}):

$$E = \begin{cases} E_{ini} - vt_{el}, \ t_{el} \leq \frac{|E_{ini} - E_{rev}|}{v} \\ E_{rev} + v\left(t_{el} - \frac{|E_{ini} - E_{rev}|}{v}\right), \ t_{el} > \frac{|E_{ini} - E_{rev}|}{v} \end{cases} \qquad (5.10)$$

By solving the diffusion equation (Eqn. 5.5) with the boundary conditions (Eqn. 5.6-5.9), the concentration functions of H_2O_2 and O_2 can be derived. Therefore, the current I (A) measured at the electrode can be calculated from:

$$I = 2FSD_{O_2} \frac{\partial c_{O_2}(t,x)}{\partial x}\Big|_{x=0} \qquad (5.11)$$

where S refers to the surface area of the electrode.

The resulting problem was solved numerically by means of the LU decomposition method, the details of which can be found in the literature.[25] The simulation programme was written by Dr. Lin in Matlab R2017a and performed using an Intel(R) Xeon(R) 3.60G CPU.

Figure 5.1 shows two example cyclic voltammograms and the corresponding scan rate dependence simulated from the above model. The disproportionation rate constant of hydrogen peroxide decomposition at the electrode is set to be 10^{-5} m s^{-1} (see below); the initial concentration of hydrogen peroxide is 1.0 mM; the diffusion coefficients of hydrogen peroxide and oxygen are found in the literature to be 1.43 x 10^{-9} and 1.96 x 10^{-9} m^2 s^{-1} in room temperature, respectively; [29-31] as oxygen reduction reaction is irreversible,

the effective electron transfer k_0' is set to be 10^{-7} m s^{-1}, the transfer coefficient is 0.3 and each oxygen transfers two electrons during the reduction. In Figure 5.1a, the waiting times before commencing the linear potential sweep to the electrode t_{wait} are set to be 20 s (the blue line) and 300 s (the red line). The scan rate is 0.05 V s^{-1} in Figure 5.1a. The voltammograms of 20s and 300s t_{wait} have similar waveshapes but a longer t_{wait} leads to a much larger reaction current. In Figure 5.1b, the peak currents of 20s and 300s t_{wait} simulated with various scan rates are compared with the case of irreversible two-electron transfer reaction. The peak current for an irreversible *n* electron transfer is calculated from the Randles-Ševčík equation[32] and shown by the black line in Figure 5.1b:

$$i_p = 2.99 \times 10^5 SD^{0.5} Cv^{0.5} n(n' + \alpha)^{0.5} \quad (5.12)$$

where *v* is the scan rate, *C* is the concentration of the reactant, *D* is the diffusion coefficient of the reactant, *n* is the electrons transferred corresponding to one reactant (*n* = 2), *n'* is the electron transferred before the rate-determining step (we infer *n*' = 0). From Figure 5.1b, it is found that for fast scan rates, the peak current based on the CE mechanism deviates from the Randles-Ševčík equation for a simple two-electron transfer reaction. This is because that in a CE reaction, the preceding chemical step sets up a reaction layer adjacent to the electrode surface where the redox species is generated for the following electrochemical reaction. At high scan rates, when the chemical reaction rate is slower than the diffusion speed, the reaction is controlled by the preceding chemical step and the current is smaller than the diffusion-limited value as predicted in Eqn. 5.12.

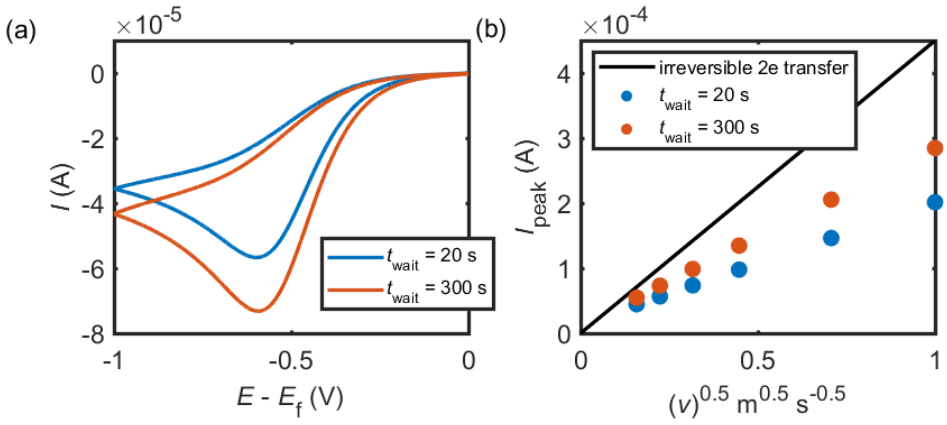


Figure 5.1 (a) Simulated cyclic voltammograms based on the theoretical model with a waiting time of 20s (the blue line) and 300 s (the red line); (b) Scan rate dependence of the peak currents. The black line is the calculated peak current for an irreversible two electron transfer reaction. Blue and red marks correspond to the simulation of 20 s and 300 s waiting times.

Figure 5.2 are the concentration profiles of O_2 related to the two reactions in Figure 5.1 as a function of the reaction time and the space distance. Figure 5.2a and 5.2b are the concentration profiles with 20 s and 300 s t_{wait}, respectively. To show the concentration variation clearly, each concentration profile is divided into two parts: the left part corresponds to the heterogeneous disproportionation reaction of hydrogen peroxide, where a layer of oxygen is generated adjacent to the electrode surface (x = 0), and the right part is the time during the cyclic voltammetry, where the generated oxygen is reduced at the electrode. In the time period of the heterogeneous disproportionation reaction, the layer of generated O_2 of the 300s t_{wait} in Figure 5.2b is broader than that of the 20s t_{wait}, reflecting on the larger reaction current of the 300s t_{wait} in Figure 5.1a.

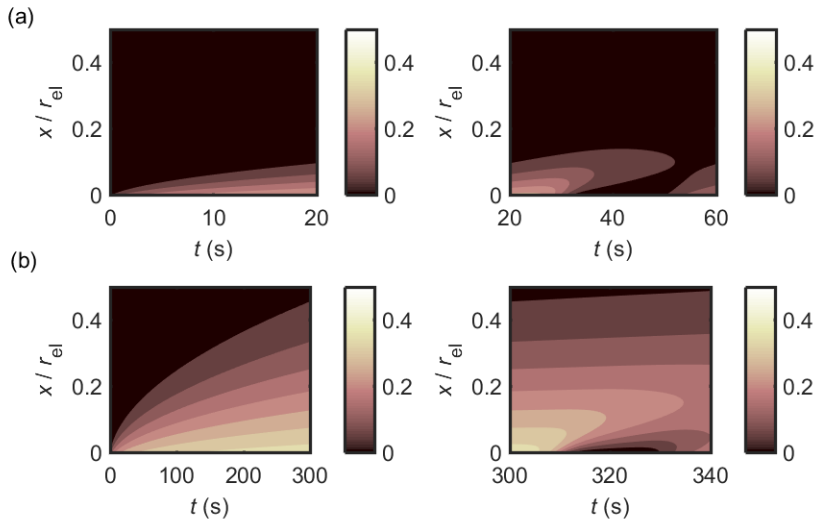


Figure 5.2 (a) Concentration profile of O_2 with 20 s waiting time; (b) Concentration profile of O_2 with 300 s waiting time. The concentration profile corresponds to the cyclic voltammograms in Figure 5.1a.

5.3 Experimental

5.3.1 Chemical reagents

The chemical reagents monosodium phosphate (NaH_2PO_4, ≥ 99.0%), disodium phosphate (Na_2HPO_4, ≥ 99.0%) and silver nanoparticles (AgNPs) dispersion were purchased from Sigma-Aldrich. The AgNPs with a diameter of 10 nm and concentration of 0.02 mg/mL were capped by sodium citrate (as supplied). The transmission electron microscopy image can be found from the website[33] of AgNPs product, confirming the presence of the nanoparticles. Hydrogen peroxide was obtained from Fisher Scientific International, Inc. All the reagents were used as received without any further purification. All solutions were prepared with ultrapure water (18.2 MΩ cm at 25 °C, Millipore, MA, USA)

5.3.2 Apparatus and electrochemical measurements

Electrochemical experiments were conducted with an Autolab PGSTAT128N potentiostat (Metrohm Autolab, Utrecht, Netherlands) and NOVA software. A three-electrode

configuration was used consisting of a platinum (Pt) coil counter electrode and a Ag/AgCl reference electrode along with a boron-doped-diamond working electrode described below. A 0.1 M phosphate buffer solution (PBS, pH = 7.2) was used as the electrolyte for all experiments. Degassed solutions were bubbled with N_2 for 15 min, whilst oxygenated solutions were saturated with compressed air.

5.3.3 Electrode modification

The boron-doped-diamond wafer (Element Six Co.) with a boron doping concentration of ~ 5×10^{20} atoms cm^{-3} was used as the working electrode, and mounted in a home-made polytetrafluoroethylene (PTFE) holder as previously described[34] with a circular area of 0.37 cm^2 exposed to the electrolyte. Prior to each use, the boron-doped-diamond electrode was polished using alumina powder (Buehler, MicroPolish II) in the particle size sequence of 1 µm, 0.3 µm and 0.05 µm and diamond suspension (Buehler, MetaDi) in the size of 9 µm, 1 µm and 0.1 µm on lapping pads to ensure a clean surface.[35] To modify the BDDE, 100 µL of AgNPs dispersion was drop-cast onto the BDDE surface and allowed to dry to form the electrode herein referred to as AgNPs-BDDE. The surface morphology of the silver-modified BDDE was characterized by a Hitachi S-4300 field emission scanning electron microscopy (SEM) with a 20 kV acceleration voltage.

5.4 Results and Discussion

This section outlines the successful modification of a boron-doped-diamond electrode with silver nanoparticles, followed by a report of the voltammetry in the presence (and absence) of hydrogen peroxide and oxygen. A full mechanistic simulation is used to interpret the experimental voltammetry.

Under monolayer conditions, the diffusion layers of neighbouring AgNPs overlap heavily and consequently a monolayer coverage of nanoparticles will lead to a voltammetric

response corresponding closely to 1D linear diffusion to the geometric area of the substrate.[21] Low coverage results in the local change of mass transport[36] while high coverage leads to aggregation and porosity.[37-38] Therefore in this work a monolayer coverage is only considered to avoid introducing a further variable so as to focus on the H_2O_2 reduction mechanism. A boron-doped-diamond electrode was modified by placing 100 µL of a suspension containing 0.02 mg/mL 10 nm (diameter) silver nanoparticles (corresponding to 3.6×10^{11} nanoparticles, or *ca.* one monolayer coverage) onto the surface and allowing it to dry. The modified electrode was then characterised by scanning electron microscopy. Figure 5.3 shows an SEM image of silver modified BDDE. The particles are dispersed over the surface, demonstrating the successful modification of the electrode.

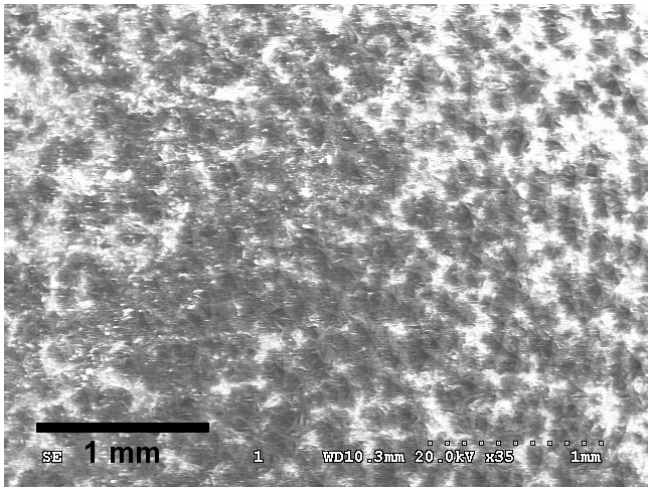


Figure 5.3 SEM of AgNPs-BDDE under 35× magnification.

The modified electrode was then immersed for *ca.* 15 minutes in a degassed solution containing PBS buffer and increasing concentrations (0 – 19.2 mM) of hydrogen peroxide. A cyclic voltammogram (CV) was recorded by sweeping the potential from 0.0 V to -1.0 V vs Ag/AgCl at a scan rate of 0.05 V s^{-1} (Figure 5.4). In the presence of hydrogen peroxide, a peak appears on the forward scan at *ca.* - 0.6 – -0.9 V vs Ag/AgCl (with a peak potential

of -0.6 V in concentrations ≤ 1.2 mM), and the reductive peak current increases linearly (see Figure 5.4c) with the hydrogen peroxide concentration.

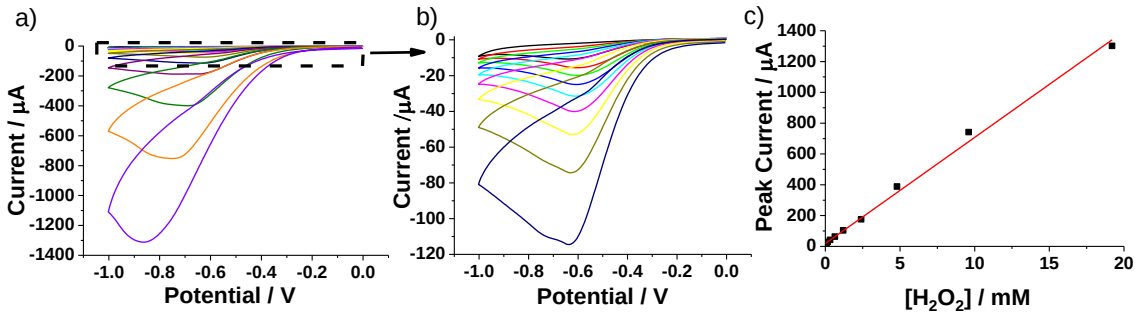
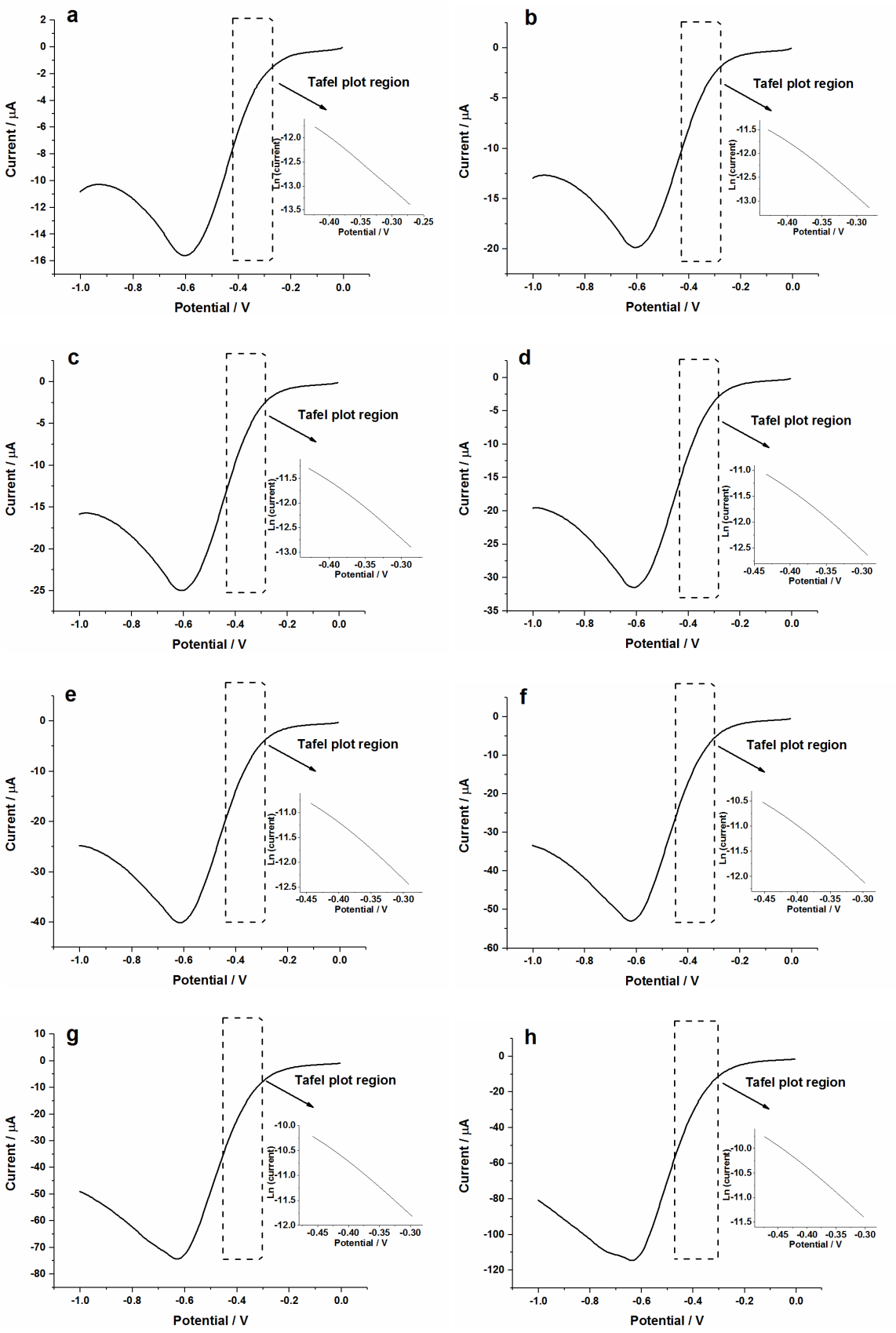


Figure 5.4 CVs of AgNPs-BDDE measured after ca. 15 minutes immersion in N_2-saturated PBS with H_2O_2 at a concentration of a) 0 mM (black), 0.01 mM (red), 0.02 mM (green), 0.04 mM (blue), 0.08 mM (cyan), 0.16 mM (magenta), 0.32 mM (yellow), 0.64 mM (dark yellow), 1.2 mM (navy), 2.4 mM (purple), 4.8 mM (olive), 9.6 mM (orange), and 19.2 mM (violet). b) is the zoomed-in area for lower H_2O_2 concentrations, c) is the peak current (baseline corrected) plotted against the hydrogen peroxide concentration, with $R^2 = 0.996$.

Having established the response of AgNPs-BDDE in the presence of hydrogen peroxide, further analysis of the voltammetry was performed in order to understand the electron transfer process. Tafel analysis was performed on the voltammograms (averaging data from 3 experiments at each concentration, shown in Figure 5.5), with the slope and the corresponding transfer coefficient α, being reported in Table 5.1. The average α value was calculated to be 0.26 ± 0.04 across all concentrations.


a
Tafel plot region
Current / μA
Potential / V
Ln (current)
Potential / V
b
Tafel plot region
Current / μA
Potential / V
Ln (current)
Potential / V
c
Tafel plot region
Current / μA
Potential / V
Ln (current)
Potential / V
d
Tafel plot region
Current / μA
Potential / V
Ln (current)
Potential / V
e
Tafel plot region
Current / μA
Potential / V
Ln (current)
Potential / V
f
Tafel plot region
Current / μA
Potential / V
Ln (current)
Potential / V
g
Tafel plot region
Current / μA
Potential / V
Ln (current)
Potential / V
h
Tafel plot region
Current / μA
Potential / V
Ln (current)
Potential / V

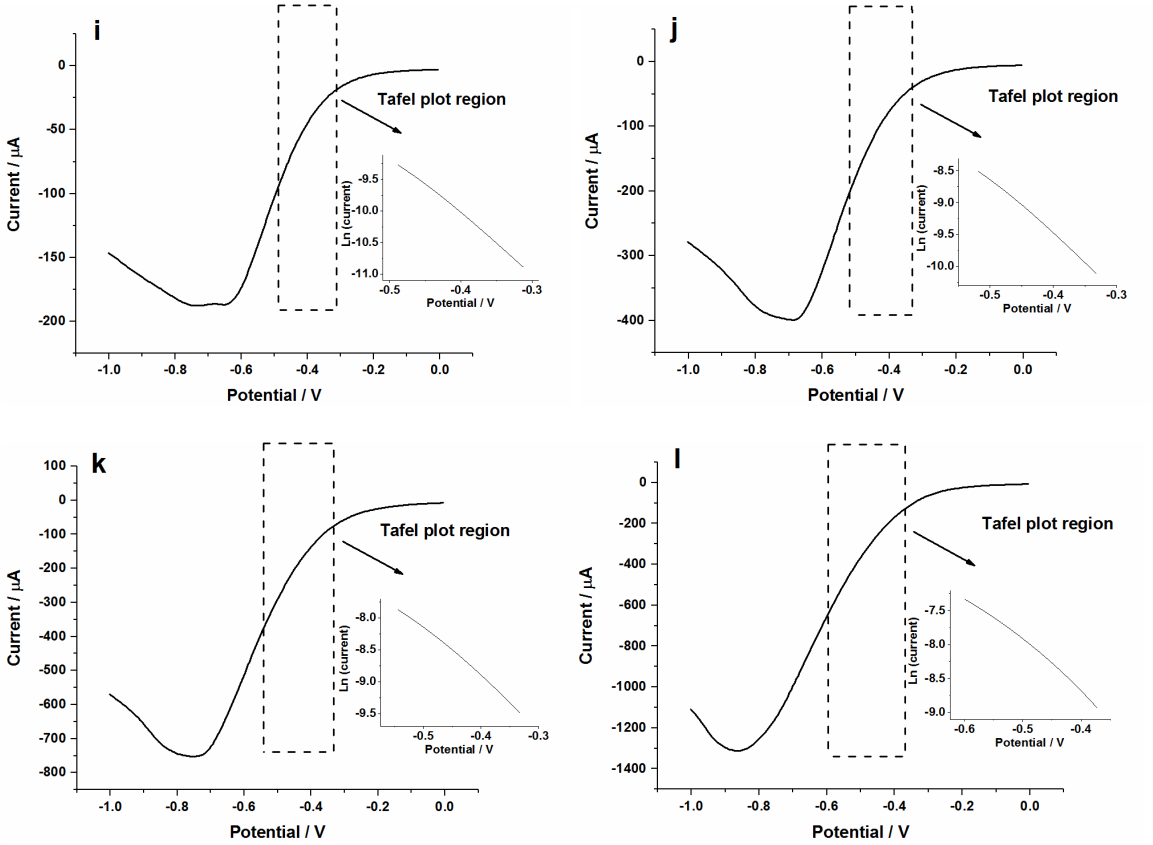


Figure 5.5 Tafel plots for AgNPs-BDDE recorded at a scan rate of 0.05 V s^{-1} with variable H_2O_2 concentrations of 0.01 mM (a), 0.02 mM (b), 0.04 mM (c), 0.08 mM (d), 0.16 mM (e), 0.32 mM (f), 0.64 mM (g), 1.2 mM (h), 2.4 mM (i), 4.8 mM(j), 9.6 mM (k), and 19.2 mM (l).

Table 5.1 The measured transfer coefficient ($\alpha = 0.26 \pm 0.04$) according to the Tafel slopes with the increasing H_2O_2 concentration for AgNPs-BDDE recorded at a scan rate of 0.05 V s^{-1}.

H_2O_2 concentration (mM)	Tafel slope	α	α (average)
0.01	-10.4 ± 0.38	0.27 ± 0.0097	0.26 ± 0.04
0.02	-11.2 ± 0.22	0.29 ± 0.0057	

0.04	-11.2 ± 0.23	0.29 ± 0.0059
0.08	-10.9 ± 0.24	0.28 ± 0.0062
0.16	-10.5 ± 0.34	0.27 ± 0.0086
0.32	-10.1 ± 0.38	0.26 ± 0.0098
0.64	-9.6 ± 0.45	0.25 ± 0.011
1.2	-9.2 ± 0.47	0.24 ± 0.012
2.4	-8.9 ± 0.55	0.23 ± 0.014
4.8	-8.3 ± 0.39	0.21 ± 0.010
9.6	-7.4 ± 0.38	0.19 ± 0.010
19.2	-6.9 ± 0.34	0.18 ± 0.010

Using the transfer coefficient obtained above, insight into the number of electrons transferred can be achieved through theoretically predicting the peak current using the Randles-Ševčík equation for irreversible electron transfer Eqn. 5.12. When varying the hydrogen peroxide concentration from 0 to 20 mM, the corresponding peak currents are measured and compared to the theoretical Randles-Ševčík peak currents. In the experiment, the electrode area of BDDE is 3.7 x 10^{-5} m^2, the scan rate is 0.05 V s^{-1}, the diffusion coefficient is 1.43 x 10^{-9} m^2 s^{-1}, and the transfer coefficient is 0.26. Figure 5.6 shows the theoretically calculated peak currents based on the above parameters with different values for the number of electrons transferred (n = 2, red and n = 4, green) compared with the experimental peak currents (black). The experimental peak currents show close agreement

with the calculated values for a two electron transfer, indicating this to be the likely number of electrons transferred during the process. Note that for this to be true, the layer of oxygen adjacent to the electrode needs to be much greater than the diffusion layer around the electrode during the voltammetric sweep. This condition is set by the time of waiting used in the experiment reported above.

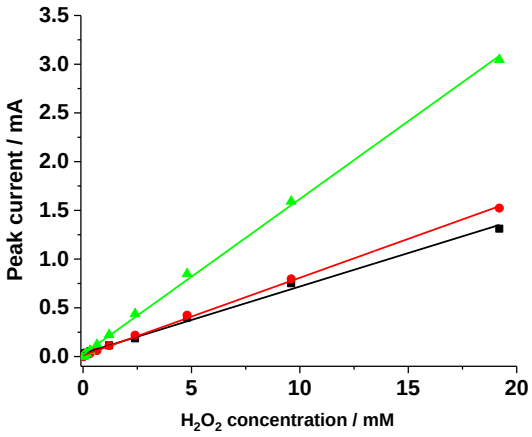


Figure 5.6 Plots of the experimental (black) and theoretical peak currents (red is n=2, and green is n=4) vs. H_2O_2 concentration.

If the postulated mechanism for the electroreduction of hydrogen peroxide broadly accepted in the literature,[4-8] whereby hydrogen peroxide is first reduced to an adsorbed hydroxide ($OH_{(ads)}$) before being reduced to water (Eqn. 5.1 and 5.2), operates, one might expect oxygen reduction to be largely unrelated to the voltammetry produced from hydrogen peroxide. In order to test the mechanism proposed in Eqn. 5.3 and 5.4, solutions containing PBS in the *absence* of hydrogen peroxide were saturated with air.

A modified electrode was then immersed in a solution of PBS saturated with air, and a CV was recorded by sweeping the potential from 0.0 V to -1.0 V vs Ag/AgCl. Figure 5.7 shows the current response obtained at different scan rates from 0.01 to 0.2 V s^{-1}. In each case, a peak at *ca.* -0.6 – -0.7 V appeared on the forward scan. The plot of peak current versus the

square root of scan rate in the inset of Figure 5.7 is linear, indicating it is a diffusion controlled process.

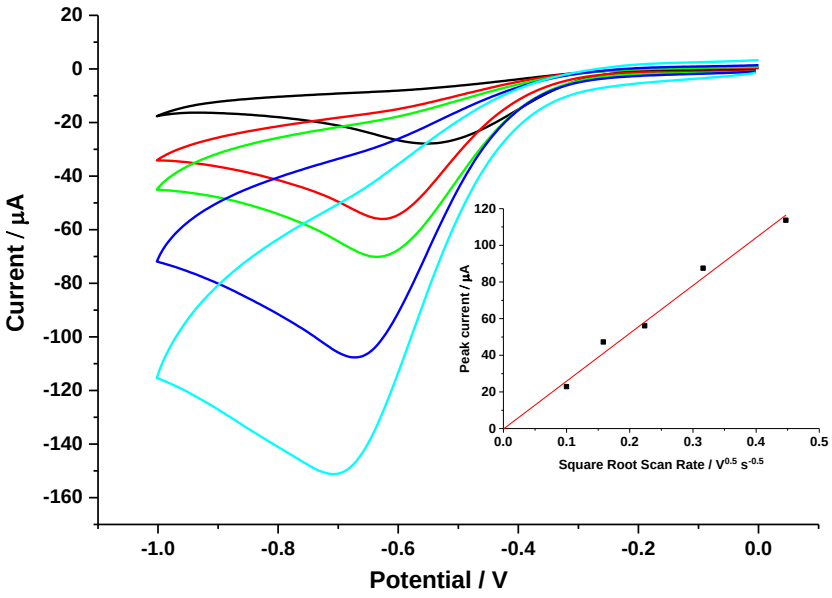


Figure 5.7 Cyclic voltammogram of AgNPs-BDDE in air-saturated PBS solution at 0.01 V s^{-1} (black), 0.025 V s^{-1} (red), 0.05 V s^{-1} (green), 0.1 V s^{-1} (blue), and 0.2 V s^{-1} (cyan). Inset is the plot of peak current vs square root of the scan rate.

To characterise the electron transfer process, Tafel analysis for the above process was once again undertaken on the experimental voltammetry (n = 3, Figure 5.8), and the mean and the errors are listed in Table 5.2. The mean transfer coefficient, α, was calculated from the Tafel slopes to be 0.28 ± 0.03.

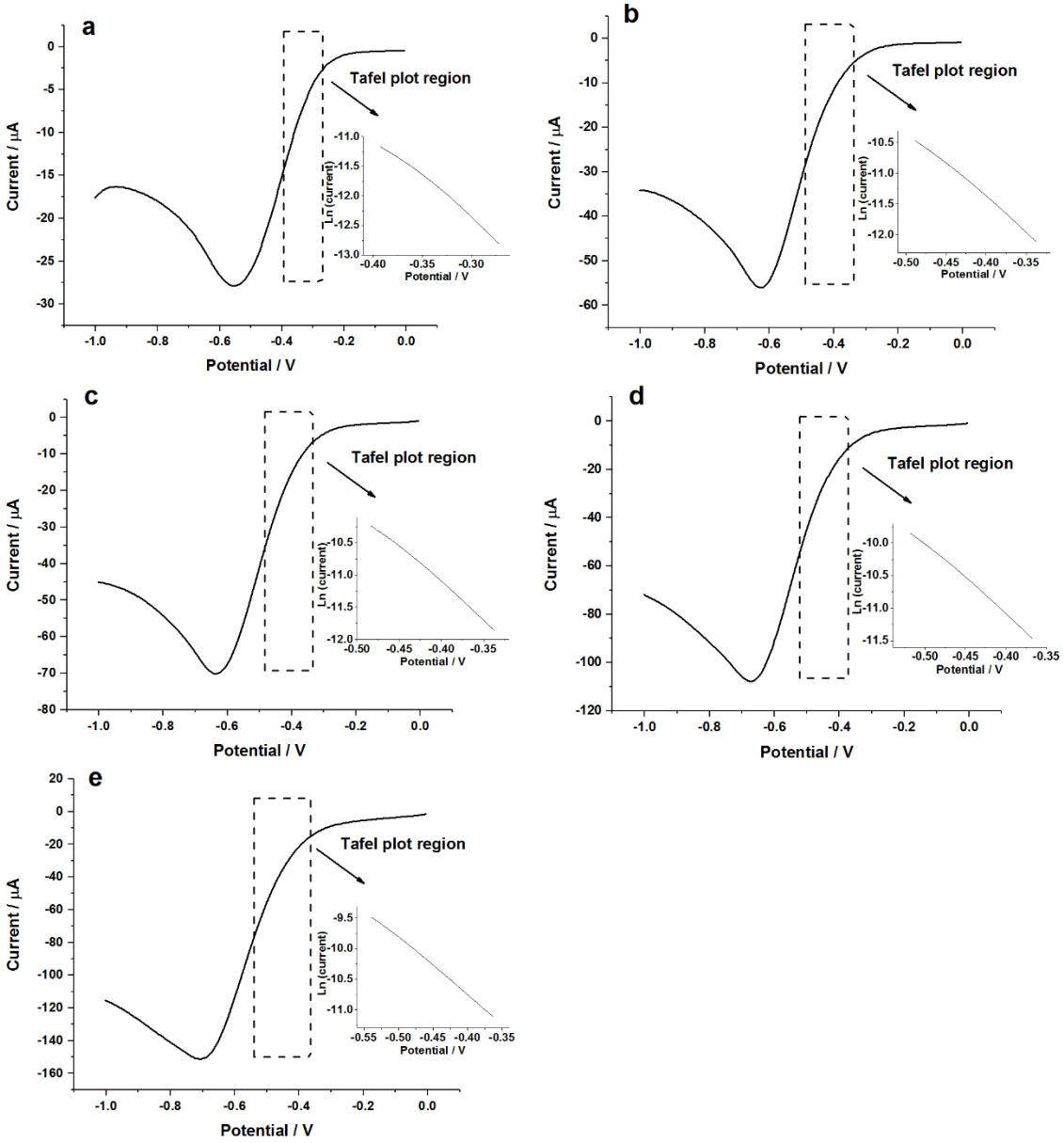


Figure 5.8 Tafel plots for AgNPs-BDDE in air-saturated PBS solution recorded at different scan rates of 0.01 V s^{-1} (a), 0.025 V s^{-1} (b), 0.05 V s^{-1} (c), 0.1 V s^{-1} (d), and 0.2 V s^{-1} (e).

Table 5.2 The measured transfer coefficient ($\alpha = 0.28 \pm 0.03$) according to the Tafel slopes from 0.01 to 0.2 V s^{-1} for AgNPs-BDDE in air-saturated PBS solution.

Scan rate (V s^{-1})	Tafel slope	α	α (average)
0.01	-13.1 ± 0.74	0.34 ± 0.019	0.28 ± 0.03
0.025	-11.3 ± 0.31	0.29 ± 0.0079	
0.05	-10.6 ± 0.63	0.27 ± 0.016	
0.1	-10.6 ± 0.19	0.27 ± 0.0049	
0.2	-9.6 ± 0.18	0.25 ± 0.0045	

The Randles-Ševčík equation for irreversible electron transfers can be once again utilized to predict the theoretical current response, setting $D = 1.96 \times 10^{-9}$ m^2 s^{-1}, and $C = 0.26$ mM.[31] Figure 5.9 shows the calculated peak currents (n=2, red and n=4, green) and the experimental peak currents (black). Excellent agreement is observed with the theoretical prediction for the oxygen reduction reaction involving an approximately four electron transfer process, leading to the formation of water. It has been reported that oxygen can be reduced either by a direct 4-electron pathway (Eqn. 5.13):[39]

$$O_2 + 4H^+ + 4e^- \rightarrow 2H_2O \qquad (5.13)$$

or by two 2-electron processes (Eqn. 5.4, reproduced below, and 5.14) where two electrons are transferred sequentially with hydrogen peroxide production as an oxygen reduction reaction (ORR) intermediate:[2-3]

$$O_2 + 2e^- + 2H^+ \rightarrow H_2O_2 \qquad (5.4)$$

$$H_2O_2 + 2H^+ + 2e^- \rightarrow 2H_2O \qquad (5.14)$$

The first electron transfer to produce the superoxide ion ($O_2^{\bullet-}$) is reported to be the rate determining step.[40]

Furthermore, the kinetics of ORR on silver nanoparticles supported on glassy carbon have been investigated.[16] The voltammetry of ORR was described very satisfactorily with a two-proton, two-electron reduction process yielding H_2O_2. Moreover, the hydrogen peroxide has been directly detected as an oxygen reduction intermediate for silver electrode using scanning electrochemical microscopy.[41] It demonstrates that the amount of hydrogen peroxide is related to number of electrons transferred and n varies as a function of potential.

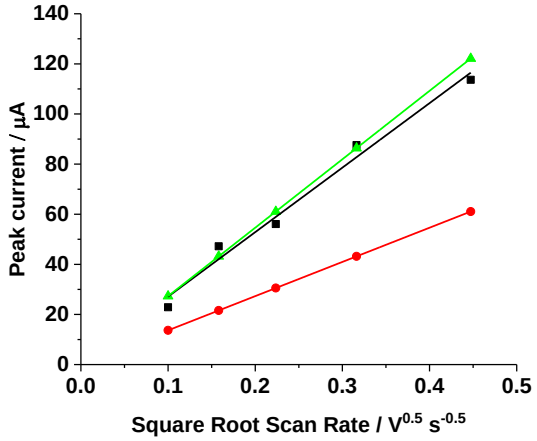


Figure 5.9 Plot of the experimental (black) and theoretical peak currents (red is n=2, and green is n=4) vs square root scan rate in air-saturated PBS solution.

Having investigated the electron transfer processes for both oxygen and hydrogen peroxide reduction, we next compare these two processes and investigate whether oxygen reduction plays a role in the hydrogen peroxide reduction. Figure 5.10 shows overlaid experimental voltammograms of oxygen in the absence of hydrogen peroxide (black), and degassed PBS in the presence of different hydrogen peroxide concentrations (0.16 mM (red), 0.32 mM

(green), and 0.64 mM (blue)). In terms of waveshape, the voltammograms look very similar, and the peak potentials of both processes are the same within experimental error, namely E_p = -0.62 ± 0.01 V and E_p = -0.63 ± 0.01 V for hydrogen peroxide and oxygen respectively. Combining this information with the similar transfer coefficient values of 0.26 ± 0.04 and 0.28 ± 0.03 for the reduction of hydrogen peroxide and oxygen reduction respectively, suggests that the electron transfer step in the reduction of hydrogen peroxide plausibly involves oxygen, O_2.

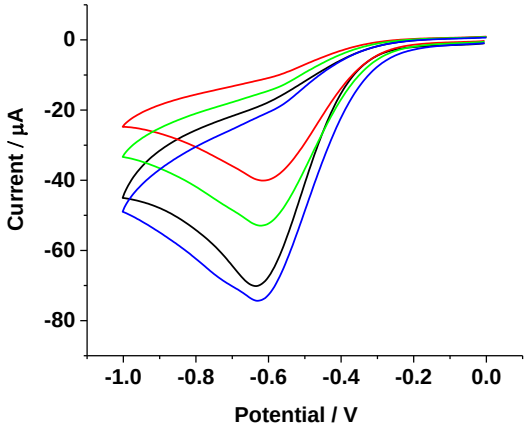


Figure 5.10 CV recorded on AgNPs-BDDE at a scan rate of 0.05 V s^{-1}. Black is in air-saturated PBS at 0 mM H_2O_2, while others are in N_2-saturated PBS at different H_2O_2 concentrations of 0.16 mM (red), 0.32 mM (green), and 0.64 mM (blue).

To further test the proposed mechanism outlined in Eqn. 5.3 and 5.4, a time dependency study was undertaken. The disproportionation of hydrogen peroxide on silver (outlined in Eqn. 5.3) is relatively slow[16] and so time is required to saturate the diffusion layer adjacent to the electrode. Hence if the suggested mechanism operates, the peak current would be expected to increase with the time that the hydrogen peroxide is in contact with the electrode up to a limiting value corresponding to a thick layer of O_2 adjacent to the electrode. Not only this, but the wave shape would differ from that observed from an E

mechanism. Note that previous investigations of this mechanism neglected to account for any effect of the time, and produced a composite rate constant of $k_0 \exp\left(-\frac{\alpha F E_f}{RT}\right)$ (at presumably long time scales) describing the reduction of H_2O_2 *via* an adsorbed hydroxide intermediate of 0.4 cm s^{-1}.[36]

A modified electrode was submerged into a degassed PBS solution containing 0.32 mM H_2O_2. After a predetermined waiting time (from 5 seconds to 15 minutes), a CV was recorded by sweeping the potential from 0.0 V to -1.0 V vs Ag/AgCl at a scan rate of 0.05 V s^{-1} (Figure 5.11a). Figure 5.11b is the plot of average peak current *vs* waiting time. It shows that the peak current increases the longer the electrode is in contact with hydrogen peroxide before the scan is recorded. This indicates the distinct probability of a catalytic decomposition of hydrogen peroxide on the silver surface. As the hydrogen peroxide is chemically decomposed into oxygen, more oxygen accumulates adjacent to the electrode, and it is this oxygen that is then reduced. If hydrogen peroxide was reduced to water (as in Eqn. 5.14), it would be anticipated that the peak current should be independent of waiting time, further supporting the proposed mechanism in Eqn. 5.3 and 5.4.

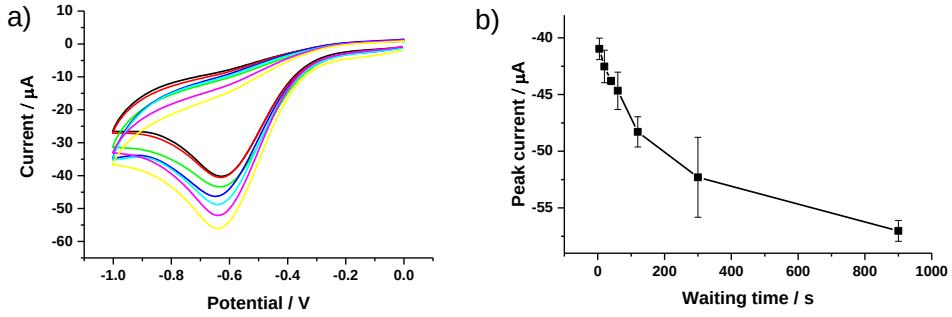


Figure 5.11 a) CV of AgNPs-BDDE in N_2-saturated PBS containing 0.32 mM H_2O_2 after different interacting time between Ag and H_2O_2 at a scan rate of 0.05 V s^{-1}. Black is 5 s, red 20 s, green 40 s, blue1 min, cyan 2 min, magenta 5 min, and yellow 15 min. b) is the plot of peak current vs waiting time.

To better understand the proposed mechanism, a simulation to the voltammograms in Figure 5.12 was performed (as detailed in the Theory section). Figure 5.12 shows the experimental voltammetry (black) compared with simulated voltammetry (red), where the kinetic parameters k_{het}, k_0' and α were optimised to take values of $8x10^{-6}$ m s^{-1}, $1x10^{-7}$ m s^{-1}, and 0.3 respectively, over a range of waiting times t_{wait}. To present the dependence of the reaction current on the waiting time, the currents measured from experiment and calculated from simulation are normalized by the experimental peak current of 900 s t_{wait} and the simulated peak current of 900 s t_{wait}, respectively. It shows in Figure 5.12 that the simulation fits the time dependence well with above kinetic parameters. The value of k_{het} is approximately one order of magnitude slower than inferred in the literature[16] for significantly larger sized silver nanoparticles, partly suggesting a size effect on the chemical disproportionation reaction.

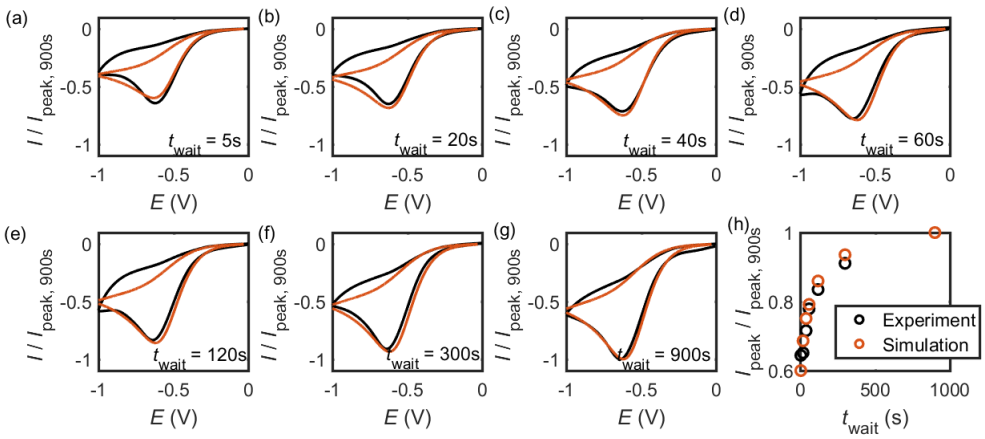


Figure 5.12 (a)-(g) Cyclic voltammograms from experiment (black) and simulation (red) with various waiting time t_{wait}; (h) Time dependence of the peak currents as a function of waiting time t_{wait}. The experiment and simulation currents are normalized by the experimental and simulated peak currents of the 900s t_{wait}, respectively.

The variance of the peak current with waiting time, and the close resemblance of the voltammetry of oxygen and hydrogen peroxide (both in terms of peak potentials and transfer coefficients), combined with the close agreement of the simulation with the experimental voltammetry provide strong evidence for the reduction of hydrogen peroxide on silver occurring *via* a CE mechanism at neutral pH. This mechanistic insight is likely to prove valuable in the applications of hydrogen peroxide reduction broadly, and represents a significant advancement in our understanding of the electrochemical process.

5.5 Conclusions

The reduction of hydrogen peroxide on silver nanoparticle modified BDD electrodes is concluded to follow a CE mechanism, whereby the hydrogen peroxide decomposes to oxygen, and the oxygen is electrochemically reduced to hydrogen peroxide as shown in Figure 5.13. The hydrogen peroxide produced may be reduced simultaneously with the oxygen reduction process.

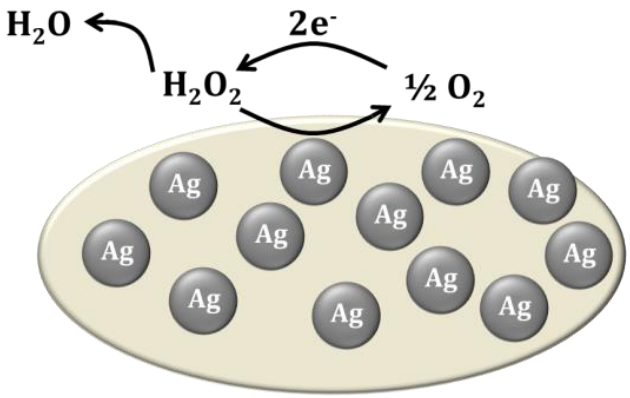


Figure 5.13 A scheme of the CE mechanism.

References

1. Cai, X. S.; Tanner, E. E. L.; Lin, C. H.; Ngamchuea, K.; Foord, J. S.; Compton, R. G., The mechanism of electrochemical reduction of hydrogen peroxide on silver nanoparticles. *Phys Chem Chem Phys* **2018,** *20* (3), 1608-1614.

2. Welch, C. M.; Banks, C. E.; Simm, A. O.; Compton, R. G., Silver nanoparticle assemblies supported on glassy-carbon electrodes for the electro-analytical detection of hydrogen peroxide. *Anal Bioanal Chem* **2005,** *382* (1), 12-21.

3. Chen, S. H.; Yuan, R.; Chai, Y. Q.; Hu, F. X., Electrochemical sensing of hydrogen peroxide using metal nanoparticles: a review. *Microchim Acta* **2013,** *180* (1-2), 15-32.

4. Chen, Z. Y.; Li, C. L.; Ni, Y. Y.; Kong, F. T.; Zhang, Y. B.; Kong, A. G.; Shan, Y. K., TCNQ-induced in-situ electrochemical deposition for the synthesis of silver nanodendrites as efficient bifunctional electrocatalysts. *Electrochim Acta* **2017,** *239*, 45-55.

5. Ramezani, H.; Azizi, S. N.; Hosseini, S. R., NaY zeolite as a platform for preparation of Ag nanoparticles arrays in order to construction of H_2O_2 sensor. *Sensor Actuat B-Chem* **2017,** *248*, 571-579.

6. Zhang, N.; Sheng, Q. L.; Zhou, Y. Z.; Dong, S. Y.; Zheng, J. B., Synthesis of FeOOH@PDA-Ag nanocomposites and their application for electrochemical sensing of hydrogen peroxide. *J Electroanal Chem* **2016,** *781*, 315-321.

7. Wang, Q.; Hu, S. S.; Yang, T.; Ma, S. S.; Liu, Y. H.; Ma, C. X.; Wan, M. M.; Mao, C., A novel H_2O_2 biosensor based on three-dimensional micro/nano-biointerfaces. *J Mater Chem B* **2017,** *5* (22), 4233-4238.

8. Kurowska-Tabor, E.; Jaskula, M.; Sulka, G. D., Sensitive Amperometric Sensing of Hydrogen Peroxide Using Ag Nanowire Array Electrode. *Electroanal* **2015,** *27* (8), 1968-1978.

9. Wang, H. D.; Wang, H. H.; Li, T. F.; Ma, J.; Li, K.; Zuo, X., Silver nanoparticles selectively deposited on graphene-colloidal carbon sphere composites and their application for hydrogen peroxide sensing. *Sensor Actuat B-Chem* **2017,** *239*, 1205-1212.

10. Jiang, L. Y.; Hu, J. P.; Foord, J. S., Electroanalysis of Hydrogen Peroxide at Boron Doped Diamond Electrode Modified by Silver Nanoparticles and Haemoglobin. *Electrochim Acta* **2015,** *176*, 488-496.

11. Habibi, B.; Jahanbakhshi, M., Sensitive determination of hydrogen peroxide based on a novel nonenzymatic electrochemical sensor: silver nanoparticles decorated on nanodiamonds. *J Iran Chem Soc* **2015,** *12* (8), 1431-1438.

12. Bartlett, T. R.; Holter, J.; Young, N.; Compton, R. G., Nanoelectrode array formation by electrolytic nanoparticle impacts. *Nanoscale* **2016,** *8* (29), 13908-13914.

13. Mattarozzi, L.; Cattarin, S.; Comisso, N.; Guerriero, P.; Musiani, M.; Verlato, E., Preparation of porous nanostructured Ag electrodes for sensitive electrochemical detection of hydrogen peroxide. *Electrochim Acta* **2016,** *198*, 296-303.

14. Niu, X. H.; Shi, L. B.; Pan, J. M.; Qiu, F. X.; Yan, Y. S.; Zhao, H. L.; Lan, M. B., Modulating the Assembly of Sputtered Silver Nanoparticles on Screen-Printed Carbon Electrodes for Hydrogen Peroxide Electroreduction: Effect of the Surface Coverage. *Electrochim Acta* **2016,** *199*, 187-193.

15. Shamkhalichenar, H.; Choi, J. W., An Inkjet-Printed Non-Enzymatic Hydrogen Peroxide Sensor on Paper. *Journal of the Electrochemical Society* **2017,** *164* (5), B3101-B3106.

16. Neumann, C. C. M.; Laborda, E.; Tschulik, K.; Ward, K. R.; Compton, R. G., Performance of silver nanoparticles in the catalysis of the oxygen reduction reaction in neutral media: Efficiency limitation due to hydrogen peroxide escape. *Nano Res* **2013,** *6* (7), 511-524.

17. Guidelli, R.; Compton, R. G.; Feliu, J. M.; Gileadi, E.; Lipkowski, J.; Schmickler, W.; Trasatti, S., Defining the transfer coefficient in electrochemistry: An assessment (IUPAC Technical Report). *Pure Appl Chem* **2014,** *86* (2), 245-258.

18. Guidelli, R.; Compton, R. G.; Feliu, J. M.; Gileadi, E.; Lipkowski, J.; Schmickler, W.; Trasatti, S., Definition of the transfer coefficient in electrochemistry (IUPAC Recommendations 2014). *Pure Appl Chem* **2014,** *86* (2), 259-262.

19. Dickinson, E. J. F.; Limon-Petersen, J. G.; Rees, N. V.; Compton, R. G., How Much Supporting Electrolyte Is Required to Make a Cyclic Voltammetry Experiment Quantitatively "Diffusional"? A Theoretical and Experimental Investigation. *J Phys Chem C* **2009,** *113* (25), 11157-11171.

20. Ngamchuea, K.; Eloul, S.; Tschulik, K.; Compton, R. G., Advancing from Rules of Thumb: Quantifying the Effects of Small Density Changes in Mass Transport to Electrodes. Understanding Natural Convection. *Anal Chem* **2015,** *87* (14), 7226-7234.

21. Davies, T. J.; Banks, C. E.; Compton, R. G., Voltammetry at spatially heterogeneous electrodes. *J Solid State Electr* **2005,** *9* (12), 797-808.

22. Godino, N.; Borrise, X.; Munoz, F. X.; del Campo, F. J.; Compton, R. G., Mass Transport to Nanoelectrode Arrays and Limitations of the Diffusion Domain Approach: Theory and Experiment. *J Phys Chem C* **2009,** *113* (25), 11119-11125.

23. Davies, T. J.; Ward-Jones, S.; Banks, C. E.; del Campo, J.; Mas, R.; Munoz, F. X.; Compton, R. G., The cyclic and linear sweep voltammetry of regular arrays of microdisc electrodes: Fitting of experimental data. *J Electroanal Chem* **2005,** *585* (1), 51-62.

24. Belding, S. R.; Campbell, F. W.; Dickinson, E. J. F.; Compton, R. G., Nanoparticle-modified electrodes. *Phys Chem Chem Phys* **2010,** *12* (37), 11208-11221.

25. Compton, R. G.; Laborda, E.; Ward, K. R., *Understanding Voltammetry: Simulation of Electrode Processes*. Imperial College Press: London, 2014; p 1-249.

26. Fick, A., On Liquid Diffusion. *J Membrane Sci* **1995,** *100* (1), 33-38.

27. Butler, J. A. V., Studies in heterogeneous equilibria. Part II.-The kinetic interpretation of the nernst theory of electromotive force. *Transactions of the Faraday Society* **1924,** *19* (March), 729-733.

28. Erdey-Grúz, T.; Volmer, M., Zur theorie der wasserstoff überspannung. *Zeitschrift für physikalische Chemie* **1930,** *150A* (1), 203-213.

29. van Stroe-Biezen, S. A. M.; Everaerts, F. M.; Janssen, L. J. J.; Tacken, R. A., Diffusion Coefficients of Oxygen, Hydrogen Peroxide and Glucose in a Hydrogel. *Anal Chim Acta* **1993,** *273* (1-2), 553-560.

30. Shimizu, K.; Sepunaru, L.; Compton, R. G., Innovative catalyst design for the oxygen reduction reaction for fuel cells. *Chem Sci* **2016,** *7* (5), 3364-3369.

31. Sokolov, S. V.; Sepunaru, L.; Compton, R. G., Taking cues from nature: Hemoglobin catalysed oxygen reduction. *Applied Materials Today* **2017,** *7*, 82-90.

32. Compton, R. G.; Banks, C. E., *Understanding Voltammetry*. 2nd ed.; Imperial College Press: 2011; p 1-429.

33. Wang, H.; Zhu, L. L.; Yang, L. L.; Liao, F.; Sheng, M. Q.; Jiang, B. B.; Shao, M. W., Prominent electrocatalytic methanol oxidation from cauli-flower shape gold with high-index facets. *Mater Chem Phys* **2017,** *186*, 301-304.

34. Gan, P.; Foord, J. S.; Compton, R. G., Surface Modification of Boron-Doped Diamond with Microcrystalline Copper Phthalocyanine: Oxygen Reduction Catalysis. *ChemistryOpen* **2015,** *4* (5), 606-612.

35. Cardwell, T. J.; Mocak, J.; Santos, J. H.; Bond, A. M., Preparation of microelectrodes: Comparison of polishing procedures by statistical analysis of voltammetric data. *Analyst* **1996,** *121* (3), 357-362.

36. Campbell, F. W.; Belding, S. R.; Baron, R.; Xiao, L.; Compton, R. G., Hydrogen Peroxide Electroreduction at a Silver-Nanoparticle Array: Investigating Nanoparticle Size and Coverage Effects. *J Phys Chem C* **2009,** *113* (21), 9053-9062.

37. Toh, H. S.; Batchelor-McAuley, C.; Tschulik, K.; Uhlemann, M.; Crossley, A.; Compton, R. G., The anodic stripping voltammetry of nanoparticles: electrochemical evidence for the surface agglomeration of silver nanoparticles. *Nanoscale* **2013,** *5* (11), 4884-4893.

38. Cloake, S. J.; Toh, H. S.; Lee, P. T.; Salter, C.; Johnston, C.; Compton, R. G., Anodic Stripping Voltammetry of Silver Nanoparticles: Aggregation Leads to Incomplete Stripping. *ChemistryOpen* **2015,** *4* (1), 22-26.

39. Katsounaros, I.; Schneider, W. B.; Meier, J. C.; Benedikt, U.; Biedermann, P. U.; Auer, A. A.; Mayrhofer, K. J. J., Hydrogen peroxide electrochemistry on platinum: towards understanding the oxygen reduction reaction mechanism. *Phys Chem Chem Phys* **2012,** *14* (20), 7384-7391.

40. Appleby, A. J., Oxygen Reduction and Corrosion Kinetics on Phase-Oxide-Free Palladium and Silver Electrodes as a Function of Temperature in 85% Orthophosphoric Acid. *Journal of the Electrochemical Society* **1970,** *117* (11), 1373-1378

41. Sanchez-Sanchez, C. M.; Bard, A. J., Hydrogen Peroxide Production in the Oxygen Reduction Reaction at Different Electrocatalysts as Quantified by Scanning Electrochemical Microscopy. *Anal Chem* **2009,** *81* (19), 8094-8100.

Chapter 6 Investigating the effects on hydrogen peroxide electro-reduction at silver nanoparticle modified boron doped diamond electrodes

The previous Chapter 5 has revealed the electro-reduction mechanism of hydrogen peroxide on silver nanoparticles, and thus this Chapter further focuses on the analytical determination of hydrogen peroxide. The aim of this Chapter is to explore several factors involving the hydrogen peroxide reduction behaviour, including silver loading, nanoparticle size, and nanoparticle modification method for a preliminary research as a guideline when it comes to optimise electroanalytical activity of silver modified electrodes towards the reduction of H_2O_2 for detection.

6.1 Introduction

Detection of hydrogen peroxide (H_2O_2) is of significance due to its wide applications in the paper product, environmental industry, and food processing sector as a sterilising and chlorine-free bleaching chemical.[1-3] Despite being greatly useful in industry, hydrogen peroxide may create negative side effects including food poisoning due to excessive amounts of residuals such as in noodles and udon,[4] which promotes the development of H_2O_2 detection methods. Among the techniques for H_2O_2 sensing, including chemiluminescence and spectrometry, electrochemistry has been shown to be a simple and effective approach, and thus extensively used for the detection of H_2O_2. Recent studies have showed that silver nanoparticles (AgNPs) exhibit excellent electrocatalytic activity for the reduction of H_2O_2,[5-7] and have attracted increasing attention, due to easy synthesis, quantum characteristics of small granule diameter, and large specific surface area with a high thermal and electrical conductivity.[8-9] Importantly, hydrogen peroxide electro-

reduction mechanism at AgNPs modified boron doped diamond (BDD) substrates has been revealed in Chapter 5,[10] which provides a general understanding background for application-focused electrochemical determination studies in order to optimise any system that depends on H_2O_2 reduction. During the detection, the reduction of oxygen and hydrogen peroxide may occur simultaneously.

It is known that the catalytic performance for chemically modified electrodes utilizing metal nanoparticles relies significantly on many factors including particle structure, and particle size.[11] For example, flowerlike silver microspheres with nanostructure has been fabricated for H_2O_2 detection.[12] Waqas et al have synthesised AgNPs with three different shapes including spheres, stars and pyramids, and the star shape AgNPs exhibit highest performance towards hydrogen peroxide reduction.[13] In addition, capping agents are generally introduced to the commercial nanoparticle surface to improve the stability of nanoparticles. However, it may result in the changed activity such as lower catalytic performance.[14] For comparison, AgNPs can be freshly electrodeposited without capping agents or dropped cast onto electrodes using citrate capping agents in terms of electrode decoration routes. However, there are few reports on the direct electroanalytical determination of H_2O_2 using pure AgNPs modified electrodes, and many factors remain unclear. Therefore in this study, the aim of this Chapter is to explore these effects, to be specific, AgNPs loading, the nanoparticle size and the deposition method of AgNPs on the electrochemical catalytic performance of AgNPs/BDD electrodes towards hydrogen peroxide reduction.

6.2 Experimental

6.2.1 Chemical reagents

The chemical reagents sodium dihydrogen phosphate (NaH_2PO_4, ≥ 99.0%), Sodium hydrogen phosphate (Na_2HPO_4, ≥ 99.0%), and silver nanoparticles dispersion were bought from Sigma-Aldrich. The diameters of AgNPs at a concentration of 0.02 mg mL^{-1} are 10 nm and 60 nm, respectively. Hydrogen peroxide was purchased from Fisher Scientific International, Inc. The chemicals including sodium acetate (CH_3COONa), acetic acid (CH_3COOH), silver nitrate ($AgNO_3$, ≥ 99.0%) were obtained from Sigma-Aldrich and are of A.C.S. reagent grade. All the reagents were used as supplied, and all solutions were made with purified water (18.2 MΩ cm resistivity at 25 ^oC, Millipore, MA, USA).

6.2.2 Apparatus and electrochemical measurements

Electrochemical experiments were carried out using an Autolab PGSTAT128N potentiostat (Metrohm Autolab, Utrecht, Netherlands). A three-electrode system was utilised including a platinum (Pt) coil counter electrode, a Ag/AgCl reference electrode and a boron-doped-diamond working electrode. All the potentials reported in this study were measured against the Ag/AgCl electrode, unless specified. The supporting electrolyte for all experiments was 0.10 M phosphate buffer solution (PBS, pH = 7.2). Degassed solutions were bubbled with nitrogen for 15 min.

6.2.3 Electrode modification

The boron-doped-diamond substrate (Element Six Co.) with a boron doping level of ~ 5×10^{20} atoms cm^{-3} was mounted in a home-made polytetrafluoroethylene holder as previously described[15] with an exposed circular area of 0.37 cm^2 to the electrolyte. Before each experiment, the BDD electrode was polished and cleaned on lapping pads using alumina

powder (Buehler, MicroPolish II) in the size sequence of 1 μm, 0.3 μm and 0.05 μm and diamond suspension (Buehler, MetaDi) in the size of 9 μm, 1 μm and 0.1 μm.[16]

To modify the BDD electrode (BDDE), different amount of AgNPs dispersion was drop-cast onto the electrode surface, and left to dry, herein referred to as AgNPs-BDDE. The silver modified electrode was characterised by a Hitachi S-4300 field emission scanning electron microscopy (SEM, Japan). The AgNPs-BDDE was also prepared by electrodeposition. A constant potential of - 0.1 V *vs.* Ag/AgCl was applied in the electrolyte of 0.10 M acetate buffer containing 1.0 mM $AgNO_3$ for different deposition times of 70, 100, 200 s at room temperature to compare with the drop-cast method.

The chronoamperometry experiments were performed by applying -0.6 V (vs. Ag/AgCl) on successive injection of hydrogen peroxide into the stirring 0.10 M PBS in a format of rotating disk electrode at a speed of 1200 revolutions per minute.

6.3 Results and Discussion

6.3.1 Effect of silver nanoparticle loading

There are a number of effects on the electrocatalytic reduction of hydrogen peroxide, and mass loading of electrocatalysts would have come to the mind at first. So different loadings of Ag nanoparticles were drop-coated on the BDDE for the electroanalysis of hydrogen peroxide. The morphology of AgNPs of 10 nm modified boron doped diamond electrode was characterised by scanning electron microscopy as a typical example. Figure 6.1 shows that the silver nanoparticles are dispersed over the BDDE surface, demonstrating the successful modification of the electrode via drop-casting. Some nanoparticle aggregations or assemblies can be observed in Figure 6.1.

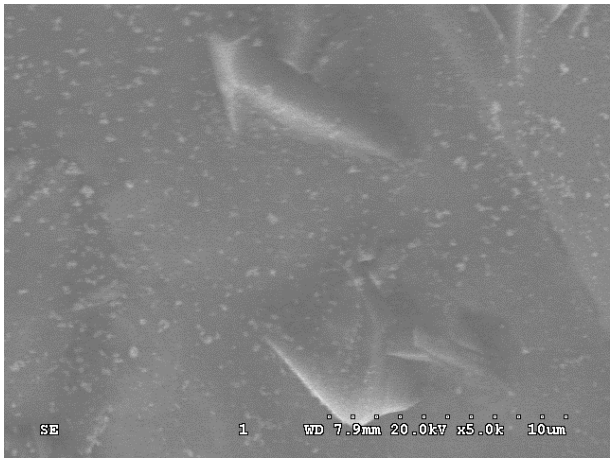


Figure 6.1 SEM images of AgNPs-BDDE with a mass loading of 2.0 μg at a magnification of 5000×.

AgNPs deposits were characterised by performing cyclic voltammetry experiments in 0.10 M PBS. Figure 6.2(a) shows the cyclic voltammograms (CVs) obtained at the bare BDDE and AgNPs-BDDE at a scan rate of 0.05 V s^{-1}. For the bare BDDE, no redox peak can be observed in the whole scan range. For AgNPs (10 nm)-BDDE, CV scans were conducted with different loadings of AgNPs for 10, 25, 50 and 100 μl of their respective dispersions. Anodic and cathodic peaks for each loading are observed in Ag-modified BDDE, which are assigned to the stripping of electrodeposited silver and reduction of Ag^+ to Ag, respectively, and could demonstrate the existence of AgNPs.[17-18] In addition, it also shows that the oxidation peak current increases with increasing amount of Ag.

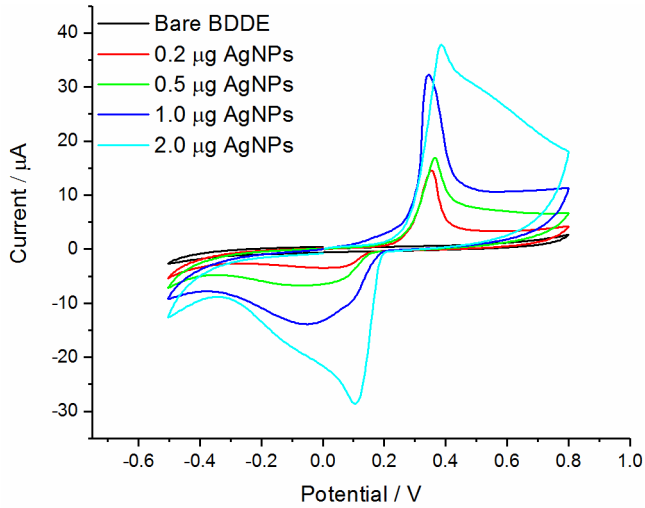


Figure 6.2 CVs of Ag peak for the bare BDDE and prepared AgNPs-BDDE with different Ag loadings in 0.10 M deoxygenated PBS recorded at a scan rate of 0.05 V s^{-1}.

In order to test the electrocatalytic response properties of the AgNPs-BDDE towards hydrogen peroxide reduction, a series of voltammetric experiments was conducted with different loading deposits obtained by drop casting. The four deposit modified electrodes were characterised in 0.10 M PBS containing different concentrations of 0.08 - 0.64 mM H_2O_2 at a scan rate of 0.05 V s^{-1}. As shown in Figure 6.3, for all the different loadings of AgNPs, the cathodic peak current increases with the H_2O_2 concentration from 0.08 to 0.64 mM, indicating the typical electrocatalytic behaviour towards the H_2O_2 reduction. With the increase amount of AgNPs, the H_2O_2 reduction peak shape is becoming clearly defined, especially for the silver loading of 2.0 µg, which is a monolayer coverage and used as a standard loading reference for the following experiments. Furthermore, it is interesting to study the electrochemical response difference with different AgNPs loading for the same concentration of H_2O_2 and therefore 0.64 mM was chosen as an example for comparison. As shown in Figure 6.3(e), it shows four curves corresponding to increasing AgNPs loading on the electrode surface. As the mass loading increases, the reduction peak is becoming more obvious and shifts positively to smaller overpotentials. This sensitivity for

the voltammograms to mass loading or coverage agree with the previous report due to diffusion layers of neighbouring nanoparticles becoming more heavily overlapping.[19] In addition, for each loading of AgNPs separately, the relationship between peak current and H_2O_2 concentration is linear in Figure 6.3(f). For the same H_2O_2 concentration, the H_2O_2 reduction peak current enhances as well with the increasing of AgNPs loadings, indicating more Ag deposits onto BDDE are responsible for highly sensitive electrocatalytic H_2O_2 reduction process.

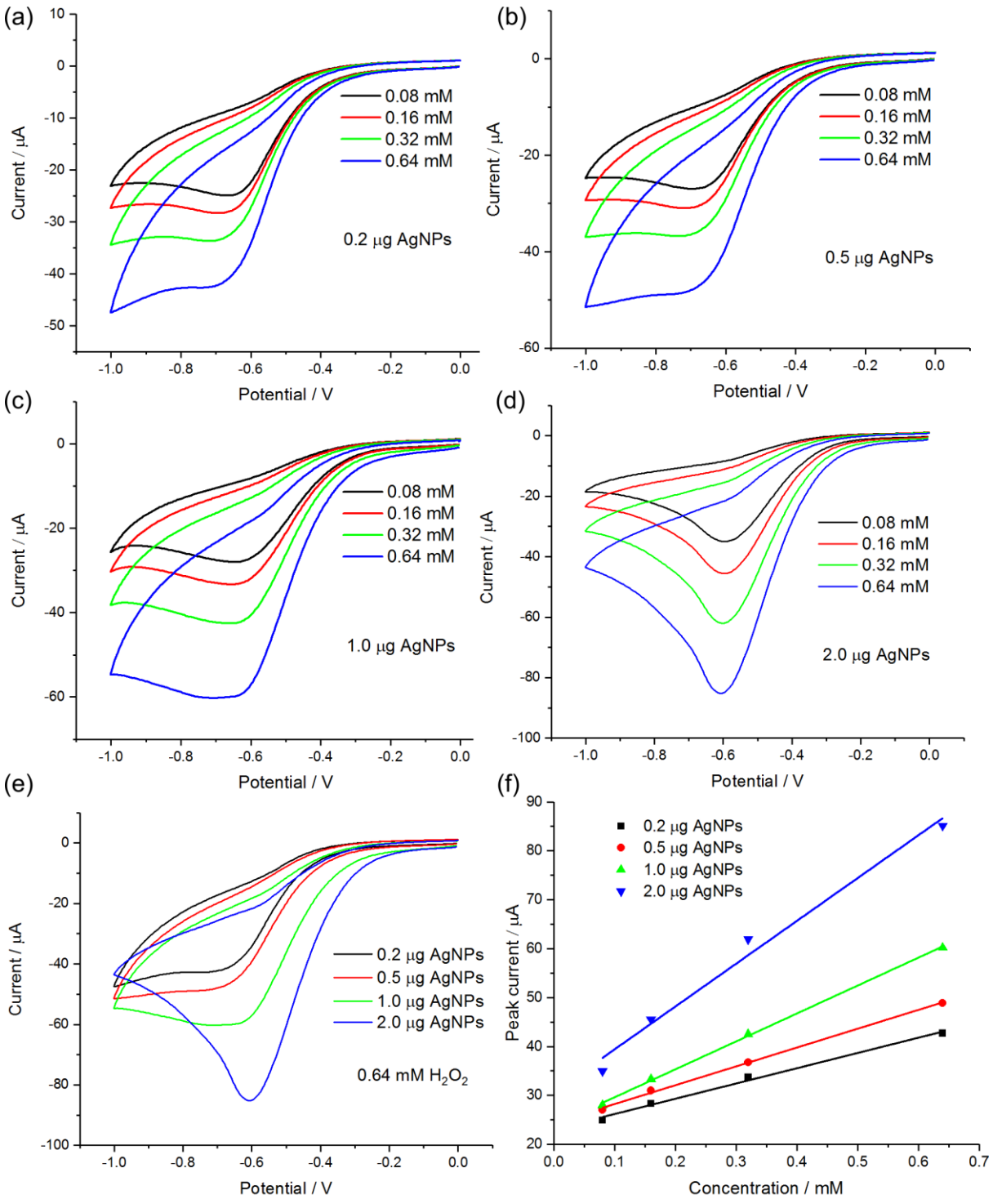


Figure 6.3 CVs of various H_2O_2 concentrations (0.08 - 0.64 mM) in 0.10 M PBS at BDDE modified by AgNPs (10nm) of different loadings of (a) 0.2 µg, (b) 0.5 µg, (c) 1.0 µg, and (d) 2.0 µg at a scan rate of 0.05 V s^{-1}, (e) CVs of 0.64 mM H_2O_2 at different loading AgNPs, (f) the fitting plot of H_2O_2 reduction peak current *versus* H_2O_2 concentration.

6.3.2 Effect of silver nanoparticle size

It is of significance to evaluate the effect of particle sizes to attain the optimal conditions for nanoparticle based device applications. Therefore two different sizes of 10 nm and 60 nm AgNPs were compared. The mass loading for both was chosen at the same amount of 2.0 µg using their respective dispersions of 100 µl. The surface coverage can be estimated at about 76% and 13% according to the nanoparticle size and the number concentrations of 3.6×10^{12} NPs/mL and 1.7×10^{10} NPs/mL for 10 nm and 60 nm, respectively. The characteristic AgNPs peak was examined as shown in Figure 6.4(a), where the oxidation peak current for 10 nm AgNP is about 30 times higher than that of 60 nm AgNP. Furthermore the effect of nanoparticle size was analysed on the electrocatalytic activity towards H_2O_2 reduction by cyclic voltammetry in 0.10 M PBS solution within the potential range of 0 to -1.0 V. As shown in Figure 6.4(b), for AgNPs (10nm)-BDDE, obvious H_2O_2 reduction peaks are observed, indicating that Ag nanoparticles exhibits good electrocatalytic ability towards the H_2O_2 reduction. Meanwhile, H_2O_2 reduction peak current increases gradually with the increasing of H_2O_2 concentration from 0.01 mM to 0.04 mM. However, for AgNPs (60 nm)-BDDE, although it still shows higher reduction current response with the increment of H_2O_2 concentration, a significant peak shape response cannot be observed in the whole scan range compared to Ag of 10 nm. This may be a result of increasing of effective electroactive surface area and better electron transfer of AgNPs in terms of the larger surface-to-volume ratio of the smaller AgNPs of 10 nm compared to 60 nm,[7] accounting for the better electrocatalytic H_2O_2 reduction using smaller AgNPs.[18]

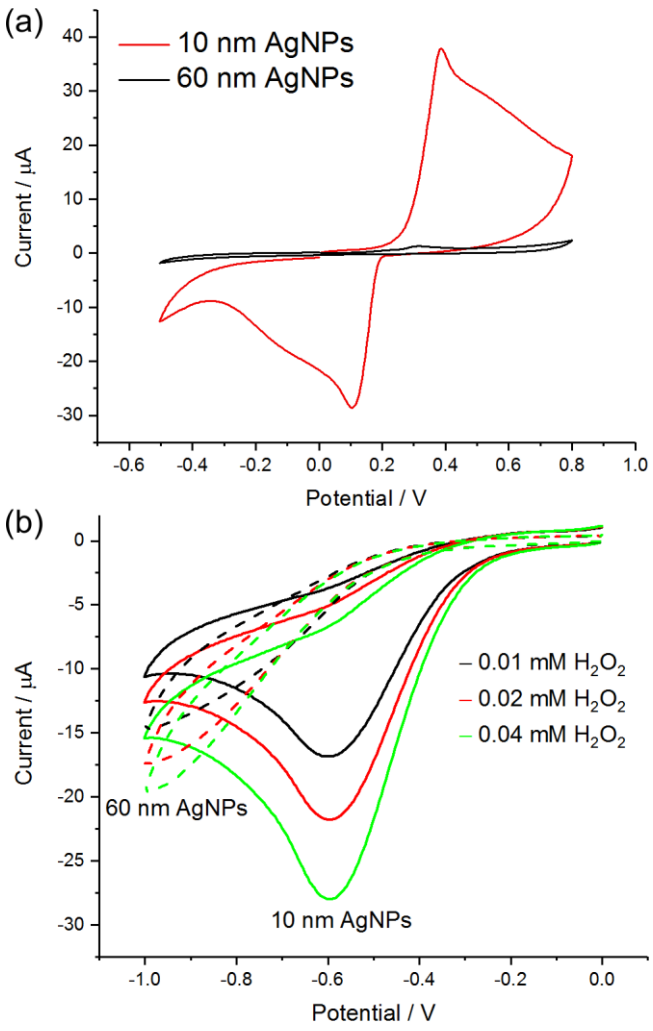


Figure 6.4 (a) CVs of AgNPs with different sizes of 10 and 60 nm in 0.10 M PBS solution; (b) CVs of various H_2O_2 concentrations (0.01, 0.02, and 0.04 mM) in 0.10 M PBS solution using AgNPs of 10 and 60 nm at a scan rate of 0.05 V s^{-1}.

6.3.3 Comparison of electrodeposition and drop-casting methods

Electrodeposition method has been commonly employed for preparation of metal nanoparticles onto electrode surface since it can offer an advantage of excellent electronic conductivity between particles and working electrode, compared to the drop coating of pre-synthesized metal NPs onto electrodes.[20] Therefore for comparison, silver was prepared by chronoamperometry electrodeposition technique onto BDDE through the reduction of metallic ions in 0.10 M acetate buffer containing 1.0 mM $AgNO_3$ at an applied potential

of -0.1 V vs Ag/AgCl. As it is generally known that deposition time influences the mass amount,[21] different deposition times of 70 s, 100 s and 200 s have been investigated, and the corresponding deposition curves are shown in Figure 6.5. For all the three curves, an initial high cathodic current is observed as a result of the double-layer charging, and nuclei are formed at this early stage. Then, the current decays which follows Cottrell's law, corresponding to a planar diffusion regime due to the overlapping of the growing hemispherical diffusion fields of neighbouring nanoparticles.[22]

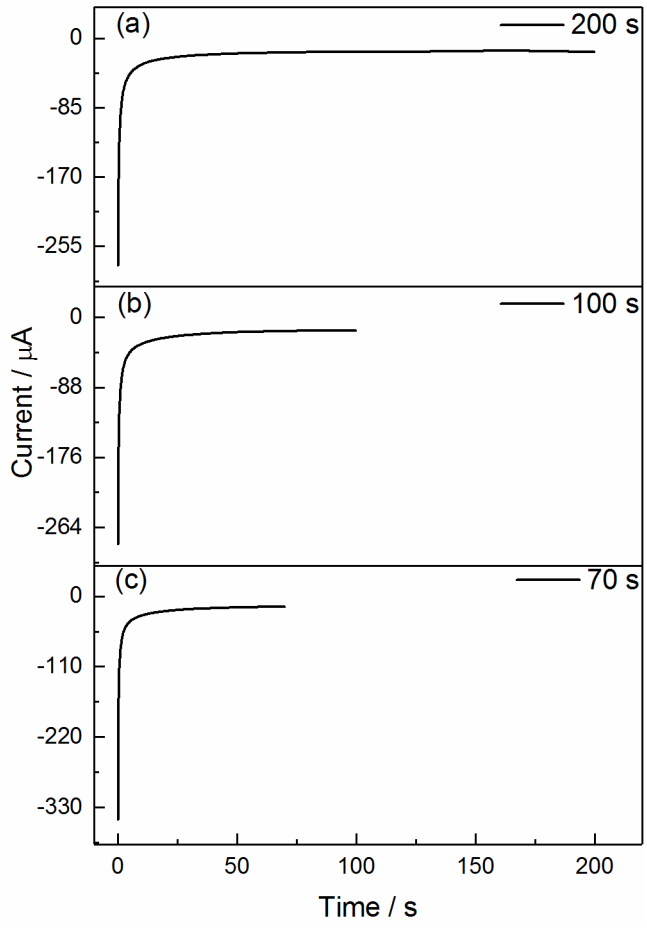


Figure 6.5 The current-time transient curves of silver electrodeposition by applying a constant potential of -0.1 V for different times of (a) 200 s, (b) 100 s, (c) 70 s in 0.10 M acetate buffer containing 1.0 mM $AgNO_3$.

The silver peaks were characterised, and as shown in Figure 6.6, the anodic and cathodic peak are at 0.41 and 0.086 V, respectively. Meanwhile, the silver peaks increase with the longer deposition time.

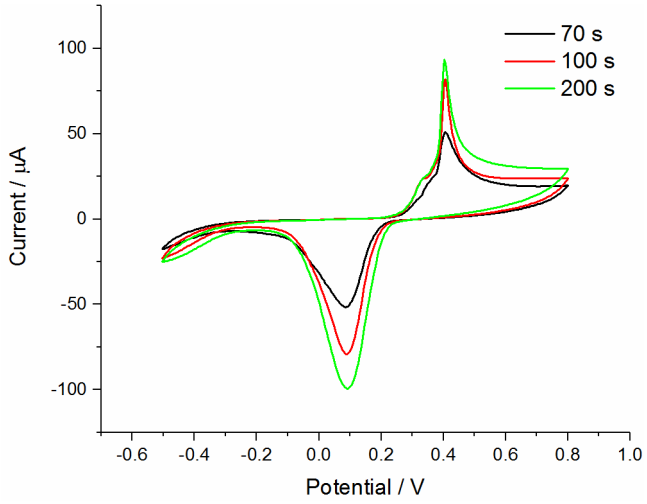


Figure 6.6 CVs of AgNPs for different electrodeposition times at a scan rate of 0.05 V s^{-1}.

The deposition amount of silver can be calculated from coulometry, which is 1.9, 2.6, 4.4 µg for different deposition times of 70 s, 100 s, 200 s, respectively. The deposition amount of 1.9 µg is comparable with that using drop-casting of 100 µl AgNPs dispersion (10 nm, 2.0 µg), which is used for further comparison of the following experiments. In order to characterise the deposits, SEM were performed. As shown in Figure 6.7(a), the silver particles synthesized by chronoamperometry technique at a deposition time of 70 s are dispersed uniformly on the BDDE. From Figure 6.7(b), most of the AgNPs are dozens of nanometres while fewer bigger nanoparticles are about 100 nm.

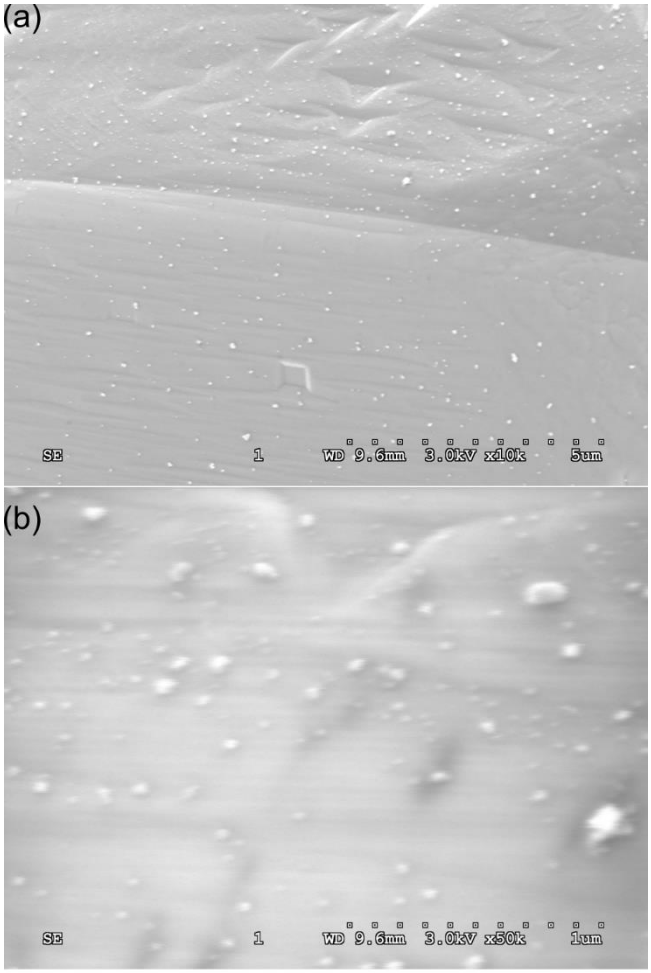


Figure 6.7 SEM images of AgNPs-BDDE by chronoamperometry deposition technique for 70 s under different magnifications of 10000× (a), and 50000× (b).

Then the response performance of AgNPs for drop casting and electrodeposition methods towards H_2O_2 reduction are compared. The low H_2O_2 concentrations of 0.01, 0.02, 0.04 mM were tested to evaluate the response using the above two modified electrodes by drop-casting of 10 nm (2.0 μg) and electrodeposition of 1.9 μg. As shown in Figure 6.8, the H_2O_2 reduction peak current using electrodeposition method is larger than that using drop-casting method, showing better electrocatalytic ability for H_2O_2 reduction. In addition, the reduction peak shifts positively from -0.6 to -0.57 V when AgNPs decoration switches from drop-casting to electrodeposition. These observations may be due to better kinetics between silver and electrode arising from uniform distribution of AgNPs and better

interaction between Ag and BDDE surface via electrodeposition enabling electron transfer during H_2O_2 reduction process.

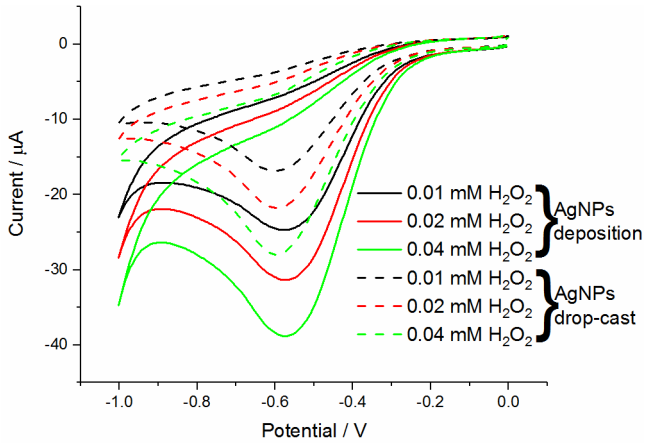


Figure 6.8 CVs of AgNPs-BDDE prepared by drop-casting and electrodeposition at a scan rate of 0.05 V s^{-1} in 0.10 M PBS containing different H_2O_2 concentrations of 0.01, 0.02 and 0.04 mM.

6.3.4 Amperometric determination of H_2O_2

The analytical detection for the AgNPs modified BDDE was evaluated using amperometric technique. Amperometric experiments were conducted at an applied potential of -0.6 V with injection of different H_2O_2 concentrations into a continuous stirred PBS. The above two superior AgNPs-BDDE were selected for amperometric experiment comparison.

Figure 6.9(a) shows the amperometric current response for the two AgNPs-BDDEs. The current increases with the successive addition of hydrogen peroxide. For the injection of same H_2O_2 concentration, the current response of AgNPs-BDDE by electrodeposition is higher that of drop-casting. The current response *versus* H_2O_2 concentrations is depicted in Figure 6.9(b), which shows a linear relationship from 0.08 to 1.2 mM. From the slope of the corresponding calibration curves, the sensitivities were calculated to be 18.3 and 5.5 µA/mM for electrodeposition and drop-casting, respectively. Accordingly, these two

modified electrodes display a limit of detection (LOD) of 3.99 μM and 5.85 μM at a signal-to-noise ratio of 3, respectively. These results suggest that the AgNPs-BDDE modified by electrodeposition exhibits better performance on H_2O_2 determination with higher sensitivity and better LOD, which is consistent with the results discussed above.

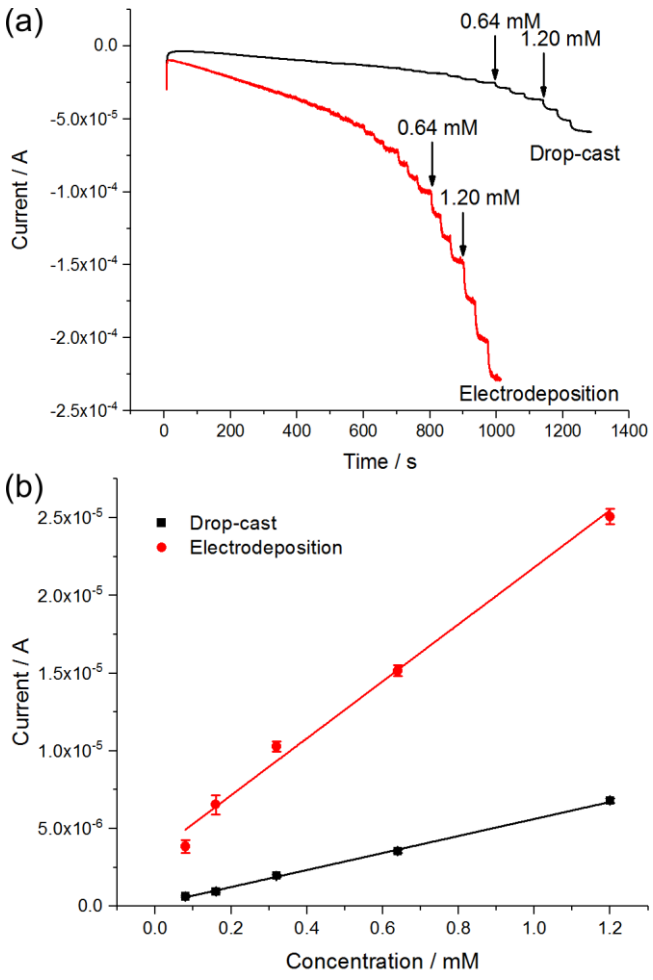


Figure 6.9 (a) Amperometric response of H_2O_2 using different AgNPs-BDDEs by drop-casting and electrodeposition methods; (b) the plot of response current *vs.*H_2O_2 concentration at an applied potential of -0.6 V.

6.4 Conclusions

Silver nanoparticle modified boron doped diamond electrodes via drop-casting and electrodeposition were employed to study the electrochemically irreversible reduction of

hydrogen peroxide. A number of factors are involved in influencing the performance during the hydrogen peroxide reduction behaviour. The hydrogen peroxide reduction peak shifts positively with increasing nanoparticle mass loading while decreasing the nanoparticle size promotes the electrocatalytic ability towards H_2O_2 reduction. Homogeneous silver nanoparticles can be deposited onto electrodes for short electrodeposition times by chronoamperometry technique, which provides better analytical response towards hydrogen peroxide detection than drop casting for the comparable silver mass loading. The resulting observations may have important implications for the development of nanoparticle-based sensors.

References

1. Kurowska, E.; Brzozka, A.; Jarosz, M.; Sulka, G. D.; Jaskula, M., Silver nanowire array sensor for sensitive and rapid detection of H_2O_2. *Electrochim Acta* **2013,** *104*, 439-447.

2. Chekin, F.; Ghasemi, S., Silver nanoparticles prepared in presence of ascorbic acid and gelatin, and their electrocatalytic application. *Bull Mater Sci* **2014,** *37* (6), 1433-1437.

3. Chen, W.; Cai, S.; Ren, Q. Q.; Wen, W.; Zhao, Y. D., Recent advances in electrochemical sensing for hydrogen peroxide: a review. *Analyst* **2012,** *137* (1), 49-58.

4. Lu, C. P.; Lin, C. T.; Chang, C. M.; Wu, S. H.; Lo, L. C., Nitrophenylboronic Acids as Highly Chemoselective Probes To Detect Hydrogen Peroxide in Foods and Agricultural Products. *J Agr Food Chem* **2011,** *59* (21), 11403-11406.

5. Jiang, L. Y.; Hu, J. P.; Foord, J. S., Electroanalysis of Hydrogen Peroxide at Boron Doped Diamond Electrode Modified by Silver Nanoparticles and Haemoglobin. *Electrochim Acta* **2015,** *176*, 488-496.

6. Safavi, A.; Maleki, N.; Farjami, E., Electrodeposited Silver Nanoparticles on Carbon Ionic Liquid Electrode for Electrocatalytic Sensing of Hydrogen Peroxide. *Electroanal* **2009,** *21* (13), 1533-1538.

7. Maji, S. K.; Dutta, A. K.; Srivastava, D. N.; Paul, P.; Mondal, A.; Adhikary, B.; Adhikary, U., Electrocatalytic Activity of Silver Nanoparticles Modified Glassy Carbon Electrode as Amperometric Sensor for Hydrogen Peroxide. *J Nanosci Nanotechno* **2013,** *13* (7), 4969-4974.

8. Chen, S. H.; Yuan, R.; Chai, Y. Q.; Hu, F. X., Electrochemical sensing of hydrogen peroxide using metal nanoparticles: a review. *Microchim Acta* **2013,** *180* (1-2), 15-32.

9. Gan, X.; Liu, T.; Zhong, J.; Liu, X. J.; Li, G. X., Effect of silver nanoparticles on the electron transfer reactivity and the catalytic activity of myoglobin. *Chembiochem* **2004,** *5* (12), 1686-1691.

10. Cai, X. S.; Tanner, E. E. L.; Lin, C. H.; Ngamchuea, K.; Foord, J. S.; Compton, R. G., The mechanism of electrochemical reduction of hydrogen peroxide on silver nanoparticles. *Phys Chem Chem Phys* **2018,** *20* (3), 1608-1614.

11. Chikae, M.; Idegami, K.; Kerman, K.; Nagatani, N.; Ishikawa, M.; Takamura, Y.; Tamiya, E., Direct fabrication of catalytic metal nanoparticles onto the surface of a screen-printed carbon electrode. *Electrochem Commun* **2006,** *8* (8), 1375-1380.

12. Zhao, B.; Liu, Z. R.; Liu, Z. L.; Liu, G. X.; Li, Z.; Wang, J. X.; Dong, X. T., Silver microspheres for application as hydrogen peroxide sensor. *Electrochem Commun* **2009,** *11* (8), 1707-1710.

13. Waqas, M.; Zulfiqar, A.; Ahmad, H. B.; Akhtar, N.; Hussain, M.; Shafiq, Z.; Abbas, Y.; Mehmood, K.; Ajmal, M.; Yang, M. H., Fabrication of highly stable silver nanoparticles with shape-dependent electrochemical efficacy. *Electrochim Acta* **2018,** *271*, 641-651.

14. Plowman, B. J.; Tschulik, K.; Young, N. P.; Compton, R. G., Capping agent promoted oxidation of gold nanoparticles: cetyl trimethylammonium bromide. *Phys Chem Chem Phys* **2015,** *17* (39), 26054-26058.

15. Gan, P.; Foord, J. S.; Compton, R. G., Surface Modification of Boron-Doped Diamond with Microcrystalline Copper Phthalocyanine: Oxygen Reduction Catalysis. *ChemistryOpen* **2015,** *4* (5), 606-612.

16. Cardwell, T. J.; Mocak, J.; Santos, J. H.; Bond, A. M., Preparation of microelectrodes: Comparison of polishing procedures by statistical analysis of voltammetric data. *Analyst* **1996,** *121* (3), 357-362.

17. Azizi, S. N.; Ghasemi, S.; Mikhchian, M., Microwave-assisted synthesis of NaA nanozeolite from slag and performance of Ag-doped nanozeolite as an efficient material for determination of hydrogen peroxide. *RSC Adv* **2016,** *6* (57), 52058-52066.

18. Afraz, A.; Rafati, A. A.; Hajian, A., Analytical sensing of hydrogen peroxide on Ag nanoparticles-multiwalled carbon nanotube-modified glassy carbon electrode. *J Solid State Electr* **2013,** *17* (7), 2017-2025.

19. Campbell, F. W.; Belding, S. R.; Baron, R.; Xiao, L.; Compton, R. G., Hydrogen Peroxide Electroreduction at a Silver-Nanoparticle Array: Investigating Nanoparticle Size and Coverage Effects. *J Phys Chem C* **2009,** *113* (21), 9053-9062.

20. Zhang, Y.; Wang, Z. Y.; Liu, S.; Zhang, T., In situ growth of Ag-reduced graphene oxide-carbon nanotube on indium tin oxide and its application for electrochemical sensing. *Mater Res Bull* **2016,** *84*, 355-362.

21. Lounasvuori, M. M.; Nelson, G. W.; Foord, J. S., Nanoparticle-Based Diamond Electrodes. In *Novel Aspects of Diamond: From Growth to Applications*, Second ed.; Yang, N., Ed. Springer: Cham, 2019; pp 257-312.

22. Hezard, T.; Fajerwerg, K.; Evrard, D.; Colliere, V.; Behra, P.; Gros, P., Influence of the gold nanoparticles electrodeposition method on Hg(II) trace electrochemical detection. *Electrochim Acta* **2012,** *73*, 15-22.

Chapter 7 Conclusions

This thesis has investigated the electrochemical behaviour of boron doped diamond electrodes modified by metal nanoparticles towards three different analytes that are commonly used in the food industry, namely sulphite, nitrite, and hydrogen peroxide. Boron doped diamond as a substrate shows great mechanical robustness and resistance to chemical corrosion, which makes it highly durable and easy to clean for reuse. Its low background current and anti-fouling properties make it an excellent material for electrochemical detection applications.

First, the electro-oxidation of sulphite has been investigated in acid media on gold macroelectrodes and gold nanoparticle modified boron doped diamond electrodes. Electrodeposition of gold particles was realised through a nucleation-growth pulse approach, which enabled the control over the particle size and morphologies with varying surface coverages. The sulphite oxidation on gold was shown to proceed through a one-electron transfer process followed by a chemical reaction of second order, overall an EC_2 mechanism. The mechanistic interpretation of sulphite electro-oxidation is of significance for application-focused sulphite detection when using electrochemical methods.

The electrodeposition of gold particles was further extended, and cyclic voltammetry deposition was compared with previous pulse deposition for nitrite electrochemical detection. Different deposit behaviours were reported. Cyclic voltammetry deposition resulted in an inhomogeneous distribution with increase of cyclic scans while pulse deposition was found to afford better size, morphology, and distribution control of the particles. Larger electroactive effective surface areas with higher surface coverages were indicated for pulse deposition while involving a lower amount of gold deposits and were responsible for the discussed better electroanalytical response towards nitrite detection.

Furthermore, the detection limit for such modified electrodes in nitrite determination via electrochemical detection is better than that using capillary electrophoresis technique where it is generally limited to μM or above, and meanwhile is comparable to that ranging between 0.02 and 2 μM using Griess assay based spectrophotometry. Spectrofluorimetric methods may show excellent limits of detection of around nM level. Although the detection limit for electrochemical detection needs to be improved, its low-cost and portability of devices offer appealing options with the extensive application of modified electrodes in nitrite detection.

In addition, the reduction of hydrogen peroxide on silver nanoparticle modified boron doped diamond electrodes has been analysed. A CE mechanism (a homogeneous chemical reaction followed by an electron transfer step) was proposed, whereby specifically the hydrogen peroxide decomposed to oxygen and water on the silver surface, and the oxygen was electrochemically reduced to hydrogen peroxide. This finding may be beneficial for optimising applications that involve hydrogen peroxide reduction such as sensing.

Finally, several factors involved in the hydrogen peroxide reduction behaviour were further examined. Increasing the mass loading and decreasing the size of silver nanoparticles promoted the electrocatalytic reduction process with enhanced peak current response. Silver nanoparticles by potentiostatic electrodeposition showed better electrical communication with boron doped diamond electrodes and higher electroanalytical capability towards hydrogen peroxide reduction than those using drop-casting method.

In summary, the results discussed in this thesis highlight the potential of using electrochemical methods to decipher the mechanistic process for a specific electrode reaction. Underpinning this work in fundamental studies, chemical reactions that are coupled to the electron transfer step, following or preceding the electron transfer, should

be considered, which may be homogeneous process (e.g. dimerization) or heterogeneous one (e.g. catalytic decomposition) on the electrode surface. In addition, this thesis demonstrates the modification of electrodes using metal particles by facile electrodeposition methods, which can control the morphology, size, loading, and coverage of metal particles on electrodes. Meanwhile this work emphasises a correlation between these effects and the analytical performance of the resulting modified electrodes towards analyte detection.

Last several efforts for future work can be suggested. For example, the effect of hydrogen- and oxygen-terminated boron doped diamond on the analyte detection might be explored. Although boron doped diamond plays an important role as an electrode material in sensing applications, different carbon forms such as glassy carbon owning different chemical properties are of interest in electrochemical studies and may be comparatively examined in order to establish desirable sensing platforms.